SMIP16

SMIP16 SEMINAR ON
UTILIZATION OF STRONG-MOTION DATA

Irvine, California
October 6, 2016

PROCEEDINGS

Sponsored by

California Strong Motion Instrumentation Program
California Geological Survey
California Department of Conservation

Co-Sponsors

California Seismic Safety Commission
California Governor's Office of Emergency Services
Office of Statewide Health Planning and Development
California Department of Transportation

The California Strong Motion Instrumentation Program (CSMIP), a program within the California Geological Survey (CGS) of the California Department of Conservation, records the strong shaking of the ground and structures during earthquakes for analysis and utilization by the engineering and seismology communities, through a statewide network of strong motion instruments (www.conservation.ca.gov/CGS/smip). CSMIP is advised by the Strong Motion Instrumentation Advisory Committee (SMIAC), a committee of the California Seismic Safety Commission. Major program funding is provided by an assessment on construction costs for building permits issued by cities and counties in California, with additional funding from the California Governor's Office of Emergency Services (Cal OES), the Office of Statewide Health Planning and Development (OSHPD) and the California Department of Transportation (Caltrans)

In July 2001, the California Governor's Office of Emergency Services (Cal OES) began funding for the California Integrated Seismic Network (CISN), a newly formed consortium of institutions engaged in statewide earthquake monitoring that grew out of TriNet, funded by FEMA, and including CGS, USGS, Caltech and UC Berkeley. The goals are to record and rapidly communicate ground shaking information in California, and to analyze the data for the improvement of seismic codes and standards (www.cisn.org). CISN produces ShakeMaps of ground shaking, based on shaking recorded by stations in the network, within minutes following an earthquake. The ShakeMap identifies areas of greatest ground shaking for use by OES and other emergency response agencies in the event of a damaging earthquake.

The Center for Engineering Strong Motion Data (CESMD) is operated by the CSMIP in cooperation with the National Strong-Motion Project (NSMP), a part of the Advanced National Seismic System (ANSS) of the U.S. Geological Survey (USGS). The CESMD builds on and incorporates the CISN Engineering Data Center and will continue to serve the California region while expanding to serve other ANSS regions. The Data Center provides strong-motion data rapidly after a significant earthquake in the United States. Users also have direct access to data from previous earthquakes and detailed information about the instrumented structures and sites. The CESMD also provides access to the U.S. and international strong ground motion records through its Virtual Data Center (VDC). The Data Center is co-hosted by CGS and USGS at www.strongmotioncenter.org

DISCLAIMER

SMIP16

SMIP16 SEMINAR ON
UTILIZATION OF STRONG-MOTION DATA

Irvine, California
October 6, 2016

PROCEEDINGS

Edited by

Moh Huang

Sponsored by

California Strong Motion Instrumentation Program
California Geological Survey
California Department of Conservation

Co-Sponsors

California Seismic Safety Commission
California Governor's Emergency Services
Office of Statewide Health Planning and Development
California Department of Transportation

PREFACE

The California Strong Motion Instrumentation Program (CSMIP) in the California Geological Survey of the California Department of Conservation established a Data Interpretation Project in 1989. Each year CSMIP funds several data interpretation contracts for the analysis and utilization of strong-motion data. The primary objectives of the Data Interpretation Project are to further the understanding of strong ground shaking and the response of structures, and to increase the utilization of strong-motion data in improving post-earthquake response, seismic code provisions and design practices.

As part of the Data Interpretation Project, CSMIP holds annual seminars to transfer recent research findings on strong-motion data to practicing seismic design professionals, earth scientists and post-earthquake response personnel. The purpose of the annual seminar is to provide information that will be useful immediately in seismic design practice and post-earthquake response, and in the longer term, useful in the improvement of seismic design codes and practices. Proceedings and individual papers for each of the previous annual seminars are available at http://www.conservation.ca.gov/cgs/smip/docs/seminar/Pages/default.aspx in PDF format. Due to the State budget restraints, CSMIP did not fund as many projects as in other years and did not hold an annual seminar in 2010 or 2011. The SMIP16 Seminar is the twenty-fifth in this series of annual seminars.

The SMIP16 Seminar is divided into two sessions in the morning and two sessions in the afternoon. There are a total of nine presentations including one invited presentation and eight presentations on the results from CSMIP-funded projects. The sessions in the morning include four presentations. Dr. C.B. Crouse of AECOM is invited to present the development of new ground-motion maps for Los Angeles. It will be followed by a presentation by Dr. Imbsen of SC Solutions on the fragility curves for rapid post-earthquake safety evaluation of a suspension bridge. The second session will focus on results from building response data: building periods and modal damping ratios by Professor Zareian of UC Irvine and dynamic foundation stiffnesses and input motions for buildings by Professor Taciroglu of UCLA.

The afternoon session will start with presentation of the results on the implications of vertical array data for modeling of site response by Professor Stewart of UCLA. Professor Taciroglu of UCLA will present theoretical basis for spatial variability of bridge foundation input motions. The last session will include presentations of ground motions recorded during the 2014 South Napa Earthquake by Drs. Kishida and Mazzoni of UC Berkeley, one-dimensional site response by Professor Motamed of University of Nevada Reno, and improved ground motion intensity measures for estimating the collapse of structures by Professor Miranda of Stanford University. Individual papers and the proceedings are available to the SMIP16 participants in an USB flash drive, and will be available at the CSMIP website.

Moh Huang
CSMIP Data Interpretation Project Manager

Appreciation to Members of the Strong Motion Instrumentation Advisory Committee

Main Committee

Farzad Naeim, Chair, Farzad Naeim, Inc.
Norman Abrahamson, Pacific Gas & Electric Company
Bruce Clark, Leighton & Associates
Martin Eskijian, California State Lands Commission (retired)
David Gutierrez, DWR Division of Safety of Dams
Wilfred Iwan, California Institute of Technology
Mark Mahan, Caltrans
Marshall Lew, Amec Foster Wheeler
Bret Lizundia, Rutherford + Chekene
Chris Tokas, Office of Statewide Health Planning and Development
Robert Anderson (ex-officio), Seismic Safety Commission

Ground Response Subcommittee

Marshall Lew, Chair, Amec Foster Wheeler
Abbas Abghari, Caltrans
Brian Chiou, Caltrans
Geoffrey Martin, Univ. of Southern California
Marcia McLaren, Pacific Gas & Electric Company (retired)
Ben Tsai, Pacific Gas & Electric Company (retired)

Buildings Subcommittee

Bret Lizundia, Chair, Rutherford + Chekene
Lucie Fougner, Degenkolb Engineers
Ifa Kashefi, City of Los Angeles
David Leung, City of San Francisco
Eduardo Miranda, Stanford University
John Robb, Structural Engineer
Roy Lobo, Office of Statewide Health Planning and Development
Chia-Ming Uang, UC San Diego

Lifelines Subcommittee

Martin Eskijian, Chair, California State Lands Commission (retired)
Craig Davis, Los Angeles Dept. of Water and Power
David Gutierrez, DWR Division of Safety of Dams
Mark Mahan, Caltrans

Data Utilization Subcommittee

Wilfred Iwan, Chair, California Institute of Technology
Representatives from each Subcommittee

TABLE OF CONTENTS

SMIP16 SEMINAR ON UTILIZATION OF STRONG-MOTION DATA

October 6, 2016

Calit2 Building
University of California, Irvine, California

PROGRAM

8:15 am **REGISTRATION**

9:15 am **WELCOMING REMARKS**
Farzad Naeim, Strong Motion Instrumentation Advisory Committee (SMIAC)
John Parrish, State Geologist, California Geological Survey

INTRODUCTION
Anthony Shakal, Manager, California Strong Motion Instrumentation Program
Moh Huang, California Strong Motion Instrumentation Program

Session I

Moderator: *Farzad Naeim*, Farzad Naeim, Inc. and SMIAC

9:30 am **Development of New Ground-Motion Maps for Los Angeles Based on 3-D Numerical Simulations and NGA West2 Equations**
C.B. Crouse, AECOM and *Tom Jordan*, SCEC, University of Southern California (invited speaker)

10:00 am **Fragility Curves for the Rapid Post-Earthquake Safety Evaluation of Bridges**
Roy Imbsen, *Shah Vahdani*, *M. Saiid Saiidi*, *Hassan Sedarat* and *Farid Nobari*, SC Solutions

10:30 am Break

Session II

Moderator: *Bret Lizundia*, Rutherford + Chekene and SMIAC

11:00 pm **Identification and Validation of Natural Periods and Modal Damping Ratios for Seismic Design and Building Code**
Yijun Xiang, *Angie Harris*, *Farzad Naeim* and *Farzin Zareian*, UC Irvine

11:30 pm **Identification of Dynamic Foundation Stiffnesses and Input Motions from Strong Motion Data Recorded at CSMIP Instrumented Buildings**
S. Farid Ghahari and *Ertugrul Taciroglu*, UC Los Angeles

12:00 pm **Lunch**
Lunch will be provided

Session III

Moderator: *Martin Eskijian*, California State Lands Commission and SMIAC

12:50 pm **Implications of California Vertical Array Data for Modeling of Non-Ergodic Site Response.**
Kioumars Afshari and *Jonathan Stewart*, UC Los Angeles.

1:20 pm **Identification of Spatial Variability in Bridge Foundation Input Motions: Theoretical Basis**
Ertugrul Taciroglu and *S. Farid Ghahari*, UC Los Angeles

1:50 pm Break

Session IV

Moderator: *Marshall Lew*, AMEC Foster Wheeler and SMIAC

2:10 pm **Investigation of Ground Motions Recorded during the 2014 South Napa Earthquake**
Tadahiro Kishida, Silvia Mazzoni, Yousef Bozorgnia, Brian Chiou, Robert Darragh, Hamid Haddadi, Robert Kayen, Christopher Markham, Sifat Muin and *Walt Silva*, UC Berkeley

2:40 pm **Evaluation of One-Dimensional Site Response in California Downhole Arrays**
Ramin Motamed, Gangjin Li and *Steve Dickenson*, University of Nevada, Reno

3:10 pm **Towards Improved Ground Motion Intensity Measures for Estimating the Collapse of Structures**
Eduardo Miranda and Héctor Dávalos, Stanford University

3:40 pm **Adjourn**

DEVELOPMENT OF NEW GROUND-MOTION MAPS FOR LOS ANGELES BASED ON 3-D NUMERICAL SIMULATIONS AND NGA WEST2 EQUATIONS

C.B. Crouse
AECOM, Seattle

T.H. Jordan
Southern California Earthquake Center
University of Southern California, Los Angeles

Abstract

The Utilization of Ground Motion Simulation (UGMS) committee of the Southern California Earthquake Center (SCEC) is currently developing risk-targeted Maximum Considered Earthquake (MCE_R) maps for possible inclusion as an amendment to the ASCE 7-16 edition of the Los Angeles City Building Code (LACBC). These maps are scheduled for release in 2017. The maps will be based on 3-D numerical ground-motion simulations and ground motions computed using the empirical ground-motion prediction equations (GMPEs) from the Pacific Earthquake Engineering Research (PEER) Center NGA West2 project. A web-based lookup tool, similar to the USGS lookup tool, will be posted so users can obtain the MCE_R response spectrum for a specified latitude and longitude and for a specified site class or 30-m average shear-wave velocity, V_{s30}. The acceleration ordinates of the MCE_R response spectrum will be provided at multiple natural periods in the 0 to 10-sec band; values of S_{DS} and S_{D1}, per the requirements in Section 21.4 of ASCE 7-16, will also be listed.

Introduction

The ultimate goal of the UGMS committee, since its establishment by the SCEC in the spring of 2013, has been to develop improved long-period response spectral acceleration maps for the Los Angeles region for inclusion in the 2020 NEHRP Seismic Provisions, ASCE 7-22 standard, and LACBC. In the interim, MCE_R maps are currently being developed for possible inclusion as an amendment to the ASCE 7-16 edition of the LACBC.

The 20-member UGMS committee consists of seismologists, geotechnical engineers, and structural engineers, mostly from California. This mix of technical disciplines was considered essential if the maps were to be accepted by the structural engineers of southern California and local building officials. Various calculations leading to the production of the MCE_R maps are performed by SCEC technical staff under the direction of the UGMS committee.

The work of the UGMS committee is being coordinated with (1) the SCEC Ground Motion Simulation Validation Technical Activity Group (GMSV-TAG), (2) other SCEC projects, such as CyberShake and the Uniform California Earthquake Rupture Forecast (UCERF) model of earthquake recurrence, and (3) the USGS national seismic hazard mapping project.

Background and Motivation for Improved Long Period Ground Motion Maps

Section 11.4 in the current ASCE 7-10 (and forthcoming ASCE 7-16) standard specifies a general procedure for developing MCE_R response spectral accelerations at intermediate and long periods. These long period accelerations depend on two parameters, S_{M1} and T_L, where S_{M1} is the MCE_R response spectral acceleration at 1-sec period that accounts for the effect of the local site geology through the site coefficient, F_v, and T_L is the period that defines the transition in the MCE_R spectrum from constant spectral velocity to constant spectral displacement.

The T_L parameter was introduced in the ASCE 7-05 standard to provide a more realistic estimate of the response spectrum at long periods. The values of T_L vary from 4 sec to 16 sec depending on location in the US. During its development, deficiencies in the T_L concept were recognized, but a better representation of the long period motions was not possible at the time because the existing GMPEs did not extend to long periods.

The subsequent NGA West and NGA West2 projects, culminating in 2008 and 2013, produced GMPEs for computing response spectra to 10-sec period from shallow crustal earthquakes in the western US. Although these GMPEs were derived from an extensive world-wide ground-motion database, relatively few truly strong ground motion records in this database were from earthquakes in the Los Angeles area, where the effects of the complex 3-D basin structures were known to have significant influences on long period motions. Furthermore, the earthquakes on the local faults contributing to the MCE_R motions in Los Angeles have not occurred during the last several decades when the region was populated with arrays of strong motion instruments.

The available ground motion data for southern California did suggest a correlation between long period ground motions and basin depth. Thus, NGA West, NGA West2, and a few previous generation GMPEs incorporated a basin depth term to model the effect of the basins. However, this parameterization ignores the 3-D effect, as well as the location and orientation of the fault rupture with respect to the basins. Recognizing this deficiency in the empirical GMPEs, SCEC launched a program to simulate ground motions numerically using a physics-based 3-D fault-rupture and wave-propagation model of Southern California. The computations were done with the CyberShake platform that utilized supercomputers to generate millions of simulations covering the range of potential moderate to large magnitude earthquakes on Southern California faults included in the UCERF models the USGS has used to develop the MCE_R ground-motion maps for the region.

The potential feasibility of using CyberShake to develop long period ground motion maps was demonstrated by SCEC (Graves et al., 2010; Wang and Jordan, 2014), and it eventually led to the formation of the SCEC UGMS committee.

MCE_R Response Spectra Generated by UGMS for Southern California

MCE_R response spectra were computed separately for the NGA West2 GMPEs and CyberShake to obtain indications of the differences in these spectra at sites outside and within the region's basins. The GMPE-based MCE_R response spectra were computed by substituting the appropriate values of the basin-depth terms, $Z_{1.0}$ and $Z_{2.5}$ (the depths to the tops of the layers with

shear-wave velocities of 1.0 km/sec and 2.5 km/sec), and the V_{s30} value from Wills and Clahan (2006), into the Abrahamson et al. (2014), Boore et al. (2014), Campbell and Bozorgnia (2014), and Chiou and Youngs (2014) GMPEs and conducting the seismic hazard analyses according to the procedures in Chapter 21 of the ASCE 7-10 standard.

The MCE_R response spectra were initially computed at 14 sites in southern California (Figure 1); however, the spectra at four of these sites (PAS, CCP, LADT, and COO) in the Los Angeles area illustrate the general trends observed at other sites. The PAS site (old seismological laboratory of the California Institute of Technology) is a rock site; the CCP (Century City Plaza) and LADT (downtown Los Angeles) sites are near the edge of the Los Angeles basin; and, the COO (Compton) site is in the deep part of the Los Angeles basin. The MCE_R response spectra at these four sites are shown on log-log plots in Figure 2, where the vertical axis is 5% damped pseudovelocity, PSV, selected to better illustrate the differences between the NGA West2 and CyberShake MCE_R response spectra, and the horizontal axis is natural period, T. The CyberShake-based response spectra at the three basin sites are greater than the GMPE-based response spectra at the longer periods; this difference is greatest for the COO site, where the CyberShake-based response spectra are ~50% greater than the GMPE-based response spectra at a natural period T = 5 sec, and ~100% greater for T = 7 – 10 sec.

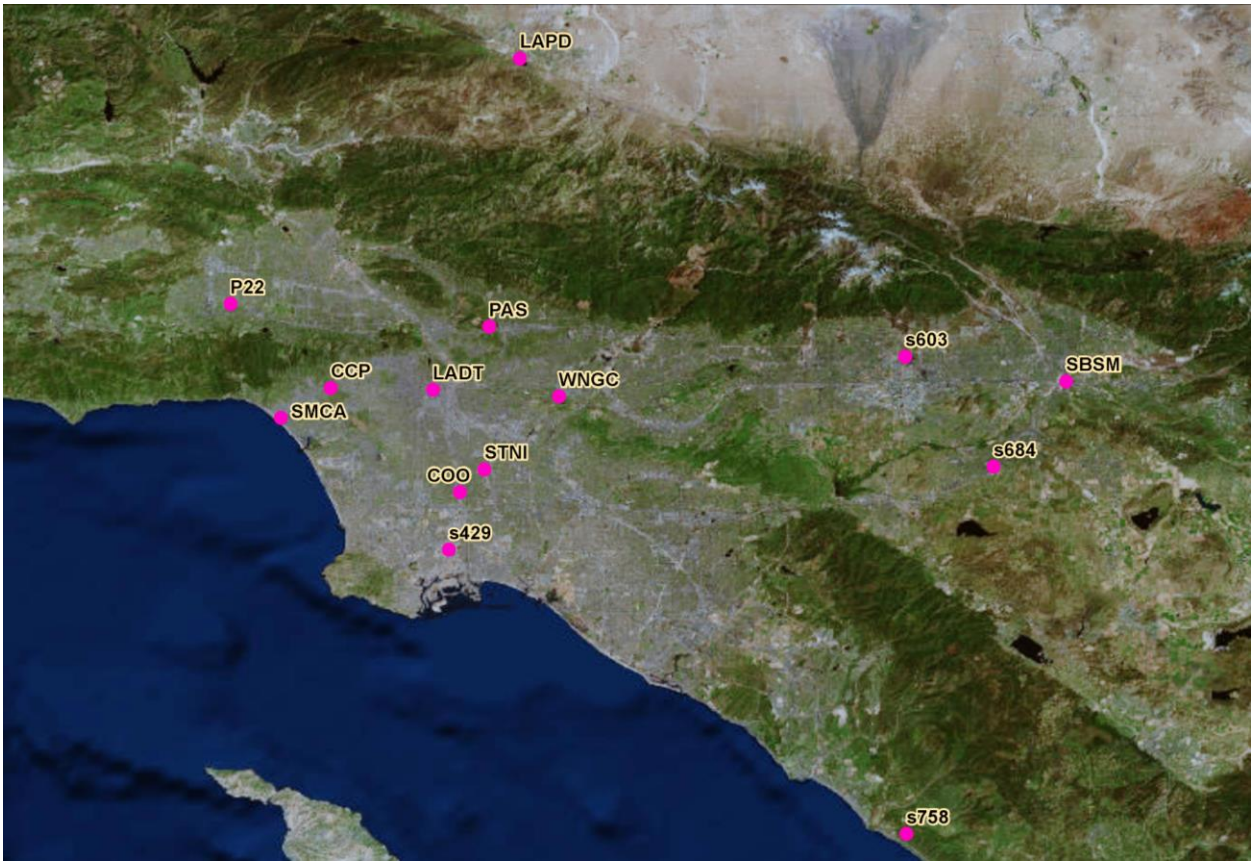

Figure 1. Location of 14 of the CyberShake sites.

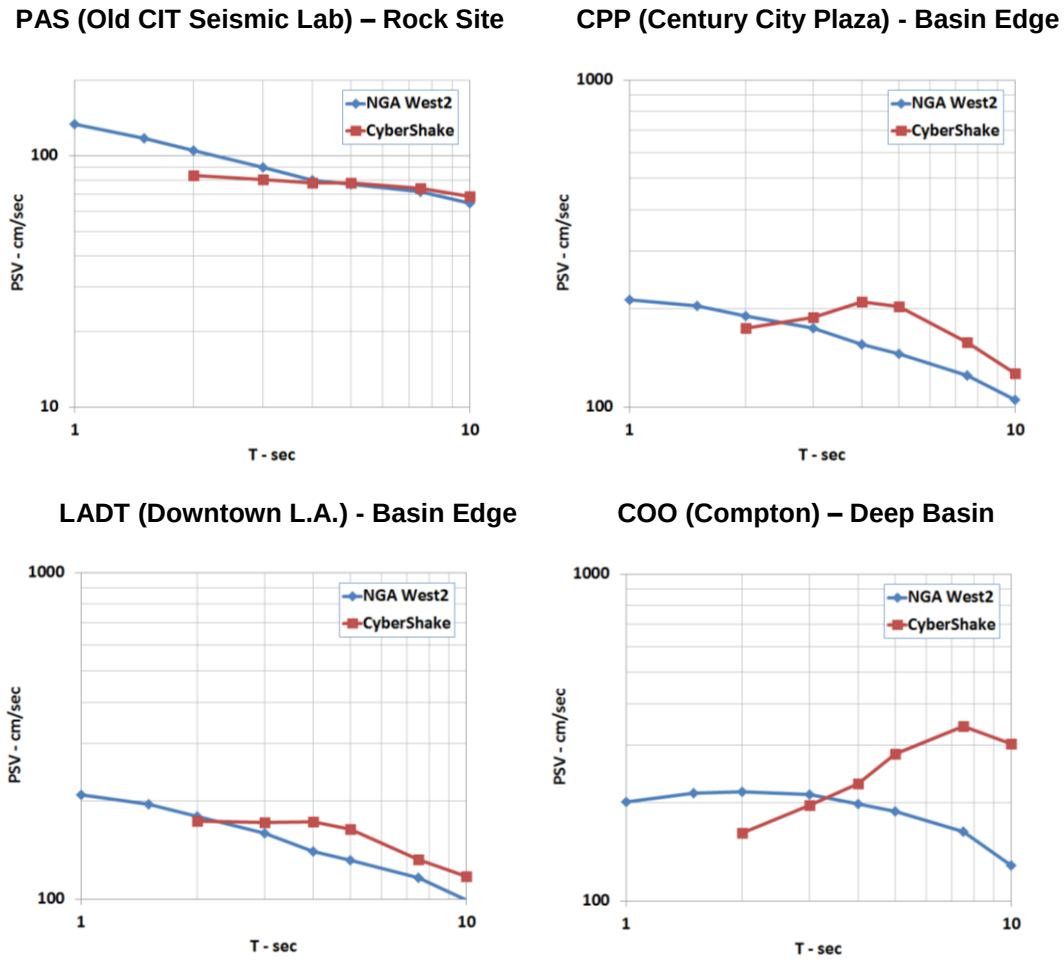

Figure 2. PSV MCE_R response spectra at PAS, CCP, LADT, and COO sites.

Based on MCE_R response spectra computed at these four sites and 59 other sites in southern California, the UGMS committee developed an approach to combine the MCE_R response spectra from the NGA West2 GMPEs with the MCE_R response spectra from CyberShake. The approach is illustrated in the logic tree shown in Figure 3. The final MCE_R response spectra are the weighted geometric average of the MCE_R response spectra from the NGA West2 GMPEs and from the CyberShake simulations; the weights assigned to each vary depending on the natural period, T, with the MCE_R response spectra from the NGA West2 GMPEs receiving all the weight for $T \leq 1.0$ sec. As T increases, the weights for the MCE_R response spectra from the NGA West2 equations decrease, and the weights for the CyberShake MCE_R response spectra increase; for $T \geq 5.0$ sec, the weights are equal. An additional requirement, namely that these "averaged" MCE_R response spectra cannot be less than the MCE_R response spectra from NGA West2 equations, was imposed to account for the underestimation of the CyberShake MCE_R response spectra at $T < \sim 2$ sec, due to the size of the mesh representing the 3-D velocity structure for southern California; this requirement also resulted in smoother MCE_R response spectra.

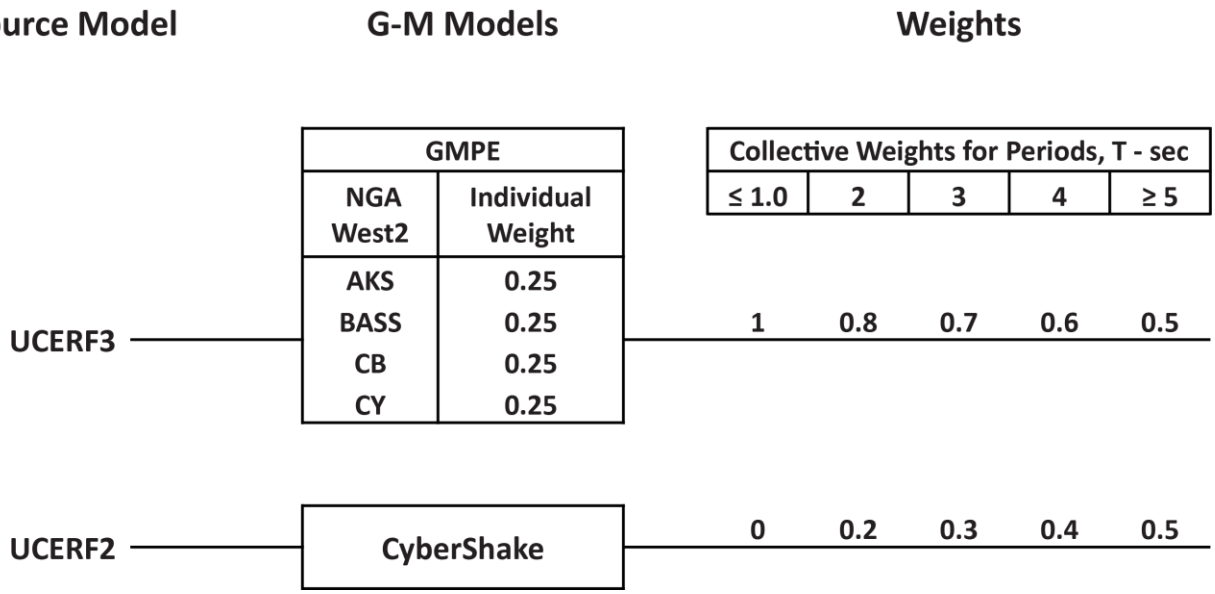

Figure 3. Logic tree illustrating the weights applied to NGA West2 and CyberShake. UCERF is Uniform California Earthquake Rupture Forecast recurrence model. UCERF2 was developed in 2008; this model was updated to UCERF3 in 2014.

The resulting MCE_R response spectra for the LADT and COO sites are shown in Figures 4 and 5, respectively; these spectra are labeled "Site-Specific". In each figure the left-hand plot is log (PSV) versus log T, and the right-hand plot is linear S_a versus linear T, where S_a is the response spectral acceleration, $S_a = (2\pi/T)$ PSV. Also in the left-hand plot is the ASCE 7-16 MCE_R response spectrum constructed from the S_{MS} and S_{M1} values, which were derived from the 2014 USGS map values of S_S and S_1 for the sites and the applicable site coefficients, F_a and F_v, in the ASCE 7-16 standard. The LADT and COO sites were Site Class C and Site Class D, respectively; and, $T_L = 8$ sec for both sites.

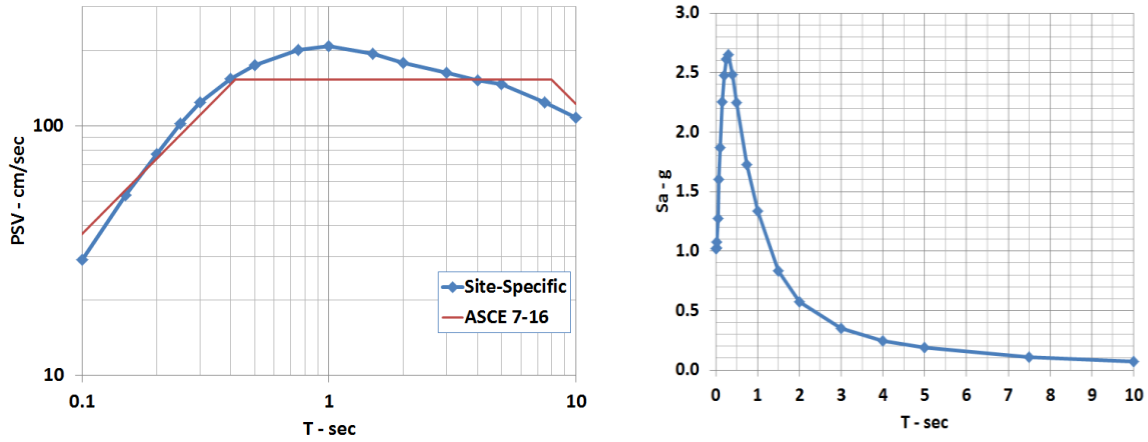

Figure 4. PSV and S_a MCE_R response spectra for LADT site. The ASCE 7-16 MCE_R response spectrum is only plotted on the PSV figure to more clearly illustrate differences with the site-specific MCE_R response spectrum.

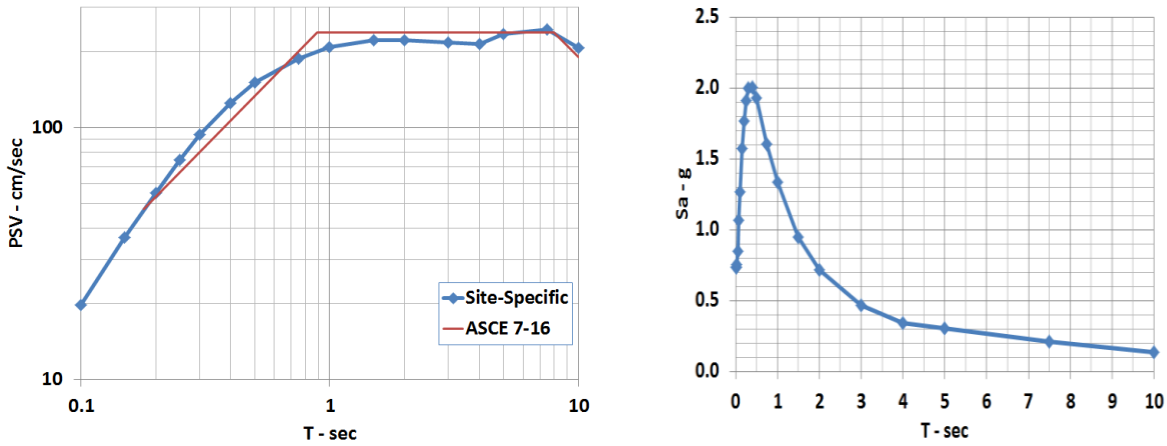

Figure 5. PSV and S_a MCE_R response spectra for COO site.

The parameters to construct the MCE_R response spectra in Figures 4 and 5 were as follows:

LADT: S_{MS} = 2.367, S_{M1} = 0.983; V_{s30} = 390 m/sec, $Z_{1.0}$ = 0.31 km, $Z_{2.5}$ = 2.08 km

COO: S_{MS} = 1.709, S_{M1} = 1.525; V_{s30} = 280 m/sec, $Z_{1.0}$ = 0.73 km, $Z_{2.5}$ = 4.28 km.

Web-Based Lookup Tool

A web-based lookup tool, similar to the USGS lookup tool, is currently being developed by SCEC under the UGMS direction. This tool will enable users to obtain the MCE_R response spectrum for a specified latitude and longitude and for a specified site class or Vs30. If either of these local geologic parameters is not known, the tool will automatically select a default value of V_{s30} from Wills and Clahan (2006). The output will consist of a table of acceleration ordinates of the MCE_R response spectrum at multiple natural periods in the 0 to 10-sec band; a plot of the spectrum will also be included. Values of S_{DS} and S_{D1}, per the requirements in Section 21.4 of ASCE 7-16, will also be listed. The UGMS also plans to include links to other information, such as source and magnitude-distance deaggregation data, and the GMPE-based and CyberShake-based MCE_R response spectra, before the averaging.

Acknowledgements

The work done by Scott Callaghan, Kevin Milner, and Philip Maechling of SCEC to compute the MCE_R response spectra and prepare the CyberShake MCE_R web site with these and other data related to the calculations, is greatly appreciated, as well as the contributions of the UGMS committee members and corresponding members.

References

Abrahamson, N.A., Silva, W.J., and R. Kamai, 2014, Summary of the ASK14 ground motion relation for active crustal regions. Earthquake Spectra, **30**, 1025-1055.

Boore, D.M., Stewart, J.P., Seyhan, E., and G.M. Atkinson, 2014, NGA-West2 equations for predicting PGA, PGV, and 5% damped PSA for shallow crustal earthquakes. Earthquake Spectra, **30**, 1057-1088.

Campbell, K.W., and Y. Bozorgnia, 2014, NGA-West2 ground motion model for the average horizontal components of PGA, PGV, and 5% damped linear acceleration response spectra. Earthquake Spectra, **30**, 1087-1115.

Chiou, B.S.-J., and R.R. Youngs, 2014, Update of the Chiou and Youngs NGA model for the average horizontal component of peak ground motion and response spectra. Earthquake Spectra, **30**, 1117-1153.

Graves, R., and 12 coauthors, 2010, CyberShake: a physics-based seismic hazard model for Southern California. Pure Appl. Geophys., DOI:10.1007/s00024-010-0161-6.

Wang, F., and T. H. Jordan, 2014, Comparison of probabilistic seismic hazard models using averaging-based factorization. Bull. Seismol. Soc. Am., **104**, 1230-1257, DOI:10.1785/0120130263.

Wills, C. J., and K. B. Clahan, 2006, Developing a map of geologically defined site-condition categories for California. Bull. Seismol. Soc. Am., **96**, 1483-1501, DOI:10.1785/0120050179.

FRAGILITY CURVES FOR THE RAPID POSTEARTHQUAKE SAFETY EVALUATION OF BRIDGES

Roy A. Imbsen[1], Shah Vahdani[2], M. Saiid Saiidi[3], Hassan Sedarat[1], and Farid Nobari[1]

[1]SC Solutions, Inc. Sunnyvale
[2]Applied GeoDynamics, Inc., El Cerrito
[3] Infrastructure Innovation, LLC, Reno

Abstract

A new procedure for rapid post-earthquake safety evaluation of bridges has been developed, using existing strong motion records, fragility curves and ground motion data immediately available following an earthquake that will provide the engineer or person directly in charge of the bridge to make a more informed decision to close or keep a bridge open to traffic. The recently constructed Carquinez I80 West Bridge (Alfred Zampa Memorial Bridge) was selected to demonstrate the procedure. This paper describes the detailed time history finite element analysis conducted using strong motion data for the 26 scenario earthquake events and the development of the fragility curves using shake table test results on reinforced concrete columns tested through five damage states to final failure. Fragility functions are developed for various seismic parameters for each damage state and calibrated for maximum drift ratios for inclusion into the rapid safety evaluation of the Carquinez Bridge.

Introduction

This study, entitled *Rapid Post-Earthquake Safety Evaluation of the New Carquinez Bridge Using Fragility Curves and Recorded Strong-Motion Data* is part of the Data Interpretation Project of the California Strong Motion Instrumentation Program (CSMIP) in the Department of Conservation (DOC) California Geological Survey. The purpose of this project is to accelerate the application of the strong-motion data in reducing risk due to the strong earthquake shaking which occurs in California.

Overview of the Safety Evaluation Procedure

The application of the procedure undertaken in this study is to provide for the selected New Carquinez Bridge, as shown in Figure 1, the ability to assess the damage immediately following an earthquake using the ground motion parameters of the earthquake event and fragility curves developed for the bridge so that a decision can be made on the continued use or closure of the bridge.

Figure 1: Aerial View of the New Carquinez Bridge

Background

SC Solutions (SCS) was tasked to develop a system to improve the current Caltrans rapid post-earthquake decision making process for critical bridges. Immediately after any earthquake, Caltrans has to make decisions about the post-earthquake conditions of bridges. The decision making process will be based on the magnitude of the earthquake event, location of a bridge, instrument data, the understanding of the performance of the bridge in the subject earthquake, and factors related to risk and consequences. Most of the critical bridges that are in high seismic zones are instrumented. These instrument data are monitored in real time and can be used for this decision making process. The foundation or free field ground motions near the bridge and some of the structural performance can be obtained immediately after an earthquake. However, this limited instrument data doesn't provide adequate information about the conditions of all critical components of bridges immediately after an event. Therefore, additional understanding of the bridge performance and fragility functions should be developed for each of these critical bridges to assist the post-earthquake decision making process.

To develop fragility functions, first a set of pre-earthquake scenario events must be selected based on the location of the bridge and the active faults in the vicinity of the bridge site. For this task SC Solution proposed to use the New Carquinez Bridge for the case study. After selecting a set of scenario earthquakes for the New Carquinez Bridge, the existing SCS bridge model could be used to simulate the effects of these ground motions to understand the performance of each critical component in the bridge. After conducting these pre-earthquake seismic analyses, a relationship can be developed between the earthquake intensity parameter (e.g. magnitude, distance and spectral acceleration) and the primary response parameter of a critical component.

As one example, the primary response parameter can be a drift for a critical tower. Based on the primary response parameter value, a damage index (or damage potential) can be developed for each critical component. This damage potential can be related to the seismic intensity parameter as a fragility function for each critical component.

Pre-Event Data Processing

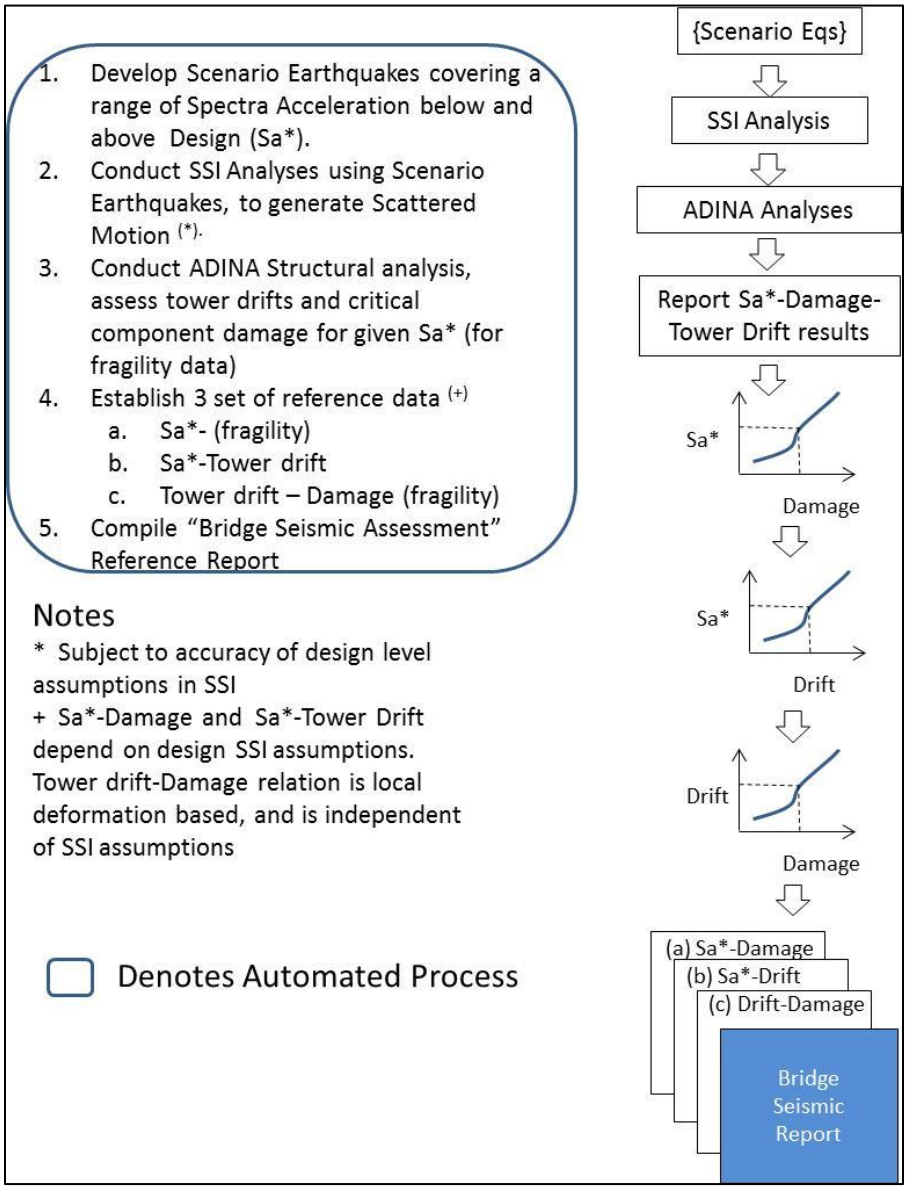

Figure 2: Pre-Event Data Processing

As shown in Figure 2, prior to an event, several automated procedures will be completed and compiled in a "Bridge Seismic Assessment" report, as a reference document for Caltrans decision making, after an event. The steps include the following:

a. Establish Scenario Earthquakes

To develop fragility functions, a set of pre-earthquake scenario events must be selected based on the location of the bridge and the active faults in the vicinity of the bridge site. For the purpose of this project, 26 sets of scenario ground motions were generated based on different

magnitude earthquakes on regional faults. These motions ranged from low fault activity and spectral acceleration, through Design Spectra, and spectral acceleration values both less than and greater than design levels prescribed for the site. The characteristics of each motion were identified by moment magnitude (Mw), distance to the fault (R), and spectral acceleration (Sa).

b. Develop Input Ground Motions at the Bridge Site

Using the available site specific ground motion, generation tools and design spectra, the SSI analytical model customized for the Carquinez site was used to bring the scenario earthquakes to the site and to generate scattered motions.

c. Dynamic Analyses of Bridge under Scenario Ground Motions (Demand)

The existing detailed Finite Element model of the New Carquinez Bridge [13, 21, 29], developed by SCS, was used in the demand analyses subjected to the scenario ground motions. Drift values of the critical components of the bridge were related to the motion characteristics (Mw, R, Sa). For each critical component, a primary response parameter should be identified. In this project, the proposed approach and scope-of-work is demonstrated for Tower 3 drift as the primary response parameter to reflect the damage state of Critical Tower Components, as an example of the process. This methodology can be applied to different primary response parameters to reflect damage status of other critical components.

d. Pushover Analysis (Capacity)

A Finite Element model of Tower 3 was used to perform pushover analysis. Values of drift and strain (concrete and reinforcement) were extracted and correlated.

e. Evaluation of Tower Drift and Component Damage (relationship between demand and capacity)

Governing tower drifts as the primary response parameters were documented vs. motion characteristics (Mw, R, and Sa), and finally a series of relationships between the motion characteristics (Mw, R, and Sa), Tower Drift, and strain values (damage) of the critical tower were generated.

f. Develop Fragility Data versus Earthquake Intensity and Tower Drift

Based on the analyses, the following response parameters were related to the scenario earthquake intensity, fault, and distance to site:

- Relation between damage states (DS) and strain (Fragility),
- Relation between strain and drift (pushover analysis)
- Using the above, obtain Relation between damage state (DS) and drift (Fragility),
- Relation between (Mw, R, Sa) and drift (26 time-history analyses)

Description of the New Carquinez Bridge and Local Seismic Design Hazard

Description

The New Carquinez Bridge spans the Carquinez Strait with a 2,388 ft. main span bounded by a south span (towards Oakland) of 482 ft. and a north span (towards Sacramento) of 594 ft. as shown in Figure **3**. The principal components of this suspension bridge include

reinforced concrete towers supported on large-diameter concrete pile foundations, parallel-wire cables, gravity anchorages, and a closed orthotropic steel box deck system. The main concrete towers are approximately 400 ft. tall, and are tied together with a strut below the deck and upper strut between the cable saddles as shown in the Typical Section view included in Figure **3**. The lower strut supports the deck vertically using two rocker links and transversely through a shear key.

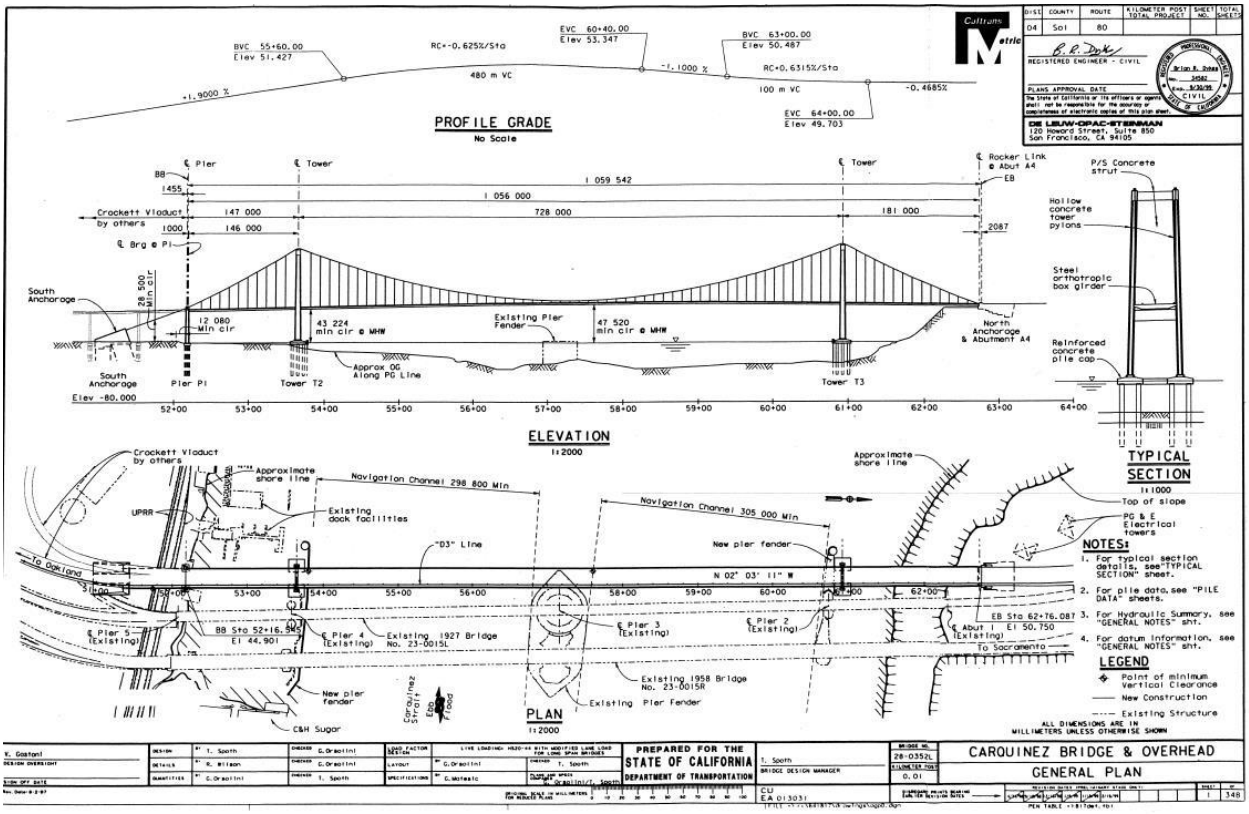

Figure 3: General Plan

Local Seismic Design Hazard

The bridge site, located approximately twenty miles northeast of San Francisco, is located in an active seismic zone. Seismic hazard assessments have shown that the site could be subject to strong ground motions originating on the San Andreas Fault, the Hayward Fault, Concord-Green Valley Fault, Napa Valley Fault, and the Franklin Fault. However, studies have shown that the Hayward fault, Concord-Green Valley fault system, and the Napa Valley seismic zones are the dominant sources of seismic hazard for the bridge's frequency range.

The seismic design of the New Carquinez Bridge considers both the Safety Evaluation Earthquake (SEE) and the lower level Functional Evaluation Earthquake (FEE). Caltrans performance requirements for these events are higher than the minimum level required for all transportation structures but below that required for an Important Bridge. As much as possible, the Important Bridge criteria are to be met for the Safety Evaluation Earthquake (SEE) corresponding to a maximum credible event which has a mean return

period in the range of about 1,000 to 2,000 years. In this earthquake, the bridge can be subject to primarily "minor" damage with some "repairable" damage to piles, pile caps and anchorage blocks and still remain open.

Structural Analysis

A detailed finite element model of the New Carquinez Bridge was developed based on the marked up drawings [10], using the ADINA FE program [31]. All structural components of the new Carquinez Bridge were explicitly modeled. A cross-section of the steel box girders and the bulkhead details are shown in Figure 4. The side elevation view is shown in Figure 5. The key structural components that were included in the global FE model are summarized in Table 1. Suspension bridges belong to a category of bridges that are highly nonlinear in geometry and therefore, during the construction simulation and for their seismic evaluation, large displacement capability was included in the analysis. Geometry iteration was used for the construction sequence of the NCB FE detailed model [7, 22].

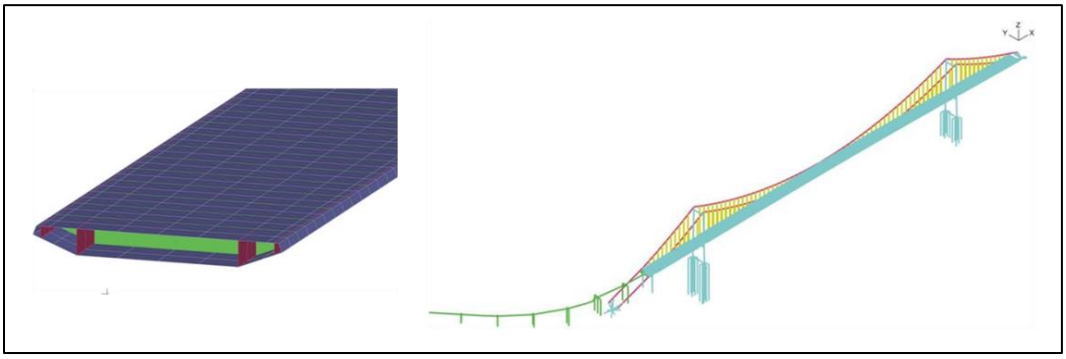

Figure 4: Detailed FE Model of the New Carquinez Bridge (Alfred Zampa Memorial Bridge)

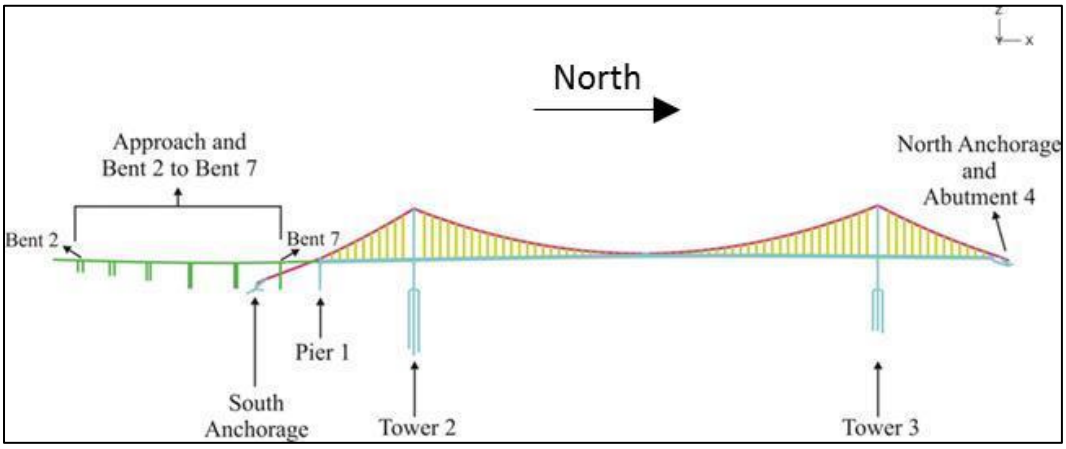

Figure 5: Elevation View of Detailed Model

Pushover Analysis of Tower 3 (Capacity Calculation) - Drift-Strain Curves

The stand-alone FE model of Tower T3 was developed with a fixed base. The pushover profile is proportional to the first longitudinal mode of vibration for the tower, which was obtained from the global model. The main reason to perform pushover analysis is to obtain drift-strain curves (capacity), which will be used as an input to the fragility analysis.

Table 1: Key Structural Components [29]

Component	Description / Model
Main Cables	37-strand cables with 232-wires per strand Linear elastic beam elements with (partially non-composite moment of inertia)
Hangers (suspenders)	four galvanized structural steel ropes Linear elastic truss elements
Towers	Reinforced concrete box section Localized plasticity at the location of plastic hinges ADINA moment-curvature beam elements
Superstructure	Orthotropic steel deck 8-noded shell elements with orthotropic properties
Rocker Links	Steel rocker Beam elements
Anchorages at the North and South sides	Reinforced concrete Rigid links
Piles	Reinforced concrete Moment-curvature beam elements
SSI modeling at piles	PY Nonlinear plastic truss elements TZ and QZ Nonlinear elastic spring elements
SSI modeling at anchorages	Soil impedance General elements: Stiffness, damping and mass matrices

Force-Displacement Curves from Pushover Analysis

The pushover analysis of Tower T3 was performed using the first longitudinal mode of the tower. The inflection point location varies as the push forces increase. The force-displacement of the tower is shown in Figure 6. The values of strain in confined concrete and steel are also shown in this figure. The steel and concrete strain values along with the location of the point of inflection are summarized in Table 2. The steel and concrete strain limits, based on the design criteria [6] are 0.012, and 0.06 for concrete and steel, respectively. The steel strain reached its limit, before the concrete, and at about a 6-ft displacement at the top of the tower. The maximum relative top-to-bottom displacement of tower T3 from the PS&E analysis is 1.45-ft [8].

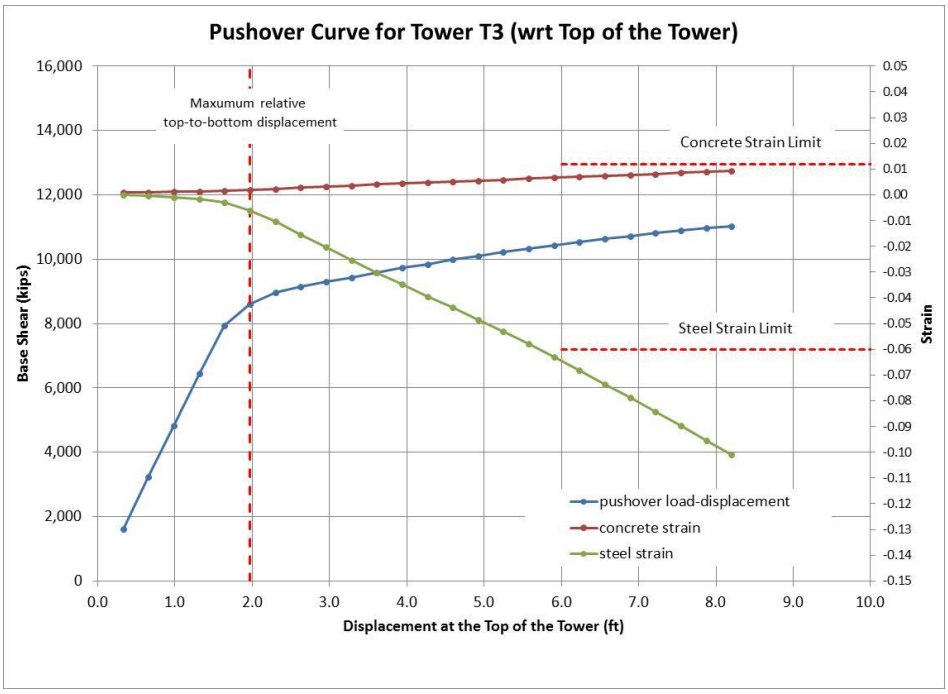

Figure 6: Total Base Shear - Displacement Relationships of Tower T3

Nonlinear Dynamic Analyses of the Detailed Model of the NCB – (Mw, R)-Strain Relation

In order to obtain a relationship between ground motion characteristics (Mw, R) and damage (from fragility analysis), the relationship between the ground motion characteristics (Mw, R) and the strain in concrete and steel should be obtained first. The relationship between the capacity drift and strain was obtained from the pushover analysis. In this study, the demand values which are the relationship between the ground motion characteristics (Mw, R) and drift has been obtained from 26 nonlinear time-history analyses for the 26 scenario ground motions. The relationship between the ground motion characteristics (Mw, R) and strain can be obtained by combining the results obtained from the pushover analysis and time-history analyses, as described Table 3 and Figure 7**.**

Table 2: Force-Displacement-Strain Relationships of Tower T3

step	relative displacement (ft) lower strut to base Δ	relative displacement (ft) upper strut to base Δ	PI (ft)	base shear (kip)	strains at base	
1.01	0.15	0.33	112.32	1.61E+03	6.18E-05	9.06E-04
1.02	0.30	0.66	112.32	3.23E+03	-4.80E-04	1.10E-03
1.03	0.44	0.98	112.32	4.83E+03	-1.06E-03	1.25E-03
1.04	0.59	1.31	112.32	6.44E+03	-1.66E-03	1.39E-03
1.05	0.74	1.64	112.22	7.93E+03	-2.89E-03	1.60E-03
1.06	0.89	1.97	111.35	8.61E+03	-6.09E-03	1.98E-03
1.07	1.03	2.30	110.17	8.96E+03	-1.04E-02	2.35E-03
1.08	1.18	2.62	108.89	9.15E+03	-1.54E-02	2.76E-03
1.09	1.33	2.95	107.64	9.31E+03	-2.04E-02	3.22E-03
1.1	1.48	3.28	106.42	9.44E+03	-2.54E-02	3.69E-03
1.11	1.62	3.61	105.23	9.58E+03	-3.02E-02	4.12E-03
1.12	1.77	3.94	104.08	9.73E+03	-3.48E-02	4.50E-03
1.13	1.92	4.27	102.97	9.85E+03	-3.94E-02	4.88E-03
1.14	2.07	4.59	101.88	9.99E+03	-4.38E-02	5.23E-03
1.15	2.21	4.92	100.82	1.01E+04	-4.84E-02	5.57E-03
1.16	2.36	5.25	99.79	1.02E+04	-5.29E-02	5.91E-03
1.17	2.51	5.58	98.79	1.03E+04	-5.79E-02	6.28E-03
1.18	2.66	5.91	97.80	1.04E+04	-6.29E-02	6.66E-03
1.19	2.81	6.23	96.84	1.05E+04	-6.81E-02	7.04E-03
1.2	2.95	6.56	95.90	1.06E+04	-7.35E-02	7.41E-03
1.21	3.10	6.89	94.98	1.07E+04	-7.88E-02	7.79E-03
1.22	3.25	7.22	94.07	1.08E+04	-8.42E-02	8.17E-03
1.23	3.40	7.55	93.18	1.09E+04	-8.97E-02	8.56E-03
1.24	3.54	7.87	92.28	1.10E+04	-9.53E-02	8.96E-03
1.25	3.69	8.20	91.40	1.10E+04	-1.01E-01	9.35E-03

Table 3: Ground Motion (M/R) – Relative Drift at the Top of Tower and at PI – Strain in Steel and Concrete at the Base of the Tower

North-West Leg						combine Pushover - TH		strain at the base	
						Relative Drift @ Top	Relative Drift @ PI		
GM run ID	Scenario	RSN	Ground Motion Name	M	R (km)	(ft)	(ft)	steel	concrete
1	1	1176	1999 Kocaeli Turkey	7.51	1.38	1.31	0.39	-1.655E-03	1.387E-03
2	3	1244	1999 Chi-Chi Taiwan	7.62	9.94	1.43	0.43	-2.086E-03	1.461E-03
3	16	8099	2011 Christchurch New Zealand	6.2	17.86	0.40	0.12	-5.989E-05	9.496E-04
4	17	4078	2004 Parkfield-02 CA	6	22.45	0.33	0.10	6.180E-05	9.063E-04
5	21	1120	1995 Kobe Japan	6.9	1.46	1.48	0.44	-2.289E-03	1.496E-03
6	22	159	1979 Imperial Valley-06	6.53	0.00	1.19	0.36	-1.438E-03	1.338E-03
7	2	292a	1980 Irpinia Italy-01	6.9	6.78	0.95	0.28	-9.954E-04	1.236E-03
8	4	864	1992 Landers	7.28	11.03	1.08	0.32	-1.234E-03	1.292E-03
9	5	5831	2010 El Mayor-Cucapah Mexico	7.2	14.80	0.76	0.23	-6.635E-04	1.148E-03
10	6	1045 a	1994 Northridge-01	6.69	2.11	0.72	0.22	-5.949E-04	1.130E-03
11	7	1114	1995 Kobe Japan	6.9	3.31	1.14	0.34	-1.345E-03	1.317E-03
12	8	161	1979 Imperial Valley-06	6.53	8.54	0.73	0.22	-5.893E-04	1.147E-03
13	9	4847	2007 Chuetsu-oki Japan	6.8	9.43	0.90	0.27	-9.113E-04	1.213E-03
14	10	6961	2010 Darfield New Zealand	7	13.37	0.62	0.19	-4.251E-04	1.080E-03
15	11	6923	2010 Darfield New Zealand	7	30.53	0.50	0.15	-2.145E-04	1.005E-03
16	12	292b	1980 Irpinia Italy-01	6.9	6.78	0.63	0.19	-4.111E-04	1.107E-03
17	13	8123	2011 Christchurch New Zealand	6.2	5.11	0.79	0.24	-7.121E-04	1.161E-03
18	14	1045 b	1994 Northridge-01	6.69	2.11	0.55	0.16	-3.030E-04	1.036E-03
19	15	313a	1981 Corinth Greece	6.6	10.27	0.49	0.15	-2.109E-04	1.003E-03
20	18	569	1986 San Salvador	5.8	3.71	0.43	0.13	-1.128E-04	9.685E-04
21	19	147	1979 Coyote Lake	5.74	8.47	0.47	0.14	-1.742E-04	9.903E-04
22	20	149	1979 Coyote Lake	5.74	4.79	0.45	0.13	-1.330E-04	9.757E-04
23	23	1054	1994 Northridge-01	6.69	5.54	1.31	0.39	-1.662E-03	1.388E-03
24	24	1236	1999 Chi-Chi Taiwan	7.62	37.48	0.81	0.24	-7.528E-04	1.171E-03
25	25	2111	2002 Denali Alaska	7.9	42.99	0.38	0.11	-2.552E-05	9.374E-04
26	26	313b	1981 Corinth Greece	6.6	10.27	0.55	0.16	-3.025E-04	1.036E-03

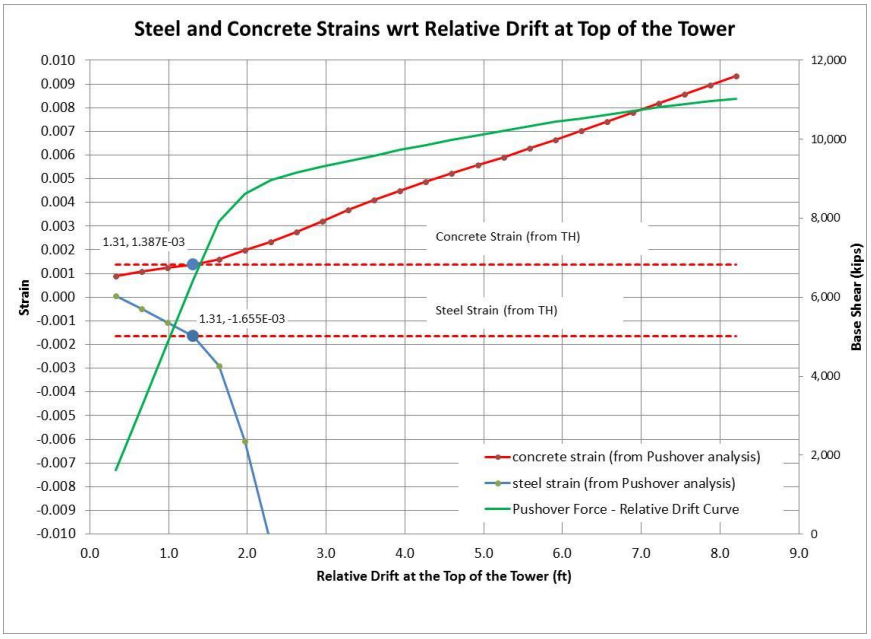

Figure 7: Drift and Strain in Concrete and Steel using TH Analysis and Pushover Curves (Run ID1: 1999 Kocaeli Turkey -- Typical)

Development of Fragility Relationships

This section presents a summary of the work on development of fragility relationships for the Carquinez Bridge east tower subjected to earthquakes in the longitudinal direction of the bridge. The purpose of the curves is to provide a probabilistic estimate of damage states as a function of the maximum drift ratio, which is relatable to the spectral acceleration (S_a), the moment magnitude (M_w) and the distance to the site (D), expressed as $S_a(M_w, D)$.

Experimental Database

The objective of this step was to develop fragility curves for the Carquinez Bridge Tower 3 (T3) using experimental database [20] obtained at the University of Nevada, Reno (UNR), and analytical ADINA response data. More than 100 shake table test data from studies of over 20 reinforced concrete (RC) bridge column models conducted at the University of Nevada, Reno (UNR) was used. The test columns were designed based on recent or current seismic design provisions used at Caltrans [20].

Definition of Damage States

Six apparent damage states (DS) were developed for RC columns in cooperation with Caltrans engineers involved in the reconnaissance investigations [20]. These damage states were correlated with different seismic response parameters. The apparent damage states and the corresponding maximum longitudinal bar strains (MLS) were used respectively as limit states and the response parameter. The damage states (see Figure 8 to Figure 10) are defined as:

- DS-1: Flexural cracks;
- DS-2: Minor spalling and possible shear cracks;
- DS-3: Extensive cracks and spalling;
- DS-4: Visible lateral and/or longitudinal reinforcing bars;
- DS-5: Compressive failure of the concrete core edge (imminent failure); and
- DS-6: Failure.

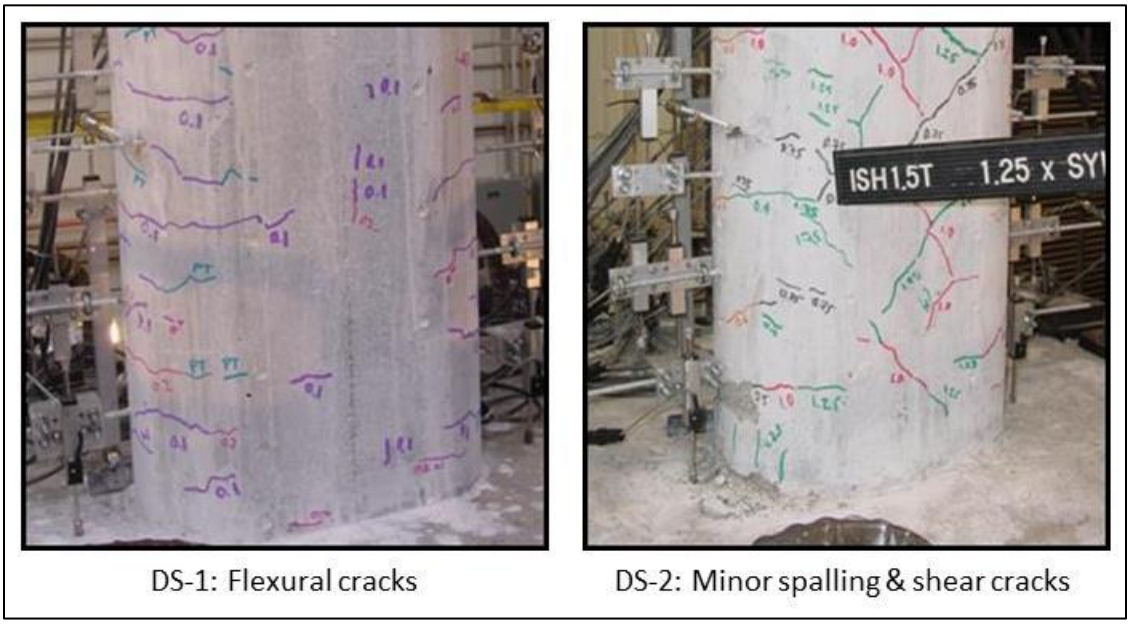

Figure 8: Damage States 1 and 2 - Apparent damage states in the RC bridge columns [20]

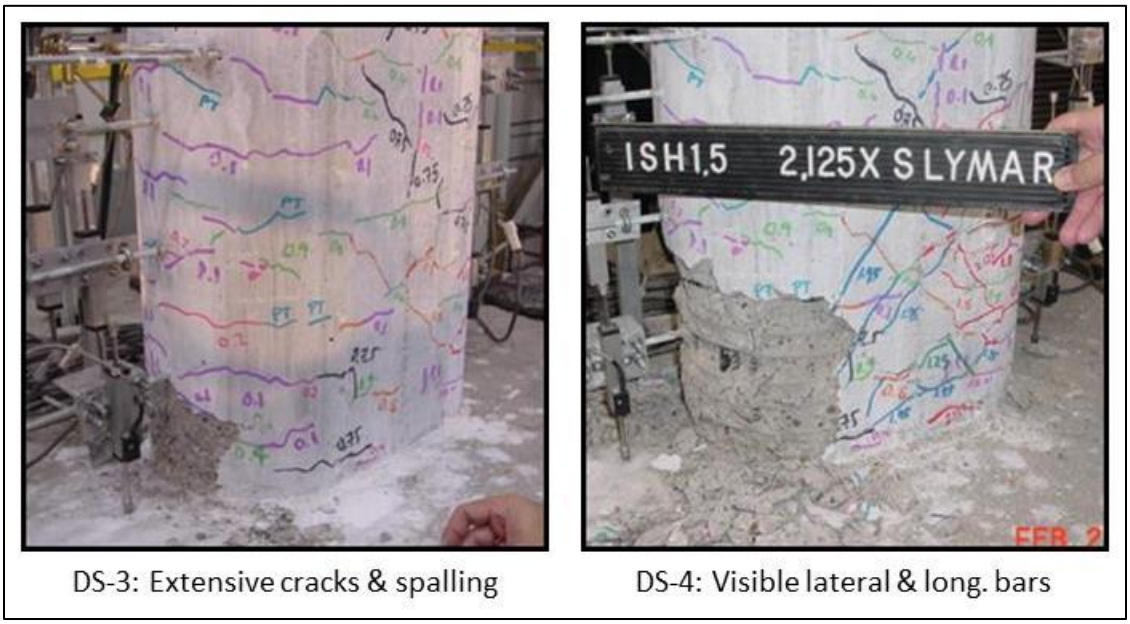

Figure 9: Damage States 3 and 4 - Apparent damage states in the RC bridge columns [20]

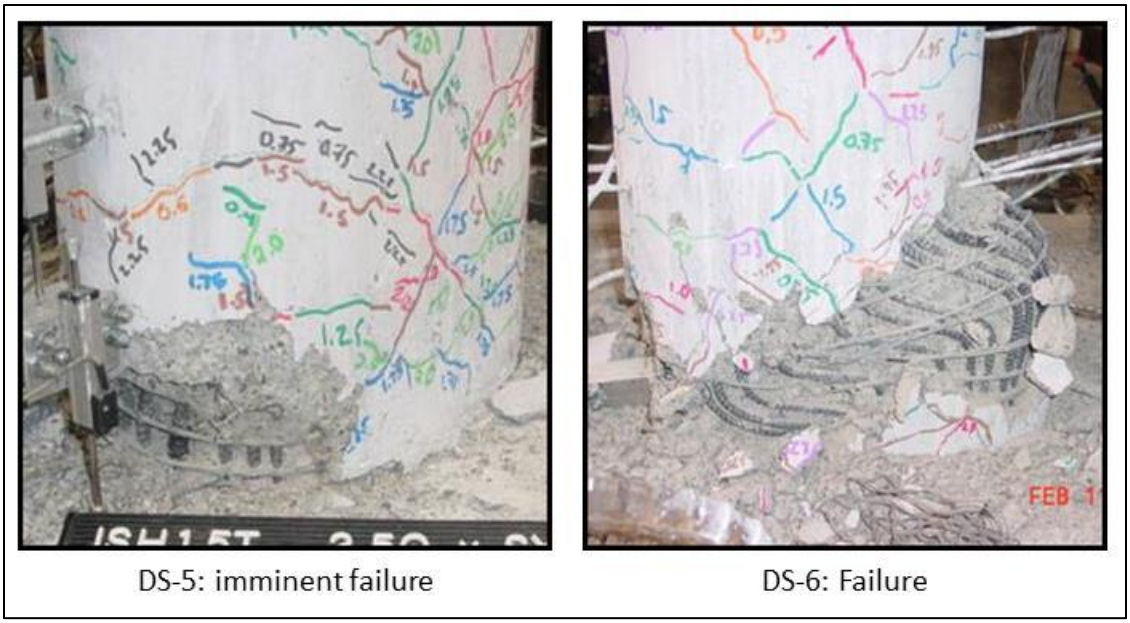

Figure 10: Damage States 5 and 6 - Apparent damage states in the RC bridge columns [20]

Lognormal cumulative distribution function was used to correlate damage states to response parameters. The correlation between the first 5 damage states and MLS is presented in Figure 11.

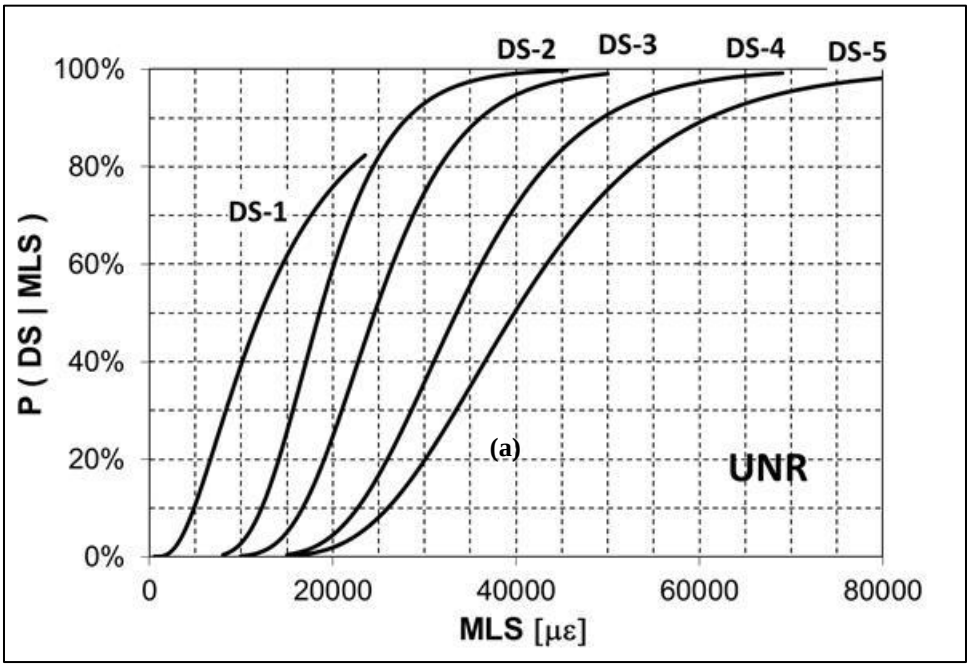

Figure 11: MLS Fragility Curves for UNR Shake Table Database

Calibration of Experimental Fragility Curves for Tower T-3

The column test models mostly had circular sections. A method was developed to calibrate the measured MLS fragility curves for the hollow section of Tower T-3. Steel and concrete strains were used as indicators of the damage states. Flexural cracks are formed on the tensile side of an RC member. Therefore, MLS is a reasonable indicator for DS-1 and consequently the measured MLS fragility curve for DS-1 was used directly for T-3. Apparent DS-2 to DS-5 are due to damage in concrete on the compressive side. Therefore, the maximum compressive strain in concrete was viewed as an indicator of these damage states. Since the experimental database is based on MLS for all damage states, a calibration factor was developed for MLS at DS-2 to DS-5 assuming that the extreme compression fiber strains in T-3 are the same as those in the circular columns of the experimental database. If the ratio of concrete to steel strain in the extreme fibers of circular columns is α and that of T-3 is β, the calibration factor for DS-2 to DS-5 (Figure 12) is α/β.

- α is the ratio of concrete to steel strain in the extreme fibers of circular columns, and
- β is the ratio of concrete to steel strain in the extreme fibers of T3

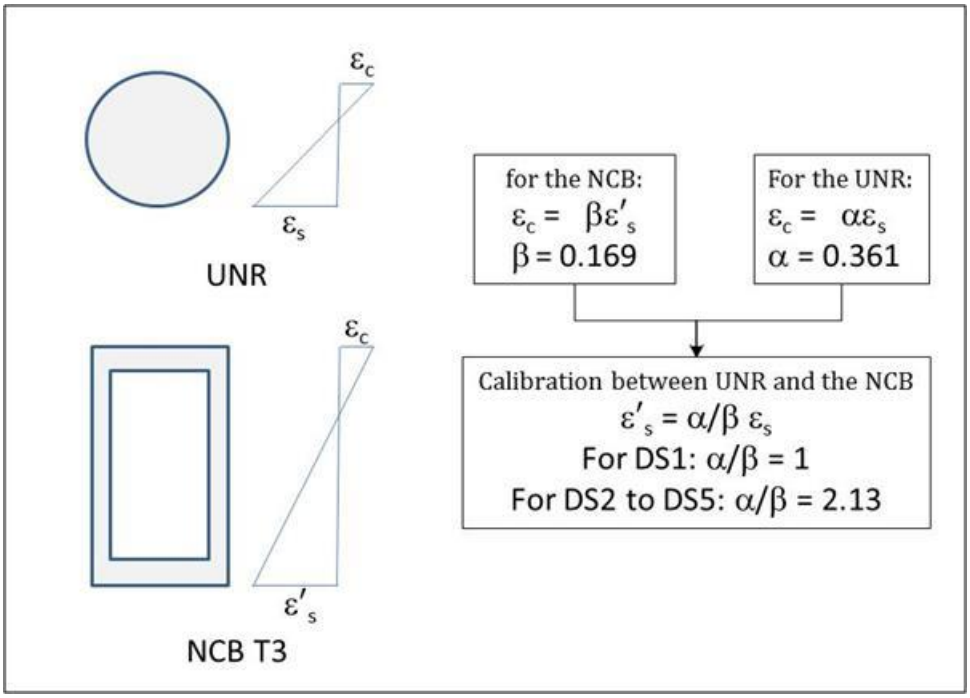

Figure 12: Schematic of Strain Ratios used for Calibration Procedure (for DS-2 to DS-5)

Figure 13 illustrates the strain diagram in a circular RC column. In this figure, ε_c and ε_s are extreme fiber strains in concrete and steel, respectively, ε_t is extreme tensile fiber strain, c is the compression depth, and D is diameter of the circular column. It can be assumed that ε_s and ε_t are approximately the same. Therefore, α was calculated as 0.361 using the following equation:

$$\alpha = \frac{\varepsilon_c}{\varepsilon_s} = \frac{1}{\frac{1}{c/D} - 1} \tag{1}$$

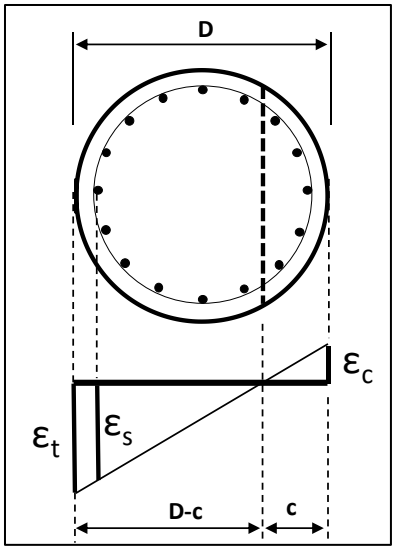

Figure 13: Strain diagram in a circular RC column

The c/D ratio for circular columns was calculated using the following equation [35]:

$$c/D = 0.2 + 0.65\frac{P}{f'_{ce}A_g} \tag{2}$$

Where P is axial force, f'_{ce} is concrete expected strength, and A_g is the gross section area of the circular column. β was calculated as 0.169 (see Figure 12) based on the strain data listed in Table 3 at the maximum compressive concrete strain of 0.003. The resulting calibration factor (α/β) was 2.13 (see Figure 12).

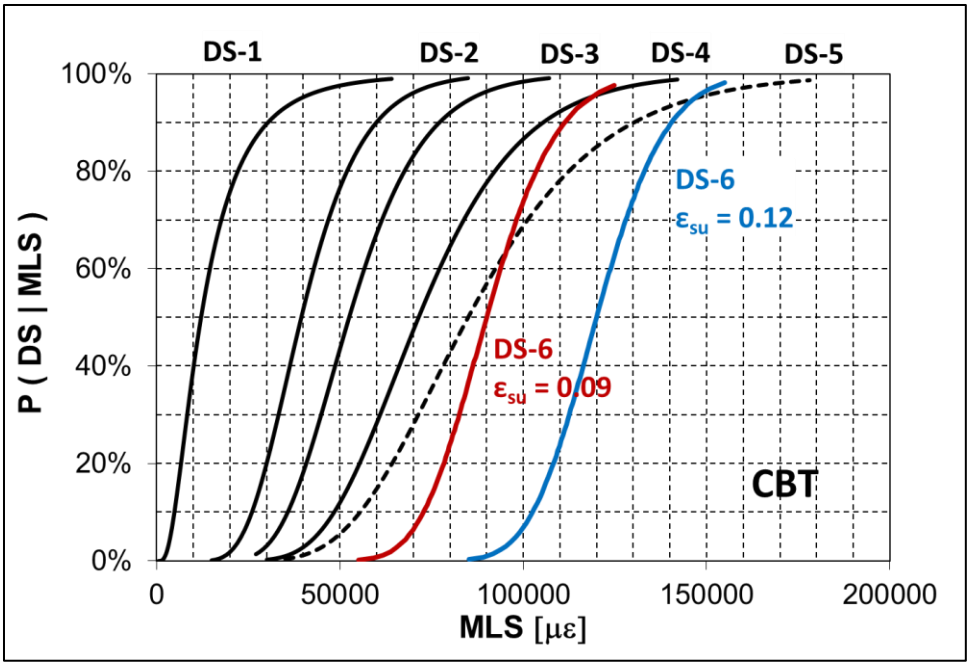

Figure 14: Calibrated maximum longitudinal bar strains (MLS) fragility curves for T-3

Fragility Curves for Tower 3 (T3)

The maximum drift ratio (MDR) fragility curves were developed for T-3 based on the correlation between MLS and MDR. The relationship between MLS and MDR was identified based on strain data and pushover analysis (see Figure 6 and Table 2) after the calculated curve was idealized with a bilinear curve. The relation between maximum drift ratio (MDR) and maximum longitudinal strain (MLS) is shown in Figure 15 . The relation between drift fragility and MDR is shown in Figure 16 . Therefore, knowing MLS, the value of MDR can be estimated (Figure 15**)** Using the value of MDR and (Figure 15**)** the value of fragility can be estimated. The fragility curves (Figure 16) were prepared for six Damage States (DS) and relate the maximum drift ratio (MDR) to the probability of occurrence (POC) for each DS.

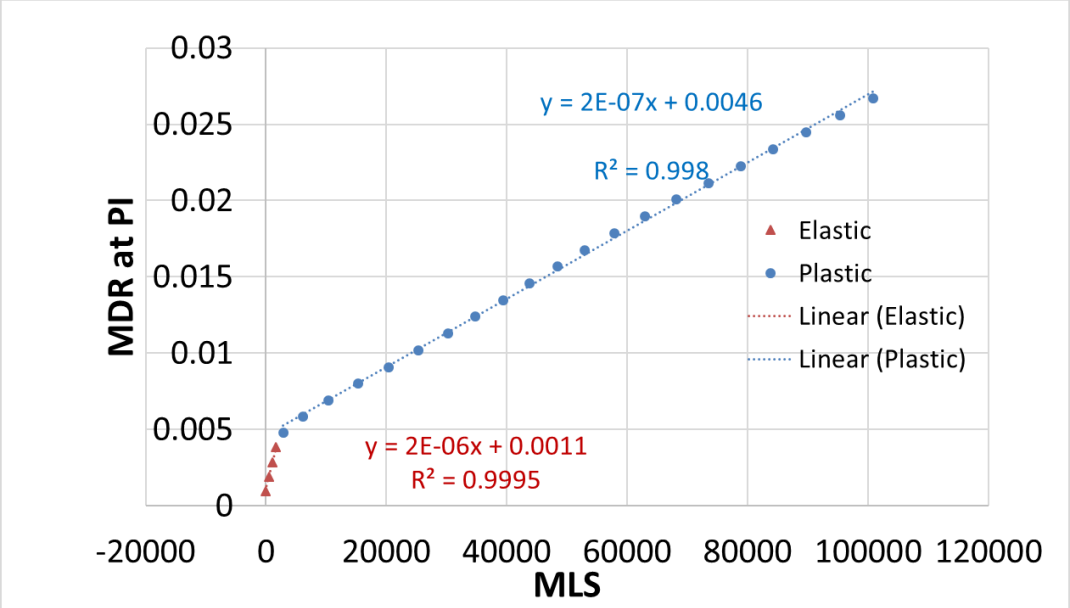

Figure 15: MLS-MDR relationship in T-3 at Inflection Point

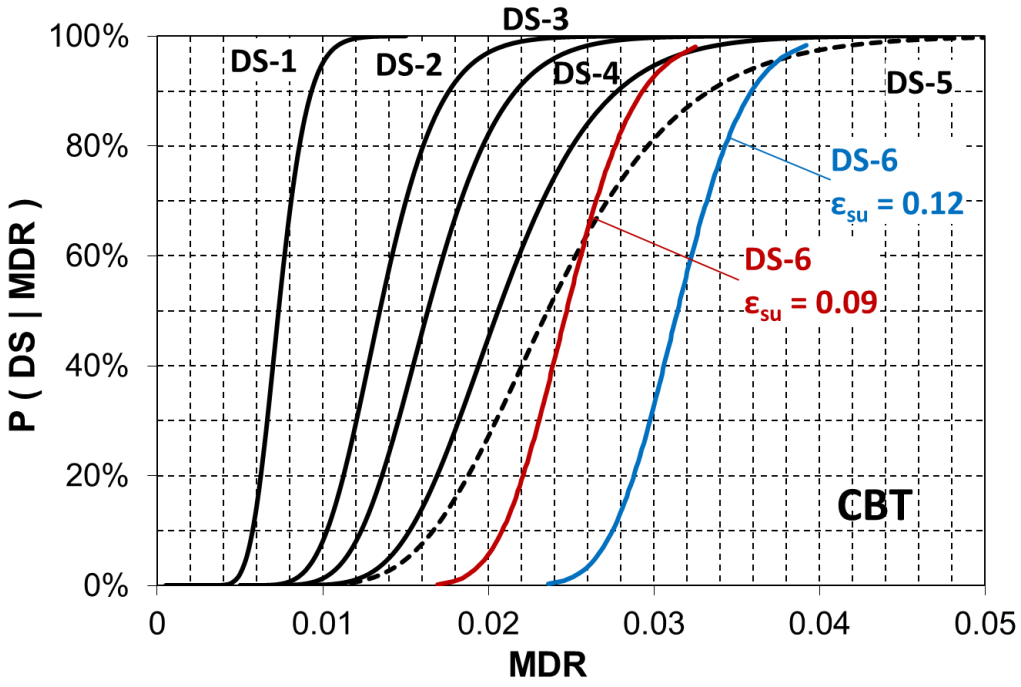

Figure 16: Maximum drift ratio fragility curves for T-3

Application of Proposed Rapid Safety Evaluation Procedure

Immediately after Event

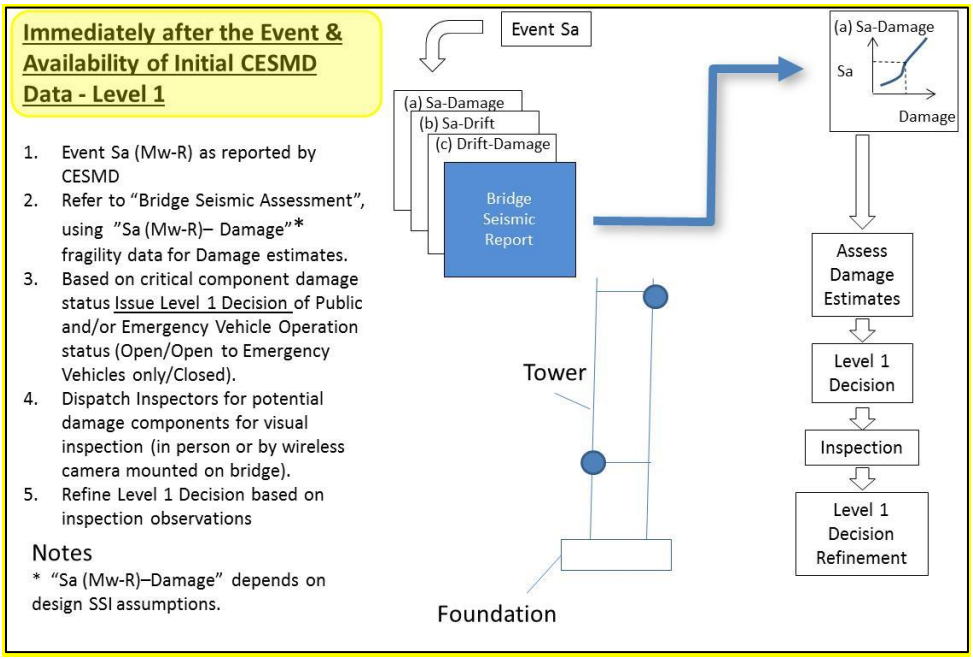

Figure 17: Immediately after Event Data Processing

As shown in Figure 17, immediately after an event, two levels of decisions can be made:

Level 1: this is a quick, but educated, decision making based on the relationship between spectra acceleration and damage.

Level 2: This is a more rigorous evaluation which requires the recoded data, and therefore takes more time. Using the measured drift values, use the fragility curves to estimate potential damage.

The followings are steps to be followed for this stage of data processing:

1. Use Spectra acceleration Sa(Mw-R) versus Damage generated in the pre-event data processing. This is "level 1" decision making based on the potential damage in the bridge.
2. Recover tower drift from CSMIP measured data.
3. Assess damage from the relationship between fragility and drift obtained in step 6 of the pre-event data processing.
4. Using the measured drift values and fragility curves, estimate the potential damage in the bridge. This is "level 2" decision making.
5. Alert inspection crew for anticipated damage and request for confirmation.

Post Event Data Processing

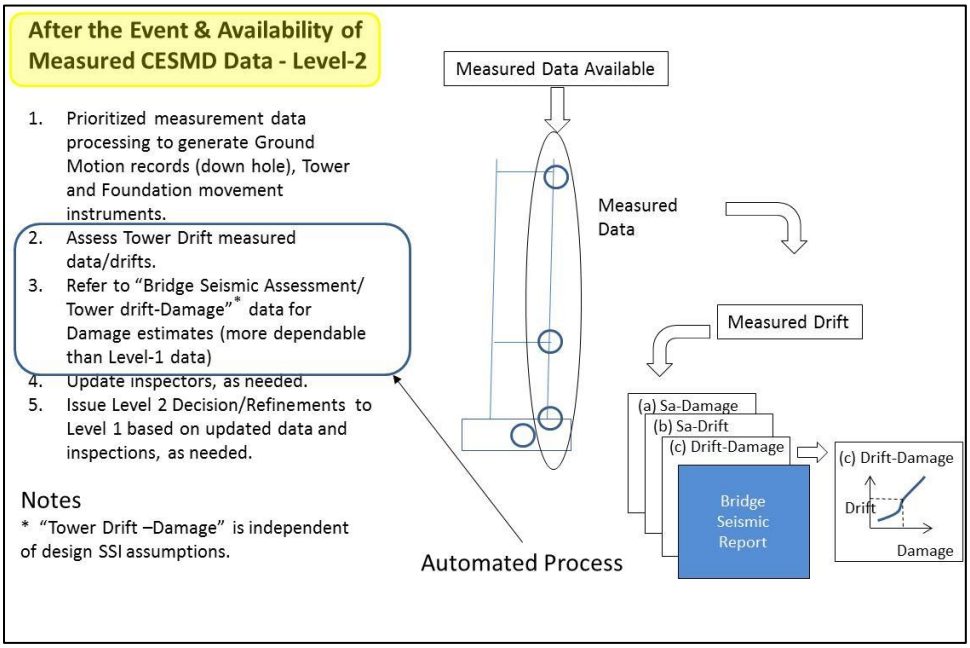

Figure 18: After Event Data Processing

In the "Post Event" data processing (see Figure 18), there is more time to improve on modeling of the structure as well as soil and interaction between the two. Also, the measured data can be studied in more detail. The following steps will be taken in this stage:

1. Compare measured scattered motion at the foundation with the estimated motions that were calculated in "pre-event" step 2.
2. Improve assumptions in the ground motion generation in "pre-event" step 2 based on the differences between the measured and calculated data.
3. Repeat and refine drift and fragility data analysis (steps 1 to 5 of the "pre-event" Figure 2), based on the improved ground motions

Conclusions

In this study, the prototype for a procedure was successfully developed to assess the damage immediately following an earthquake using the ground motion parameters of the earthquake event and fragility curves developed for the bridge so that a decision can be made on the continued use or closure of the bridge. This procedure, in this prototype, was implemented the west tower (T3) of the New Carquinez Bridge. For the 26 scenario ground motions the damage was observed for the longitudinal direction using the MDR and the fragility curves. The following steps were taken to successfully evaluate the damage state for the tower in the longitudinal direction. The scope of the current study is to evaluate seismic performance of Tower T3 in the longitudinal direction as "a critical component" of the bridge. The procedure

that is presented in this report can be equally applied to all other key components of the bridge, to produce system-wide fragility information, and base the bridge serviceability decision on the response of the governing key component.

1. A pushover analysis was performed to obtain the force-strain-drift relation of the tower.
2. The fragility curves for the Carquinez Bridge (NCB) Tower 3 (T3) were developed using experimental database obtained at the University of Nevada, Reno (UNR), and analytical ADINA response data were obtained for the demand. More than 100 shake table test data from studies of over 20 reinforced concrete (RC) bridge column models conducted at the University of Nevada, Reno (UNR) was used. The test data were calibrated for the cross section of the tower leg and the fragility curves for the Tower T3 were developed. The fragility curves (Figure 16, also shown in Figure 19) were prepared for six Damage States (DS) and relate the maximum drift ratio (MDR) to the probability of occurrence (POC) for each DS.
3. Values of MDR were computed and summarized in Table 4 for 26 scenario ground motions, using nonlinear time-history analysis of the detailed 3D model of the NCB. As shown in this table, each scenario has been defined by Mw, R, and Sa as well as the name of the event. Relative drift at the top of the tower T3 and at the location of point of inflection (PI) as well as maximum strain values in concrete and steel are summarized in this table. Therefore, this table provides a database of event (Mw, R, Sa) and MDR for tower T3.
4. For any MDR in this table, and using Figure 19, the fragility can be readily obtained; indicating that for all the 26 scenario cases there will be 0% POC for MS1. This is in conformance with the values of strain in steel and concrete summarized in Table 4.
5. While no damage was detected in the longitudinal Tower direction (i.e. subject of the study), the condition of other key components in a comprehensive system-wide evaluation may result in critical damage states.
6. These steps can be applied to evaluate the performance of all key bridge components to the corresponding system-wide and governing fragility curves.

Table 4: North-West Leg of Tower T3

					Sa (FN & FP)	Rel. Drift		strain		MDR
Scenario	RSN	Ground Motion Name	M	R (km)	(g)	at top (ft)	at PI (ft)	steel	concrete	ratio at PI
20	149	1979 Coyote Lake	5.74	4.79	0.10	0.45	0.13	-0.00013	0.00098	0.0013
19	147	1979 Coyote Lake	5.74	8.47	0.10	0.47	0.14	-0.00017	0.00099	0.0014
18	569	1986 San Salvador	5.80	3.71	0.10	0.43	0.13	-0.00011	0.00097	0.0013
17	4078	2004 Parkfield-02 CA	6.00	22.45	0.05	0.33	0.1	0.00006	0.00091	0.0010
13	8123	2011 Christchurch New Zealand	6.20	5.11	0.20	0.79	0.24	-0.00071	0.00116	0.0023
16	8099	2011 Christchurch New Zealand	6.20	17.86	0.10	0.4	0.12	-0.00006	0.00095	0.0012
22	159	1979 Imperial Valley-06	6.53	0.00	0.40	1.19	0.36	-0.00144	0.00134	0.0035
8	161	1979 Imperial Valley-06	6.53	8.54	0.38	0.73	0.22	-0.00059	0.00115	0.0021
15	313a	1981 Corinth Greece	6.60	10.27	0.10	0.49	0.15	-0.00021	0.00100	0.0015
26	313b	1981 Corinth Greece	6.60	10.27	0.10	0.55	0.16	-0.00030	0.00104	0.0016
14	1045b	1994 Northridge-01	6.69	2.11	0.20	0.55	0.16	-0.00030	0.00104	0.0016
6	1045a	1994 Northridge-01	6.69	2.11	0.35	0.72	0.22	-0.00059	0.00113	0.0021
23	1054	1994 Northridge-01	6.69	5.54	0.35	1.31	0.39	-0.00166	0.00139	0.0038
9	4847	2007 Chuetsu-oki Japan	6.80	9.43	0.23	0.9	0.27	-0.00091	0.00121	0.0026
21	1120	1995 Kobe Japan	6.90	1.46	0.48	1.48	0.44	-0.00229	0.00150	0.0043
7	1114	1995 Kobe Japan	6.90	3.31	0.32	1.14	0.34	-0.00135	0.00132	0.0033
12	292b	1980 Irpinia Italy-01	6.90	6.78	0.20	0.63	0.19	-0.00041	0.00111	0.0018
2	292a	1980 Irpinia Italy-01	6.90	6.78	0.40	0.95	0.28	-0.00100	0.00124	0.0027
10	6961	2010 Darfield New Zealand	7.00	13.37	0.12	0.62	0.19	-0.00043	0.00108	0.0018
11	6923	2010 Darfield New Zealand	7.00	30.53	0.12	0.5	0.15	-0.00021	0.00101	0.0015
5	5831	2010 El Mayor-Cucapah Mexico	7.20	14.80	0.18	0.76	0.23	-0.00066	0.00115	0.0022
4	864	1992 Landers	7.28	11.03	0.33	1.08	0.32	-0.00123	0.00129	0.0031
1	1176	1999 Kocaeli Turkey	7.51	1.38	0.48	1.31	0.39	-0.00166	0.00139	0.0038
3	1244	1999 Chi-Chi Taiwan	7.62	9.94	0.52	1.43	0.43	-0.00209	0.00146	0.0042
24	1236	1999 Chi-Chi Taiwan	7.62	37.48	0.20	0.81	0.24	-0.00075	0.00117	0.0023
25	2111	2002 Denali Alaska	7.90	42.99	0.10	0.38	0.11	-0.00003	0.00094	0.0011

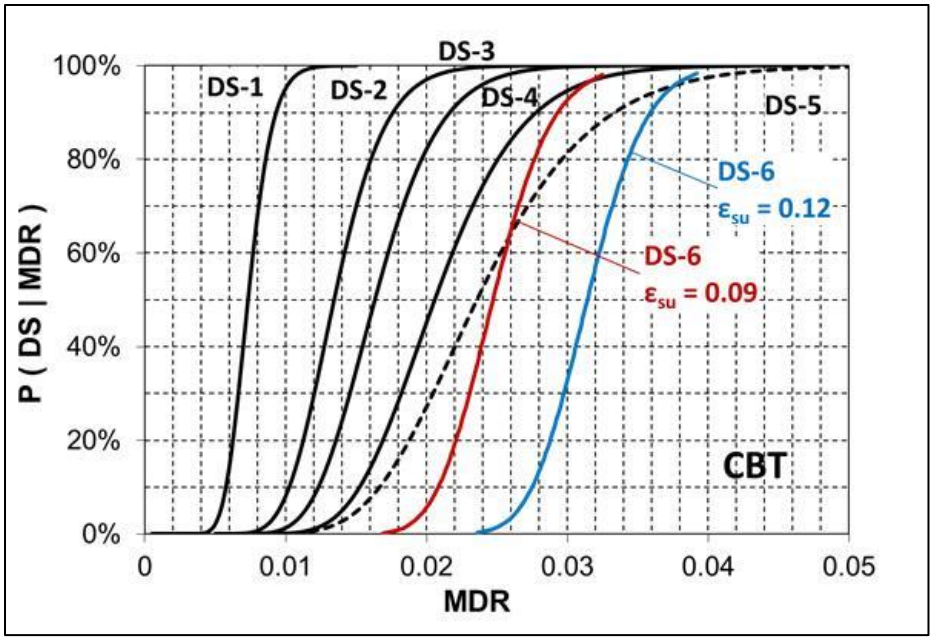

Figure 19: Maximum drift ratio fragility curves for T-3

References

1. Lilhanand, K. and Tseng W.S. (1987), "Generation of synthetic time histories compatible with multiple-damping response spectra.", Lausanne: SMiRT-9. K2/10.
2. Lilhanand, K. and Tseng W.S. (1988), "Development and application of realistic earthquake time histories compatible with multiple damping response spectra", Tokyo, Japan: Ninth World Conf. Earthquake Engineering, 1988. 819-824.
3. Somerville, P.G., N.F. Smith, R.W. Graves, and N.A. Abrahamson (1997). "Modification of empirical strong ground motion attenuation relations to include the amplitude and duration effects of rupture directivity", Seismological Research Letters 68, 199-222.
4. Mander et al. (1988), "Theoretical Stress-Strain Model for Confined Concrete", J. B. Mander; M. J. N. Priestley; and R. Park, Fellow, Journal of Structural Engineering, ASCE, Volume 14, Issue 8, September 1988.
5. American Society of Civil Engineers (1998). "Seismic Analysis of Safety-Related Nuclear Structures and Commentary." Reston, VA: ASCE, 4-98. 978-0-7844-0433-1.
6. Design Criteria (1999), Third Carquinez Strait Bridge Structural Design Criteria, Revision 6, 1 March, 1999, Prepared for the State of California, Department of Transportation, Division of Structures, Sacrament, California, by De Leuw, OPAC, Steinman, under contract 59A007.
7. Sedarat (1999), SC-Cable, Suspension Bridge Construction Sequence Application, Hassan Sedarat, SC Solutions, Inc., Sunnyvale, CA.

8. De Leuw–OPAC–Steinman (DLOS) (1999), "3rd Carquinez Strait Bridge Seismic Report", 100% submittal, Report, Submitted by: De Leuw – OPAC –Steinman, Caltrans Contract No. 59A0007, February, 1999.
9. Abrahamson, N.A. (2000) "Effects of rupture directivity on probabilistic seismic hazard analysis", Proceedings of the Sixth International Conference on Seismic Zonation, Earthquake Engineering Research Inst., Oakland, California.
10. DWG (2002), Construction Marked up Drawings of Alfred Zampa Memorial Bridge the Drawings.
11. Sleeter B.B., Calzia J.P., Walter S. R., Wong, F.L., and Saucedo G. J., (2004), "Earthquakes and faults in the San Francisco Bay Area (1970-2003)" http://pubs.usgs.gov/sim/2004/2848/, Last access, 085/27/2015.
12. ASCE 43-05 (2005), American Society of Civil Engineers (2005). "Seismic Design Criteria for Structures, Systems, and Components in Nuclear Facilities": American Society of Civil Engineers, 2005. ASCE/SEI 43-05.
13. SCS-NIST (2008), "Cyber-Enabled Wireless Monitoring Systems for the Protection of Deteriorating National Infrastructure Systems" Project, sponsored by NIST as part of the NIST TIP 2008 program, Development of detailed Finite Element Model of the New Carquinez Bridge, SC Solutions, 2008.
14. Baker, J. W., and Jayaram, N. (2008) "Correlation of spectral acceleration values from NGA ground motion models." Earthquake Spectra, 24(1), 299-317.
15. Atik, L.A. and Abrahamson, N. (2009) "An Improved Method for Nonstationary Spectral Matching." Earthquake Spectra, Vol. 26, No. 3, pp 601-617.
16. Vosooghi, Ashkan and Saiidi, M. Saiid (2010), "Seismic Damage States and Response Parameters for Bridge Columns" ACI Special Publication Series SP-271, Structural Concrete in Performance -Based Seismic Design of Bridges, 271 CD, 2010.
17. Baker, J. W. (2011), "Conditional Mean Spectrum: Tool for ground motion selection." Journal of Structural Engineering, 137(3), 322-331. http://dx.doi.org/10.1061/(ASCE)ST.1943-541X.0000215.
18. Gülerce, Z. and Abrahamson, N.A. (2011), "Site-Specific Design Spectra for Vertical Ground Motion." Earthquake Spectra: November 2011, Vol. 27, No. 4, pp. 1023-1047.
19. Shahi, S.K. and Baker, J. W. (2011), "An Empirically Calibrated Framework for Including the Effects of Near-Fault Directivity in Probabilistic Seismic Hazard Analysis." Bulletin of the Seismological Society of America, Vol. 101, No. 2, pp. 742-755.
20. Vosooghi, Ashkan and Saiidi, M. Saiid (2012), "Experimental Fragility Curves for Seismic Response of Reinforces Concrete Bridge Columns" ACI Structural Journal, November/December, 2012 pp 825-834.
21. Kurata, M., Kim, J., Lynch, J. P., van der Linden, G. W., Sedarat, H., Thometz, E., Hipley, P., Sheng, L. H (2013). "Internet-enabled Wireless Structural Monitoring Systems: Development and Permanent Deployment at the New Carquinez Suspension Bridge," Journal of Structural Engineering, ASCE, 139(10): 1688-1702.

22. Sedarat et al (2013), "Efficient Techniques in Finite Element Analysis and Seismic Evaluation of Suspension Bridges", Hassan Sedarat, Alexander Kozak, Joyce Lee, Alex Krimotat, Vince Jacob, Steve Mitchell, 7NSC -- Seventh National Seismic Conference on Bridges & Highways, Oakland, CA, May 20-22, 2013.

23. EMI (2014), "Kinematic Soil Pile Interaction for New Carquinez Bridge." Technical Memorandum, March 24, 2014, Earth Mechanics, Inc., Fountain Valley, CA.

24. Abrahamson, Silva and Kamai (2014), "NGA-West 2 equations for predicting PGA, PGV, and 5%-Damped PSA for shallow crustal earthquakes," Earthquake Spectra, 30.

25. Boore, D.M., J.P. Stewart, E. Seyhan, and G.M. Atkinson (2014), "NGA-West 2 equations for predicting PGA, PGV, and 5%-Damped PSA for shallow crustal earthquakes," Earthquake Spectra, 30.

26. Campbell, K.W. and Y. Bozorgnia (2014), "NGA-West 2 equations for predicting PGA, PGV, and 5%-Damped PSA for shallow crustal earthquakes, " Earthquake Spectra, 30.

27. Chiou, B.S.-J. and R.R. Youngs (2014), "NGA-West 2 equations for predicting PGA, PGV, and 5%-Damped PSA for shallow crustal earthquakes," Earthquake Spectra, 30.

28. Ancheta, T.D., Robert B. Darragh, Jonathan P. Stewart, Emel Seyhan, Walter J. Silva, Brian S.-J. Chiou, Katie E. Wooddell, Robert W. Graves, Albert R. Kottke, David M. Boore, Tadahiro Kishida, and Jennifer L. Donahue (2014) "NGA-West2 Database," Earthquake Spectra: August 2014, Vol. 30, No. 3, pp. 989-1005.

29. ATB (2014), ADINA Toll Bridges Project, sponsored by California Department of Transportation, Caltrans, 2014.

30. SCS (2015), "Rapid Post-Earthquake Safety Evaluation of the New Carquinez Bridge Using Fragility Curves and Strong-Motion Data: Seismic Hazard Memorandum." March 18, 2015, SC Solutions, Inc., Sunnyvale CA.

31. ADINA (2016), Automatic Dynamic Incremental Nonlinear Analysis, ADINA, ADINA R&D, 71 Elton Avenue, Watertown, MA 02472, USA.

32. SCMC (2016), an in-house section analysis program developed, SC Solutions, Inc., Sunnyvale, CA.

33. ATC-58 (2009), "Guidelines for Seismic Performance Assessment of Buildings," Applied Technology Council, Washington, D.C.

34. Massey, F. J. (1951). "The Kolmogorov-Smirnov Test for Goodness of Fit," Journal of the American Statistical Association, V. 46, No. 253, March, pp. 68-78.

35. Priestley, M. J. N.; Calvi, G. M.; and Kowalsky, M. J., (2007), Displacement-Based Seismic Design of Structures, IUSS Press, Pavia, Italy, 721 pp.

36. Caltrans (2013). "Seismic Design Criteria (SDC)," version 1.4, Calif. Dept. of Transportation, Sacramento, CA.

IDENTIFICATION AND VALIDATION OF NATURAL PERIODS AND MODAL DAMPING RATIOS FOR SEISMIC DESIGN AND BUILDING CODE

Yijun Xiang, Angie Harris, Farzad Naeim, and Farzin Zareian

Department of Civil & Environmental Engineering
University of California, Irvine

Abstract

Ninety-four buildings, with a total of 1045 distinct seismic event and building direction records, were selected from the CSMIP database to identify modal quantities (i.e., natural periods and equivalent viscous damping ratios). The selected buildings include steel and reinforced concrete moment resisting frames (i.e., SMRF, and RCMRF), reinforced concrete walls (RCW), concentrically braced frames (CBF), eccentrically braced frames (EBF), masonry walls (MAW), precast concrete walls (PCW), reinforced concrete tilt-up bearing walls (RCTUW), unreinforced masonry (URM), and WOOD. Simplified and practical equations for modal quantities along with variation of such parameters to structural system types, building height, amplitude of excitation, and system identification technique for a subset of buildings were reliable data was available are presented.

Introduction

Over the past few decades, researchers have utilized modal analysis as a means to estimate the natural periods and damping ratios of structural systems. The use of equivalent damping in seismic design has been at best ambiguous and not well defined. This is a major issue for seismic design of new buildings, and retrofit of existing structures alike, because no matter what design method is implemented, an estimate of fundamental period and equivalent modal viscous damping is necessary for the structural design process. The civil engineering community has utilized experimental data from instrumented buildings and system identification to gain insight on the actual dynamic characteristics of existing buildings. Until the implementation of system identification, the estimates of these dynamic characteristics had been at best meager estimates. The following provides a succinct review of previous research in engineering assessment of structural modal properties using system identification techniques.

Natural Periods

Several researchers have utilized system identification techniques to estimate natural periods to aid in the assessment of existing buildings and to evaluate the effectiveness of existing code period formulas. Cole *et al.* (1992) estimated the natural periods of sixty-four buildings using the transfer functions of the Fourier amplitude spectrum. These building periods were then compared to the code period formulas of the 1991 Uniform Building Code–UBC-91–(UBC, 1991) and 1990 Structural Engineers Association of California (SEAOC) Blue Book (SEAOC, 1990). They concluded that in most cases, the measured periods are longer than those of the code

periods for steel and concrete moment frames, but correlate well with the upper bound period formula. In addition, the measured periods for shear walls are usually shorter than that of the code formulas. Following Cole *et al.* (1992), Goel and Chopra (1997 & 1998) performed system identification on twenty-seven Reinforced Concrete Moment Resisting Frames (RCMRF), forty-two Steel Moment Resisting Frames (SMRF), and nine Reinforced Concrete Wall (RCW) buildings to determine their natural periods in comparison with the current code formulas of the ATC 3-06 (ATC, 1978), UBC-97 (UBC, 1997), SEAOC (1996), and National Earthquake Hazards Reduction Program (NEHRP, 1994). It was determined that the code formulas for the estimation of natural periods, at that time, were inadequate and led to shorter periods for RCMRFs and SMRFs, but longer periods than that identified for RCWs. New formulas were then derived, which have continued to be the basis for the current American Society of Civil Engineers/Structural Engineering Institute (ASCE/SEI) approximate period formulas.

Similarly, Kwon and Kim (2010) evaluated the fundamental periods of RCMRF and SMRF buildings that depicted the lower bound of code formulas and the periods of RCWs were shorter than code predicted values. Hong and Hwang (2000) performed system identification with the autoregressive exogenous (ARX) model of twenty-one RCMRF buildings in Taiwan and determined that the identified periods are less than that predicted in the UBC-97. Contrary to most studies, Lee *et al.* (2000) measured the natural periods of shear wall buildings only to find that the periods determined from the code formulas are significantly less that of the measured periods. Code period formulas, as previously noted, are based on values estimated from existing buildings through system identification. The trends seen in estimated periods can be influenced by the method of estimation, type of building studied, changes in design methods and philosophy, and the ground motions used to estimate the periods. On the other hand, several studies have explored the discrepancies between the natural periods provided through finite element models (FEM) and those estimated through system identification. This discrepancy comes from the inability of engineers to capture all forms of building lateral stiffness. This additional lateral stiffness is the result of the nonstructural elements that participate in the actual building response.

Since conventional methods being used by typical engineers to estimate dynamic response do not include the participation of all sources of stiffness, several researchers have worked to create an FEM methodology that designates all known sources of stiffness for the determination of natural periods. Hatzigeorgiou and Kanapitsas (2013) modeled twenty existing buildings, incorporating the stiffness of infill walls and soil flexibility properties to determine the natural period through numerical analysis. They formulated an expression for the estimation of the natural period based on the results of the models that account for building height, building width, shear wall ratio, and subgrade modulus, providing a comparable estimate to current code formulas. Amanat and Hoque (2006) explored the dependency of building periods on the percentage and distribution of infill walls by modeling diagonal struts to represent infill walls. They refined the UBC-97 equation for the fundamental period to include building geometry and the presence of infill panels based on the computational analysis. Similarly, Kocak and Yildirim (2011) modeled varying percentages of infill walls in SAP2000, determining that there is as much as forty-five percent change in period for buildings modeled with infill as opposed to bare frames. Skolnik *et al.* (2007) utilized the subspace state space identification method (N4SID) to compare identified modal parameters to that determined through FEM analysis. It was

determined that the participation of nonstructural components caused the natural period to be shorter for ambient vibration as opposed to low-to-moderate seismic excitation. As a result, the model was updated to account for the additional stiffness and mass using a modal-sensitivity based method.

Few studies have explored to what extent the nonstructural elements contribute to the overall stiffness of a building. Poovarodom and Charoenpong (2008), and Memari *et al.* (1999) investigated the progression of the fundamental period of reinforced concrete and steel buildings (respectively) throughout various stages of construction. The same study determined that as the completion of the building progressed and the percentage of nonstructural elements increased, the fundamental period decreased; proving the significance of the nonstructural elements' contribution to the building stiffness, and subsequently the estimation of natural periods and building performance.

Damping

The evaluation of building performance is not only dependent on the accurate estimation of its natural period, but also its damping. It is necessary for the energy dissipation of a building to be accurately modeled. However, damping continues to include much uncertainty and the ratios currently used in seismic design continue to be anything but well-defined. The Minimum Design Loads for Buildings and Other Structures, ASCE/SEI 7-10 (ASCE, 2010) requires the use of %5 damping, whereas FEMA P-58-1 (FEMA, 2012) requires that equivalent viscous damping should be within the range of %1 to %5 of the critical damping for the predominant modes. Similarly, the Los Angeles Tall Buildings Structural Design Council (LATBSDC, 2014) suggests that the additional modal or viscous damping should not exceed %2.5 of the critical damping for predominant modes. It is evident that a damping value between %1 and %5 should be used; however, the respective damping values for differing Lateral Force Resisting Systems (LFRS) are not explicitly given, providing additional uncertainty into the design process.

The history of design has included the use of classical damping, Rayleigh damping, which is only based on known building mass and stiffness. As previously discussed, stiffness is not always clearly defined. Consequently, Rayleigh damping has resulted in unrealistically large and non-conservative values. Current seismic design methods use equivalent linear viscous damping to model energy dissipation. However, these linear models, like others, have proven to provide false damping values (Bernal, 1994), especially when analyzing nonlinear behavior. Furthermore, studies have estimated damping ratios of existing buildings through system identification to explore relationships between building modal parameters, such as forecast models of period and damping (Lagomarsino 1993). Although, Lagomarsino's damping formulas were based on a viscous damping model, they did not prove that structural damping is viscous in nature.

Buildings are complex and the damping of these structures cannot solely be determined from a linear model. Frictional damping must be taken into account. Wyatt (1977) introduced the term "stiction" (static friction), where non-linear range/increase in damping can be correlated to the imperfections of the material the building is comprised of, which is aligned with fracture mechanics. The imperfections in the material are mobilized when the structure is excited; thus,

dissipating energy and increasing the structural damping. Subsequently, several studies have elaborated on Wyatt's theory, choosing to estimate equivalent damping based on known seismic excitation and system identification, showing that damping is amplitude dependent, and resulting in a myriad of equations for damping (Jeary, 1997; Li *et al.*, 1999; Davenport and Hill-Caroll, 1986; Fang *et al.*, 1999). It was found that at low amplitudes, damping seems to remain constant. As the amplitude increases, damping increases as well, in a non-linear range, until it arrives at a plateau at a higher amplitude of excitation (Jeary 1997). Tamura (2008) further explored this concept and demonstrated that damping increases only until the amplitude corresponding to the critical tip ratio is reached. The corresponding amplitude to this ratio is the critical point at which the damping begins to decrease. This idea corresponds to the assumption that as the amplitude of excitation increases, friction builds until it reaches a point when the components of the structure have "slipped" and the friction is constant, causing the damping relative to the friction forces to remain constant and eventually decrease. Satake *et al.* (2003) performed an analysis of building periods and modal damping ratios obtained from a database of 137 steel-framed buildings, twenty-five reinforced concrete buildings, and forty-three steel-framed reinforced concrete buildings. First mode damping was found to decrease with natural period (increasing with natural frequency). In addition, it was determined that the damping is amplitude dependent and increasing with mode shape number. Meanwhile, the first mode damping ratios in the small excitation amplitude region increase linearly with natural frequency or vibration amplitude. Bernal *et al.* (2012) similarly concluded that damping ratios, though they contained high amount of variability, increased with natural frequency.

On the other hand, future studies have explored damping and its dependence on the dominant building response characteristics. Bentz and Kijewski-Correa (2008) discussed the prediction of damping based on the dominance of a structural systems deformation mechanisms, shear or cantilever (i.e. flexural) action. Shear deformation takes precedence in frames where they deform from its generally square nature to a shape similar to a parallelogram. Cantilever deformation usually occurs in shear wall systems and other systems where the structure behaves like a continuous cantilever and the aspect ratio of the structure aids in the determination of the level of cantilever action. It was determined that damping values are more scattered for dual systems (between the shear and cantilever-flexure condition). As systems become more cantilever, damping values decrease. This is mainly due to reduction of effective interstory drift ratio, that is, the total interstory drift ratio minus rigid rotation of the story due to cantilever action. Reduction in effective interstory drift ratio results in the reduction of energy dissipation mechanism of the story–that is mostly friction based–and consequently leads to the reduction of damping values.

Data Collection and Description

CSMIP database of instrumented buildings contains structural records from more than 561 events in the general California crustal area. For the research study presented herein, ninety-four buildings, with a total of 1045 distinct seismic event and building direction records, are selected from the CSMIP database. The selected buildings include steel and reinforced concrete moment resisting frames (i.e., SMRF, and RCMRF), reinforced concrete walls (RCW), concentrically braced frames (CBF), eccentrically braced frames (EBF), masonry walls (MAW), precast concrete walls (PCW), reinforced concrete tilt-up bearing walls (RCTUW), unreinforced

masonry (URM) and WOOD. The list of the CSMIP instrumented buildings used in this study is presented in Appendix A (Table A.1). Among the 94 buildings used in this study, there are 25 SMRF, 11 RCMRF, 30 RCW, 11 CBF, 3 EBF, 6 MAW, 3 PCW, 2 RCTUW, 1 URM, and 2 WOOD buildings with 214, 123, 380, 145, 34, 74, 40, 9, 8 and 18 distinct seismic event and building direction records. Figure 1 provides further information on the statistics of the dataset used in this study.

System Identification

Four system identification methods are used for assessing natural periods and structural damping of the dataset. These system identification methods include: (1) ERA-OKID method (Luş *et al.*, 1999), (2) SRIM method (Juang, 1997), (3) N4SID (Van Overschee & De Moor, 1994), and (4) EFDD method (Ghahari *et al.* 2014). As the estimated frequency and damping ratio vary with the selection of different System Identification method as well as the selection of parameters for system realization especially in time-domain methods such as model order, starting point, time length and etc., a combined method is adopted for identification of a unique value of frequency and damping ratio in each mode considering all possible model parameters within all three time-domain System Identification methods. In this study, model order *N* and the time length *p* which indicate the number of layers the input and output information is stacked are considered as two parameters in SRIM method; model order *N* and the time length *p* which indicate how far the Hankel matrix is truncated are considered as two parameters in ERA-OKID method; model order *N* and the time length *p* which indicate the length of projection of future output onto input and past output are considered as two parameters in N4SID method.

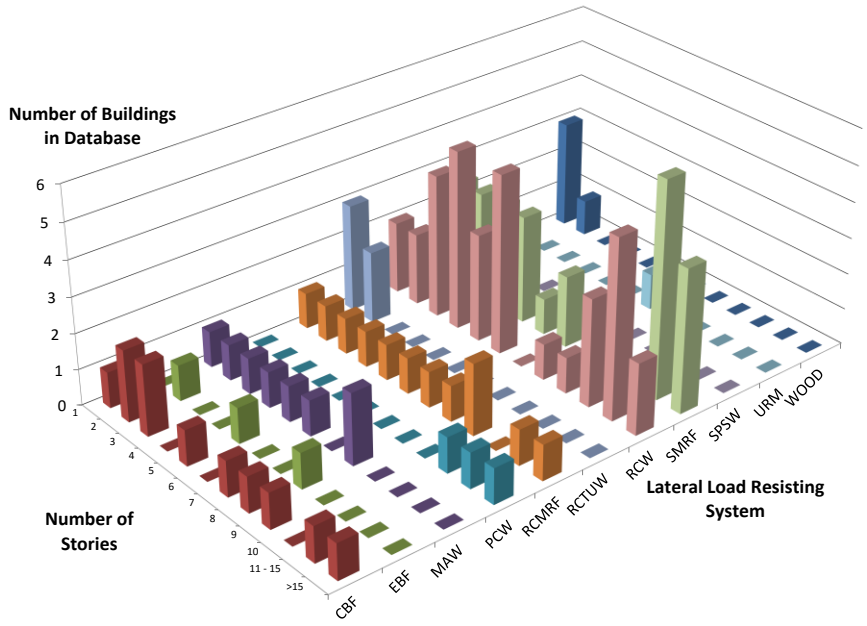

Figure 1. Statistics of the dataset used in this study

The process for combining the results of each System Identification method was developed to assure the results are encompassing and can address the variety of structural

systems in the CMSIP database. First, several combinations of model parameters are selected in each time domain method. For example, model order is selected based on the number of stories and the time length is selected based on the stability and rate of convergence of the state space model. Each specific combination of model parameters will lead to a specific estimate of frequency and damping ratio for all modes. Once a number of frequency and damping ratio estimates are obtained in each time domain method, the results are combined together after duplicating all estimates from each method based on a least common multiple of the number of estimates. The three time-domain methods are equally treated. Predominant frequencies can therefore be picked from those frequency components at peaks which represents the frequency component with the most population. Both frequency and damping ratio estimates are obtained by averaging all estimates in predominant frequency ranges. Final results are then compared to EFDD (Enhanced Frequency Domain Decomposition) estimates for verification.

To demonstrate the combination process, frequencies and damping ratios of the first three modes from the System Identification results of a 12-story SMRF building #24566 subject to the ground motion Anza 12Jun2005 with a PGA of 0.004g are shown in Figure 2. The histogram represents the population of each frequency component. Near the peaks are the mean values of frequencies and damping ratios given at the first line and the coefficients of variance given at the second line. Mode shape of each mode is plotted along with the mode shape values given at the place where sensors are implemented. Also the results obtained from combined time-domain method are compared to those obtained from EFDD (Enhanced Frequency Domain Decomposition) method for verification.

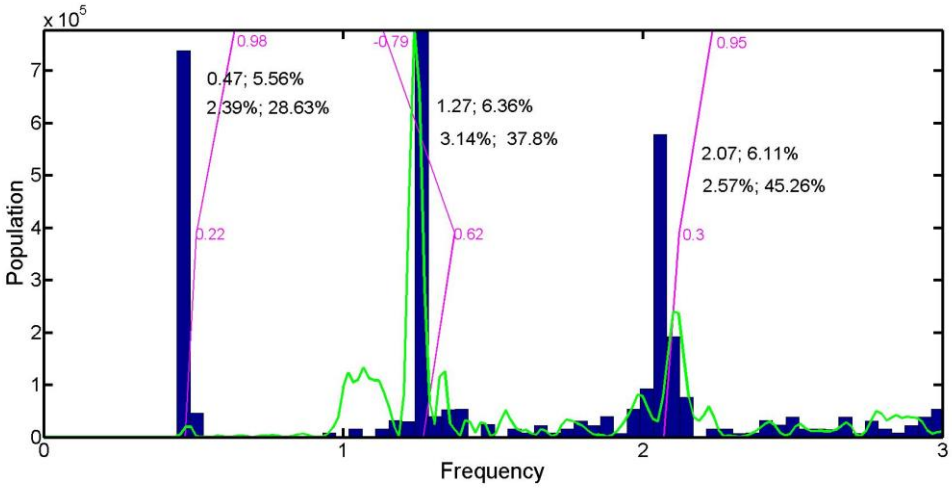

Figure 2. Frequency and damping estimates for each mode based on the combined System ID for the 12-story SMRF building #24566 subject to Anza 12Jun2005.

Equations for Natural Periods & Modal Damping Ratios for Buildings

The objectives of this study are to quantify natural periods and equivalent viscous damping ratios for buildings in the form of a set of meaningful and practical equations based on structural system types, building height and other factors that may prove to be significant. Multivariate regression analysis is utilized to fit modal properties to expressions in either linear

function or power function with building heights, building occupancy and ground motion intensity measures being considered as predictors. The goodness of fit is measured using T-tests and F-tests. In general, T-test is a test of whether an individual regression coefficient equals zero, accessing one regression coefficient at a time, while F-test accesses multiple regression coefficients simultaneously, is an overall test of whether the regression coefficients are jointly not all equal to zero. Difference between the full model and a reduced model when one or more predictors are excluded is estimated by the mean of squared errors *MSE* (sum of squared errors *SSE* divided by its degree of freedom). A *P-value* less than the significance level (usually 0.05) is considered significant, and a significant *P-value* leads to the rejection of null hypothesis and concludes that the model has better performance compared to the model with no predictors. As a measure of the goodness of regression fitting approximates data points, coefficient of determination R^2, which equals the ratio of sum of squared deviation *SSR* to total variation *SSTO*, stands for the effect of predictors in reducing the variation; the larger R^2 is, the more total variation is reduced.

Preliminary model investigation plays an important role before the modal is built. The correlation matrix is constructed to observe whether the response and each of the predictor candidates are positively or negatively correlated. Also, the correlation between predictors is indicative of collinearity. Automatic search procedure, including Best Subsets algorithm and Stepwise Regression method, serves to select the most proper set of predictors without evaluating all of the possible combinations. Five criteria for model selection are utilized: coefficient of determination; adjusted coefficient of determination which takes the total number of predictors into consideration as a penalty; mean of squared errors *MSE*, *Mallow's Cp* which compares the precision and bias of the full model with models including only a subset of the predictors; *PRESSp* which measures the sum of the squared prediction errors while a single prediction error is defined as the difference between fitted response with the deletion of a single case and the observed response. Best Subsets regression identifies the best among several models with respect to specified criterion for each number of predictors included in the model. Unlike Best Subset regression accepting several models, the forward stepwise regression develops a single model by adding or deleting a predictor variable at each step, and the criterion for adding or deleting a predictor is defined through a T-test involving the difference between model including that predictor and model excluding that predictor. The ultimate model with suitable predictors decided through model selection is then examined by hypothesis tests.

The aptness of the regression model should be examined before any inference is undertaken. Diagnostics involving residuals are considered, including tests for normality, test for constancy, test for outliers and influential cases and the lack of fit test. Two tests are employed for the examination of the normality of error terms: *Ryan-Joiner* normality test and *Kolmogorov-Smirnov* normality test.

For ascertaining the constancy of error variance, *Brown-Forsythe* test, which is independent of normality, is applied. For identification of outlying observations, as well as, influential cases, *Hat Matrix Leverage values*, *Studentized Deleted residuals*, *DFFITS* and *Cook's Distance* are calculated and the corresponding T-tests or F-tests are employed. For determining whether a specific function is a good fit for the data, F-test for lack of fit, which requires repeat cases at one or more predictors' levels, is taken up. In addition, the standardized regression model is introduced for diagnostics of lack of comparability due to differences in the

variables units and diagnostics of multicollinearity when predictor variables are correlated. Variance Inflation Factor (*VIF*) which represents the level of collinearity is also computed from the standardized model, and a large value of *VIF* is indicative of serious multicollinearity problem and then interaction terms need to be included in the model.

Remedial measures need to be carried out when diagnostics demonstrate that the regression model is not appropriate enough for the data. For non-normality of error terms, *Box-Cox Transformation* alters the shape and the spread of the distribution of response to correct the skewness of the distribution of error terms. Weighted least squares method helps to reduce unequal error variances by introducing weights into the regression, while weights are affected by the absolute residuals or squared residuals. Robust regression is taken up in the same manner if the error terms exhibit outliers and influential cases. *IRLS* robust regression is employed in this study by the use of weights that vary inversely with the magnitude of scaled residuals. Several iterations may be required to keep on revising the weights until convergence criteria is satisfied. Since predictor multicollinearity is not detected in this study, remedial techniques modifying the sampling distribution of regression coefficients to overcome multicollinearity problem, such as *Ridge* regression, is not considered.

Aside from the linear regression model that takes the logarithm of response (natural period, damping ratio) and predictors (building heights, ground motion intensity measure, etc.), nonlinear regression models involving these variables are studied for comparison purposes. In this study, the Gauss-Newton method numerically searches the solution using Taylor series expansion to approximate a nonlinear model with linear terms, and the linear model solution obtained before is selected as the nonlinear initial guess.

Modal Properties and for Steel Moment Resisting Frames (SMRF)

Dynamic properties of 25 SMRF buildings representing 195 building-events (data points) were computed using System Identification methods. Building Height ranges from 26 ft to 692.5 ft, *PGA* ranges from 0.004g to 0.299g, *PGV* ranges from 0.187cm/s to 24.404 cm/s, and *PGD* ranges from 0.008cm to 12.639cm. The buildings were divided into two subcategories as far as occupancy is concerned: (1) Residential, office and commercial buildings, (2) Hospitals. Our recommended regression equation for estimating the fundamental period, and first mode damping of SMRF buildings is given in Eq. (1), and Eq. (2), respectively; units are: T_1 (sec), *PGV* (cm/sec), *H*(ft). Comparison of regression results for fundamental period of SMRFs at *PGV* = 10cm/s and ASCE 7-10 formula are shown in Figure 3. The 95% confidence and prediction intervals for the damping regression equation are presented in Figure 4.

$$T_1 = \begin{cases} 0.017H^{0.82}PGV^{0.06} & \text{Hospital} \\ 0.026H^{0.82}PGV^{0.06} & \text{Other} \end{cases} \qquad \text{Eq. (1)}$$

$$\xi_1 = 8.86H^{-0.16} \qquad \text{Eq. (2)}$$

Modal Properties and for Reinforced Concrete Moment Resisting Frames (RCMRF)

Dynamic properties of 11 RCMRF buildings representing 123 building-events (data points) were computed using System Identification methods. Building height ranges from 30 ft to 168.8 ft, *PGA* ranges from 0.003g to 0.453g, *PGV* ranges from 0.161cm/s to 54.904 cm/s, and *PGD* ranges from 0.008cm to 13.778cm. Our recommended regression equation for estimating the fundamental period, and first mode damping of RCMRF buildings is given in Eqs. (3) and (4). Comparison of regression results for T_1 at *PGV*=10cm/s and ASCE 7-10 formula are shown in Figure 5. The 95% confidence and prediction intervals for the equation presented for first modal damping are presented in Figure 6.

$$T_1 = 0.01H^1 PGV^{0.12} \quad \text{Eq. (3)}$$

$$\xi_1 = 3.89\, PGV^{0.05} \quad \text{Eq. (4)}$$

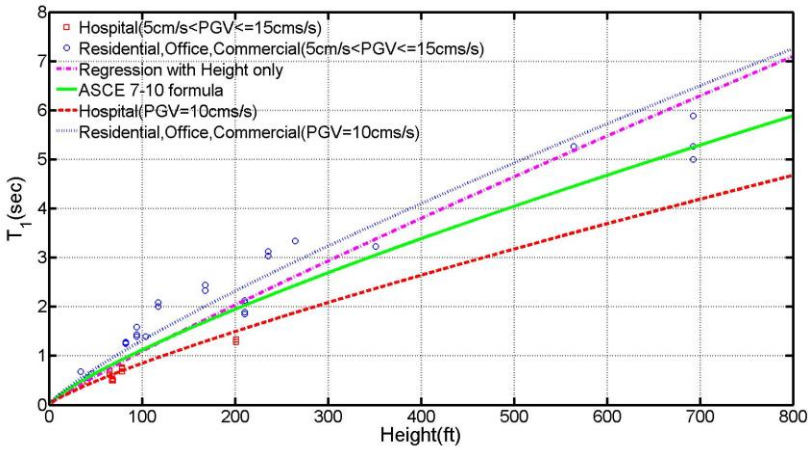

Figure 3. Fundamental period for SMRF buildings regressed on Height vs. ASCE 7-10 formula

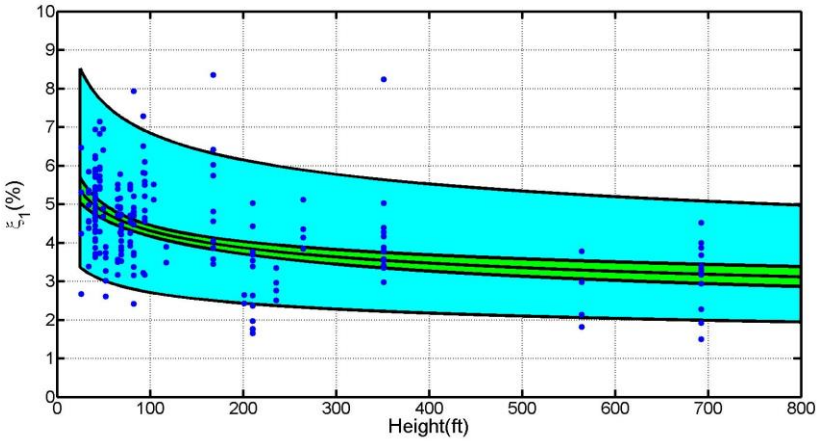

Figure 4. 95% confidence and prediction range for first mode equivalent damping of SMRF

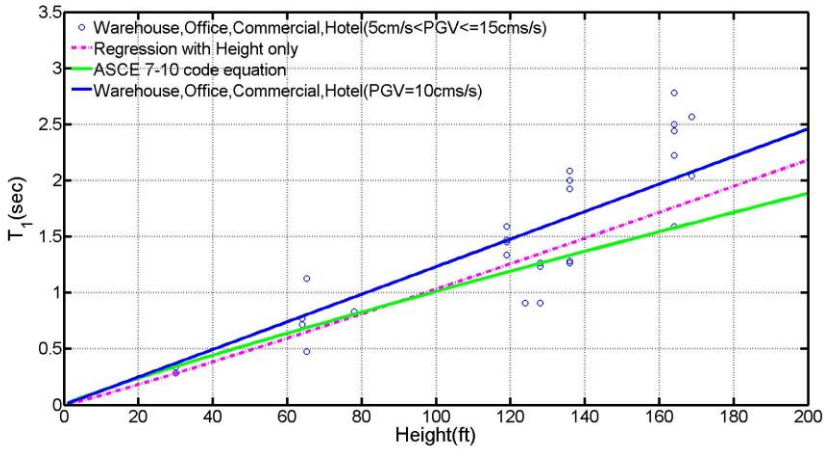

Figure 5. Fundamental period for RCMRF buildings regressed on Height vs. ASCE 7-10 formula

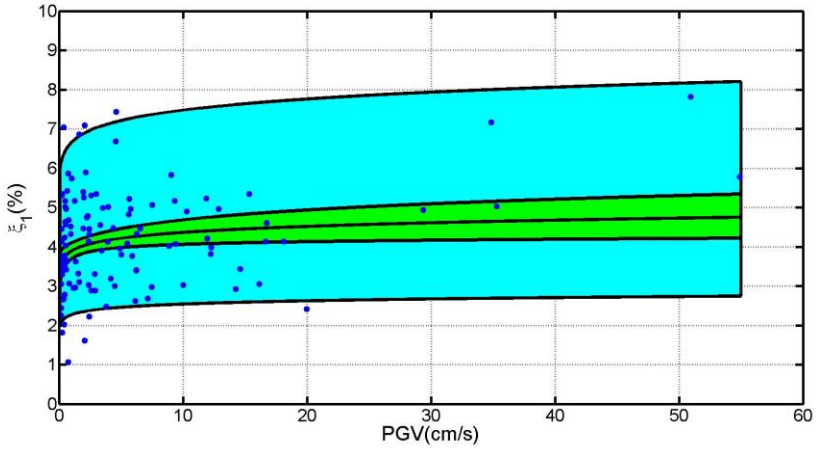

Figure 6. 95% confidence and prediction range for first mode equivalent damping of RCMRF

Modal Properties and for Reinforced Concrete Walls (RCW)

Thirty RCW buildings, with heights ranging from 27.5 ft. to 229.33 ft, representing 336 building-events (data points) were used for quantifying their dynamic properties. *PGA*, *PGV*, and *PGD* range from 0.001g to 0.798g, 0.062cm/s to 112.139 cm/s, and 0.003cm to 28.298cm, respectively. The buildings were divided into two subcategories: (1) Library, Residential, Office, Hotel, Commercial buildings and Parking Structures, and (2) Schools and Hospitals. Recommended equations for T_1 and ξ_1 of RCW buildings is given in Eqs. (5) & (6). Comparison of regression results for *PGV*=10cm/s and ASCE 7-10 formula are shown in Figure 7. The 95% confidence and prediction intervals for the regression equation are presented in Figure 8.

$$T_1 = \begin{cases} 0.009H^{0.87}PGV^{0.02} & \text{School/Hospital} \\ 0.013H^{0.87}PGV^{0.02} & \text{Other} \end{cases} \qquad \text{Eq. (5)}$$

$$\xi_1 = 5.06H^{-0.08} \qquad \text{Eq. (6)}$$

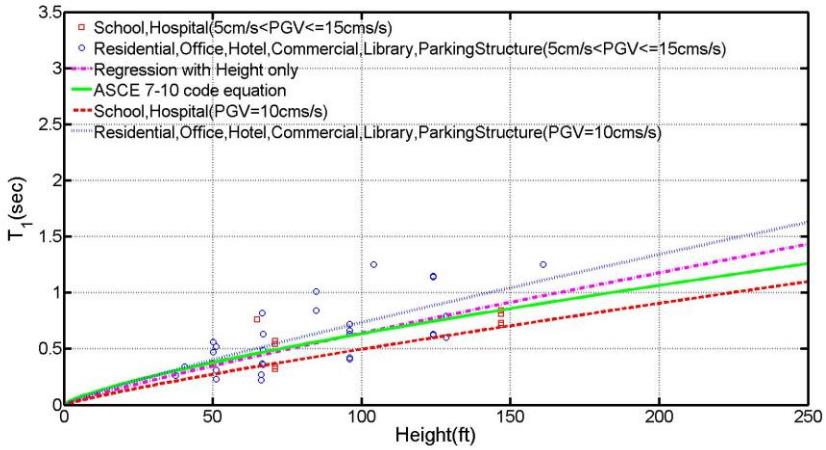

Figure 7. Fundamental period for RCW buildings regressed on Height vs. ASCE 7-10 formula

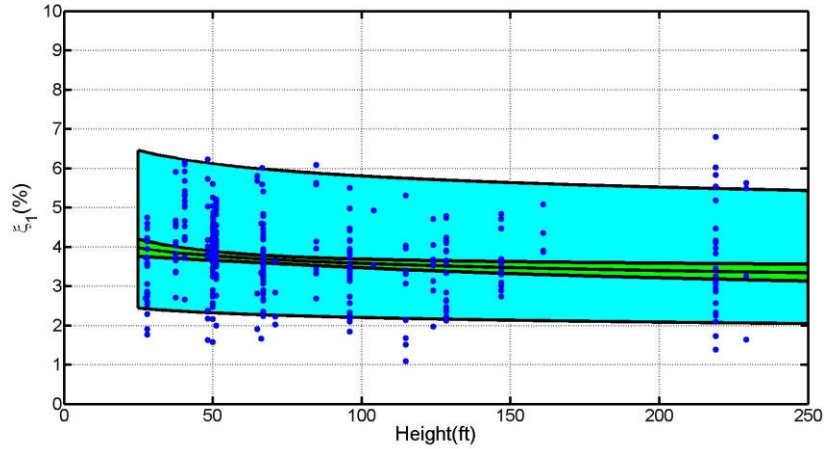

Figure 8. 95% confidence and prediction range for first mode equivalent damping of RCW

Modal Properties and for Concentrically Braced Frames (CBF)

Dynamic properties of 11 CBF buildings representing 144 building-events were computed; 31.92' < *H* < 716', 0.001g < *PGA* < 0.327g, 0.001 cm/s< *PGV* < 29.640cm/s, and 0.003cm < *PGD* < 9.813cm. The buildings were divided into two subcategories: (1) Industrial, Office, Commercial buildings and Parking Structures, and (2) Jails and Hospitals. The recommended equations for T_1 and ξ_1 of CBF buildings is given in Eqs. (7) & (8). Comparison of regression results and ASCE 7-10 formula are shown in Figure 9. The 95% confidence and prediction intervals for the regression equation are presented in Figure 10.

$$T_1 = \begin{cases} 0.005H^{1.02} & \text{Jail/ Hospital} \\ 0.007H^{1.02} & \text{Other} \end{cases} \qquad \text{Eq. (7)}$$

$$\xi_1 = 3.37 \qquad \text{Eq. (8)}$$

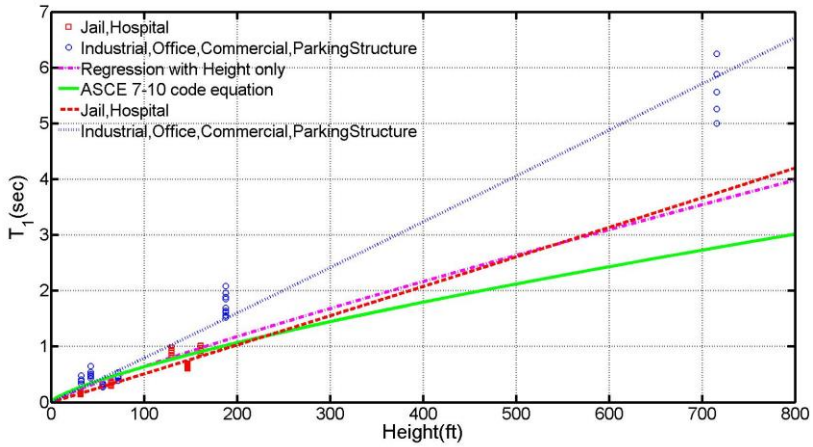

Figure 9. Fundamental period for CBF buildings regressed on Height vs. ASCE 7-10 formula.

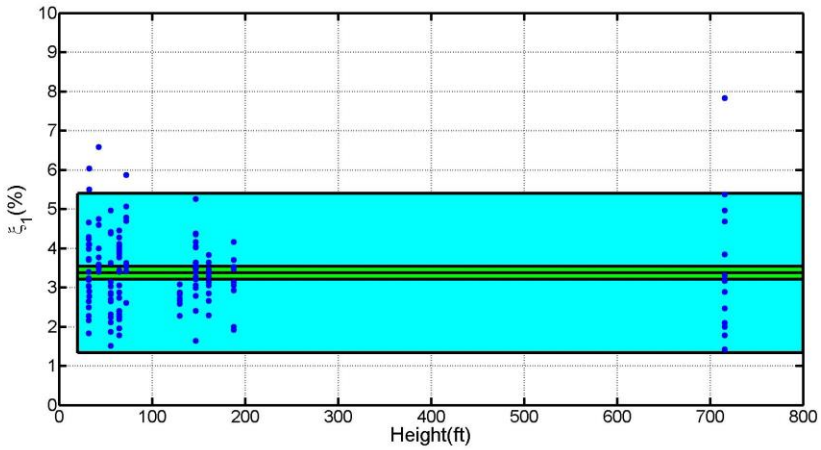

Figure 10. 95% confidence and prediction range for first mode equivalent damping of CBF

Modal Properties and for Eccentrically Braced Frames (EBF)

11 EBF buildings representing 144 building-events were used to generate equations for their fundamental period and first modal damping; see Eqs. (9) & (10). Building height ranges from 31.92ft to 716 ft, *PGA* ranges from 0.001g to 0.327g, *PGV* ranges from 0.001cm/s to 29.640 cm/s, and *PGD* ranges from 0.003cm to 9.813cm. The buildings were divided into two subcategories: (1) Industrial, Office, Commercial buildings and Parking Structures, and (2) Jails and Hospitals. Comparison of regression results and ASCE 7-10 formula are shown in Figure 9. The 95% confidence and prediction intervals for the regression equation are presented in Figure 10.

$$T_1 = 0.07 H^{0.46} PGV^{0.04} \qquad \text{Eq. (9)}$$

$$\xi_1 = 6.43 H^{-0.13} \qquad \text{Eq. (10)}$$

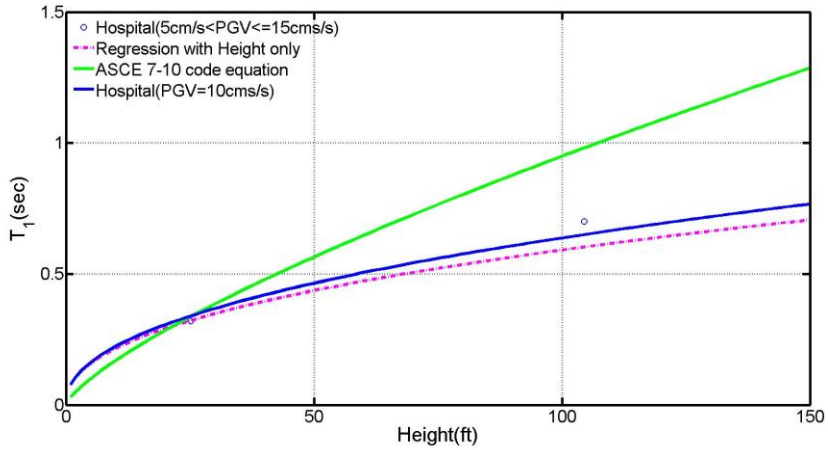

Figure 11. Fundamental period for EBF buildings regressed on Height vs. ASCE 7-10 formula.

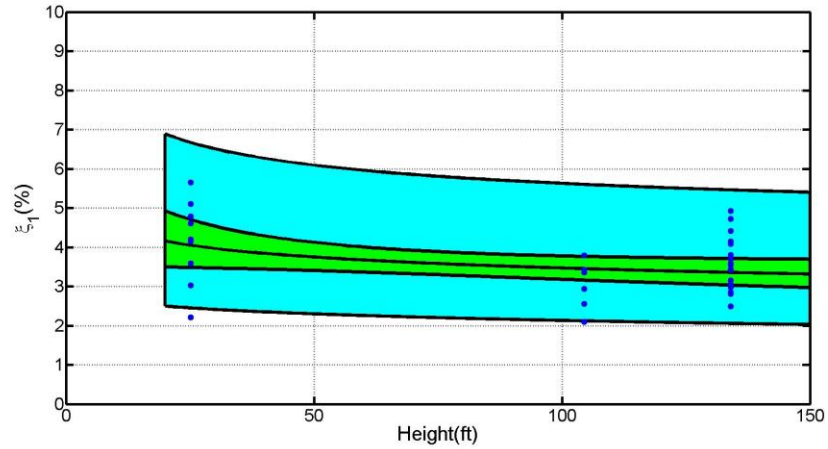

Figure 12. 95% confidence and prediction range for first mode equivalent damping of EBF

Modal Properties and for Masonry Walls (MAW)

Eqs. (11) & (12) show our suggested formulation for T_1 and ξ_1 of MAWs. 5 MAW buildings representing 72 building-events were utilized with building height ranges from 22ft to 85ft. Data point suggest a *PGA* range between 0.002g to 0.258g, *PGV* range between 0.091cm/s to 33.003cm/s, and *PGD* range from 0.006cm to 7.900cm. Comparison of regression results and ASCE 7-10 formula are shown in Figure 13. The 95% confidence and prediction intervals for the regression equation are presented in Figure 14.

$$T_1 = 0.004\,H^{1.09} \qquad \text{Eq. (11)}$$

$$\xi_1 = 3.62 \qquad \text{Eq. (12)}$$

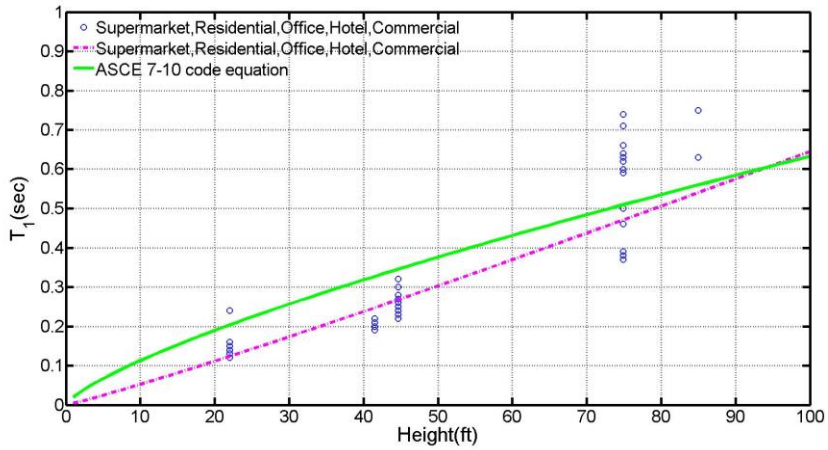

Figure 11. Fundamental period for MAW buildings regressed on Height vs. ASCE 7-10 formula.

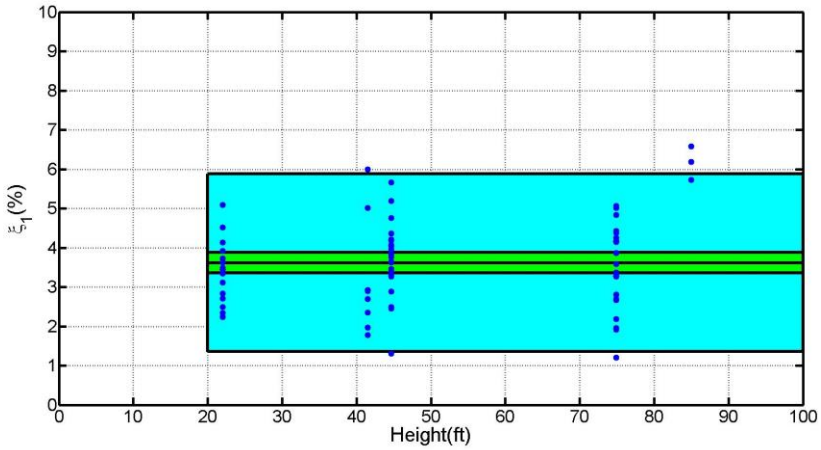

Figure 12. 95% confidence and prediction range for first mode equivalent damping of MAW

Acknowledgements

The contents of this report were developed under Agreement No. 1014-962 from the California Department of Conservation, California Geological Survey, Strong Motion Instrumentation Program. However, these contents do not necessarily represent the policy of that agency nor endorsement by the State Government.

References

ATC (1978). Tentative provisions for the development of seismic regulations for buildings. *Rep. No. ATC 3-06*, Applied Technological Council, Palo Alto, Calif.

Amanat, K. M., & Hoque, E. (2006). A rationale for determining the natural period of RC building frames having infill. *Engineering Structures*, **28**(4), 495-502.

ASCE-American Society of Civil Engineers (2010). *Minimum Design Loads for Buildings and Other Structures* (ASCE/SEI 7–10). American Society of Civil Engineers: Reston, VA.

Bentz, A., & Kijewski-Correa, T. (2008). Predictive models for damping in buildings: the role of structural system characteristics. In *Proceedings of the 2008 Structures Congress, 18th Analysis and Computation Specialty Conference, Vancouver, Canada*.

Bernal, D. (1994). Viscous damping in inelastic structural response. *ASCE Journal of Structural Engineering*, **120**(4): 1240-1254.

Bernal, D., Mozaffari Kojidi, S., Kwan, K., & Döhler, M. (2012). Damping identification in buildings from earthquake records. *SMIP12 Seminar on Utilization of Strong-Motion Data, p. 39 - 56.*

Cole, E. E., Tokas, C. V., & Meehan, J. F. (1992). Analysis of recorded building data to verify or improve 1991 Uniform Building Code (UBC) period of vibration formulas. *Proc. SMIP92. Strong Motion Instrumentation Program, Division of Mines and Geology, California Department of Conservation*. Sacramento, Calif.

Davenport, A. G., & Hill-Carroll, P. (1986). Damping in tall buildings: its variability and treatment in design. In *Building motion in wind*, p. 42-57. ASCE.

Fang, J. Q., Jeary, A. P., Li, Q. S., & Wong, C. K. (1999). Random damping in buildings and its AR model. *Journal of Wind Engineering and Industrial Aerodynamics*, **79**(1), 159-167.

Federal Emergency Management Agency (FEMA), 2012. *Seismic Performance Assessment of Buildings Volume 1 – Methodology, Tech. Rep. P-58-1*, Washington, D.C.

Ghahari, S.F., Abazarsa, F., Ghannad, M.A., Celebi, M., & Taciroglu, E. (2014). Blind modal identification of structures from spatially sparse seismic response signals. *Earthquake Engineering and Structural Dynamics*, **21**(6): 649-674.

Goel, R., & Chopra, A.K. (1997). "Period formulas for moment-resisting frame buildings". *Journal of Structural Engineering*; **123**(11): 1454 – 1461.

Goel, R., & Chopra, A.K. (1998). "Period formulas for concrete shear wall frame buildings". *Journal of Structural Engineering*; **124**(4): 426 – 433.

Hatzigeorgiou, G. D., & Kanapitsas, G., 2013. Evaluation of fundamental period of low-rise and mid-rise reinforced concrete buildings. *Earthquake Engineering & Structural Dynamics*, **42**(11), 1599-1616.

Hong, L. L., & Hwang, W. L. (2000). Empirical formula for fundamental vibration periods of reinforced concrete buildings in Taiwan. *Earthquake engineering & structural dynamics*, **29**(3), 327-337.

Jeary, A. P. (1997). Damping in structures. *Journal of Wind Engineering and Industrial Aerodynamics*, 72: 345 – 55.

Kocak, A., & Yildirim, M. K. (2011). Effects of Infill Wall Ratio on the Period of Reinforced Concrete Framed Buildings. *Advances in Structural Engineering* **14**(5), 731-744.

Kutner, M. H., Nachtsheim, C.J., Neter, J., & Li, W. (2005). *Applied Linear Statistical models*. Fifth Edition.

Kwon, O. S., & Kim, E. S. (2010). Evaluation of building period formulas for seismic design. *Earthquake Engineering & Structural Dynamics*, **39**(14), 1569-1583.

Lagomarsino, S. (1993). Forecast models for damping and vibration periods of buildings. *Journal of Wind Engineering and Industrial Aerodynamics*, **48**(2), 221-239.

Lee, L. H., Chang, K. K., & Chun, Y. S. (2000). Experimental formula for the fundamental period of RC buildings with shear-wall dominant systems. *The Structural Design of Tall Buildings*, **9**(4), 295-307.

Li, Q. S., Liu, D. K., Fang, J. Q., Jeary, A. P., & Wong, C. K. (2000). Damping in buildings: its neural network model and AR model. *Engineering Structures*, **22**(9), 1216-1223.

Ljung, L. (1999) *System Identification: Theory for the User*, Upper Saddle River, NJ, Prentice-Hal PTR.

LATBSDC (2014). *An Alternative Procedure for Seismic Analysis and Design of Tall Buildings Located in The Los Angeles Region.* Los Angeles Tall Buildings Structural Design Council.

Luş, H., Betti, R., & Longman, R. W. (1999). Identification of linear structural systems using earthquake induced vibration data. *Earthquake Engineering and Structural Dynamics*, 28:1449-1467.

Memari, A. M., Aghakouchak, A. A., Ashtiany, M. G., & Tiv, M., (1999). Full-scale dynamic testing of a steel frame building during construction, *Engineering Structures*, **21**(12), 1115-1127.

NCHRP (1994). *Recommended Provisions for the Development of Seismic Regulations for New Buildings*, National Earthquake Hazards Reduction Program, Building Seismic Safety Council.

Poovarodom, N., & Charoenpong, K., 2008. Identification of Dynamic Properties of Low-Rise RC Building by Ambient Vibration Measurements During Construction, in *Proceedings, 14th World Conference on Earthquake Engineering*, 12–17 October, 2008, Beijing, China.

Meeting of the Architectural Institute of Japan (AIJ), p. 379-380.

Satake, N., Suda, K. I., Arakawa, T., Sasaki, A., & Tamura, Y. (2003). Damping evaluation using full-scale data of buildings in Japan. *Journal of structural engineering*, **129**(4), 470-477.

Skolnik, D., Yu, E., Wallace, J., & Taciroglu, E. (2007). Modal System Identification & Finite Element Model Updating of a 15-story Building using Earthquake & Ambient Vibration Data. *In Structural Engineering Research Frontiers*, p. 1-14. ASCE.

SEAOC (1988). *Recommended Lateral Force Requirements,* Structure Engineers Association of California, Seismology Committee.

SEAOC (1990). *Recommended Lateral Force Requirements,* Structure Engineers Association of California, Seismology Committee.

SEAOC (1996). *Recommended Lateral Force Requirements,* Structure Engineers Association of California, Seismology Committee.

Tamura, Y., & Yoshida, A. (2008). Amplitude dependency of damping in buildings. In *Proceedings of the 18th Analysis and Computation Specialty Conference* (Vol. 315).

UBC (1991). International Conference of Building Officials, *Uniform Building code*, 1991 Edition.

UBC (1997). International Conference of Building Officials, *Uniform Building code*, 1997 Edition.

Van Overschee, P., & De Moor, B. (1994). N4SID: Subspace algorithms for the identification of combined deterministic-stochastic systems. *Automatica*, **30**(1), 75-93.

Wyatt, T. A. (1977, May). Mechanisms of damping. In *Proceeding of a Symposium of Dynamic Behavior of Bridges at the Transpor and Road Research Laboratory, Crowthorne, Berkshire, England, May 19, 1977*. (No. TRRL Rpt. 275 Proceeding).

Appendix A

Table A.1. Set of buildings used in this study

Index	Building Station	Primary VLLR	Building Height (ft)	Number of Stories	Number of Eqs X Dir
1	12299	SMRF	65.5	4	8
2	13312	SMRF		13	10
3	14323	SMRF	104.0	7	2
4	14533	SMRF	265.0	15	6
5	23481	SMRF	94.4	7	10
6	23515	SMRF	117.6	9	2
7	23516	SMRF	41.3	3	18
8	23634	SMRF	69.0	5	10
9	24104	SMRF	41.0	2	16
10	24198	SMRF	34.0	2	8
11	24288	SMRF	351.2	32	16
12	24370	SMRF	82.5	6	14
13	24566	SMRF	168.0	12	12
14	24569	SMRF	236.0	15	4
15	24609	SMRF	78.5	5	8
16	24629	SMRF	692.5	54	14
17	54388	SMRF	26.0	2	4
18	57357	SMRF	210.6	13	12
19	57562	SMRF	49.5	3	4
20	58261	SMRF	52.5	4	6
21	58354	SMRF	201.1	13	4
22	58506	SMRF	46.2	3	12
23	58532	SMRF	564.0	47	4
24	58755	SMRF	92.5	6	4
25	68669	SMRF	67.9	4	6
26	12493	RCMRF	64.0	4	12
27	23511	RCMRF	30.0	3	20
28	24322	RCMRF	164.0	13	14
29	24386	RCMRF	65.2	7	15
30	24454	RCMRF	39.0	4	2
31	24463	RCMRF	119.0	5	18
32	24464	RCMRF	168.8	20	8
33	24571	RCMRF	136.0	9	12
34	24579	RCMRF	128.0	10	14
35	57355	RCMRF	124.0	10	6
36	58490	RCMRF	78.0	6	2
37	12267	RCW	48.3	4	10
38	12284	RCW	50.2	4	20
39	13329	RCW		8	6
40	13589	RCW	146.9	11	14
41	13620	RCW	27.5	2	2
42	14311	RCW	71.0	5	4
43	23285	RCW	67.0	5	28
44	23287	RCW	51.1	6	36
45	24514	RCW	96.0	6	10
46	24655	RCW	67.0	6	12
47	24680	RCW	161.0	14	4

48	25339	RCW	114.9	12	12
49	47459	RCW	66.3	4	4
50	57355	RCW	124.0	10	7
51	57356	RCW	96.0	10	15
52	58224	RCW	28.0	2	24
53	58334	RCW		3	20
54	58337	RCW		11	16
55	58348	RCW	40.6	3	20
56	58364	RCW	128.5	10	22
57	58394	RCW	104.0	9	2
58	58462	RCW	84.8	6	8
59	58479	RCW	65.0	6	6
60	58480	RCW	229.3	18	4
61	58483	RCW	219.0	24	24
62	58488	RCW	50.0	4	10
63	58503	RCW	37.5	3	12
64	68387	RCW	66.7	5	2
65	68489	RCW	124.0	14	2
66	89770	RCW	50.0	4	24
67	13698	CBF	42.5	2	8
68	13702	CBF	161.0	7	12
69	14654	CBF	188.0	14	10
70	24248	CBF	147.0	9	22
71	24332	CBF	72.5	5	8
72	24602	CBF	716.0	57	14
73	24713	CBF	130.0	8	8
74	47796	CBF	65.0	3	24
75	54331	CBF	31.9	2	18
76	57948	CBF	32.5	2	5
77	58196	CBF	55.8	5	16
78	24249	EBF	134.0	8	18
79	57594	EBF	104.5	5	6
80	58496	EBF	25.2	3	10
81	23544	MAW	85.0	6	3
82	24232	MAW	50.0	4	2
83	24517	MAW	41.5	3	8
84	58492	MAW	74.9	8	22
85	89473	MAW	22.0	1	16
86	89494	MAW	44.7	5	23
87	24385	PCW	88.0	10	20
88	24601	PCW	149.7	17	6
89	58639	PCW	114.0	13	14
90	23540	RCTUW	29.0	2	1
91	57502	RCTUW	31.6	2	8
92	24541	URM	82.1	6	8
93	12759	WOOD	12.3	2	12
94	36531	WOOD	13.2	2	6

IDENTIFICATION OF DYNAMIC FOUNDATION STIFFNESSES AND INPUT MOTIONS FROM STRONG MOTION DATA RECORDED AT CSMIP INSTRUMENTED BUILDINGS

S.F. Ghahari and E. Taciroglu

Department of Civil & Environmental Engineering

University of California, Los Angeles

Abstract

Substructure method is commonly used in engineering practice to take Soil-Structure Interaction (SSI) effects into account in seismic design. In this method, soil is modeled using discrete spring elements—ideally Impedance Functions (IF)—that are attached to the superstructure; and the Foundation Input Motions (FIMs) are applied at the remote ends of these springs. While the application of the substructure method is simple and its computational cost is low, the determination of FIMs and the IFs are generally challenging. This paper presents results of a two-year project during which a new method was developed to identify IFs and to back-calculate FIMs from earthquake data recorded at CSMIP-instrumented buildings. The method features a flexible-based Timoshenko beam idealization of the superstructure and its soil-foundation system, and is based on updating the parameters of this model such that its responses match real-life data. Details of the said method are briefly reviewed first, followed by a presentation of the results it produced on currently available CSMIP data.

Introduction

Soil-Structure Interaction (SSI) has been a research subject for more than 40 years (Jennings & Kuroiwa, 1968; Richat, 1975; Wolf, 1976). SSI effects can be classified into two distinct effects: *kinematic* and *inertial* (Wolf & Deeks, 2004). Dubbed the Foundation Input Motions (FIMs), the earthquake excitations experienced by a structure-foundation system are altered by the foundation stiffness and distinct geometry. Therefore, FIMs are generally different from the Free-Field Motions (FFMs) that would have been recorded in the absence of the foundation. The effects causing the said differences in FIMs and FFMs are collectively referred to as kinematic effects. Inertial interaction effects are due to the mass of the foundation-superstructure system, which imparts inertial forces onto the surrounding soil and causes the foundation to experience a response that is different from the FIM. Due to inertial effects, the vibrating structure operates as a wave source and alters the wave field around the foundation system (Abrahamson et al., 1991).

The direct and the substructure methods are two approaches used for taking SSI effects into account in seismic response analyses. In the direct method, a complete—usually a Finite Element (FE)—model of the soil-structure system is created wherein the soil medium is represented as a semi-infinite domain (Pak & Guzina, 1999; Rizos & Wang, 2002). Due to its labor-intensive model development and high computational costs, the direct method is typically avoided in engineering practice. In the substructure method, the SSI problem is typically

decomposed into three distinct parts (Stewart et al., 1998): (*i*) estimation of FIMs, (*ii*) determination of the frequency-dependent soil-foundation Impedance Functions (IFs), and (*iii*) dynamic analysis of the super-structure supported on a compliant base represented by the IFs and subjected to the FIMs.

Accurate estimation of FIMs and IFs control the accuracy of the substructure method. However, available formulations for estimation/determination of FIMs and IFs are primarily limited to analytical studies (Gazetas, 1983; Iguchi & Luco, 1981; Çelebi et al., 2006), which are typically confined to simple foundation geometry and soil conditions, or experimental data with relatively low-amplitude excitations (Tileylioglu et al., 2010). Motivated by this, the present project's aim has been to develop a robust, accurate, and broadly applicable method to identify IFs and FIMs from earthquake-induced response signals recorded on instrumented buildings. Using real-life data is key, because neither field (e.g., forced vibration) nor laboratory (e.g., centrifuge) tests can mimic the range of complexities encountered in the field—the former cannot induce strong motion amplitudes at broad frequency bands, and the latter cannot provide the full set of complexities of soil constitutive behavior or wave propagation patterns.

The method devised in the present effort is based on representing the superstructure-foundation-soil systems through flexible-base Timoshenko beam models, and subsequently estimating models parameters (i.e., soil-foundation IFs and Timoshenko beam properties) by minimizing the discrepancy between the model-predicted and real-life dynamics responses.

The simplified model adopted in the present study (i.e., the flexible-base Timoshenko) nominally precludes the investigation of the frequency-dependency of the foundation system of a single building. However, because the devised identification method was applied to a large set of buildings here, it produced results that illuminate the behavior of several classes of foundation systems at a range of excitation frequencies. This study involved analyses of 373 earthquake datasets from 21 steel and 40 concrete instrumented buildings of the California Strong Motion Instrumentation Program (CSMIP) (see, Huang and Shakal, 2001). These records were judiciously selected from the current CSMIP building inventory using a Matlab-based (Matlab, 2013) data classification toolbox named CSMIP-CIT that was developed for the present project, into which the developed identification method is also implemented (Ghahari et al., 2015).

As the basic formulation, verification, and application of the developed identification method to a particular case—namely, the Millikan Library in Pasadena CA were previously presented (Taciroglu et al., 2016a and b)—, only a brief overview of the method is provided in what follows. The remainder of the manuscript is devoted to the presentation of the selected data, the results obtained from those data, and finally a discussion of findings in comparison to previous key studies on SSI.

The Proposed Identification Method

Consider a Timoshenko beam (1921) resting on a sway-rocking foundation as shown in Figure 1. Through modal superposition, the absolute acceleration of the beam under horizontal base acceleration—i.e., $\ddot{u}_g(t)$, which can be a real-life recording—, can be written as

$$\ddot{y}^t(x,t) = \sum_{j=1}^{n} W_j(x)\ddot{q}_j(t) \;\; + \ddot{u}_g(t) \tag{1}$$

where $\ddot{q}_j(t)$ is relative acceleration of a SDOF system under $\beta_j \ddot{u}_g(t)$ with β_j being the modal contribution factor. $W_j(x)$ is a function that describes the *j*-th normal mode shape for lateral displacements, and can be obtained via modal analysis of the model as described in (Taciroglu et al., 2016a). This function has 5 dimensionless parameters; namely,

$$s^2 = \frac{EI}{GA_sL^2}, \quad b_j^2 = \frac{\rho A {\omega_j}^2 L^4}{EI}, \; k_T = \frac{K_T}{GA_s/L}, \quad k_R = \frac{K_R}{EI/L} \quad R^2 = \frac{I}{AL^2} \tag{2}$$

where E, G, ρ, and A are the Young's and shear moduli, mass density, and section area, respectively. To consider the non-uniform distribution of shear stress within the Timoshenko beam's cross-section, $A_s = \kappa A$ is used as the effective shear cross-sectional area, where κ can be approximated as 0.85 for rectangular sections (Cowper, 1966). ω_j is the *j*-th natural frequency, and K_T and K_R are the nominally frequency-dependent soil-foundation stiffnesses, which are assumed to be frequency independent in the proposed method for simplicity. To calculate the modal coordinates ($\ddot{q}_j(t)$), modal orthogonality with respect to mass matrix (**M**) can be used (Han et al., 1999). Hence, $q_j(t)$, and consequently its time derivatives, can be identified from the equation below

$$\ddot{q}_j(t) + {\omega_j}^2 \, q_j(t) = \beta_j \ddot{u}_g(t) \tag{3}$$

where the modal contribution factor is $\beta_j = L_j^*/m_j^*$. Here L_j^* and m_j^* denote, respectively, the generalized influence factor and mass, and are defined as

$$L_j^* = \rho A \int_0^L W_j(x)\, dx \;, \quad m_j^* = \int_0^L \boldsymbol{\varphi}_j(x)^T \, \mathbf{M} \, \boldsymbol{\varphi}_j(x) \tag{4}$$

where

$$\boldsymbol{\varphi}_j(x) = \begin{bmatrix} W_j(x) \\ \Theta_j(x) \end{bmatrix} \tag{5}$$

where $\Theta_j(x)$ is a function describing the *j*-th normal mode shape for rotational deformations. To consider damping, while retaining the normal-mode assumption, we add a term $2\,\omega_j\,\xi_j\,\dot{q}_j(t)$ with ξ_j being the *j*-th modal damping ratio to Eq. (3), to make it similar to the response of a damped SDOF system (Chopra, 2001).

For the proposed identification method, we assume that the absolute acceleration of a flexible-base building is available at three levels—namely, the foundation level $\ddot{y}^t(0,t)$, the mid-height level $\ddot{y}^t(x_m,t)$, and the roof $\ddot{y}^t(L,t)$. According to Eqs. (1) and (3), each of these response signals can be expressed in the frequency domain as

$$\ddot{y}^t(x,\omega) = \left[\sum_{j=1}^{n} W_j(x)\,\beta_j H_j(\omega) + 1\right] \ddot{u}_g(\omega) \tag{6}$$

with

$$H_j(\omega) = \frac{-\omega^2}{{\omega_j}^2 - \omega^2 + 2i\xi_j\omega_j\omega}. \tag{7}$$

Accordingly, the response at mid-height and the roof can be predicted by the response of the foundation level by eliminating the input excitation as in

$$\ddot{y}^t(x,\omega) = \frac{\left[\sum_{j=1}^{n} W_j(x)\,\beta_j H_j(\omega) + 1\right]}{\left[\sum_{j=1}^{n} W_j(0)\,\beta_j H_j(\omega) + 1\right]} \ddot{y}^t(0,\omega). \tag{8}$$

Therefore, by defining and solving a proper minimization problem, the unknown parameters of the system can be identified. A similar approach has been successfully used by Lignos and Miranda (2014) to identify the input motion of fixed-base structures, who linked shear and flexural beams to represent their parametric models.

We define the following optimization problem here

$$\min_{\bar{b},s,k_T,k_R,\xi_1,\ldots,\xi_n} \left\|\ddot{y}^t(x_m,t) - \ddot{\tilde{y}}^t(x_m,t)\right\| + \left\|\ddot{y}^t(L,t) - \ddot{\tilde{y}}^t(L,t)\right\| \tag{9}$$

where $\ddot{\tilde{y}}^t(x_m,t)$ and $\ddot{\tilde{y}}^t(L,t)$ denote the response signals recorded at mid-height and roof levels, respectively, and $\ddot{y}^t(x_m,t)$ and $\ddot{y}^t(L,t)$ are their counterparts predicted by Eq. (8) and transformed to the time domain through Inverse Fourier Transform. We replace the dimensionless parameter b_j with $\bar{b} = b_j/\omega_j$ to make it mode-independent. This optimization problem is non-convex and may have several local minima. We, therefore devise constraints to decrease the possibility of being trapped in a local minimum. As the first flexible-base natural frequency can be easily detected from the Fourier spectrum of the roof response using simple peak-picking, we add this information as a constraint to the optimization problem. Moreover, we start the optimization procedure with multiple random starting points.

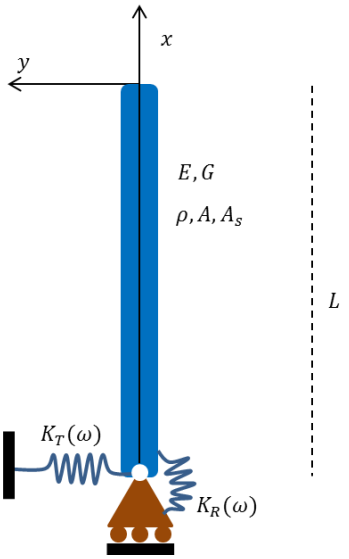

Figure 1. Timoshenko beam model of a soil-structure system.

Once the unknown parameters are identified by solving the optimization problem, the unknown input motion, $\ddot{u}_g(\omega)$, can be back-calculated through Eq. (6) using any of the available measured response signals. Additionally, the foundation rocking response can be estimated by converting the foundation translational response, as in

$$\ddot{\alpha}(x,\omega) = \frac{\left[\sum_{j=1}^{n} \Theta_j(0)\,\beta_j H_j(\omega)\right]}{\left[\sum_{j=1}^{n} W_j(0)\,\beta_j H_j(\omega) + 1\right]}\,\ddot{y}^t(0,\omega) \tag{10}$$

To identify the pseudo-flexible and fixed base damping ratios (Stewart & Fenves, 1998), we can easily define optimization problems similar to Eq. (9).

For the pseudo-flexible model, we can predict the response of mid-height and roof levels by analyzing a pseudo-flexible base Timoshenko beam subjected to horizontal foundation response, using Eq. (6). In this case, all modal properties—i.e., ω_j, ξ_j, m_j^*, L_j^*, and $W_j(x)$—must be calculated for a pseudo-flexible Timoshenko beam, while $\ddot{u}_g(\omega)$ must be $\ddot{y}^t(0,\omega)$. The damping ratio is then identified by solving a minimization problem such that the predicted mid-height and roof level responses match the recorded responses.

For the fixed-flexible model, we can predict the response at mid-height and roof levels by analyzing a fixed-base Timoshenko beam subjected to horizontal and rocking foundation responses, and by minimizing the difference between predicted and recorded signals. Note that the foundation-rocking response is already predicted through Eq. (10). To predict the response of a fixed-base Timoshenko beam model under horizontal ($\ddot{u}_g(\omega)$) and rocking ($\ddot{\theta}_g(\omega)$) base excitations, we have

$$\ddot{y}^t(x,\omega) = \left[\sum_{j=1}^{n} W_j(x)\,\beta_j H_j(\omega) + 1\right]\ddot{u}_g(\omega) + \left[\sum_{j=1}^{n} W_j(x)\,\bar{\beta}_j H_j(\omega) + x\right]\ddot{\theta}_g(\omega) \tag{11}$$

where again $\beta_j = L_j^*/m_j^*$ and $\bar{\beta}_j = \bar{L}_j^*/m_j^*$. The terms L_j^* and m_j^* are calculated using Eq. (4), and $H_j(\omega)$ is calculated using Eq. (7) wherein the fixed-base mode shapes and natural frequencies must be used. $\bar{L}_j^*$ is the generalized influence factor for rocking excitation and must be calculated as in

$$\bar{L}_j^* = \rho\, I \int_0^L \Theta_j(x)\, dx + \rho\, A \int_0^L x\, W_j(x)\, dx \qquad 12)$$

using the fixed-base mode shapes.

Studied Data

CSMIP Database

Established in 1972, the California Strong Motion Instrumentation Program (CSMIP) aims to collect seismic response data from ground stations as well as representative structures (bridges, dams, and buildings). At the present time, there are more than 900 stations (650+ ground-response stations, 170+ buildings, 20 dams, and 60+ bridges). CSMIP stations are configured to collect data, when triggered by a seismic event, and the resulting records are archived for public use in searchable database—*viz.*, the Center for Engineering Strong Motion Database (CESMD)[1].

Data Classification

CESMD provides station metadata in addition to seismic recordings. These metadata enable the classification of building stations into sub-categories. Nevertheless, CESMD only offers basic search and sorting capabilities. Motivated by the need to look at behavior across different types (structural systems, foundation systems, and heights), we developed the CSMIP-CIT toolbox (as briefly described above), which automatically harvests the response data and station metadata, enables user-guided classification, and applies the identification method presented above (Ghahari et al 2015). This toolbox features a graphical user interface (Figure 2), and is able automatically generate a short report (Figure 3).

We employ the classification capability of CSMIP-CIT and processed the available data in CESMD[2]. Table 1 displays a summary of available *building* data. As seen, there are currently 377 instrumented buildings in CESMD (a complete list can be found in Taciroglu et al., 2016c). It is expedient to note here that only the data collected by California Geological Survey (CGS) was used in the present study, primarily out of necessity, because the channel numbers in both the instrumentation layout plans and the data files are identical only in the CGS data. As it can be seen from Figure 4, less than 70% of the buildings are instrumented by the CGS, which is equivalent to 259 buildings. Out of all 259 buildings instrumented by CGS, data from only 216 buildings are useable at the present time, due to the availability of both earthquake data and the instrumentation layouts (Table 2).

[1] www.strongmotioncenter.org

[2] The CSMIP-CIT database was last updated on 03/28/2016.

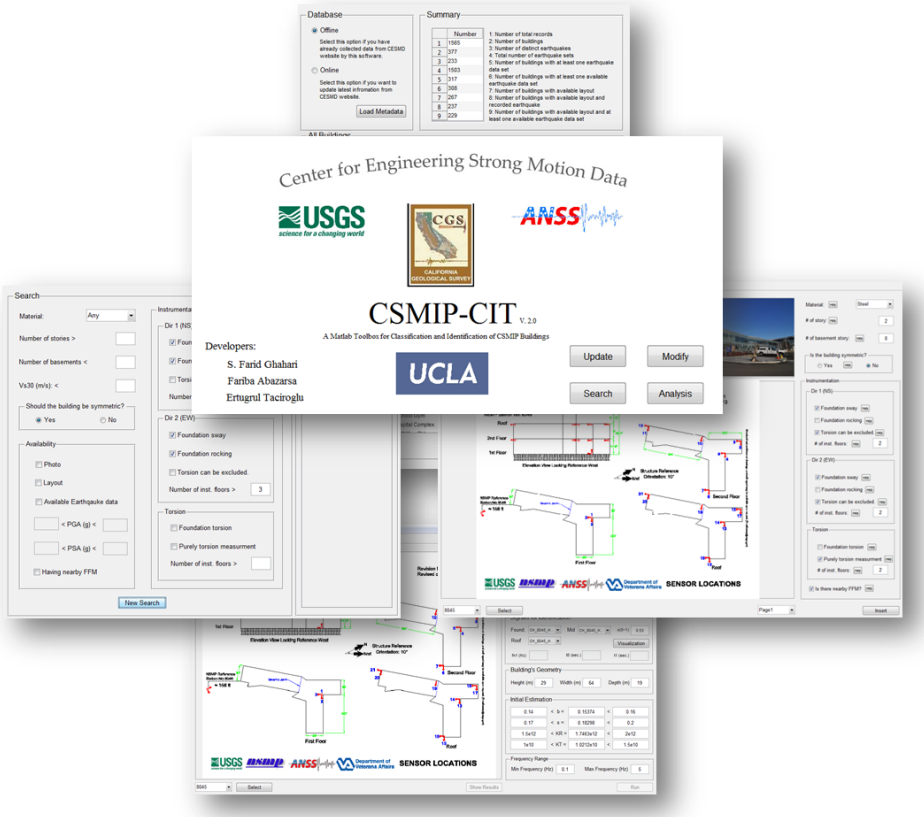

Figure 2. Graphical user interface of the CSMIP-CIT software.

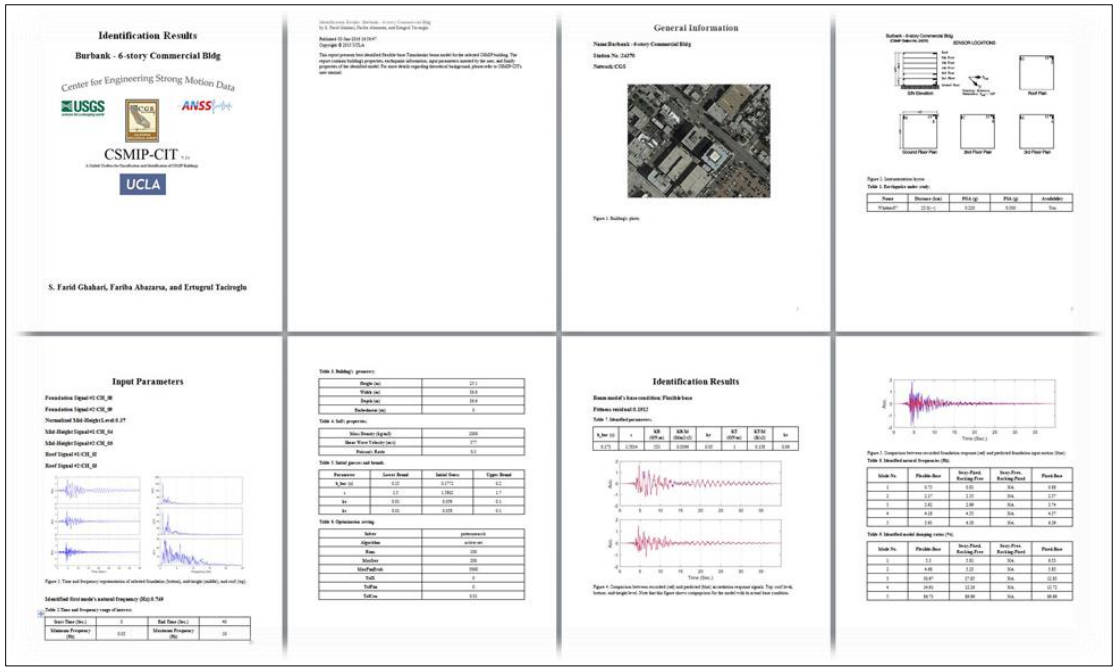

Figure 3. Report automatically generated by CSMIP-CIT software.

Table 1. Available building data in CESMD.

Item Description	Number
Number of total records	1643
Number of buildings	377
Number of earthquakes	254
Number of earthquae sets	1588
Number of buildings with at least one earthquake	322
Number of buildings with at least one available earthquake	314
Number of buildings with available layout	272
Number of buildings with available layout and at least one recorded earthquake	243
Number of buildings with available layout and at least one available earthquake	236

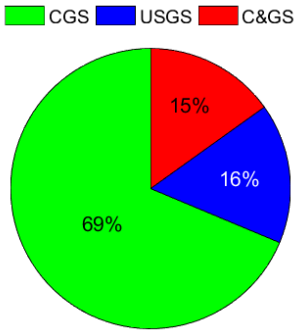

Figure 4. Distribution of the available data.

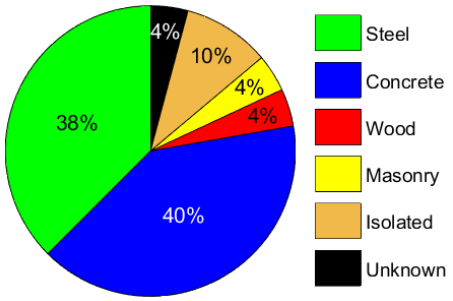

Figure 5. Materials of all 216 useable CGS buildings.

Table 2. Available building data in CESMD instrumented by CGS.

Item Description	Number
Number of buildings	259
Number of buildings with at least one available earthquake	218
Number of buildings with available layout	242
Number of buildings with available layout and at least one available earthquake	216

In the present study, we study only steel and concrete ordinary buildings (i.e., wood, masonry, and base isolation structures were excluded). Figure 5 indicates that ~80% of the 216 instrumented buildings are potentially subject of the present study, which are 168 buildings. Note that "Unknown" category in Figure 5 denotes those buildings whose lateral system could not be identified from their layout or description provided at CESMD.

It is well accepted that the identification of buildings from their earthquake-induced response signals is directly affected by the number and distribution of the sensors. Theoretically, soil-foundation flexibilities can be identified by investigating the difference between the so-called flexible-based and fixed-base system's properties (Stewart & Fenves, 1998). To identify both the fixed- and flexible-base properties, the FFM, foundation sway, foundation rocking, and building responses must be measured. However, the number of CSMIP buildings with necessary instrumentation for this purpose is very limited. As shown in Figure 6, under

Case 1, out of the 168 selected buildings, the total number of steel and concrete buildings that have instrumentation layouts, available earthquake records, nearby Free-Field Motion (FFM) stations, foundation sway and rocking instrumentations, and at least one instrumented floor is less than 10. It is useful to note that it may be possible to find FFM stations close to some of other buildings, but the aforementioned classification is based on FFM stations shown on the instrumentation layouts available in CESMD.

If we can relax the FFM requirement, then the number of buildings increases to 23 (denoted as Case 2). Such a number is still very small and cannot be used to extract aggregate results from which broad conclusions can be drawn. Another critical limitation is the availability of the foundation rocking measurement. The identification method devised in the present project is, therefore, a key tool, because with this method, it is now possible to quantify soil-structure interaction effects *even without foundation rocking measurements*. By relaxing the rocking measurement condition, the number of available buildings increases from 23 to around 164 (denoted as Case 3). Having only one sensor on the structure may not be able to capture contribution of different modes. Therefore, it is more favorable to have additional sensors, as used in Eq. (9). As the figure shows, by adding one more sensor as an additional requirement (denoted as Case 4), the number of buildings available for the study decreases, but not significantly (~129) [3]. Based on this fact, we designed CSMIP-CIT only for Case 4, through which 129 buildings can be analyzed at the present time.

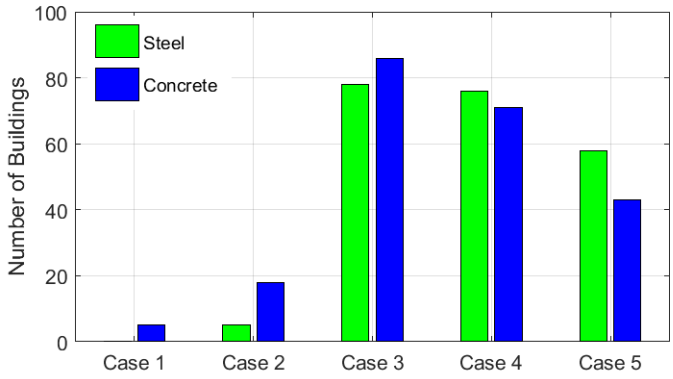

Figure 6. Number of instrumented buildings for various instrumentation scenarios.

Finally, because the current version of our identification method (and consequently CSMIP-CIT) is developed only for two-dimensional (2D) problems, we have to select those buildings whose two perpendicular directions are torsionally uncoupled. According to the available layouts, and based on the sensor locations and the distributions of mass and stiffness, we concluded that there are 44 steel and 58 concrete (a total of 102) buildings in the database whose data can be analyzed by the current version of CSMIP-CIT. A complete list of these candidate buildings is presented in Table A (of Appendix A). In this table, it is indicated—by using "Y" (yes) and "N" (no)—whether the instrumentation deployment is capable or incapable to measure 2D responses of the building in each direction. The table also provides the types of lateral structural system in each direction (for those having suitable sensor deployments). Note that a "+" sign indicates that several structural systems work in parallel, while the moniker

[3] Requiring one additional sensor beyond that would reduce this number to 101 (Case 5).

"combined" indicates that there is a combination of structural systems along the height of the building. So, out of the listed 102 buildings, we only analyzed specific direction(s) of buildings whose instrumentation layouts are labeled as "Y" and whose structural systems are not "combined". Also, we deselected very short buildings (most stiff buildings that are less than 5-story high), to make sure that there are at least two contributing modes, because the proposed identification method requires modal superposition. It is also useful to note here that various metadata errors were encountered in some of the buildings (e.g., CSMIP 58479, CSMIP 3300, CSMIP 24232, etc.), and these stations are therefore excluded them from the study, even though they nominally satisfied the criteria mentioned above.

The final set of selected buildings is tagged by a **green color** and the analysis direction is displayed in the last column of the Table A. Finally, as seen, 21 steel (28 if each direction is counted as a building) and 40 concrete (65) buildings are analyzed in the present study by using the CSMIP-CIT toolbox.

Results

In this section, comprehensive results of the application of the proposed method to data from the selected buildings (see previous section) are presented. As there are several earthquake data sets for some of these buildings, we analyzed a total of **373** earthquake data sets. While the primary purpose of this study is to extract frequency-dependent soil-foundation Impedance Functions (IFs) and Foundation Input Motion (FIMs), we also investigated fixed-base-system modal properties as a byproduct of this study. Therefore, in the following sub-sections, we present results on both the superstructure (i.e., fixed-based-system) and the overall (structure-foundation-soil) flexible-base system properties. The proposed identification method allows an accurate delineation of the superstructure flexible-base system properties, whether the building as a whole exhibited/experienced SSI effects (foundation sway/rocking) or not.

After the superstructure properties are discussed and comparisons of fixed- and flexible-based system properties are made, the results for flexible-base systems are presented in more detail. In that sub-section, we provide specific examples of the identified IFs and FIMs, as well as aggregate results—such as those that demonstrate the amplitude- and frequency-dependency of IFs. It is also important to note here that some of the studied buildings' dynamic characteristics have apparently changed significantly over time (possibly due to earthquake damage, retrofitting efforts, or through the addition of seismic mitigation devices). In the present study, we also investigated such buildings separately so that the aggregation of identification results could be made properly.

Detailed results of all 373 analysis cases are presented in Appendix B, and further details are available in (Taciroglu et al., 2016c).

Key Observations

Permanent Changes

First, we present buildings whose dynamic characteristics have permanently changed, because of possible damage experienced in a severe earthquake event or due to elements added as part of a retrofit. Figure 7 shows fundamental flexible-base natural frequency of the Van Nuys

Hotel (CSMIP 24386) obtained from 5 earthquakes. As seen, there are two significant variations in the natural frequency. First, the fundamental natural frequency significantly drops during the 1994 Northridge Earthquake, indicating damage. The building was then retrofitted in the EW direction by adding several concrete shear walls. These additional shear walls increased the lateral stiffness, and consequently the natural frequency in the EW direction by a factor of 4 which are clearly seen from identified frequencies from two recent earthquakes—namely, 2008 Chino Hills and 2014 Encino earthquakes. Therefore, this building in the EW-direction must be considered as three different buildings—a different building each, for the Landers/Big Bear, Northridge, and Chino Hills/Encino earthquakes.

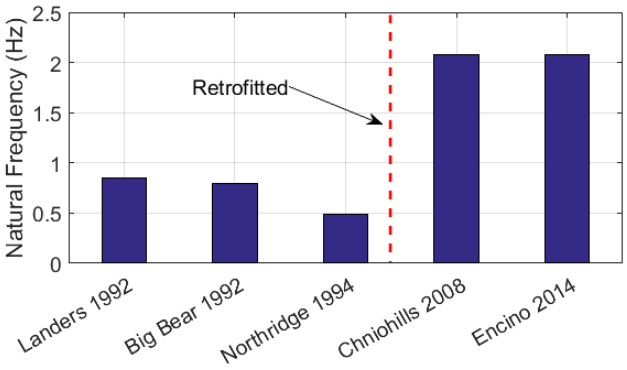

Figure 7. Chronological variation of flexible-base natural frequency of CSMIP 24386 in EW direction.

Figure 8 displays the fundamental flexible-base natural frequency of the CSMIP 24322 obtained from 5 earthquakes. This building has also experienced some damages during Northridge earthquake (1994), so it was retrofitted after this time. As it can be seen, natural frequency has significantly increased in three following earthquakes after 1994. Hence, this building in EW direction should be considered as two different buildings, one before 2008 and one after this year.

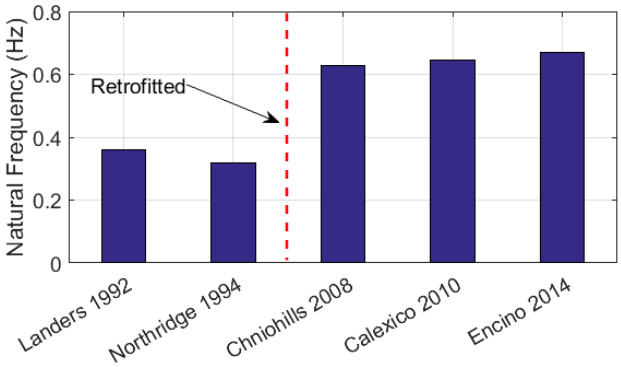

Figure 8. Chronological variation of flexible-base natural frequency of CSMIP 24322 in EW direction.

Note that these two buildings are stations whose retrofit (permanent change) are clearly stated in the CESMD. Otherwise, by looking at flexible-base natural frequency, it is not reliable to conclude about permanent structural variations, because both the soil and the structural nonlinearities can cause frequency reductions. For example, the variation of the flexible-base natural frequency of CSMIP 12299 in three earthquakes is shown in Figure 9. As seen, the

flexible-base natural frequency varies from earthquake to earthquake. However, the fixed-base natural frequency is almost constant. So, by comparing these two frequencies, we can conclude that this building's superstructure has not experienced any damage

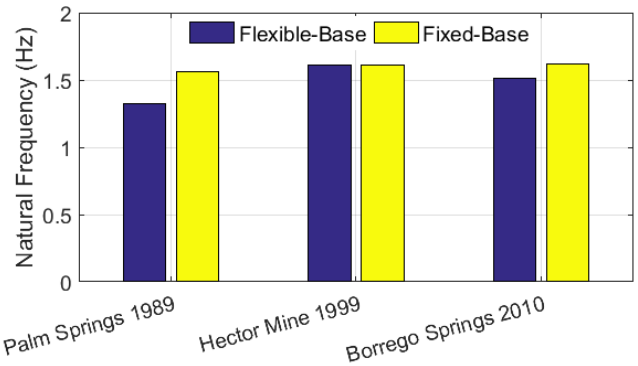

Figure 9. Chronological variation of fixed- and flexible-base natural frequencies of CSMIP 12299 in the EW-direction.

With this in mind, we can study the CSMIP 24386 and 24322 buildings again. Our analysis shows that CSMIP 24322 is fixed-base structure, but CSMIP 24386 has foundation sway. Figure 10 displays a similar graph as Figure 7 but this time fixed-base natural frequencies are used. This figure is in agreement with what we concluded from Figure 7. Also, by comparing this figure with Figure 7, we can conclude that level of soil and structural nonlinearity is different for the Landers and the Big Bear earthquakes.

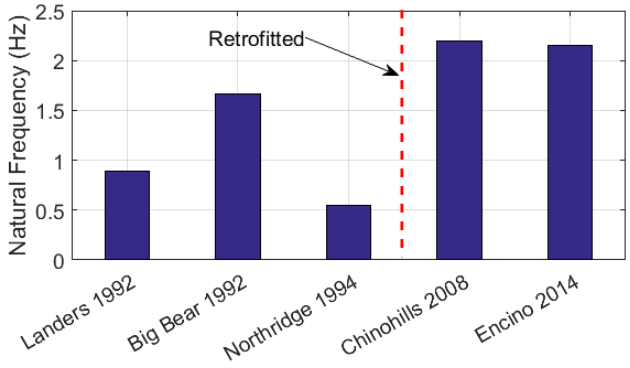

Figure 10. Chronological variation of the fixed-base natural frequency of CSMIP 24386 in the EW-direction.

To show the importance of the fact mentioned above, it is useful to look at the variation of the flexible-base natural frequency of CSMIP 57355 in the EW-direction during three earthquakes. As seen in Figure 11, the frequency goes down during the 1989 Loma Prieta earthquake in comparison to the 1984 Morgan Hill earthquake; and then it goes up again during the 2007 Alum Rock earthquake. Using only the *flexible-base natural frequencies*, it is possible to reach three different conclusions for the observed variation: (1) the building can be fixed and the observed variation is only due to the structural nonlinearity without permanent damage; (2) the building is a flexible-base structure and this variation is related to soil nonlinearities; and finally (3) the structure is damaged but the level of soil nonlinearity is masking this. Without the additional information provided by the fixed-base properties, it is not possible to distinguish

between the three possibilities. Fortunately, by having identified the fixed-base natural frequencies, we can offer a clearer interpretation of what has happened to this building.

As it can be seen in Figure 11, the fixed-base natural frequency does not change after its drop during Loma Prieta earthquake, so the building has likely suffered a permanent damage during that 1989 event. Due to the higher level of excitation during the Loma Prieta earthquake, soil has also experienced larger strains, and hence there is a difference between the flexible-base and fixed-base natural frequencies in this earthquake, while this pattern is not seen in the Alum Rock 2007 earthquake data. Therefore, this building in the EW-direction should be treated as *two different* buildings for data before and after the Loma Prieta earthquake (1989).

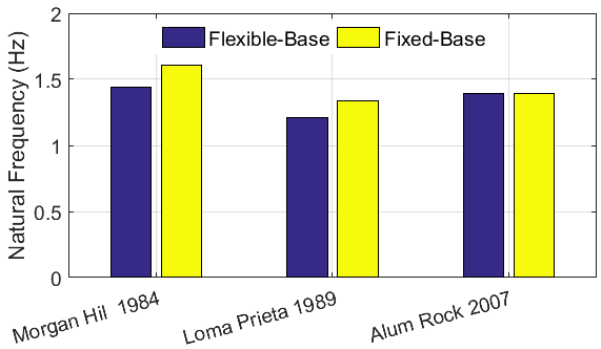

Figure 11. Chronological variation of fixed- and flexible-base natural frequencies of CSMIP 57355 in EW direction.

The last building in which we could identify permanent damage is the CSMIP station 12284 in the NS-direction. As seen in Figure 12, after the 1986 Palm Springs earthquake, there is a permanent stiffness reduction in this building. Note that the current approach to identify permanently changed buildings cannot be used for those buildings that have frequency drops only during their latest earthquake, because we use an equivalent linearization method. For example, the frequency variation of CSMIP 24601 in three successive earthquakes in both directions is shown in Figure 13. As it can be seen, there is a drop during the last earthquake, but it is not possible to conclude at the present time whether this is due to a permanent damage or it is an equivalent frequency identified for a nonlinear system. In the present study, we consider such buildings as *undamaged* buildings.

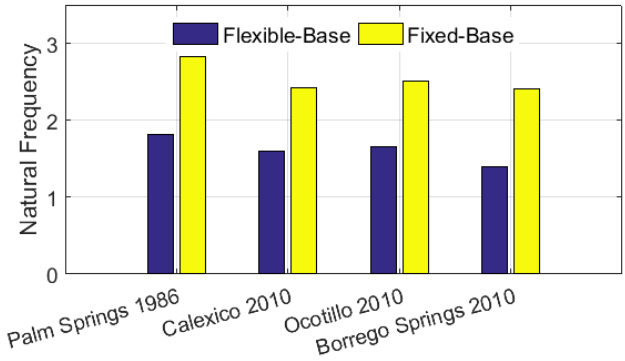

Figure 12. Chronological variation of fixed- and flexible-base natural frequencies of CSMIP 12284 in the NS-direction.

In addition to the permanent changes due to changes in stiffness, one of the buildings under study was equipped with dampers. Herein, we examine whether this building should be considered as a single case or not. Figure 14 shows variation of the damping ratio of the CSMIP 57357 in the EW-direction obtained from 5 earthquakes. This building has been equipped with dampers after the Loma Prieta earthquake. As expected, the building's damping ratio has increased after this earthquake, as it can be seen in Figure 14. To make sure that this damping increase is due to the additional dampers, and not the earthquake intensity (because it is well accepted that damping is significantly amplitude-dependent), we have added the variation of the Peak Foundation Acceleration (PFA) during these five earthquakes. As this figure shows, while level of excitation is much lower in the Milpitas (2010) and the Morgan Hill (2011) earthquakes, the level of identified damping ratios is still higher than previous earthquakes, which clearly indicates the contribution of the installed dampers. So, for interpretation of the identified damping, this building should be considered as two buildings, one before 1989 and one after this year.

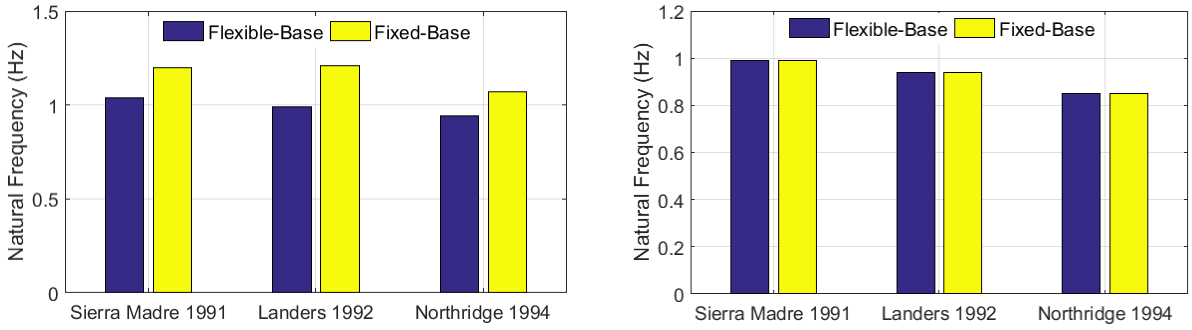

Figure 13. Chronological variation of fixed- and flexible-base natural frequencies of CSMIP 24601 in (left) EW and (right) NS-directions.

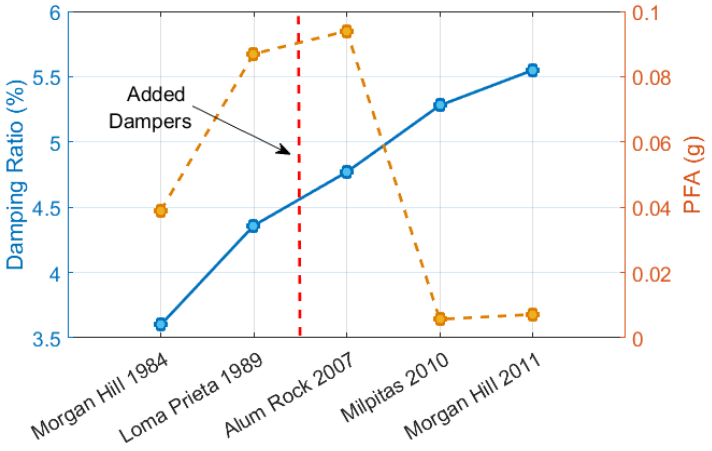

Figure 14. Chronological variation of flexible-base damping ratio and Peak Foundation Acceleration (PFA) of CSMIP57357 in EW direction.

In concluding this section, we now consider and implement the changes listed in Table 3 into our CSMIP-CIT database for future analyses.

Table 3. Modifications to the database due to permanent changes in buildings.

No.	CSMIP No.	Dir.	Case	Earthquakes
1	24386	EW	1	≤ 1992
			2	= 1994
			3	≥ 2008
2	24322	EW	1	< 2008
			2	≥ 2008
3	12284	NS	1	≤ 1986
			2	> 1986
4	57355	EW	1	≤ 1984
			2	> 1984
5	57357	NS, EW	1	≤ 1989
			2	> 1989

Soil and Structural Nonlinearities

In the previous section, we showed how to take advantage of the identified fixed- and flexible-base natural frequencies to identify and quantify the permanent changes in instrumented buildings, and to update the database accordingly. In this section, we investigate the observed nonlinear behavior in the soil-foundation system and/or the superstructure by using the identified fixed- and flexible-base natural frequencies. We need to carry out this investigation so that we can appropriately select data points in subsequent sections—e.g., to retrieve frequency-dependent soil-foundation impedance functions by aggregating results from several buildings. Before going through this investigation, it is worth noting that it is not appropriate to assign a single label—e.g., *fixed-base*—to a building. In other words, a building can behave in a fixed-based manner in an earthquake, and yet its foundation can move with respect to the ground during another event that has different level of intensity and/or frequency content. As an example, Figure 15 shows the frequency variation of CSMIP 58261 in the EW-direction during three different earthquakes. As seen, during the severe 1989 Loma Prieta earthquake (PFA = 0.16*g*, which is ~5 times higher than the two other earthquakes), there is significant soil-foundation flexibility. That is, this building behaved in a fixed-base manner in two earthquakes, but exhibited flexible-base response during the Loma Prieta earthquake.

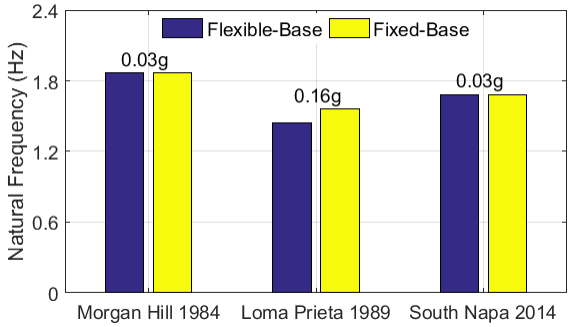

Figure 15. Chronological variation of fixed- and flexible-base natural frequencies of CSMIP 58261 in EW direction.

Excluding special cases like CSMIP 58261, we can generally classify buildings under study into following five groups according to the identified results[4]:

- *Linear Fixed-Base*: For these buildings, no sign of soil-structure interaction effect was observed in their analyzed earthquake data. Also, almost the same natural frequencies were obtained using different earthquakes. An example of such buildings is shown in Figure 16(a). As seen, a single type of natural frequency is shown, meaning that there was no soil-foundation flexibility. Also, the identified natural frequencies from 6 different earthquakes from 1978 to 2013 were almost equal.
- *Nonlinear Fixed-Base*: For these buildings, while the building is fixed at its base, the superstructure parameters significantly varied from event to event. As an illustration, the variation of natural frequencies of CSMIP 23511 (NS direction) is shown in Figure 16(b).
- *Linear Flexible-Base*: These types of buildings were flexible-base in all analyzed earthquake data sets (contrary to, for example, CSMIP 58261). However, there was less amplitude-dependency in both their fixed- and flexible-base properties. An example of such buildings is shown in Figure 17. As seen, the fixed- and flexible-base natural frequencies were constant from 2002 to 2014.
- *Flexible-Base with Nonlinear Soil-Foundation*: The difference between this group of buildings and the previous one is that while the superstructure has not changed in multiple earthquakes, the soil-foundation system exhibited amplitude-dependency. An example of these types of buildings is shown in Figure 18. As seen, while the fixed-base natural frequency is almost constant, the flexible-base natural frequency significantly varies from earthquake to earthquake.
- Nonlinear Flexible-Base: This group of building showed amplitude-dependency in both the substructure and the superstructure (we could not find cases for which the superstructure showed amplitude-dependency, while substructure did not). An example of these buildings is shown in Figure 19.

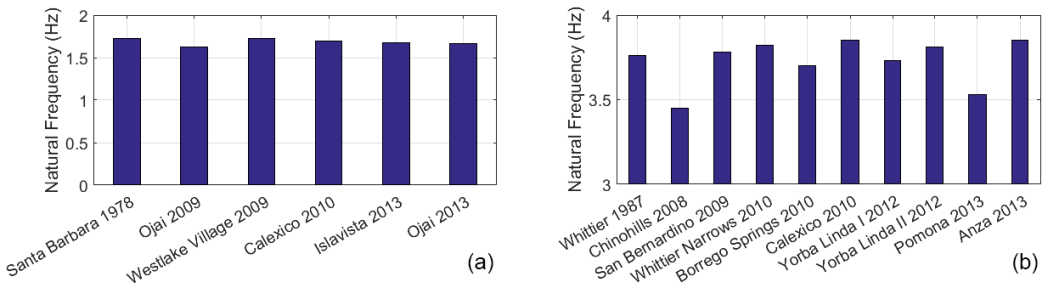

Figure 16. (a) CSMIP 25339-EW and (b) CSMIP 23511-NS representing linear and nonlinear fixed-base systems, respectively.

[4] It is obvious that this classification can change and become more refined by recording more earthquake data.

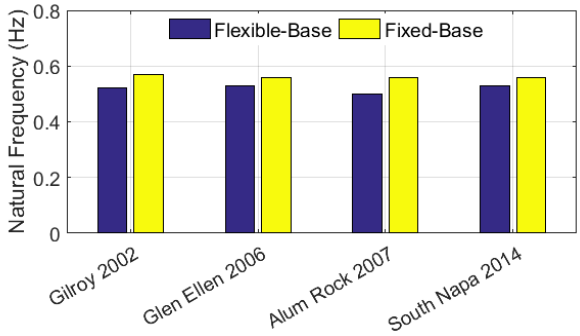

Figure 17. CSMIP 58615-EW as an example of linear flexible-base system.

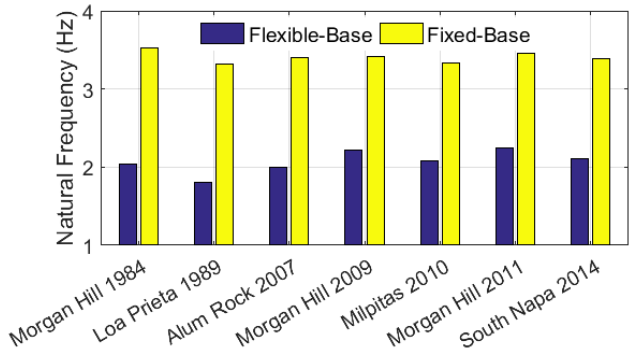

Figure 18. CSMIP 57356-EW as an example of nonlinear flexible-base system with linear superstructure.

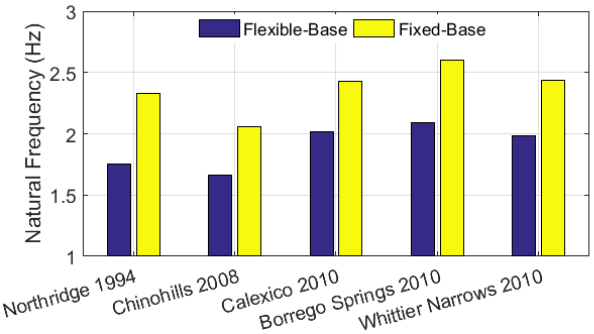

Figure 19. CSMIP 14606-NS as an example of nonlinear flexible-base system with nonlinear superstructure.

Superstructure Parameters

Natural Frequencies

Shear wave velocity in building structures can be used as a simple measure to predict their natural frequencies (in the fixed-base condition) (see, for example, Todorovska & Trifunac, 2008). Figure 20 shows the probability density function estimated from the identified shear wave velocity of the buildings using $\sqrt{G/\rho} = L/(\sqrt{k}s\bar{b})$. First, we neglect amplitude-dependency effects and use all available data points. As seen in Figure 20(left), buildings with moment frames—i.e., Moment Resisting Steel Frames (MRSFs) or Reinforced Concrete Frames (RCFs)—have the lowest shear-wave velocity. It is worth noting that the mean value does not appear to depend on the material type, and is almost the same for both MRSFs and RCFs. This figure shows that the shear wave velocity in steel structures increases from MRSF to S-Dual to

BSF. This order is expected, because buildings with Braced Steel Frames (BSFs) usually have higher stiffness. A similar order is not completely established for concrete buildings, which may be due to two main reasons: First, amplitude-dependency plays a higher role for them, and/or there are misclassifications in the metadata. The latter reason is unlikely, because metadata did not bear many ambiguities. However, we can explore the former effect by using data from weak earthquakes. As such, we repeated Figure 20(left) on the right-side by using the weakest earthquake data (causing the highest fixed-base natural frequency). As seen, the aforementioned problem is almost removed. Also, the two-peak pattern already observed in Figure 20(left) for RCF, BSF, and CSW are significantly reduced in Figure 20(right). Finally, it can be seen from both figures that buildings having dual systems are mostly affected by the stiffest sub-system. That is, S-Dual is closer to BSF than MRSF and C-Dual is closer to CSW than RCF.

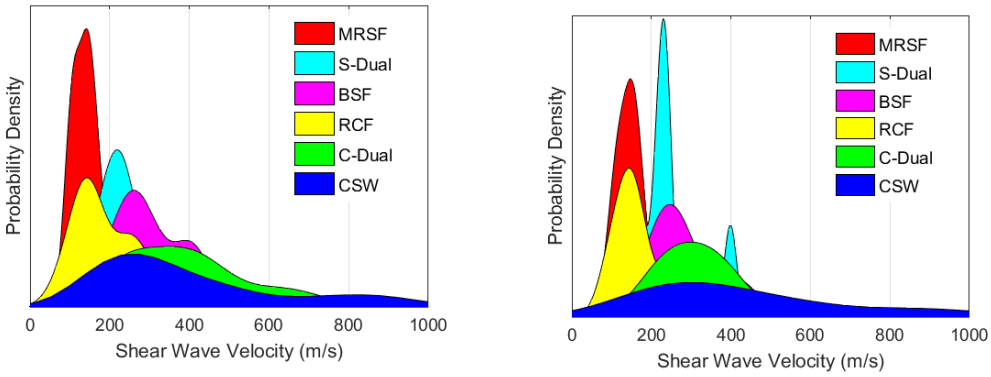

Figure 20. Probability distribution of shear wave velocity in fixed-base buildings. Left: full data, Right: weak earthquake data.

Having an average value of $\sqrt{G/\rho}$ for different types of structural systems as identified from Figure 20, we can predict the fixed-base natural frequency of any building through the Timoshenko beam model, if we can also have an estimation for shear-to-bending stiffness values—i.e., G/E. Using the identified parameters, we can back-calculate G/E as $I/(s^2 A_s L^2)$ for different types of structural systems. Histograms of G/E for all six structural systems are shown in Figure 21. Although the number of data points is limited in the current study, this approach can be used in the future when as a larger data set becomes available. G/E corresponding to the peaks of Figure 21 are reported in Table 4. Also, values of $\sqrt{G/\rho}$ corresponding to the peaks of Figure 20 are reported in this table. Now, it is possible to estimate fixed-base natural frequency of a building having a specific lateral system through the frequency equation of a fixed-base Timoshenko beam by using following parameters

$$\bar{b} = 3.46 \frac{1}{\sqrt{G/\rho}} \sqrt{G/E} \frac{L^2}{D} = \frac{3.46 L^2 \sqrt{\rho/E}}{D} \tag{13}$$

$$s = \frac{1}{3.19\sqrt{G/E}} \frac{D}{L} \tag{14}$$

Note that, a rectangular section has been assumed for deriving equation above.

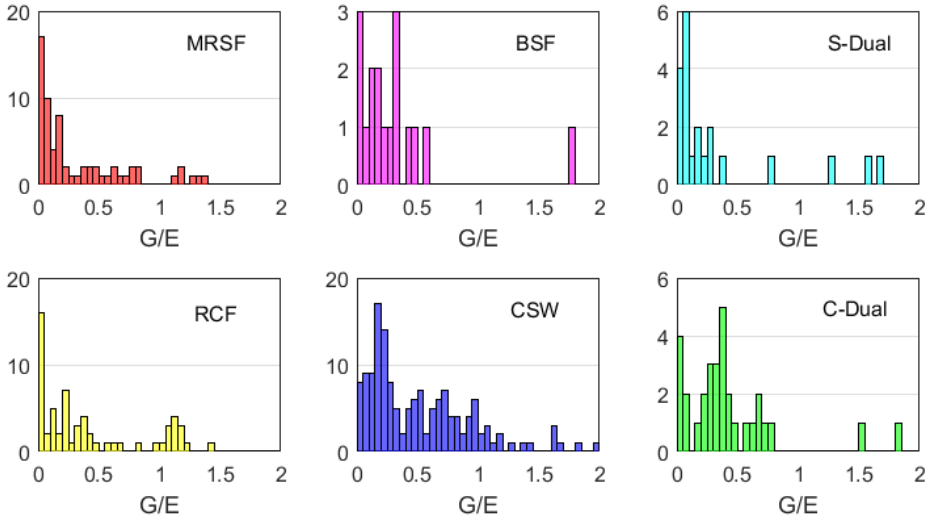

Figure 21. Histograms of identified G/E for various types of structural systems.

Table 4. Identified factors for natural frequency prediction.

Structural Type	G/E	$\sqrt{G/\rho}$ $(m/\sec^2)$
MRSF	0.03	148
BSF	0.03, 0.33	250
S-Dual	0.07	230
RCF	0.03, 0.23	144
CSW	0.17	300
C-Dual	0.37	300

Using Eqs. (13) and (14) and approximate values presented in Table 4, the fixed-base natural frequencies of buildings for a wide range of structural height and plan-depth are plotted in Figure 22. In this figure, we also show actual building data points (for BSF and RCF, we used G/E equal to 0.03 and 0.23, respectively). As it can be seen from this figure, the proposed values for Timoshenko beam model can represent the average behavior of all Timoshenko beam models identified for buildings under study.

Herein, we compare our predictive formulas for fixed-base natural frequencies with other available formulas. These reference formulas are summarized in Table 5 and their details and history can be found in (Taciroglu et al., 2016c). As seen on Table 5, there is no prior study in which the fixed-base natural frequency is explicitly extracted from real-life data. However, it should be made clear that if the buildings under investigation in any of the studies listed in Table 5 were physically fixed-base, then the identified flexible-base or pseudo-flexible base natural frequencies should be comparable with our results. Herein, we compare our results with those formulas available in the latest version of the ASCE-7, 2010. Figure 23 presents this comparison for four types of structural systems[5]. As seen, for tall buildings in which SSI is mostly negligible,

[5] We did not carry out a comparison for CSW and C-Dual systems, because the ASCE-7 formulae for these systems require detailed information on shear walls.

the formula presented in ASCE 7-10 is nearly matched to the fixed-base natural frequencies we predict for plan-depth of ~80 m, which is expected. However, for short structures for which SSI effects have a higher proportion of contribution to the overall response, the fixed-base natural frequencies identified here are larger than that from the ASCE formula. This suggests that there is an implicit portion of soil-foundation flexibility (pseudo-flexible base) embedded in the ASCE formula. Moreover, the observed difference is much larger for systems having BSFs, which are stiffer in comparison to three other systems.

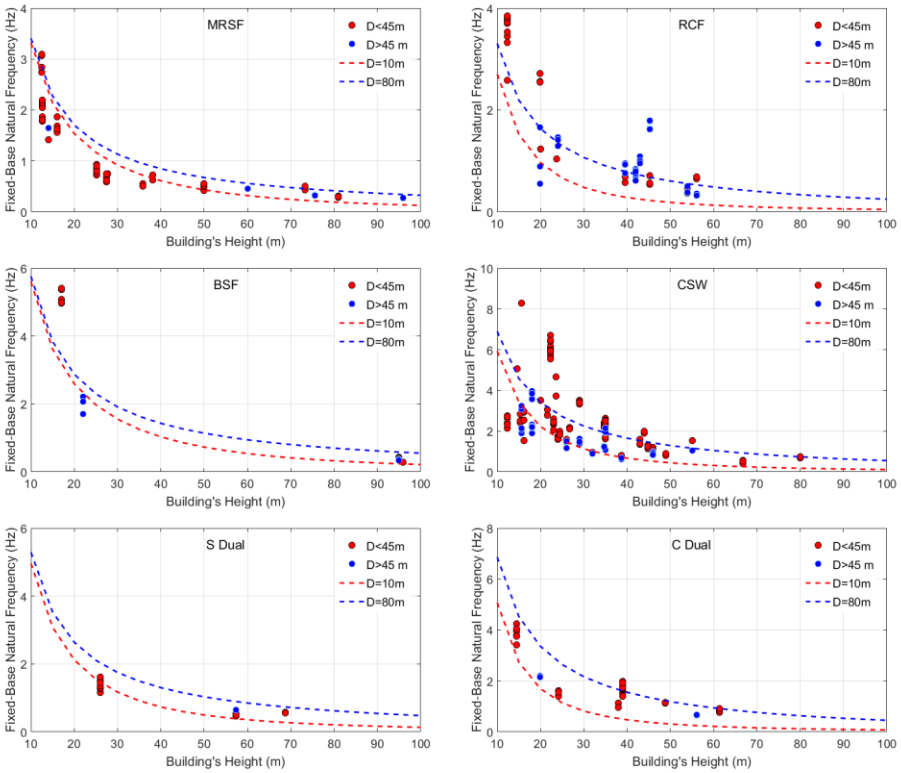

Figure 22. Fixed-base natural frequency predicted for various structural systems.

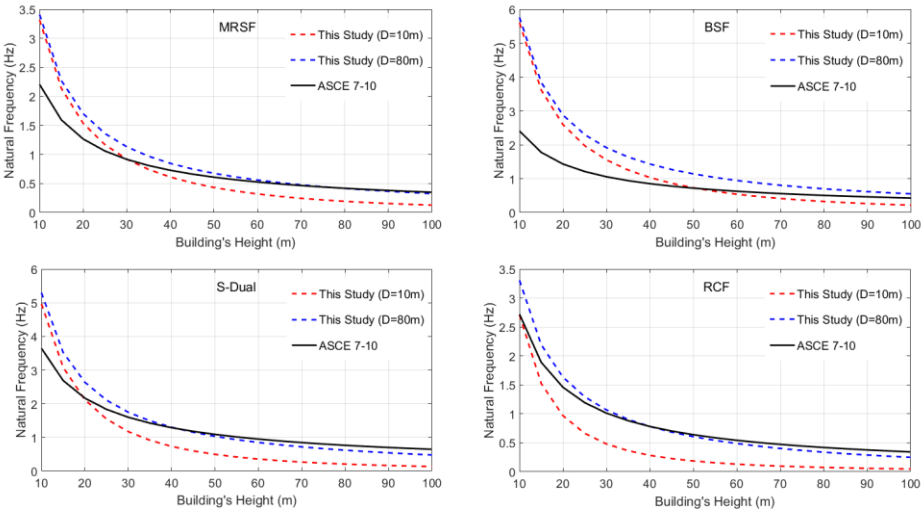

Figure 23. Comparison between fixed-base natural frequency predicted by the present study and ASCE 7-10 (2010) for various structural systems.

Table 5. Available approximate formulae for estimating the fundamental natural frequencies (in the expressions below, f_1 is in Hz, the building dimensions L and D are in feet. N denotes number of stories, and A_e is the effective area defined in Goel & Chopra, 1998).

Case	Proposed Formula	Building Type	Base* Condition	Developers	Reference
1	$f_1 = 33L^{-3/4}$	RCF	Pseudo-Flexible	UBC97, NEHRP94, SEAOC96	(UBC, 1997; NEHRP, 1994; SEAOC, 1996)
2	$f_1 = 40L^{-3/4}$	RCF	Pseudo-Flexible	ATC3-06	(ATC, 1978)
3	$f_1 = 29L^{-3/4}$	MRSF	Pseudo-Flexible	ATC3-06, UBC97, NEHRP94, SEAOC96	(ATC, 1978; UBC, 1997; NEHRP, 1994; SEAOC, 1996)
4	$f_1 = 50L^{-3/4}$	CSW	Pseudo-Flexible	NEHRP94, SEAOC96	(NEHRP, 1994; SEAOC, 1996)
6	$f_1 = 20D^{1/2}L^{-1}$	CSW	Pseudo-Flexible	ATC3-06	(ATC, 1978)
7	$f_1 = 11D^{1/2}L^{-1}$**	CSW	Pseudo-Flexible	NBCC95	(NRC, 1995)
8	$f_1 = 56L^{-1}$**	RCF	Flexible	Lagomarsino	(1993)
9	$f_1 = 59L^{-0.92}$	RCF	Pseudo-Flexible	Goel & Chopra	(1997)
10	$f_1 = 29L^{-0.805}$	MRSF	Pseudo-Flexible	Goel & Chopra	(1997)
11	$f_1 = 435L^{-1}A_e^{0.5}$	CSW	Pseudo-Flexible	Goel & Chopra	(1997)
12	$f_1 = 100L^{-1}$**	CSW	Flexible	Farsi & Bard	(2004)
13	$f_1 = 20L^{-3/4}$**	CSW	Pseudo-Flexible	NRC/IRC 2010	(NRC/IRC, 2010)
14	$f_1 = 58L^{-1.032}$**	CSW	Flexible	Gilles & McClure	(2012)
15	$f_1 = 36L^{-0.8}$	MRSF	Pseudo-Flexible	ASCE 7-10	(2010)
16	$f_1 = 50L^{-0.75}$	S-Dual	Pseudo-Flexible	ASCE 7-10	(2010)
17	$f_1 = 63L^{-0.9}$	RCF	Pseudo-Flexible	ASCE 7-10	(2010)
18	$f_1 = 33L^{-0.75}$	BSF	Pseudo-Flexible	ASCE 7-10	(2010)

* This is the actual base condition not the purpose of the usage. Indeed, natural frequencies estimated from approximate formulas of building codes are usually assumed fixed-base.

** Dimensions in this formula are in meters.

Damping Ratios

Building damping is one of the most challenging parameters to estimate in earthquake engineering, as it is not directly computable and many factors contribute to it. Due to this ambiguity, as well as computational convenience, viscous damping models are usually used, whereas the inherent damping responses of structural systems are not necessarily so. As modal combination has been the basis of all classic seismic design, damping had been specified by defining modal damping ratios. As these parameters cannot be directly derived from first principles at the present time, identification of damping ratios from real-life vibration data is the only viable path to quantification. While this route has been known, there have been only a few attempts to date to relate damping ratios to detailed specifications of structures, because of

ambiguities in damping sources, inadequacies of data, and the inabilities of identification methods, as well as inherent uncertainties in the identification processes (Kijewski-Correa & Pirnia, 2007). Not surprisingly, seismic design codes could only provide general and vague recommendations, and usually constant damping ratios for many years (%5 for concrete/masonry structures and %2 for steel structures). For example, in the latest version of ASCE 7-2010 (ASCE7-10, 2010), the word damping is mentioned many times in many sections, but without any specific values. Here are a few examples, which are originally collected by Miranda (2014):

- Section 16.1.2: "*Mathematical models shall conform to the requirements of Section 12.7*," yet there is nothing about damping specifications in Section 12.7.
- Section 17.6.3.3: "Response-spectrum analysis shall be performed using a modal damping value for the fundamental mode in the direction of interest not greater than the effective damping of the isolation system or 30 percent of critical, whichever is less. Modal damping values for higher modes shall be selected consistent with those that would be appropriate for response spectrum analysis of the structure above the isolation system assuming a fixed base," yet the appropriate damping ratio for a fixed-base structure is not known.
- In one of the rare cases, in Section 12.9 (Modal Response Spectrum Analysis), the recommendation is to use the 5% damped spectrum as input that is using 5% damping ratios for all structures and modes.

A number of researchers suggested simplified formulae for first mode damping ratios using different parameters and calibrated these by using damping ratios estimated/identified from vibration data. Building height, material type, and vibration intensity were utilized as the primary physical parameters on these approximations. A short list of these studies is shown in Table 6 and further details can be found in (Taciroglu et al., 2016c).

Table 6. Presently available approximate formulas for building damping ratios.

Case	Proposed Formula	Building Type	Base Condition*	Developer(s)
1	$\xi_1 = \frac{0.3192}{f_1} + 0.7813 f_1$	Steel	Unknown	(Lagomarsino, 1993)
2	$\xi_1 = \frac{0.7238}{f_1} + 0.7026 f_1$	Concrete	Unknown	(Lagomarsino, 1993)
3	$\xi_1 = \frac{0.2884}{f_1} + 1.2856 f_1$	Mixed	Unknown	(Lagomarsino, 1993)
4	$\xi_1 = 1.945 + 0.195 {f_1}^{3.779}$	Mixed	Flexible	(Zhang & Cho, 2009)
5	$\xi_1 = 8.07 L^{-0.25}$**	Steel	Mixed	(Fritz et al., 2009)
6	$\xi_1 = 25.36 L^{-0.5}$**	Concrete	Mixed	(Fritz et al., 2009)
7	$\xi_1 = 1\ (L < 100)$, $\xi_1 = 198 L^{-1} (L > 100)$ **	Steel	Flexible	(PEER/ATC, 2010)
8	$\xi_1 = 2 (L < 100)$, $\xi_1 = 330 L^{-1} (L > 100)$ **	Concrete	Flexible	(PEER/ATC, 2010)
9	$\xi_1 = 1.2 + 4.26 e^{-0.013L}$**	Steel	Pseudo-Flexible	(Bernal et al., 2013, 2015)
10	$\xi_1 = 3.01 + 3.45 e^{-0.019L}$**	Concrete	Pseudo-Flexible	(Bernal et al., 2013, 2015)

* This is the actual base condition not the purpose of the usage. Indeed, natural frequencies estimated from approximate formulas of building codes are usually assumed fixed-base.
** Building height is in meters.

The results of the present study are universal in that the damping ratios identified here are only due to superstructure behavior (but not polluted by SSI effects, which should be considered and treated separately). Figure 24 shows the identified fixed-base damping ratio versus natural frequency for four structural types. Unfortunately, for CSW and C-Dual systems, we could not determine any pattern for the damping ratio. One reason for this is probably due to the amplitude-dependency, which can significantly alter damping levels in buildings having shear walls. For all other systems, we could extract a relationship between the fundamental natural frequency and the damping ratio. We selected natural frequency as the regression metric, because it produced much better fitness values in comparison to, for example, building height. Considering friction within connections or among elements, as well as the density of the presence of non-structural elements, we expect to see a direct correlation between the fixed-base natural frequency and fixed-base damping ratio. This expectation is confirmed and evident in Figure 24. Analytical formulae corresponding to the fitted curves of Figure 24 are presented in Table 7. With these expressions, it is now possible to first calculate the fixed-base natural frequencies using formulae proposed in the previous section, and then to predict the fixed-base damping ratio for the superstructure. Having the superstructure damping and the foundation damping, which will be the discussed in the next section, any SSI system can be analyzed using the substructure approach.

Table 7. Proposed approximate fixed-base damping ratios.

Case	System	Equation	R^2
1	MRSF	$\xi_1 = -5.83{f_1}^{-0.30} + 12.76$	0.33
2	RCF	$\xi_1 = 3.06{f_1}^{-1.01} + 2.23{f_1}^{-0.85}$	0.19
3	S-Dual	$\xi_1 = 2.44f_1 + 2.51$	0.19
4	C-Dual	---	---
5	BSF	$\xi_1 = 1.16f_1 + 3.44$	0.41
6	CSW	---	---

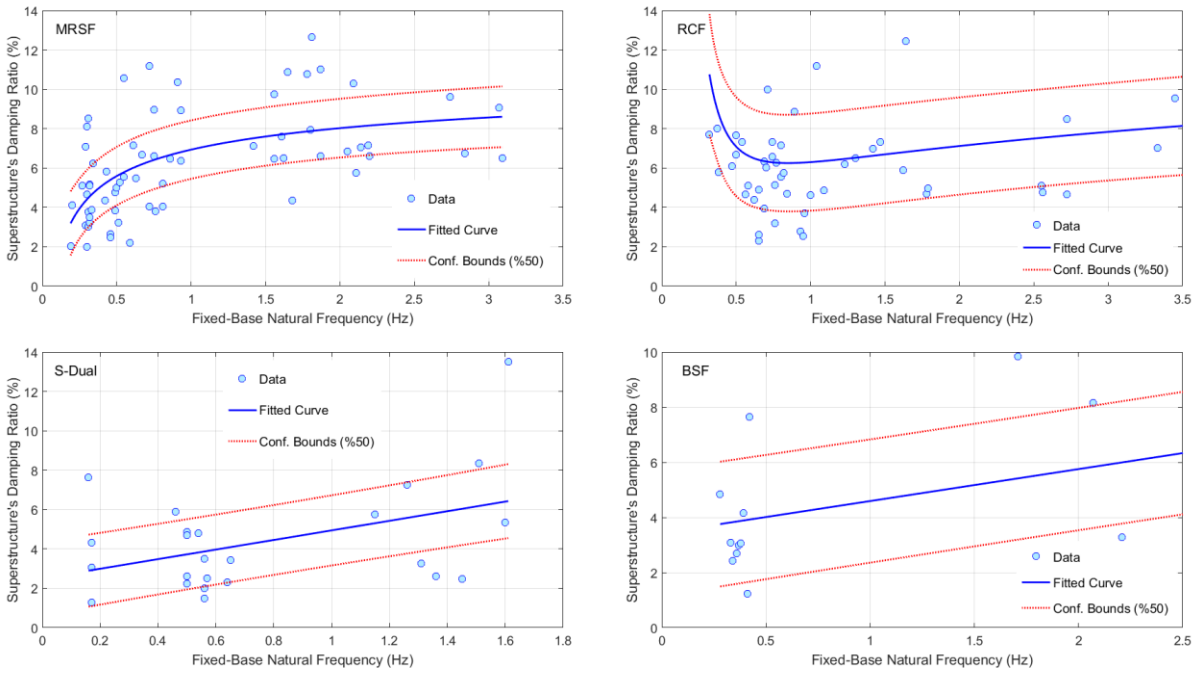

Figure 24. Variation of superstructure first mode's damping ratio versus fundamental fixed-base natural frequency and fitted curves along with their %50 confidential bounds.

Soil-Foundation Parameters

Frequency-Dependency

According to ASCE 7-10 (2010), requirements of Chapter 19 are permitted to be used in the determination of the earthquake-induced forces, if the building is flexible-base and the superstructure is modeled as fixed-base. Based on these requirements, there are two SSI-related parameters that control the base shear reduction subject (cf. Eq. 19.2-1 of ASCE 7-10). These two parameters are flexible-base natural period (T_{Flex}) and soil-foundation-structure damping ratio (ξ_{Flex}). T_{Flex} is determined based on the formulation derived by Veletsos and Meek (1974) using a SDOF structure placed on a sway-rocking foundation, and is given by

$$T_{Flex} = T_{Fixed}\sqrt{1 + \frac{\bar{k}}{K_T}\left(1 + \frac{K_T h^2}{K_R}\right)} \qquad 15)$$

where $\bar{k} = 4\pi^2 \bar{W} / \left(g {T_{Fixed}}^2\right)$ is the stiffness of the superstructure; T_{Fixed} is the fixed-base natural period; h and $\bar{W}$ are the effective height and weight of the superstructure at its first mode (typically assumed as %70 of the building's height and weight); and K_T and K_R are the soil-foundation sway and rocking stiffnesses, respectively. To calculate the soil-foundation stiffnesses, "*established principles of foundation mechanics using soil properties that are compatible with the soil strain levels associated with the design earthquake motion*" are to be used. Alternatively, "*for structures supported on mat foundations that rest at or near the ground surface or are embedded in such a way that the side wall contact with the soil is not considered to remain effective during the design ground motion, the effective period of the structure is permitted to be determined from*:

$$T_{Flex} = T_{Fixed}\sqrt{1 + \frac{25\alpha r_T h}{{V_s}^2 {T_{Fixed}}^2}\left(1 + \frac{1.12 r_T h^2}{\alpha_R {r_R}^3}\right)}. \quad 16)$$

The equation above can be rewritten as

$$T_{Flex} = T_{Fixed}\sqrt{1 + \frac{\bar{k}}{K_T^{ST}}\left(1 + \frac{K_T^{ST} h^2}{\alpha_R K_R^{ST}}\right)} \quad 17)$$

where K_T^{ST} and K_R^{ST} are the static sway and rocking soil-foundation stiffnesses for an equivalent circular foundation, which are calculated as

$$K_T^{ST} = \frac{8\,\rho {V_s}^2 r_T}{2 - \nu} \quad 18)$$

$$K_R^{ST} = \frac{8\,\rho {V_s}^2 {r_R}^3}{3(1 - \nu)} \quad 19)$$

where ν is the soil's Poisson ratio, and has been assumed 0.4 in Eq. (22). The parameters r_T and r_R denote the radius of the circular foundation that has an equal area and moment of inertia with the actual foundation, respectively. Eq. (17) indicates that the sway soil-foundation stiffness is assumed to be frequency-independent in ASCE 7-10, whereas a frequency-dependent factor α_R is considered for the rocking DOF. The value of this modification factor is obtained from Table 19.2-2 of ASCE 7-10 using the dimensionless parameter $r_R/(V_s T_{Fixed})$, which represents the superstructure-to-soil stiffness ratio.

Using our identified mass-normalized sway and rocking stiffnesses, we can evaluate how accurate the ASCE 7-10 recommendations—i.e., frequency-independent sway stiffness and α_R of Table 19.2-2—are. To carry out the said evaluation, we select data points that exhibited SSI effects (having different fixed- and flexible-base natural frequencies). Then, we multiply the mass-normalized stiffnesses of all buildings with $400L \times B \times D$ as an estimation of the total mass of the building. Next, we scale the recovered stiffnesses by static stiffnesses calculated by Eqs. (18) and (19) for sway and rocking, respectively. To use those formulas, we use small-strain shear wave velocity of site soils reported at the nearest CSMIP ground motion station (CESMD). To eliminate (or at least reduce) amplitude-dependency, we scale these shear wave velocities based on the recorded Peak Foundation Accelerations as recommended in (Givens, 2013).

Results of the identified rocking modification factors, α_R, versus the corresponding $r_R/(V_s T_{Fixed})$ are shown in Figure 25(a) as circle marks. For comparison purposes, the values recommended by ASCE 7-10 are also shown with continuous piecewise linear curves. As the maximum value of $r_R/(V_s T_{Fixed})$ in ASCE 7-10 is 0.5, we extrapolated the curve per the linear reduction of α_R after $r_R/(V_s T_{Fixed}) = 0.5$. As it can be seen, while a decreasing pattern is observed in the identified data, there is a large variability. However, the results this figure should be carefully interpreted, because we adopted several simplified assumptions (following ASCE 7-10) to carry out the comparisons. For example, we assumed that all buildings have a mass calculated using $400L \times B \times D$, all soil shear wave velocities are accurate and are correctly

scaled versus Peak Foundation Acceleration (PFA), the entire foundation contributes to the soil-foundation stiffness, and the formula used for static stiffness is accurate. Of course, it is not reasonable to expect that all of the said assumptions are valid for all of the buildings. As such, dividing the identified data into subcategories may provide a better understanding of the shortcomings of the ASCE provisions. For this purpose, we replot Figure 25(a) by clustering the results from different buildings into groups based on their common specifications in Figures 25(b-d). For example, Figure 25(b) displays data for different structural systems in a color code. As it can be deduced from these figures, most of the buildings whose identified frequency-dependent modification factor significantly deviates from the ASCE recommended values belong to non-CSW groups. This is likely because superstructures with CSW (Concrete Shear Wall) systems behave more like monolithic systems, which then allows the simplified modeling approaches that underlie the ASCE provisions to better approximate real-life behavior. This assertion is supported again by interpreting Figure 25(c), which delineates buildings with rigid (mat or interconnected) foundations whose lateral systems are not located as an interior core from those with flexible foundation systems. If we look at CSW systems with rigid foundations (Figure25d), then we find the greatest agreement between real-life data and ASCE 7-10 provisions. These results indicate that the frequency-dependent modification factors recommended in ASCE 7-10 are representative of a relatively narrow class superstructure-foundation systems, and may require amendments.

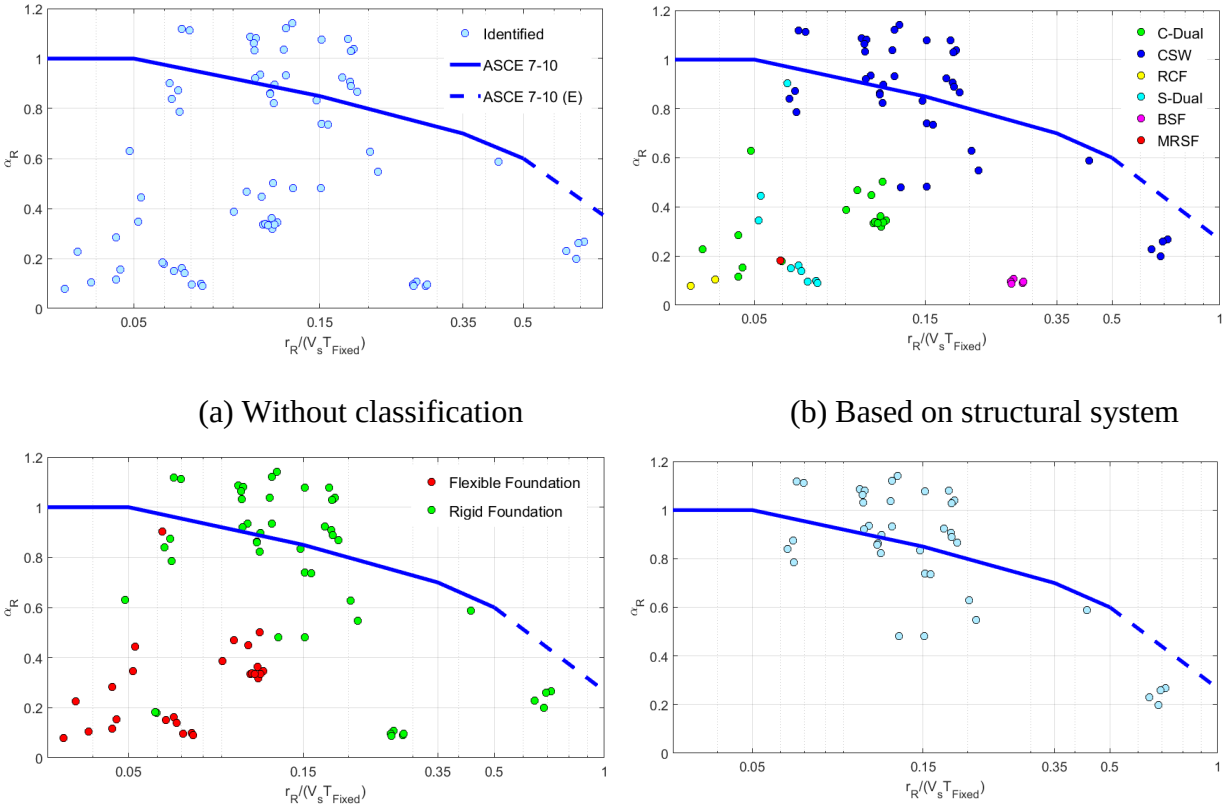

(a) Without classification

(b) Based on structural system

(c) Based on foundation rigidity

(d) CSW structures with rigid foundation

Figure 25. Comparison between identified and ASCE recommended α_R.

Frequency-dependent modification factors recommended by ASCE 7-10 are selected using the fixed-base natural periods, which is suitable for design procedures. However, as noted earlier, the primary objective of the present effort was to extract frequency-dependent soil-foundation impedance functions, which must be presented versus excitation frequency (here flexible-base natural frequency). To extract this information, we keep the vertical axes from Figure 25, but present results (for buildings with integrated foundations and CSW structural systems) versus dimensionless parameter $a_0 = \omega r/V_s$, wherein ω denotes the flexible-base fundamental frequency of each building. Figure 26 displays this graph along with the theoretical curve obtained by Veletsos and Verbic (1973), which is the basis for some of the ASCE 7-10 provisions on SSI, for comparison. As seen, the venerable Veletsos-Verbic approximation is in fair agreement with the field observations; nevertheless, the variability in the real-life data appears quite large and cannot be explained or captured by their model alone.

As mentioned above, and unlike the rocking stiffness, ASCE 7-10 (2010) provisions are based on the assumption that the foundation sway stiffness is not frequency-dependent. Figure 27 displays the α_R factor (i.e., frequency-dependency factor) for sway DOF values identified from CSMIP data versus the constant (unit) value recommended by ASCE 7-10. As seen, there is significant variability in real-life data, and this variability is most likely due to amplitude-dependent behavior of sway stiffness as well as uncertainties associated with field shear wave velocity data. Similar to Figure 26, the frequency-dependency of the sway stiffness is compared the analytical formula by Veletsos and Verbic (1973) in Figure 34. As seen, a frequency-independent factor appears to be a very good assumption for the sway stiffness.

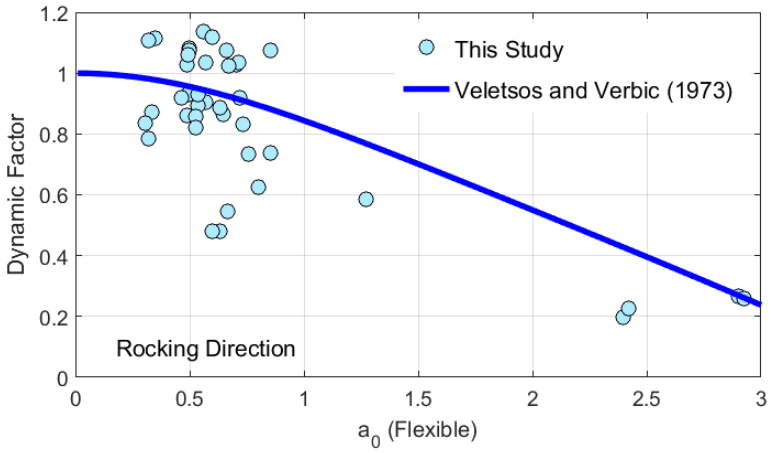

Figure 26. Frequency-dependency of soil-foundation rocking stiffness from CSMIP strong motion data versus the analytical solution by Veletsos and Verbic (1973) .

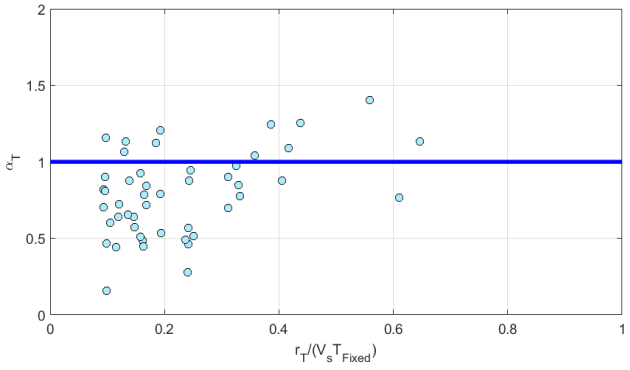

Figure 27. Frequency-dependency of the soil-foundation sway stiffness versus the ASCE 7-10 recommendation.

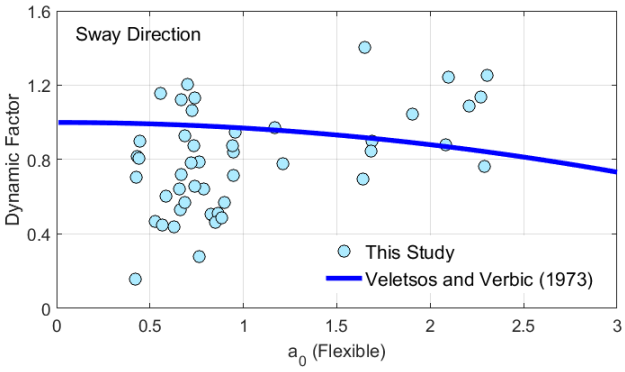

Figure 28. Frequency-dependence of soil-foundation sway stiffness versus Veletsos and Verbic (1973).

The effective damping ratio for the soil-foundation-structure system, ξ_{Flex}, is another parameter required for SSI analyses, and ASCE 7-10 recommends following formula to estimate it

$$\xi_{Flex} = \xi_0 + \frac{0.05}{\left(\frac{T_{Flexible}}{T_{Fixed}}\right)^3} \quad 20)$$

where ξ_0 is damping associated with the soil-foundation system, which includes both hysteretic and radiation damping. This formula is based on the earlier studies, including that by Veletsos and Nair (1975) who showed that the damping ratio of the soil-structure system can be calculated through the following formula using fixed-base damping ratio ξ_{Fixed}

$$\xi_{Flex} = \xi_0 + \frac{\xi_{Fixed}}{\left(\frac{T_{Flexible}}{T_{Fixed}}\right)^n} \quad 21)$$

where the exponent n depends on the type of damping (3 for viscous and 2 for hysteretic). By comparing Eq. (21) and (20), it is clear that an exponent of n = 3 and a superstructure damping of %5 are assumed in ASCE 7-10. To calculate the foundation damping ξ_0, a curve is provided in ASCE 7-10 based on the work by Veletsos and Verbic (1973), which relates the foundation damping to period elongation ($T_{Flexible}/T_{Fixed}$). However, it was later determined that the said curve was incorrectly produced by using the a_0 (introduced earlier) at fixed-base frequency instead of the flexible-base frequency (Givens, 2013). Therefore, herein, we calculate ξ_0 using Eq. (21) with n = 3 and the identified ξ_{Flex}, ξ_{Fxed}, T_{Fixed}, and $T_{Flexible}$ values, and compare our results with those predicted by Veletsos and Nair (1975), which supersedes the approach in (Veletsos & Verbic, 1973). Figure 29 presents the said comparison. This figure shows the identified and predicted foundation damping values versus $h/(V_s T_{Fixed})$. It is well accepted that the slenderness ratio of the building, h/r, plays an important role in foundation damping, and as such we present results for two levels of h/r (it is worth noting here that almost all our data

points have slenderness ratios below 2). Theoretically, the foundation damping decreases with increasing h/r, and this trend is also reflected in the identified damping values. However, results in Figure 29 also indicate that the code-based estimates (here, Veletsos & Nair, 1975) of foundation damping are generally higher then real life data.

Amplitude-Dependency

In the previous sections, we attempted to avoid the inherent amplitude-dependency of superstructure and soil-foundation impedance functions by using only low-intensity earthquake data, and by *correcting* the soil shear wave velocities, respectively. In this section, through a single case study, we show that soil nonlinearity is ever-present and must be well studied. We also show that while soil-nonlinearity is a challenge for our purposes in the present study, data recorded by instrumented buildings can be used to even identify nonlinear soil behavior—a task which is nominally carried out only through laboratory experiments (or sometimes using geotechnical downhole array data).

To demonstrate how the soil nonlinearity can alter the modal characteristics of a flexible-base system, the time-history and time-frequency distribution of the roof acceleration of CSMIP station #57356 recorded during 8 earthquakes (ranging from the 1984 Morgan Hill to the 2014 South Napa events) are shown in Figure 30, as an example. As this figure indicates, there are significant temporal variations not only from earthquake to earthquake, but also during each event.

We carried out identification for CSMIP 57356 using several earthquake data sets. For the Loma Prieta earthquake, which was a severe event at this station, we carried out identification in four successive time segments. The idenitified rocking stiffnesses (mass normalized values) versus Peak Foundation Accelerations (PFAs) are shown in Figure 31. As seen, there is a clear amplitude-dependency. That is, the rocking stiffness decreases when the level of vibration increases. This figure also shows that the soil stiffness does not quickly recover. In other words, the identified rocking stiffnesses at the third and the final time-windows for the Loma Prieta earthquake (1989) are lower than those expected for the given earthquake intensity (MH84 and ML86 have nearly the same earthquake intensity as LP89-3 and LP89-4, respectively).

Here, we show that the observed amplitude-dependency is compatible with what we expect, and incidentally identify a new research avenue in which data collected by instrumented buildings can be used to study nonlinearity their supporting soil domain. For this purpose, we first have to translate the peak foundation (~ground) acceleration to shear strain. To do so, we use the following relationship between the maximum shear strain and amplitude of a vertically propagating sinusoidal shear wave (Beresnev & Wen, 1996),

$$|\gamma_{max}| = \frac{A}{2\pi f V_s} \qquad 22)$$

where A is the acceleration amplitude, f is the wave frequency, and V_s is the soil shear wave velocity. We use amplitude of the Fourier Transform of the foundation response at first mode's flexible-base natural frequency (f) as an approximation of A. For the shear wave velocity, we use the small strain value. Figure 32 presents the same data points of Figure 31 but in different

axes. The horizontal axis is now a shear strain, which is calculated through Eq. (22), and the vertical axes is the rocking stiffness scaled by the maximum value obtained among all data points during the 2009 Morgan Hill Earthquake. For comparison, we have shown the shear reduction curve suggested by Ishibashi and Zhang (1993). The best-fit curve is obtained when the plasticity index is adjusted to 0 (i.e., sandy soil). As seen, there is very good agreement between the theoretical formula and the identified values.

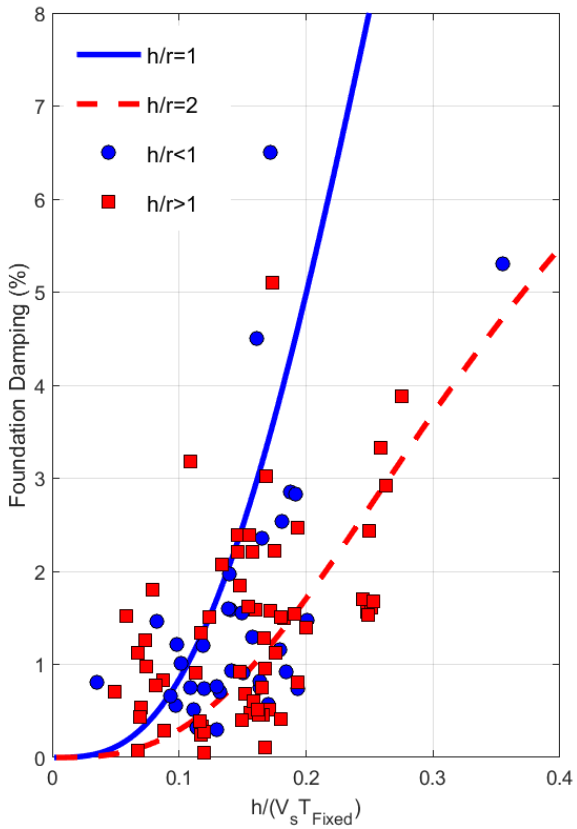

Figure 29. Comparison between identified (symbols) foundation damping values with those predicted using the model by Veletsos and Nair (1975) (solid lines).

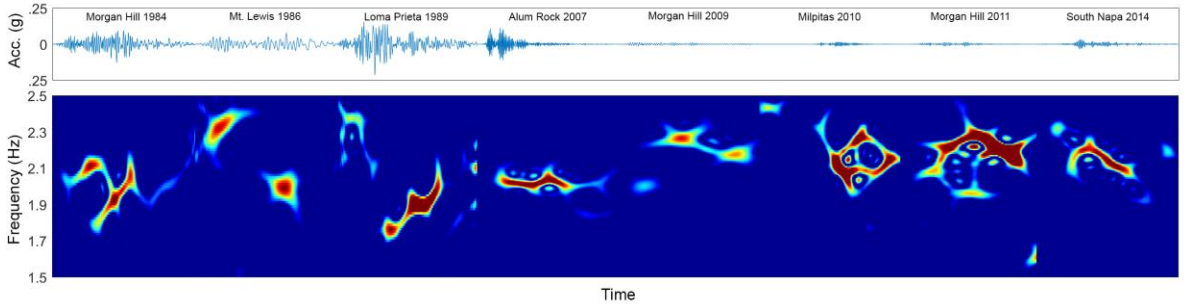

Figure 30. Time variation of the first natural frequency of CSMIP57356 during 8 earthquakes from 1984 to 2014[6].

[6] Colors do not reflect the actual signal energy at each time instant, because the signal has been scaled with its instantaneous amplitude to show its instantaneous frequencies more clearly.

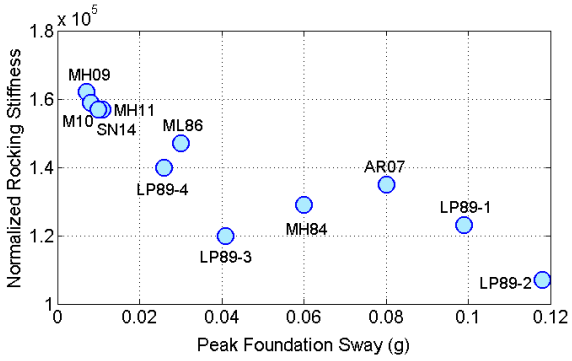

Figure 31. Amplitude-dependency of rocking stiffness observed at station CSMIP57356.

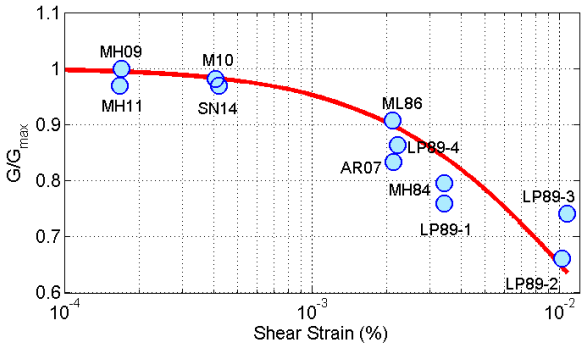

Figure 32. Soil shear modulus reduction identified in station CSMIP57356.

Kinematic Interaction/Foundation Input Motion

Kinematic Interaction (KI) is a relatively new consideration in seismic design/assessment codes (see, FEMA-440), because it is generally believed that total KI is somehow beneficial for the structure (Lin & Miranda, 2008). Moreover, the investigation of KI effects (except perhaps via analytical/numerical methods) is a challenging task because the Foundation Input Motions (FIMs) are not physically recordable. The present study is among the few efforts that offer a glimpse of FIMs extracted from real-life data, and opens a viable path towards the validation of numerical/analytical models of KI effects. An earlier study by Kim and Stewart (2003) has been one of the rare studies in this area. In that study, Kim and Stewart extracted the Transfer Functions between the nearby FFM and the recorded foundation motions. While such Transfer Functions embody KI effects, they do not isolate them, because the foundation motion is not generally equal to FIM (e.g., when foundation has a relative sway).

In the present study, we only tackle the horizontal FIM and neglect the rocking component, which is arguably a lesser effect for most structure-foundation systems (see, also, FEMA-400). It should be noted here, however, that the structure-foundation system is still allowed to rock, yet this rocking is only due to *inertial* rather than kinematic effects—which, for example, could be caused by surface or inclined body waves interacting with a large foundation slab (Mahsuli & Ghannad, 2009).

Figure 33 displays some of the identified FIMs for various buildings and earthquakes. As a rough comparison, the recorded foundation responses are also shown for each case. Note that the difference between these two signals is generated not by KI, but by inertial interaction. For cases that have an available nearby Free-Field Motion (FFM), we can now extract a Transfer Function between the recorded FFM and the recovered FIM, and subsequently compare this KI Transfer Function with those obtained through analytical/numerical models. As an example, Figure 34 displays the Transfer Function calculated between the FIM recovered for the 2011 Berkeley Earthquake from the transverse direction of Station 58503, and its nearby FFM station 58505. Per the recommendation by Kim and Stewart (2003), the Transfer Function is shown only for frequencies at which coherence (Pandit, 1991) is greater than 0.8. The theoretical Transfer Function for a rigid rectangular foundation with the same dimensions and shear wave velocity under vertical incoherent SH waves with incoherency factor of $\gamma = 0.5$ is also shown (Veletsos

et al., 1997). As seen, while the extracted Transfer Function is oscillatory, its mean value is in fair agreement with the theoretical prediction.

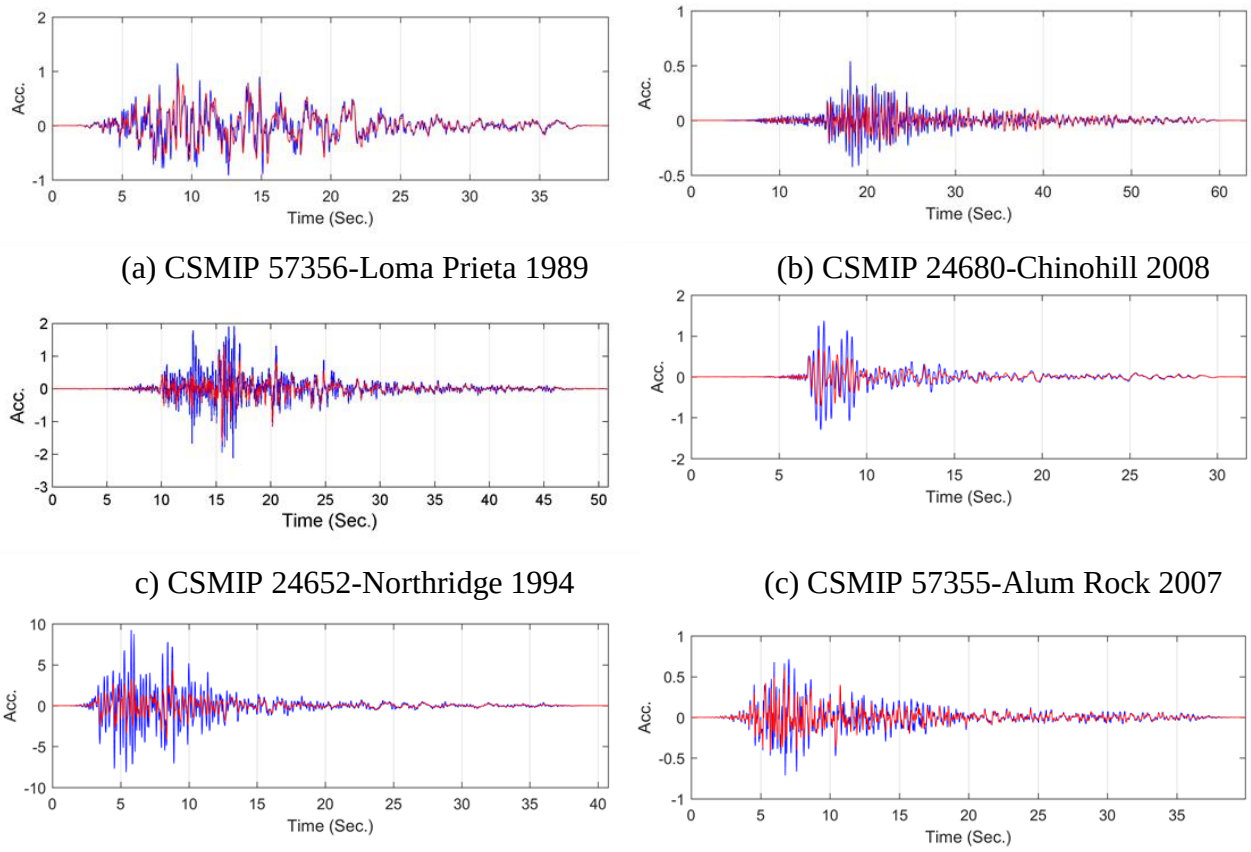

(a) CSMIP 57356-Loma Prieta 1989

(b) CSMIP 24680-Chinohill 2008

c) CSMIP 24652-Northridge 1994

(c) CSMIP 57355-Alum Rock 2007

(e) CSMIP 24386-Northridge 1994

(f) CSMIP 24332-Whittier 1987

Figure 33. Comparison between recorded the foundation responses and identified FIMs.

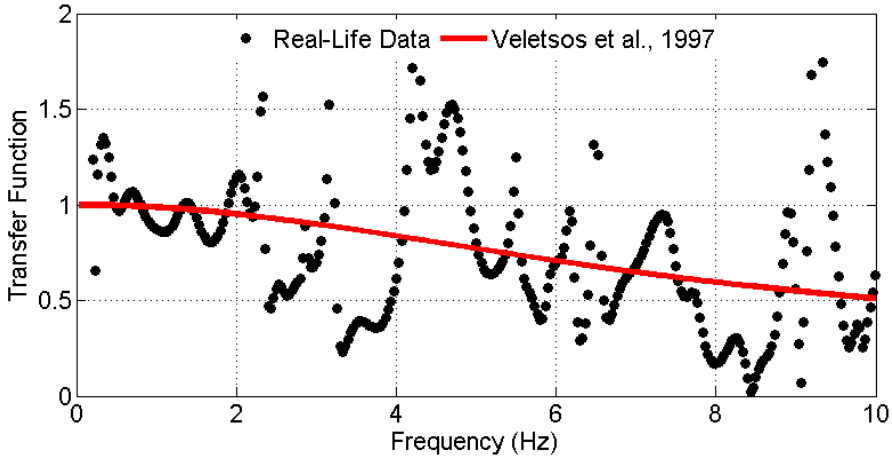

Figure 34. Comparison between the identified kinematic transfer function with that predicted through the model by Veletsos *et al.* (1997) using vertical incoherent shear wave formulation.

Conclusions

We presented the major findings of a two-year study on the identification of soil-foundation Impedance Functions and Foundation Input Motions from response signals of buildings instrumented through California Strong Motion Instrumentation Program (CSMIP). Based on station metadata and availability of records, we selected 373 earthquake data sets belonging to 61 building stations. Due to the nature of the identification problem at-hand, which required an output-only method suitable for non-stationary (i.e., strong earthquake) excitations, we devised a new method wherein the superstructure was modeled as a parametric (Timoshenko) beam for computational efficiency.

Major findings/outcomes of the obtained from the present study are:

- In order to carry out the voluminous data extraction, metadata classification, identification tasks, we developed a Matlab-based Toolbox called CSMIP-CIT. This toolbox is also able to automatically generate a concise report at the end of the analysis, and can be used in future research activities beyond the present effort.
- We developed approximation formulae to predict the fixed-base natural frequency of buildings using their plan dimensions and height, and the type of their lateral force resisting systems.
- We developed approximation formulae to predict the fixed-base damping ratios using fixed-base natural frequency.
- Identified results showed that, for buildings with Concrete Shear Wall (CSW) systems and integrated foundations, the presently available frequency-dependent soil-foundation stiffness modification factors in ASCE 7-10 are acceptable. For other building types and foundation systems, amendments may be appropriate.
- The current method for flexible-base damping ratio estimation of a soil-structure systems in ASCE 7-10 is based on a combination of fixed-base damping ratio (which is assumed to be 5%) and foundation damping, with combination weight calculated using the ratio of flexible-to-fixed base natural frequencies. However, we showed that the predicted foundation damping is generally non-conservative (i.e., higher than actual), especially for squat structures.
- The present study enabled the extraction of FIMs, and this can facilitate validation of numerical analyses (especially, those making use of direct finite element models) of Kinematic Interaction.
- While it was possible to extract FIMs for many CSMIP stations, lack of nearby Free-Field Motion stations prevents the extraction of direct KI Transfer Functions. For a single case whose FFM was available, we showed that a classic formula worked relatively well.
- The methods devised in the present study were also used the extract the amplitude-dependent (i.e., nonlinear) soil behavior; and the soil modulus reduction curve extracted from CSMIP data agreed with a theoretical formula quite well. This opens, again, the possibility to use field measured data from building structures to validate nonlinear

models of soil behavior—in effect, allowing the utilization of instrumented buildings as sensors to examine the behavior of the soils that support them.

Acknowledgments

The work presented in this manuscript was funded, in part, by the California Geological Survey (Contract No. 1014-963) and by the California Department of Transportation (Grant No. 65A0450). Authors are grateful for the support and assistance provided by Moh Huang and Anthony Shakal of California Geological Survey. Any opinions, findings, conclusions or recommendations expressed in this material are those of the authors and do not necessarily reflect the views of the sponsoring agencies.

References

Abrahamson, N.A., Schneider, J.F. & Stepp, J.C. 1991. Empirical spatial coherency functions for applications to soil-structure interaction analyses." *Earthquake Spectra,* 7(1), 1-27.

Aristizabal-Ochoa, J., 2004. Timoshenko beam-column with generalized end conditions and nonclassical modes of vibration of shear beams. *Journal of Eng. Mech.,* 130(10), 1151-1159.

ASCE (American Society of Civil Engineers), ASCE, 2010. *ASCE7-10: Minimum Design Loads for Buildings and Other Structures*, Report ASCE/SEI 7-10, Reston, VA.

ATC, (1978). Tentative provisions for the development of seismic regulations for buildings. Palo Alto, CA: Applied Technological Council.

Beresnev, I.A., & Wen, K. L., 1996. Nonlinear soil response—a reality?. *Bulletin of the Seismological Society of America*, 86(6), 1964-1978.

Bernal, D., Döhler, M., Kojidi, S. M., Kwan, K., & Liu, Y. 2015. First mode damping ratios for buildings. *Earthquake Spectra*, 31(1), 367-381.

Bernal, D., Kojidi, S.M., Kwan, K., & Döhler, M., 2013. Damping Identification in Buildings from Earthquake Records. In SMIP12 Seminar Proceedings, 39-56.

Bradford, S., Clinton, J., Favela, T. & Heaton, T., 2004. *Results of Millikan library forced vibration testing*: Earthquake Engineering Research Laboratory.

Çelebi, M., Firat, S. & Çankaya, I., 2006. The evaluation of impedance functions in the analysis of foundations vibrations using boundary element method. *Applied Mathematics and Computation*, 173(1), 636-667.

Cheng, M. & Heaton, T., 2013. Simulating building motions using the ratios of its natural frequencies and a Timoshenko beam model.. *Earthquake Spectra.*

Chopra, A., 2001. Dynamics of structures: theory and applications to earthquake engineering. 2nd ed. s.l.:Prentice-Hall.

Clough, R. & Penzien, J., 1975. *Dynamics of Structures*, McGraw-Hill.

Cowper, G., 1966. The shear coefficient in Timoshenko's beam theory. *ASME Journal of Applied Mechanics,* 33(2), 335-340.

FEMA (Federal Emergency Management Agency) (2005). *FEMA-440 Improvement of Nonlinear Static Seismic Analysis Procedures.* Federal Emergency Management Agency, Washington D.C.

Gazetas, G., 1983. Analysis of machine foundation vibrations: state of the art. *International Journal of Soil Dynamics and Earthquake Engineering,* 2(1), 2-42.

Ghahari, S., Abazarsa, F. & Taciroglu, E., 2015. *CSMIP-CIT.* V2.

Ghahari, S., Abazarsa, F., Ghannad, M. & Taciroglu, E., 2013. Response-only modal identification of structures using strong motion data. *Earthquake Engineering and Structural Dynamics,* 42(8), 1221-1242.

Ghahari, S., Abazarsa, F., Ghannad, M.A., Celebi, M. & Taciroglu, E., 2014. Blind modal identification of structures from spatially sparse seismic response signals. *Structural Control and Health Monitoring,* 21, 649-674.

Han, S., Benaroya, H. & Wei, T., 1999. Dynamics of transversely vibrating beams using four engineering theories.. Journal of Sound and Vibration, 225(5), 935-988.

Huang, M., & Shakal, A.F., 2001. Structural instrumentation in the California Strong Motion Instrumnetation Program. *Strong Motion Instrumentation for Civil Engineering Structures*, Springer Netherlands, 17-31.

IBC, 2012. *International Building Code,* Washington D.C: International Code Council.

Iguchi, M. & Luco, E., 1981. Dynamic response of flexible rectangular foundations on an elastic half-space. *Earthquake Engineering & Structural Dynamics,* 9(3), 239-249.

Ishibashi, I., & Zhang, X., 1993. Unified dynamic shear moduli and damping patios of sand and clay. *Soils and Foundations*, 33(1), 182-191.

Jennings, P. & Bielak, J., 1973. Dynamics of building-soil interaction. *Bulletin of the Seismological Society of America,* 63(1), 9-48.

Jennings, P. & Kuroiwa, J., 1968. Vibration and soil-structure interaction tests of a nine-story reinforced concrete building. *Bulletin of the Seism. Society of America*, 58(3), 891-916.

Kim, S., & Stewart, J.P., 2003. Kinematic Soil-Structure Interaction from Strong Motion Recordings. *Journal of Geotechnical and Geoenvironmental Engineering*, 129(4), 323-335.

Lignos, D. & Miranda, E., 2014. Estimation of base motion in instrumented steel buildings using output-only system identification. *Earthquake Engineering and Structural Dynamics*, 43(4), pp. 547-563.

Luco, J., Trifunac, M. & Wong, H., 1988. Isolation of soil-structure interaction effects by full-scale forced vibration tests. *Earthquake Engineering and Structural Dynamics,* 16(1), 1-21.

MATLAB, 2013. *MATLAB: The language of technical computing*., s.l.: Mathworks. The MathWorks Inc., Natick, MA.

NIST (National Institute of Standards and Technology), (2012). Soil-Structure Interaction for Building Structures, Report NIST/GCR 12-917-21, presented by NEHRP Consultants Joint Venture, J.P. Stewart (project director), September.

NEHRP, (1994). Recommended provisions for the developmement of seismic regulations for new buildings. Washington, D.C.: Building Seismic Safety Council.

NRC, (1995). *National Building Code of Canada.* Associate Committee on the National Building. Ottawa, Canada: National Research Council of Canada.

NRC/IRC, (2010). *National Building Code of Canada.* Ottawa, Ontario: National Research Council of Canada.

Pais, A. & Kausel, E., 1988. pproximate formulas for dynamic stiffnesses of rigid foundations.. *Soil Dynamics and Earthquake Engineering,* 7(4), 213-227.

Pak, R. & Guzina, B., 1999. Seismic soil-structure interaction analysis by direct boundary element methods. *International Journal of Solids and Structures,* 36(31), 4743-4766.

Pandit, S.M., 1991. Modal and Spectrum Analysis: Data Dependent Systems in State Space. Wiley-Interscience.

Richart, F., 1975. Some effects of dynamic soil properties on soil-structure interaction. *Journal of the Geotechnical Engineering Division (ASCE),* 101(2), 1193-1240.

Rizos, D. & Wang, Z., 2002. Coupled BEM–FEM solutions for direct time domain soil–structure interaction analysis. *Engineering Analysis with Boundary Elements,* 26(10), 877-888.

Seyhan, E., Stewart, J.P., Ancheta, T.D., Darragh, R.B., & Graves, R.W., 2014. NGA-West2 site database. *Earthquake Spectra*, 30(3), 1007-1024.

Snieder, R. & Safak, E., 2006. Extracting the building response using seismic interferometry: Theory and application to the Millikan Library in Pasadena, California. *Bulletin of the Seismological Society of America,* 96(2), 586-598.

Stewart, J., Seed, R. & Fenves, G., 1998. *Empirical evaluation of inertial soil-structure interaction effects*: Pacific Earthquake Engineering Research Center (PEER).

Stewart, J.P. 1996. An empirical assessment of soil-structure interaction effects on the seismic response of structures. Doctoral dissertation, University of California, Berkeley.

Stewart, J.P., & Stewart, A.F., 1997. Analysis of soil-structure interaction effects on building response from earthquake strong motion recordings at 58 sites. *Earthquake Engineering Research Center*, 97(1).

Stewart, J.P., Fenves, G.L., & Seed, R.B., 1999a. Seismic soil-structure interaction in buildings. I: Analytical methods. *Journal of Geotechnical and Geoenv. Eng.*, 125(1), 26-37.

Stewart, J.P., Seed, R.B., & Fenves, G.L., 1999b. Seismic soil-structure interaction in buildings. II: Empirical findings. *Journal of Geotechnical and Geoenv. Eng.*, 125(1), 38-48.

Taciroglu, E., Ghahari, S. & Abazarsa, F., 2016a. Efficient model updating of a multi-story frame and its foundation stiffmess from earthquake records using a Timoshenko beam model. *Soil Dynamics and Earthquake Engineering* (in print).

Taciroglu, E. & Ghahari, S., 2016b. Identification of Soil-Foundation Dynamic Stiffness from Seismic Response Signals. *ACI Special Publication* (in print).

Taciroglu, E., Ghahari, S. & Abazarsa, F., 2016c. Identification of soil-foundation-structure interaction effects using recorded strong motion response data from CSMIP-instrumneted buildings, UCLA-SGEL Report 2016-10.

Tileylioglu, S., Stewart, J. & Nigbor, R., 2010. Dynamic stiffness and damping of a shallow foundation from forced vibration of a field test structure. *Journal of Geotechnical and Geoenvironmental Engineering,* 137(4), 344-353.

Timoshenko, S., 1921. On the correction for shear of the differential equation for transverse vibrations of prismatic bars. *The London, Edinburgh, and Dublin Philosophical Magazine and Journal of Science,* 41(245), 744-746.

Todorovska, M., 2009. Soil-structure system identification of Millikan Library North–South response during four earthquakes (1970–2002): what caused the observed wandering of the system frequencies?. *Bulletin of the Seismological Society of America,* 99(2A), pp. 626-635.

UBC (Uniform Building Code), (1997). *International Conference of Building Officials.* Whittier, California.

Veletsos, A. & Verbic, B., 1973. Vibration of viscoelastic foundations. *Earthquake Engineering & Structural Dynamics,* 2(1), 87-102.

Veletsos, A.S., & Nair, V.V., 1975. Seismic interaction of structures on hysteretic foundations. *Journal of the Structural Division*, 101(1), 109-129.

Veletsos, A.S., Prasad, A.M., & Wu, W.H., 1997. Transfer functions for rigid rectangular foundations. *Earthquake engineering & structural dynamics*, 26(1), 5-17.

Wolf, J. & Deeks, A., 2004. Foundation Vibration analysis: A Strength of Materials Approach. Butterworth-Heinemann.

Wolf, J., 1976. Soil-structure interaction with separation of base mat from soil (lifting-off). *Nuclear Engineering and Design*, 38(2), 357-384.

Appendix A

Table A. List of candidate buildings for identification analyses.

No.	CSMIP	Floor No.*	NS	Type**	EW	Type**	Used Dir
1	58396	3	Y	MRSF	Y	MRSF	NS
2	13364	9	Y	MRSF	N	---	NS
3	58496	2	Y	BSF	Y	BSF	No
4	54388	2	Y	BSF	Y	MRSF	No
5	24370	6	N	---	Y	MRSF	EW
6	58661	3	Y	MRSF	Y	MRSF	No
7	24198	2	Y	MRSF	Y	MRSF	No
8	58466	4	Y	MRSF	Y	MRSF	No
9	58638	15	Y	Combined	Y	Combined	No
10	13214	5	Y	BSF	Y	BSF	No
11	14654	14	Y	BSF+MRSF	Y	BSF+MRSF	NS, EW
12	68032	3	N	---	Y	BSF+MRSF	No
13	57948	2	Y	Combined	N	---	No
14	57783	3	Y	Combined	N	---	No
15	13329	8	Y	Combined	Y	Combined	No
16	14533	15	Y	MRSF	Y	MRSF	EW
17	14323	7	Y	MRSF	Y	MRSF	EW
18	24581	14	Y	CSCF+UMW	Y	CSCF+UMW	No
19	24569	18	Y	MRSF+CSW	Y	MRSF+CSW	NS, EW
20	24643	23	Y	BSF	Y	MRSF	NS, EW
21	24332	5	Y	BSF	Y	BSF	NS
22	24288	32	Y	MRSF	Y	MRSF	NS
23	24602	52	Y	BSF+MRSF	Y	BSF+MRSF	EW
24	24629	58	Y	MRSF	N	---	No
25	24652	6	Y	BSF+MRSF	Y	BSF+MRSF	NS, EW
26	24713	8	Y	BSF	Y	BSF	No
27	31213	4	Y	Combined	N	---	No
28	57614	2	N	---	Y	BSF	No
29	12299	4	Y	MRSF	Y	MRSF	EW
30	24546	12	Y	MRSF	Y	MRSF	No
31	23481	8	Y	MRSF	N	---	NS
32	58506	3	Y	MRSF	Y	MRSF	No
33	23516	3	Y	MRSF	Y	MRSF	NS, EW
34	23515	9	Y	MRSF	Y	MRSF	NS, EW
35	03300	22	Y	MRSF	Y	MRSF	No
36	58776	15	Y	MRSF	Y	MRSF	No
37	58480	19	Y	MRSF	N	---	NS
38	58532	49	Y	MRSF	N	---	NS
39	57357	13	Y	MRSF	Y	MRSF	EW
40	57562	3	Y	MRSF	Y	MRSF	No
41	58261	4	N	---	Y	MRSF	EW
42	58593	3	N	---	Y	BSF	No
43	58199	4	N	---	Y	Combined	No
44	58506	3	Y	MRSF	Y	MRSF	NS, EW
45	24385	10	Y	CSW	Y	CSW	NS
46	58492	8	Y	CMSW	Y	CMSW	No
47	01260	6	N	---	Y	RCF	No
48	89494	5	N	---	Y	RMSW	No
49	58354	13	Y	MRSF+RCF+CSW	Y	MRSF+RCF+CSW	NS, EW
50	58488	4	N	---	Y	CSW	No
51	58462	7	Y	CSW	Y	CSW	NS, EW
52	12267	5	Y	CSW	Y	CSW	No
53	12493	5	Y	RCF+CSW	Y	RCF+CSW	NS

54	14311	5	Y	CSW	Y	CSW	EW
55	24236	14	Y	RCF	Y	RCF	NS, EW
56	24601	17	Y	CSW	Y	CSW	NS, EW
57	24463	6	Y	RCF	Y	RCF	NS, EW
58	24655	6	Y	CSW	Y	CSW	NS, EW
59	24231	7	N	---	Y	Combined	No
60	24468	9	Y	CSW	Y	CSW	NS, EW
61	57502	2	Y	CSW	Y	CSW	No
62	58641	8	N	---	Y	CSW	EW
63	13589	11	N	---	Y	CSW	EW
64	24464	22	Y	RCF	Y	RCF	NS, EW
65	58337	11	Y	CSW	Y	CSW	NS, EW
66	58639	13	Y	CSW	Y	CSW	NS, EW
67	58224	2	N	---	Y	CSW	No
68	58583	24	Y	CSW	Y	CSW	NS
69	12284	4	Y	CSW	Y	CSW	NS
70	24232	4	Y	CSW	Y	CSW	No
71	24454	4	Y	Combined	N	---	No
72	24571	11	Y	RCF	Y	RCF	NS, EW
73	58334	3	Y	CSW	Y	CSW	NS, EW
74	58348	3	N	---	Y	CSW	EW
75	23511	3	Y	RCF	Y	RCF	NS, EW
76	58503	4	Y	RCF+CSW	N	---	NS
77	13620	2	N	---	Y	CSW	No
78	23285	6	Y	CSW	Y	CSW	EW
79	23287	6	Y	CSW	Y	CSW	NS, EW
80	58490	6	Y	RCF	N	---	NS
81	03603	23	Y	Combined	Y	Combined	NS, EW
82	58437	47	Y	CSW	N	---	No
83	58411	58	Y	RCF+CSW	N	---	No
84	58479	6	Y	RCF+CSW	N	---	No
85	58389	64	N	---	Y	Combined	No
86	57355	11	Y	RCF	Y	CSW	NS, EW
87	57356	10	Y	CSW	Y	CSW	NS, EW
88	25213	3	Y	CSW	N	---	No
89	25302	4	Y	CSW	Y	CSW	NS, EW
90	48733	6	N	---	Y	RCF	EW
91	68489	14	Y	RCF+CSW	Y	RCF+CSW	NS, EW
92	68387	5	Y	CSW	Y	RCF	NS, EW
93	24322	15	Y	RCF	Y	RCF	NS, EW
94	24680	14	Y	CSW	Y	CSW	NS, EW
95	58055	4	Y	Combined	N	---	No
96	24514	6	Y	Combined	N	---	No
97	35409	3	Y	CSW	Y	CSW	NS
98	24386	7	Y	RCF	Y	RCF	NS, EW
99	25339	12	Y	CSW	Y	CSW	NS, EW
100	58364	10	Y	RCF+CSW	Y	RCF+CSW	NS, EW
101	47459	4	Y	CSW	Y	CSW	EW
102	14606	8	Y	RMSW	Y	RMSW	NS

* Counted floors above basement

** Moment Resisting Steel Frame (MRSF), Braced Steel Frame (BSF), Combination of several types along the height (Combined), Composite Steel-Concrete Frame (CSCF), Unreinforced Masonry Wall (UMW), Concrete Shear Wall (CSW), Concrete Masonry Shear Wall (CMSW), Reinforced Concrete Frame (RCF), Reinforced Masonry Shear Wall (RMSW)

Appendix B

Table B. Identified flexible base Timoshenko beam model's parameters (units are in SI).

No.	CSMIP No.	Dir	L (m)	D (m)	B (m)	Eq. Name	Eq. Year	$\bar{b}$	s	KR/M $(\times 10^3)$	KT/M $(\times 10^3)$
1	58354	EW	61.3	34.3	34.3	Loma Prieta	1989	0.373000	0.756800	R	R
2	58354	EW	61.3	34.3	34.3	Berkeley	2011	0.228900	1.250300	R	R
3	58354	NS	61.3	34.3	34.3	Loma Prieta	1989	0.445200	0.405780	118	R
4	58334	NS	22.3	22.0	35.0	San Leandro	2011	0.065380	0.117600	4159	13.992
5	58334	NS	22.3	22.0	35.0	Piedmont	2007	0.060000	0.313000	741	4.490
6	58334	NS	22.3	22.0	35.0	Berkeley	I 2011	0.061000	0.300000	1080	5.280
7	58334	EW	22.3	35.0	22.0	Loma Prieta	1989	0.048500	0.678300	R	13.648
8	58334	EW	22.3	35.0	22.0	Piedmont	2006	0.046900	0.713600	R	R
9	58334	EW	22.3	35.0	22.0	Lafayette	2007	0.047400	0.689400	R	R
10	58334	EW	22.3	35.0	22.0	Piedmont	2007	0.051000	0.632200	R	R
11	58334	EW	22.3	35.0	22.0	San Leandro	23 Aug. 2011	0.048200	0.622400	R	12.652
12	58334	EW	22.3	35.0	22.0	San Leandro	24 Aug. 2011	0.050000	0.561900	R	29.393
13	58334	EW	22.3	35.0	22.0	Berkeley	20 Oct. 2011 I	0.052400	0.658200	R	R
14	58334	EW	22.3	35.0	22.0	Berkeley	20 Oct. 2011 II	0.050800	0.663000	R	12.531
15	58334	EW	22.3	35.0	22.0	Elcerrito	2012	0.056100	0.513800	R	R
16	58334	EW	22.3	35.0	22.0	Piedmont	2015	0.053300	0.675200	R	R
17	24385	NS	26.8	22.9	66.6	Whittier	1987	0.173450	0.468120	R	R
18	24385	NS	26.8	22.9	66.6	Sierra Madre	1991	0.133020	0.761220	R	R
19	24322	NS	56.0	21.9	57.6	Encino	2014	0.075459	5.116600	R	R
20	24322	NS	56.0	21.9	57.6	Calexico	2010	0.058720	5.010800	R	R
21	24322	NS	56.0	21.9	57.6	Chinohills	2008	0.079708	4.769600	R	R
22	24322	NS	56.0	21.9	57.6	Chatsworth	2007	0.074253	4.826300	R	R
23	24322	EW	56.0	57.6	21.9	Landers	1992	0.310000	2.166000	R	R
24	24322	EW	56.0	57.6	21.9	Northridge	1994	0.941100	0.672700	R	R
25	24322	EW	56.0	57.6	21.9	Chinohills	2008	0.690800	0.215400	R	R
26	24322	EW	56.0	57.6	21.9	Calexico	2010	0.696300	0.198000	R	R
27	24322	EW	56.0	57.6	21.9	Encino	2014	0.644800	0.260100	R	R
28	58490	NS	23.8	27.4	61.0	Loma Prieta	1989	0.162500	1.404500	R	R
29	58462	EW	26.0	28.0	66.0	Alum Rock	2007	0.256210	0.329900	R	R
30	58462	EW	26.0	28.0	66.0	Loma Prieta	1989	0.262840	0.411820	R	R
31	58462	NS	26.0	66.0	28.0	Loma Prieta	1989	0.218700	0.754200	R	R
32	58462	NS	26.0	66.0	28.0	Lafayette	2007	0.128200	1.197400	R	R
33	58462	NS	26.0	66.0	28.0	Alum Rock	2007	0.137600	1.075300	R	R
34	0482	NS	60.0	50.5	50.5	Sierra Madre	1991	0.654010	0.670470	R	R
35	0482	NS	60.0	50.5	50.5	Big Bear	1992	0.694130	0.642560	R	R
36	13364	NS	38.1	35.4	66.5	Chinohills	2008	0.305530	1.221800	R	R
37	13364	NS	38.1	35.4	66.5	Lagunaniguel	2012	0.391860	0.706990	R	R
38	24370	EW	25.1	36.6	36.6	Northridge	1994	0.178130	1.875400	R	R
39	24370	EW	25.1	36.6	36.6	Sierra Madre	1991	0.179440	1.672900	R	R
40	24370	EW	25.1	36.6	36.6	Chatsworth	2007	0.140000	1.861200	R	R
41	24370	EW	25.1	36.6	36.6	Whittier	1987	0.176880	1.583600	49	R
42	24370	EW	25.1	36.6	36.6	Chinohills	2008	0.188670	1.643900	R	R
43	24370	EW	25.1	36.6	36.6	Whittier Narrows	2010	0.154820	1.688600	R	R
44	24370	EW	25.1	36.6	36.6	Calexico	2010	0.176070	1.656300	R	R
45	24370	EW	25.1	36.6	36.6	Borrego Springs	2010	0.173270	1.530800	R	R
46	23287	EW	15.6	17.7	52.5	Lomalinda	Feb. 2013	0.034318	0.747850	122	2.406
47	23287	NS	15.6	52.5	17.7	Landers	1992	0.117400	0.743600	R	1.444
48	23287	NS	15.6	52.5	17.7	Northridge	1994	0.122200	0.737300	R	2.062
49	23287	NS	15.6	52.5	17.7	Chinohills	2008	0.107000	0.747200	R	1.316
50	23287	NS	15.6	52.5	17.7	San Bernardino	2009	0.103700	0.833000	R	R
51	23287	NS	15.6	52.5	17.7	Borrego Springs	2010	0.117200	0.733800	R	9.116
52	23287	NS	15.6	52.5	17.7	Devore	2015	0.099400	0.877800	R	R
53	23287	NS	15.6	52.5	17.7	Banning	2016	0.101700	0.825400	R	R
54	14606	NS	23.0	19.0	65.0	Northridge	1994	0.137500	0.631000	56	R

55	14606	NS	23.0	19.0	65.0	Chinohills	2008	0.136430	0.552390	61	R
56	14606	NS	23.0	19.0	65.0	Calexico	2010	0.163700	0.416200	111	R
57	14606	NS	23.0	19.0	65.0	Borrego Springs	2010	0.152600	0.416200	98	R
58	14606	NS	23.0	19.0	65.0	Whittier Narrows	2010	0.127500	0.664100	91	R
59	58641	EW	24.0	10.7	15.0	Fremont	2015	0.287010	0.190180	R	R
60	58641	EW	24.0	10.7	15.0	Milpitas	2010	0.299880	0.145990	R	R
61	58641	EW	24.0	10.7	15.0	Alum Rock	2007	0.318730	0.155550	R	R
62	58641	EW	24.0	10.7	15.0	Gilroy	2002	0.296100	0.176670	R	R
63	58641	EW	24.0	10.7	15.0	Bolinas	1999	0.312050	0.146110	R	R
64	13589	EW	44.8	23.5	46.9	Landers	1992	0.331630	0.409200	R	R
65	13589	EW	44.8	23.5	46.9	Northridge	1994	0.353460	0.387770	R	R
66	13589	EW	44.8	23.5	46.9	Chinohills	2008	0.341250	0.390950	R	R
67	13589	EW	44.8	23.5	46.9	Inglewood	2009	0.302540	0.440660	R	R
68	13589	EW	44.8	23.5	46.9	Calexico	2010	0.322800	0.408370	R	0.259
69	13589	EW	44.8	23.5	46.9	Borrego Springs	2010	0.305860	0.408480	R	R
70	13589	EW	44.8	23.5	46.9	La Habra	2014	0.322800	0.408370	R	R
71	47459	EW	23.6	23.0	20.0	Morgan Hill	1984	0.065143	0.668250	203	1.692
72	47459	EW	23.6	23.0	20.0	Loma Prieta	1989	0.084400	0.636250	102	R
73	24386	NS	19.9	18.6	48.8	Westwood Village	2014	0.155830	0.324770	518	0.768
74	24386	NS	19.9	18.6	48.8	Encino	2014	0.130510	0.522700	135	1.016
75	24386	NS	19.9	18.6	48.8	Newhall	2011	0.146850	0.464940	R	0.805
76	24386	NS	19.9	18.6	48.8	Borrego Springs	2010	0.147080	0.464460	R	3.600
77	24386	EW	19.9	48.8	18.6	Big Bear	1992	0.224000	1.146700	R	0.113
78	24386	EW	19.9	48.8	18.6	Landers	1992	0.216500	1.187000	R	0.262
79	24386	EW	19.9	48.8	18.6	Northridge	1994	0.320400	1.315300	R	0.039
80	24386	EW	19.9	48.8	18.6	Chinohills	2008	0.088300	1.176300	R	1.039
81	24386	EW	19.9	48.8	18.6	Encino	2014	0.085800	1.254600	R	1.274
82	35409	NS	14.6	24.0	49.5	Maricopa	2010	0.074472	0.234860	R	1.734
83	35409	NS	14.6	24.0	49.5	Islavista	2013	0.074171	0.248940	R	2.238
84	58261	EW	16.0	35.7	66.8	South Napa	2014	0.142500	0.876280	R	R
85	58261	EW	16.0	35.7	66.8	Loma Prieta	1989	0.142500	0.876280	R	0.366
86	58261	EW	16.0	35.7	66.8	Morgan Hill	1984	0.136640	0.793480	R	R
87	24602	EW	236.0	48.0	48.0	Sierra Madre	1991	2.363900	0.436900	R	R
88	24602	EW	236.0	48.0	48.0	Northridge	1994	2.390100	0.453210	R	R
89	24602	EW	236.0	48.0	48.0	Landers	1992	2.536800	0.415460	R	R
90	24602	EW	236.0	48.0	48.0	Chinohills	2008	2.188100	0.485230	R	R
91	23515	NS	35.8	33.5	40.8	Landers	1992	0.749000	0.349500	20	R
92	23515	EW	35.8	40.8	33.5	Landers	1992	0.416000	1.123200	81	R
93	23516	NS	12.6	43.9	40.0	Landers	1992	0.057318	2.395300	R	R
94	23516	NS	12.6	43.9	40.0	Chinohills	2008	0.043297	2.710600	R	R
95	23516	NS	12.6	43.9	40.0	San Bernardino	2009	0.048140	2.730000	R	R
96	23516	EW	12.6	40.0	43.9	Whittier	1987	0.049300	2.351000	R	R
97	23516	EW	12.6	40.0	43.9	Landers	1992	0.058300	2.313500	R	R
98	23516	EW	12.6	40.0	43.9	Lake Elsinore	2007	0.074600	1.425300	R	R
99	23516	EW	12.6	40.0	43.9	Chinohills	2008	0.096800	1.086300	R	R
100	23516	EW	12.6	40.0	43.9	Inglewood	2009	0.077100	1.412500	R	R
101	23516	EW	12.6	40.0	43.9	San Bernardino	2009	0.109300	1.109100	R	R
102	23516	EW	12.6	40.0	43.9	Beaumont	2010	0.078700	1.337000	R	R
103	12284	NS	15.3	23.0	60.0	Palm Springs	1986	0.141900	0.122010	25	R
104	12284	NS	15.3	23.0	60.0	Borrego Springs	July 2010	0.163990	0.197210	14	R
105	12284	NS	15.3	23.0	60.0	Calexico	2010	0.161140	0.240760	21	R
106	12284	NS	15.3	23.0	60.0	Ocotillo	April 2010	0.153890	0.271970	22	R
107	57355	EW	43.0	25.0	58.0	Morgan Hill	1984	0.266940	0.354930	R	0.286
108	57355	EW	43.0	25.0	58.0	Loma Prieta	1989	0.317320	0.367170	R	0.232
109	57355	EW	43.0	25.0	58.0	Alum Rock	2007	0.270370	0.465510	R	R
110	57355	NS	43.0	58.0	25.0	Morgan Hill	1984	0.281000	0.680900	R	R
111	57355	NS	43.0	58.0	25.0	Loma Prieta	1989	0.400900	0.430200	R	0.302
112	57355	NS	43.0	58.0	25.0	Alum Rock	2007	0.425700	0.408600	R	0.221
113	57356	EW	29.0	19.0	64.0	Morgan Hill	1984	0.145360	0.095220	119	0.488
114	57356	EW	29.0	19.0	64.0	Loma Prieta	1989	0.155320	0.051201	120	0.257

115	57356	EW	29.0	19.0	64.0	Alum Rock	2007	0.149950	0.100200	122	0.440
116	57356	EW	29.0	19.0	64.0	Morgan Hill	2009	0.148940	0.102430	141	0.834
117	57356	EW	29.0	19.0	64.0	Milpitas	2010	0.152650	0.102080	148	0.465
118	57356	EW	29.0	19.0	64.0	Morgan Hill	2011	0.146340	0.124640	142	0.900
119	57356	EW	29.0	19.0	64.0	South Napa	2014	0.147100	0.152460	141	0.542
120	57356	NS	29.0	64.0	19.0	Morgan Hill	1984	0.136300	1.008800	R	0.419
121	57356	NS	29.0	64.0	19.0	Loma Prieta 1989	1989	0.163100	0.975900	R	0.243
122	57356	NS	29.0	64.0	19.0	Alum Rock	2007	0.146500	1.050300	R	0.559
123	58394	NS	32.0	26.0	59.0	Loma Prieta	1989	0.512280	0.102070	36	R
124	58394	EW	32.0	59.0	26.0	Loma Prieta	1989	0.321450	0.686960	R	0.187
125	58364	EW	39.0	32.0	45.0	Livermore	A 1980	0.249640	0.294790	134	0.670
126	58364	EW	39.0	32.0	45.0	Livermore	B 1980	0.240330	0.415720	119	0.402
127	58364	EW	39.0	32.0	45.0	Loma Prieta	1989	0.289130	0.305000	125	0.282
128	58364	EW	39.0	32.0	45.0	Alum Rock	2009	0.210800	0.485910	85	R
129	58364	EW	39.0	32.0	45.0	Alamo	2008	0.246970	0.378260	89	R
130	58364	EW	39.0	32.0	45.0	Berkeley	I 2011	0.204440	0.489100	92	R
131	58364	EW	39.0	32.0	45.0	Berkeley	II 2011	0.222730	0.434130	96	R
132	58364	EW	39.0	32.0	45.0	Elcerrito	2012	0.214210	0.460550	89	R
133	58364	EW	39.0	32.0	45.0	South Napa	2014	0.338600	0.191090	103	R
134	58364	EW	39.0	32.0	45.0	Concord	2015	0.236360	0.408170	90	R
135	58364	EW	39.0	32.0	45.0	San Ramon	2015	0.216010	0.485460	89	R
136	58364	NS	39.0	45.0	32.0	Alamo	2008	0.047018	2.998700	R	R
137	58364	NS	39.0	45.0	32.0	Berkeley	I 2011	0.041278	3.030000	R	R
138	58364	NS	39.0	45.0	32.0	Berkeley	II 2011	0.043805	2.902200	R	R
139	58503	NS	14.5	21.0	79.0	Loma Prieta	1989	0.115490	0.254130	R	1.075
140	58503	NS	14.5	21.0	79.0	Glen Ellen	2006	0.104480	0.248610	R	4.473
141	58503	NS	14.5	21.0	79.0	Berkeley	2011	0.092841	0.254050	R	1.332
142	58503	NS	14.5	21.0	79.0	Elcerrito	2012	0.101550	0.208170	R	0.933
143	58503	NS	14.5	21.0	79.0	South Napa	2014	0.099810	0.165940	R	1.156
144	58503	NS	14.5	21.0	79.0	Piedmont Area	2006	0.106270	0.227400	R	1.324
145	24601	EW	46.0	24.0	69.0	Sierra Madre	1991	0.430980	0.126910	141	R
146	24601	EW	46.0	24.0	69.0	Landers	1992	0.426300	0.128840	127	0.216
147	24601	EW	46.0	24.0	69.0	Northridge	1994	0.485470	0.105190	116	R
148	24601	NS	46.0	69.0	24.0	Sierra Madre	1991	0.332800	0.540080	R	R
149	24601	NS	46.0	69.0	24.0	Landers	1992	0.351930	0.533880	R	R
150	24601	NS	46.0	69.0	24.0	Northridge	1994	0.402050	0.500590	R	R
151	25339	EW	35.0	19.0	56.0	Santa Barbara	1978	0.251370	0.173230	R	R
152	25339	EW	35.0	19.0	56.0	Ojai	2013	0.253230	0.312970	R	R
153	25339	EW	35.0	19.0	56.0	Islavista	2013	0.237430	0.384810	R	R
154	25339	EW	35.0	19.0	56.0	Calexico	2010	0.224660	0.356860	R	R
155	25339	EW	35.0	19.0	56.0	Ojai	2009	0.248350	0.397600	R	R
156	25339	EW	35.0	19.0	56.0	Westlake Village	2009	0.244110	0.344760	R	R
157	25339	NS	35.0	56.0	19.0	Ojai	2013	0.289120	0.600678	R	0.388
158	24571	EW	39.6	25.9	64.9	Northridge	1994	0.285810	1.450100	16	R
159	24571	EW	39.6	25.9	64.9	Calexico	2010	0.221760	1.573600	22	0.071
160	24571	NS	39.6	64.9	25.9	Landers	1992	0.243800	1.259200	R	R
161	24571	NS	39.6	64.9	25.9	Northridge	1994	0.285200	1.057000	R	R
162	24571	NS	39.6	64.9	25.9	Whittier Narrows	2010	0.228900	1.055200	R	R
163	24571	NS	39.6	64.9	25.9	Calexico	2010	0.231100	1.071200	R	R
164	23285	EW	24.4	41.6	62.4	Fontana	2015	0.122500	0.949120	R	R
165	23285	EW	24.4	41.6	62.4	Big Bear Lake	2014	0.126430	0.902700	R	R
166	23285	EW	24.4	41.6	62.4	Fontana	2014	0.146840	0.781700	R	R
167	23285	EW	24.4	41.6	62.4	Borrego Springs	2010	0.175090	0.458690	R	R
168	23285	EW	24.4	41.6	62.4	Ocotillo	2010	0.168710	0.477330	R	R
169	23285	EW	24.4	41.6	62.4	Calexico	2010	0.172240	0.567160	R	2.018
170	24236	NS	45.3	15.5	66.1	Whittier	1987	0.832280	0.322260	R	0.052
171	24236	NS	45.3	15.5	66.1	Chinohills	2008	0.799350	0.341550	R	R
172	24236	NS	45.3	15.5	66.1	San Bernardino	2009	0.434890	0.687950	R	R
173	24236	EW	45.3	66.1	15.5	Whittier	1987	0.063994	2.339100	R	0.123
174	24236	EW	45.3	66.1	15.5	Chatsworth	2007	0.098390	1.353900	R	1.179

175	24236	EW	45.3	66.1	15.5	Chinohills	2008	0.129140	1.100100	R	0.905
176	24236	EW	45.3	66.1	15.5	San Bernardino	2009	0.180460	0.579650	R	2.078
177	24643	NS	96.0	33.5	92.3	Northridge	1994	1.849600	0.188000	R	R
178	24643	EW	96.0	92.3	33.5	Northridge	1994	1.407700	0.467100	R	R
179	12493	NS	24.2	25.8	54.9	Borrego Springs	June 2010	0.215060	0.535100	R	R
180	12493	NS	24.2	25.8	54.9	Borrego Springs	July 2010	0.261210	0.436760	R	R
181	12493	NS	24.2	25.8	54.9	Brawley	2012	0.243230	0.400000	R	R
182	12493	NS	24.2	25.8	54.9	Ocotillo	2010	0.222850	0.597760	R	R
183	12493	NS	24.2	25.8	54.9	Calexcio	2010	0.278700	0.400000	R	R
184	12493	NS	24.2	25.8	54.9	Chinohills	2008	0.227050	0.504420	R	R
185	24655	NS	18.0	69.0	82.0	Northridge	1994	0.098190	1.118400	R	0.724
186	24655	NS	18.0	69.0	82.0	Chinohills	2008	0.082608	1.215000	R	R
187	24655	NS	18.0	69.0	82.0	Calexico	2010	0.078879	1.148500	R	R
188	24655	NS	18.0	69.0	82.0	Borrego Springs	2010	0.077895	1.166400	R	R
189	24655	NS	18.0	69.0	82.0	Encino	2014	0.080010	1.201300	R	2.499
190	24655	NS	18.0	69.0	82.0	La Habra	2014	0.080815	1.217600	R	R
191	24655	EW	18.0	82.0	69.0	Northridge	1994	0.031000	2.202000	196	0.590
192	24655	EW	18.0	82.0	69.0	Chinohills	2008	0.033000	2.041000	250	0.440
193	24655	EW	18.0	82.0	69.0	Encino	2014	0.029000	2.121000	291	1.420
194	24655	EW	18.0	82.0	69.0	Lahabra	2014	0.029000	2.212000	284	R
195	68387	NS	20.0	20.0	38.0	South Napa	2014	0.132000	0.149000	120	0.570
196	68387	EW	20.0	38.0	20.0	South Napa	2014	0.216000	0.775700	R	R
197	58483	NS	66.7	23.8	64.0	Elcerrito	2012	0.874350	0.303160	R	R
198	58483	NS	66.7	23.8	64.0	Berkeley	20 Oct. 2011	0.925850	0.267540	R	R
199	58483	NS	66.7	23.8	64.0	Sanleandro	2011	0.853680	0.286530	R	R
200	58483	NS	66.7	23.8	64.0	Morgan Hill	2011	0.843520	0.303500	R	R
201	58483	NS	66.7	23.8	64.0	Alamo	2008	0.913800	0.237720	R	R
202	58483	NS	66.7	23.8	64.0	Piedmont	2007	0.891520	0.306230	R	R
203	58483	NS	66.7	23.8	64.0	Lafayette	2007	0.889700	0.285550	R	R
204	58483	NS	66.7	23.8	64.0	Loma Prieta	1989	1.286500	0.171560	R	R
205	58483	NS	66.7	23.8	64.0	South Napa	2014	0.820070	0.340070	R	R
206	58480	NS	73.3	29.3	21.3	Loma Prieta	1989	0.911830	0.466800	R	R
207	58480	NS	73.3	29.3	21.3	South Napa	2014	0.670200	0.576830	R	R
208	14654	NS	57.3	45.7	30.8	Northridge	1994	0.585900	0.481700	98	R
209	14654	NS	57.3	45.7	30.8	Chinohills	2008	0.571600	0.480100	126	R
210	14654	EW	57.3	30.8	45.7	Northridge	1994	0.931580	0.355070	R	R
211	14654	EW	57.3	30.8	45.7	Chinohills	2008	0.760490	0.476640	R	R
212	14654	EW	57.3	30.8	45.7	Inglewood	2009	0.617260	0.668900	R	R
213	14654	EW	57.3	30.8	45.7	Calexico	2010	0.801040	0.432330	R	R
214	14654	EW	57.3	30.8	45.7	Borrego Springs	2010	0.643060	0.557250	R	R
215	14654	EW	57.3	30.8	45.7	La Habra	2014	0.820970	0.400720	R	R
216	24680	NS	49.0	23.0	43.0	Chinohills	2008	0.587610	0.176880	372	R
217	24680	NS	49.0	23.0	43.0	Borrego Springs	2010	0.559940	0.173690	R	R
218	24680	NS	49.0	23.0	43.0	Encino	2014	0.619030	0.198100	R	R
219	24680	EW	49.0	43.0	23.0	Chinohills	2008	0.493400	0.284900	40	0.159
220	14323	EW	27.7	22.9	30.0	Whittier	1987	0.584960	0.309300	R	R
221	57318	EW	80.0	21.0	46.0	Alum Rock	2007	0.705280	0.274500	R	R
222	57318	EW	80.0	21.0	46.0	Morgan Hill	2011	0.526410	0.473160	R	R
223	57357	EW	50.0	45.0	45.0	Morgan Hill	1984	0.835500	0.381290	R	R
224	57357	EW	50.0	45.0	45.0	Loma Prieta	1989	0.708670	0.568850	R	R
225	57357	EW	50.0	45.0	45.0	Alum Rock	2007	0.591530	0.707190	R	R
226	57357	EW	50.0	45.0	45.0	Milpitas	2010	0.687010	0.430350	R	R
227	57357	EW	50.0	45.0	45.0	Morgan Hill	2011	0.589500	0.561710	R	R
228	58509	NS	55.0	40.0	55.0	South Napa	2014	0.299550	0.252450	R	R
229	58509	EW	55.0	55.0	40.0	South Napa	2014	0.447100	0.052300	R	R
230	24569	NS	75.6	105.0	48.0	Landers	1992	1.096400	0.488200	R	R
231	24569	EW	75.6	48.0	105.0	Landers	1992	1.099500	0.563100	R	R
232	24569	EW	75.6	48.0	105.0	Northridge	1994	1.102500	0.560850	R	R
233	58532	NS	180.0	37.0	55.0	Loma Prieta	1989	1.396700	0.860950	R	R
234	58532	NS	180.0	37.0	55.0	South Napa	2014	1.452500	0.763060	R	R

235	24463	NS	42.0	85.0	110.0	Whittier	1987	0.086482	4.075500	R	R
236	24463	NS	42.0	85.0	110.0	Northridge	1994	0.095949	4.118900	R	R
237	24463	NS	42.0	85.0	110.0	La Habra	2014	0.085610	3.947600	R	R
238	24463	NS	42.0	85.0	110.0	Encino	2014	0.079332	3.938600	R	R
239	24463	NS	42.0	85.0	110.0	Yorbalinda	2012	0.075694	3.930200	R	R
240	24463	EW	42.0	110.0	85.0	Whittier	1987	0.210300	1.533500	R	R
241	24463	EW	42.0	110.0	85.0	Borrego Springs	2010	0.223600	1.325000	R	R
242	24463	EW	42.0	110.0	85.0	Calexico	2010	0.224800	1.389800	R	R
243	24463	EW	42.0	110.0	85.0	Lahabra	2014	0.247900	1.212000	R	R
244	68489	EW	38.0	26.0	24.0	South Napa	2014	0.342160	0.445750	36	R
245	68489	NS	38.0	24.0	26.0	South Napa	2014	0.484780	0.249730	111	R
246	25302	NS	16.2	33.2	42.0	Santa Barbara	1978	0.087300	0.809400	R	R
247	25302	NS	16.2	33.2	42.0	Islavista	2013	0.087200	0.795300	R	R
248	25302	EW	16.2	42.0	33.2	Santa Barbara	1978	0.163600	0.743000	R	R
249	25302	EW	16.2	42.0	33.2	Islavista	2013	0.075900	1.173300	R	R
250	24288	NS	103.0	27.0	37.0	Chinohills	2008	0.542240	1.549900	R	R
251	24288	NS	103.0	27.0	37.0	Inglewood	2009	0.569940	1.318100	R	R
252	24288	NS	103.0	27.0	37.0	Whittier Narrows	2010	0.460980	1.558900	R	R
253	24288	NS	103.0	27.0	37.0	Calexico	2010	0.710160	1.107600	R	R
254	24288	NS	103.0	27.0	37.0	Borrego Springs	2010	0.693030	1.098800	R	R
255	24288	NS	103.0	27.0	37.0	Encino	2014	0.578820	1.297400	R	R
256	24288	NS	103.0	27.0	37.0	La Habra	2014	0.558770	1.397100	R	R
257	58348	EW	12.4	23.4	40.0	Loma Prieta	1989	0.076582	1.284900	R	R
258	58348	EW	12.4	23.4	40.0	Lafayette	2007	0.076582	1.284900	R	3.220
259	58348	EW	12.4	23.4	40.0	Piedmont	2007	0.072445	1.164200	R	3.019
260	58348	EW	12.4	23.4	40.0	Alum Rock	2007	0.069849	1.210100	R	1.061
261	58348	EW	12.4	23.4	40.0	Alamo	2008	0.069263	1.483700	R	0.892
262	58348	EW	12.4	23.4	40.0	Berkeley	20 Oct. 2011	0.074807	1.183800	R	2.241
263	58348	EW	12.4	23.4	40.0	Elcerrito	2012	0.069428	1.123510	R	R
264	58348	EW	12.4	23.4	40.0	South Napa	2014	0.079107	1.277900	R	3.926
265	58348	EW	12.4	23.4	40.0	San Ramon	2015	0.077098	1.097000	R	R
266	58348	EW	12.4	23.4	40.0	Concord	2015	0.077140	1.427400	R	R
267	14311	EW	21.6	22.8	62.0	Whittier	1987	0.116300	0.618600	R	R
268	14311	EW	21.6	22.8	62.0	Chinohills	2008	0.102100	0.652500	R	R
269	58639	EW	34.7	19.8	60.0	Bolinas	1999	0.225040	0.179640	172	1.305
270	58639	EW	34.7	19.8	60.0	Gilroy	2002	0.217940	0.175470	156	1.321
271	58639	EW	34.7	19.8	60.0	Piedmont	2007	0.227710	0.199650	182	R
272	58639	EW	34.7	19.8	60.0	Lafayette	2007	0.218131	0.334350	144	0.922
273	58639	EW	34.7	19.8	60.0	Alum Rock	2007	0.220450	0.198420	181	1.534
274	58639	EW	34.7	19.8	60.0	Elcerrito	2012	0.223320	0.200590	178	1.569
275	58639	EW	34.7	19.8	60.0	South Napa	2014	0.220490	0.207430	154	0.610
276	58639	NS	34.7	60.0	19.8	Bolinas	1999	0.234700	0.668710	R	0.571
277	58639	NS	34.7	60.0	19.8	Gilroy	2002	0.236090	0.633580	R	0.628
278	58639	NS	34.7	60.0	19.8	Piedmont	2007	0.244500	0.644810	R	0.214
279	58639	NS	34.7	60.0	19.8	Lafayette	2007	0.228480	0.650850	R	R
280	58639	NS	34.7	60.0	19.8	Alum Rock	2007	0.242070	0.646250	R	0.161
281	58639	NS	34.7	60.0	19.8	Elcerrito	2012	0.236660	0.636480	R	0.565
282	58639	NS	34.7	60.0	19.8	South Napa	2014	0.235470	0.682320	R	0.491
283	23511	EW	12.3	29.0	35.0	Whittier	1987	0.068497	0.888670	R	R
284	23511	EW	12.3	29.0	35.0	Chinohills	2008	0.095173	0.714250	R	R
285	23511	NS	12.3	35.0	29.0	Whittier	1987	0.061900	0.845400	R	R
286	23511	NS	12.3	35.0	29.0	Chinohills	2008	0.067200	0.851500	R	R
287	23511	NS	12.3	35.0	29.0	San Bernardino	2009	0.064200	0.745100	R	R
288	23511	NS	12.3	35.0	29.0	Whittier Narrows	2010	0.059800	0.887200	R	R
289	23511	NS	12.3	35.0	29.0	Borrego Springs	2010	0.063300	0.831100	R	R
290	23511	NS	12.3	35.0	29.0	Calexico	2010	0.061300	0.814800	R	R
291	23511	NS	12.3	35.0	29.0	Yorbalinda	June 2012	0.062800	0.831100	R	R
292	23511	NS	12.3	35.0	29.0	Yorbalinda	Aug. 2012	0.061200	0.834500	R	R
293	23511	NS	12.3	35.0	29.0	Pomona	2013	0.066300	0.830700	R	R
294	23511	NS	12.3	35.0	29.0	Anza	2013	0.061600	0.803100	R	R

295	14533	EW	81.0	32.0	32.0	Whittier	1987	0.782900	0.989600	R	R
296	14533	EW	81.0	32.0	32.0	Chinohills	2008	0.812300	0.987000	R	R
297	14533	EW	81.0	32.0	32.0	Inglewood	2009	0.750400	1.000600	R	R
298	14533	NS	81.0	32.0	32.0	Whittier	1987	0.778300	0.996500	R	R
299	24652	EW	26.0	29.0	29.0	Northridge	1994	0.385800	0.184100	354	R
300	24652	EW	26.0	29.0	29.0	West Hollywood	2001	0.259200	0.394500	50	R
301	24652	EW	26.0	29.0	29.0	Chinohills	2008	0.340300	0.232500	R	R
302	24652	EW	26.0	29.0	29.0	Inglewood	2009	0.343700	0.205830	52	R
303	24652	NS	26.0	29.0	29.0	Northridge	1994	0.324300	0.269000	72	0.339
304	24652	NS	26.0	29.0	29.0	West Hollywood	2001	0.205200	0.584600	47	R
305	24652	NS	26.0	29.0	29.0	Chinohills	2008	0.309400	0.280400	78	R
306	24652	NS	26.0	29.0	29.0	Inglewood	2009	0.286200	0.306700	73	R
307	24464	NS	54.0	17.4	56.0	Northridge	1994	0.996560	0.526630	R	R
308	24464	NS	54.0	17.4	56.0	Chinohills	2008	0.609050	0.766780	R	R
309	24464	EW	54.0	56.0	17.4	Whittier	1987	0.838000	0.301500	R	R
310	24464	EW	54.0	56.0	17.4	Northridge	1994	0.618200	0.920500	R	R
311	24464	EW	54.0	56.0	17.4	Chinohills	2008	0.458700	0.981300	R	R
312	24464	EW	54.0	56.0	17.4	Calexico	2010	0.476100	0.914100	R	R
313	58337	EW	35.0	21.0	60.0	Morgan Hill	2011	0.184400	0.332370	255	0.603
314	58337	EW	35.0	21.0	60.0	Sanleandro	24 Aug. 2011	0.120370	0.682870	167	0.981
315	58337	EW	35.0	21.0	60.0	Sanleandro	23 Aug. 2011	0.114680	0.696590	204	0.830
316	58337	EW	35.0	21.0	60.0	Berkeley	I 2011	0.163390	0.477520	153	R
317	58337	EW	35.0	21.0	60.0	Berkeley	II 2011	0.135490	0.640120	147	R
318	58337	EW	35.0	21.0	60.0	Berkeley	27 Oct. 2011	0.116090	0.720360	225	R
319	58337	EW	35.0	21.0	60.0	Elcerrito	2012	0.143550	0.523910	185	R
320	58337	NS	35.0	60.0	21.0	Elcerrito	2012	0.042915	2.947000	R	1.907
321	58337	NS	35.0	60.0	21.0	Berkeley	27 Oct. 2011	0.052010	2.332800	R	R
322	58337	NS	35.0	60.0	21.0	Berkeley	II 2011	0.044991	2.820000	R	0.762
323	58337	NS	35.0	60.0	21.0	Berkeley	I 2011	0.044436	2.883500	R	0.678
324	58337	NS	35.0	60.0	21.0	Sanleandro	24 Aug. 2011	0.045374	2.606100	R	1.126
325	58337	NS	35.0	60.0	21.0	Sanleandro	23 Aug. 2011	0.043691	2.884400	R	2.519
326	58337	NS	35.0	60.0	21.0	Morgan Hill	2011	0.041933	2.771200	R	1.196
327	58336	EW	48.8	40.0	40.0	Berkeley	2011	0.345600	0.445000	278	0.428
328	58336	EW	48.8	40.0	40.0	South Napa	2014	0.322900	0.516100	114	R
329	58336	EW	48.8	40.0	40.0	Piedmont	2015	0.202700	0.974600	151	R
330	48733	EW	24.0	56.0	56.0	Gilroy	2002	0.102090	1.590000	R	R
331	48733	EW	24.0	56.0	56.0	Parkfield	2004	0.108620	1.549300	R	R
332	48733	EW	24.0	56.0	56.0	Alum Rock	2007	0.120200	1.526800	R	R
333	12299	EW	16.0	24.0	45.0	Hector Mine	1999	0.048214	3.181200	R	R
334	12299	EW	16.0	24.0	45.0	Palm Springs	1986	0.074328	2.112300	R	0.214
335	12299	EW	16.0	24.0	45.0	Borrego Springs	2010	0.053447	2.853600	R	0.598
336	23481	NS	27.4	28.3	42.7	Landers	1992	0.633290	0.299130	R	R
337	23481	NS	27.4	28.3	42.7	Calexico	2010	0.721940	0.287750	R	R
338	23481	NS	27.4	28.3	42.7	Borrego Springs	2010	0.700760	0.276930	R	R
339	23481	NS	27.4	28.3	42.7	Redlands	2010	0.567700	0.301400	R	R
340	58615	EW	68.7	30.5	68.6	Alum Rock	2007	0.681950	0.485660	109	R
341	58615	EW	68.7	30.5	68.6	Glen Ellen	2006	0.632880	0.546400	205	R
342	58615	EW	68.7	30.5	68.6	Gilroy	2002	0.607730	0.576290	128	R
343	58615	EW	68.7	30.5	68.6	South Napa	2014	0.664750	0.511150	237	R
344	03603	NS	95.0	26.0	58.5	Chinohills	2008	0.918270	0.476890	R	R
345	03603	NS	95.0	26.0	58.5	San Clementels	2004	0.946850	0.467980	R	R
346	03603	NS	95.0	26.0	58.5	Borrego Springs	2010	1.087300	0.387490	R	R
347	03603	NS	95.0	26.0	58.5	Calexico	2010	1.133600	0.368200	R	R
348	03603	EW	95.0	58.5	26.0	Chinohills	2008	1.258100	0.285110	R	R
349	03603	EW	95.0	58.5	26.0	San Clementels	2004	1.161300	0.346080	R	R
350	03603	EW	95.0	58.5	26.0	Borrego Springs	2010	1.324500	0.287690	R	R
351	03603	EW	95.0	58.5	26.0	Calexcio	2010	1.392800	0.255690	R	R
352	24468	NS	38.7	19.2	46.9	La Habra	2014	0.523910	0.442350	R	R
353	24468	NS	38.7	19.2	46.9	Chinohills	2008	0.583840	0.339320	R	R
354	24468	NS	38.7	19.2	46.9	Northridge	1994	0.563620	0.533990	R	R

355	24468	NS	38.7	19.2	46.9	Yorbalinda	2012	0.367500	0.721810	R	R
356	24468	EW	38.7	46.9	19.2	Whittier	1987	0.295400	1.255500	R	R
357	24468	EW	38.7	46.9	19.2	Northridge	1994	0.281500	1.245500	R	R
358	58196	EW	17.0	31.0	79.0	Berkeley	2011	0.028196	1.589600	88	5.026
359	58196	EW	17.0	31.0	79.0	Morgan Hill	2011	0.035090	1.327000	105	2.121
360	58196	EW	17.0	31.0	79.0	Piedmont	2007	0.044912	1.007300	94	2.649
361	58196	EW	17.0	31.0	79.0	Lafayette	2007	0.031119	1.543400	86	R
362	58196	EW	17.0	31.0	79.0	Alamo	2008	0.033245	1.314200	93	R
363	05407	NS	44.0	21.0	23.0	Yorbalinda	2002	0.234000	0.269000	351	R
364	05407	NS	44.0	21.0	23.0	San Simeon	2003	0.208000	0.392000	239	0.320
365	24332	NS	22.1	66.7	73.0	Whittier	1987	0.107800	0.714200	R	0.483
366	24332	NS	22.1	66.7	73.0	Northridge	1994	0.072100	1.971200	R	R
367	24332	NS	22.1	66.7	73.0	Encino	2014	0.063400	1.843900	R	R
368	58396	NS	12.5	38.1	45.7	Berkeley	2011	0.051000	1.511000	R	R
369	58396	NS	12.5	38.1	45.7	South Napa	2014	0.080900	0.895300	R	R
370	58396	NS	12.5	38.1	45.7	Concord	2015	0.047300	1.628400	R	R
371	58396	NS	12.5	38.1	45.7	Piedmont	2015	0.052600	1.590600	R	R
372	58506	EW	14.0	24.0	50.0	Loma Prieta	1989	0.235800	0.469200	151	0.288
373	58506	NS	14.0	50.0	24.0	Loma Prieta	1989	0.045800	3.257000	R	R

IMPLICATIONS OF CALIFORNIA VERTICAL ARRAY DATA FOR MODELING OF NON-ERGODIC SITE RESPONSE

Kioumars Afshari and Jonathan P. Stewart

Department of Civil & Environmental Engineering
University of California, Los Angeles

Abstract

One-dimensional (1D) ground response analyses are often used with an expectation that they provide an unbiased estimation of site effects, and therefore improve upon site response estimates from ergodic models (i.e. site terms in ground motion models, GMMs). We use California vertical array data to (1) investigate the degree to which 1D analysis provides results compatible with observation, thus checking the typical assumption, and (2) quantify epistemic uncertainty in site response estimates from ground response analysis. Objective (1) was discussed in a previous CSMIP conference paper and a brief update is provided here. We present our methodology and preliminary results for quantifying epistemic uncertainty in site response as estimated from 1D analysis. We decompose prediction residuals into between- and within-site components, and take the between-site standard deviation as a quantification of epistemic uncertainty. Preliminary results suggest values ranging from 0.35-0.5 in natural log units.

Introduction

One-dimensional (1D) ground response analysis (GRA) uses the simulation of shear waves traveling vertically through shallow geological structures to predict the effects of site response on ground motion. The simulations are based on the layering and parameters specific to the site of interest (e.g. shear-wave velocity, modulus reduction, and damping parameters), and this method is being frequently used for predicting the effects of site response for critical projects. For simulating the behavior of the soil in 1D GRA, several approaches are available including linear, equivalent-linear (EL), and nonlinear (NL) methods, the relative benefits of which are discussed elsewhere (Kaklamanos et al, 2013, 2015; Kim et al., 2016; Zalachoris and Rathje, 2015).

When GRA are performed for engineering projects, it is usually with the expectation that they provide an unbiased, site-specific estimate of site response. The site response computed in this manner can be interpreted in the form of a site-specific amplification function, which in turn can be implemented in probabilistic seismic hazard analyses (PSHA) (e.g., McGuire et al., 2001; Stewart et al. 2014). If the ground response computed in this manner accurately reflects the primary physical mechanisms controlling site response, it provides the basis for a non-ergodic hazard analysis, which has appreciable benefits with regard to standard deviation and hazard reduction (e.g., Stewart, 2016).

The essential question in this process is whether GRA are indeed effective at predicting site response. While numerous studies of data from vertical arrays at individual sites have found

reasonably good fits to GRA results (e.g., Borja et al., 1999; Elgamal et al., 2001; Lee et al., 2006; Tsai and Hashash, 2009; Yee et al., 2013; Kaklamanos et al. 2015), another study that systematically examined a broad set of such arrays in Japan (KiK-net array; Aoi et al., 2000) found misfits for about 80% of the investigated sites (Thompson et al. 2012). California vertical array data provides an opportunity to further examine this issue for local geological conditions, which differ from those at KiK-net sites (Boore et al. 2011).

Preliminary results from the California vertical array sites were presented by Afshari and Stewart (2015). Those results indicated that the observed site response was reasonably well matched by GRA at some sites (less than 50%). Some additional sites have been investigated since that time as discussed in the next section below, although the basic conclusion has not appreciably changed.

In this paper, we seek to quantify uncertainty in the prediction of site response as estimated from GRA. This is of interest for PSHA in which site terms are taken from the results of GRA, in which case epistemic uncertainties in the site response should be considered using a logic tree (or similar) framework (Bommer et al. 2005). We present a methodology for quantifying these uncertainties, present results as derived from the California data, and compare to comparable results obtained previously for KiK-net sites (Kaklamanos et al., 2013).

Validation of 1D GRA Using California Vertical Array Sites

This paper is an extension of a previous study (Afshari and Stewart, 2015) on the effectiveness of 1D GRA at predicting site response in vertical arrays in California. In the previous study, we described how we used 228 surface/downhole recordings from 10 vertical array sites to compute empirical transfer functions (ETFs), and used linear 1D GRA using the program Deepsoil (Hashash et al., 2016) to compute theoretical transfer functions (TTFs). Thompson et al. (2012) used the Pearson's sample correlation coefficient (r) between ETF and TTF to represent the goodness of fit between the predictions and the observed site response; a value of r=0.6 was taken by Thompson et al. (2012) as the threshold for good fit. We used the same approach to quantify the goodness of fit of transfer functions, which facilitates comparisons between the two regions.

We have also studied alternative damping models for estimating material damping in linear GRA: (1) laboratory-based models (Darendeli, 2001 for clayey soils and Menq, 2003 for granular soils); (2) adjustments to the damping from (1) so that diminutive parameter κ_0 for the soil profile matches target values (Van Houtte et al. 2011); and (3) estimating damping from quality factor (Q_{ef}) as provided by Campbell (2009). Details of each approach are given by Afshari and Stewart (2015). Application in GRA showed under-prediction of damping from (1), over-prediction from (2), and a relatively unbiased prediction from (3).

Figure 1 shows example results for two sites. The Eureka site shows a case in which site response, expressed in the form of smoothed transfer functions, is reasonably well predicted by GRA. The San Bernardino site is an example of poor fit. Of the 12 sites examined to date, qualitatively 4 (33%) can be considered as having a reasonably good fit, as established from fitting criteria described in Thompson et al. (2012) and Afshari and Stewart (2015).

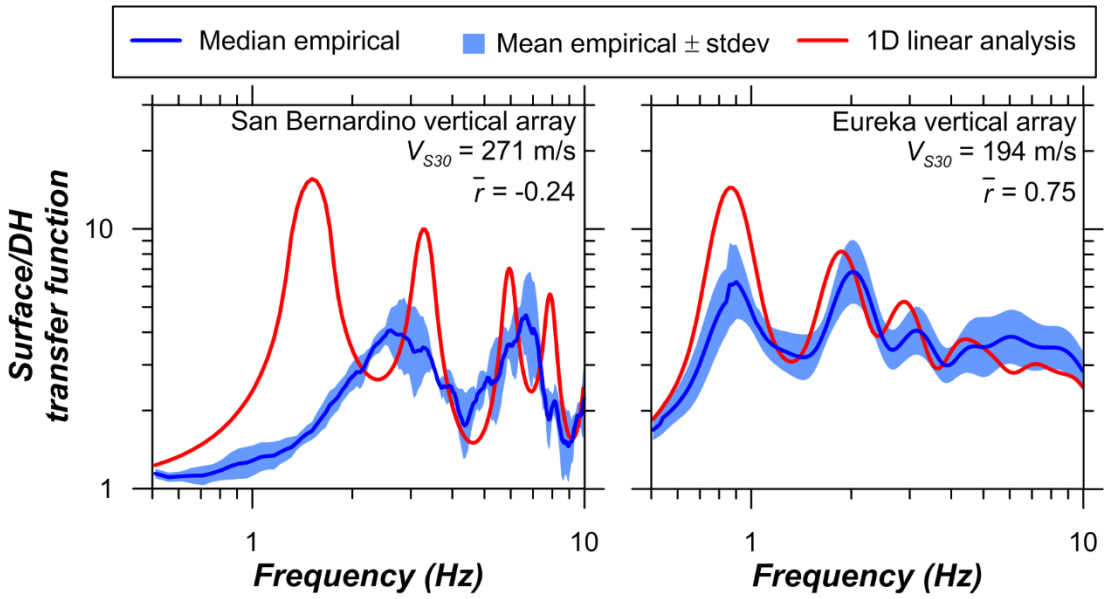

Figure 1. Surface to downhole transfer functions as observed from vertical array data and inferred from 1D analysis for the San Bernardino (poor fit) and Eureka (good fit) sites.

Quantifying Epistemic Uncertainty of GRA Predictions

Our analysis of epistemic uncertainty is based on comparing observations (in this case, the surface recordings at California vertical array sites) to predictions. The sites considered in this study are summarized in Table 1, which is expanded from the data inventory considered in Afshari and Stewart (2015) by two sites. The location of the 12 sites are shown in Figure 2.

Table 1. Summary of site characteristics for California vertical arrays considered in present study.

Station NO	Station Name	Owner	# Rec	Latitude	Longitude	V_{S30} (m/s)	V_S profile Depth (m) [2]	Depth of deepest instrument (m)	Site Period (sec)
68323	Benicia – Martinez Br S Geotech Array	CGS - CSMIP	10	38.033	-122.117	546	31	35	0.22
68206	Crockett – Carquinez Br Geotech Array #1	CGS - CSMIP	8	38.054	-122.225	345	43	45.7	0.34
1794	El Centro – Meloland Geotechnical Array	CGS - CSMIP	19	32.774	-115.449	182	240	195	1.41
89734	Eureka – Geotechnical Array	CGS - CSMIP	14	40.819	-124.166	194	225	136	1.15
24703	Los Angeles – La Cienega Geotech Array	CGS - CSMIP	20	34.036	-118.378	241	280	100	0.87

Station NO	Station Name	Owner	# Rec	Latitude	Longitude	V_{S30} (m/s)	V_S profile Depth (m) [2]	Depth of deepest instrument (m)	Site Period (sec)
24400	Los Angeles – Obregon Park	CGS - CSMIP	23	34.037	-118.178	449	64	69.5	0.54
23792	San Bernardino - I10/215 W Geotech Array	CGS - CSMIP	5	34.064	-117.298	271	92	35	0.64
68310	Vallejo – Hwy 37/Napa River E Geo. Array	CGS - CSMIP	17	38.122	-122.275	509	42	44.5	0.24
UCSB Arrays	Garner Valley Downhole Array	UCSB	10	33.401	-116.403	240	210	150	0.64
UCSB Arrays	Wildlife Liquefaction Array	UCSB	45	33.058	-115.318	203	98	100	1.41
UCSB Arrays	Borrego Valley Field Site	UCSB	21	33.259	-116.321	350	230	238	1.30
UCSB Arrays	Hollister Digital Array	UCSB	23	36.453	-121.365	359	185	192	0.85

Figure 2. The location of vertical array sites in California used in this study on Google Earth.

As used here, *observations* are 5%-damped pseudo spectral accelerations (PSAs) of the horizontal recorded surface ground motions, rotated to the median single-component value across all non-redundant azimuths (Boore 2010). The observed value for event *i*, recording *j*, and site *k* is denoted Y_{jk} (we do not retain the event subscript).

Predictions are based on single-component 1D GRA for each horizontal component. The procedures followed for these analyses are as described in Afshari and Stewart (2015); for the present calculations we use the Campbell (2009) damping model (Model 1). The GRA are performed independently for the two components, and the resulting ground surface time series are analyzed to develop RotD50 spectra. The resulting PSAs are denoted P_{jk}.

We compute total residuals between the observed and predicted PSAs as follows:

$$R_{jk} = \ln\left(Y_{jk}\right) - \ln\left(P_{jk}\right) \tag{1}$$

Figure 3 shows an example of observed and predicted spectra and residuals for the Eureka Geotechnical Array site (2010 event with **M** 6.5, R_{epi}=48 km). The elastic period of the soil column from the base instrument to the surface is T_0=1.15 sec. For reasons that will be explained further below, it is important to note the lack of site effect for $T > \sim 2T_0$. In this period range, surface and downhole spectra are nearly identical as a result of quarter wavelengths that significantly exceed the profile dimension. The analysis provides a good estimate of observed ground motions for this site.

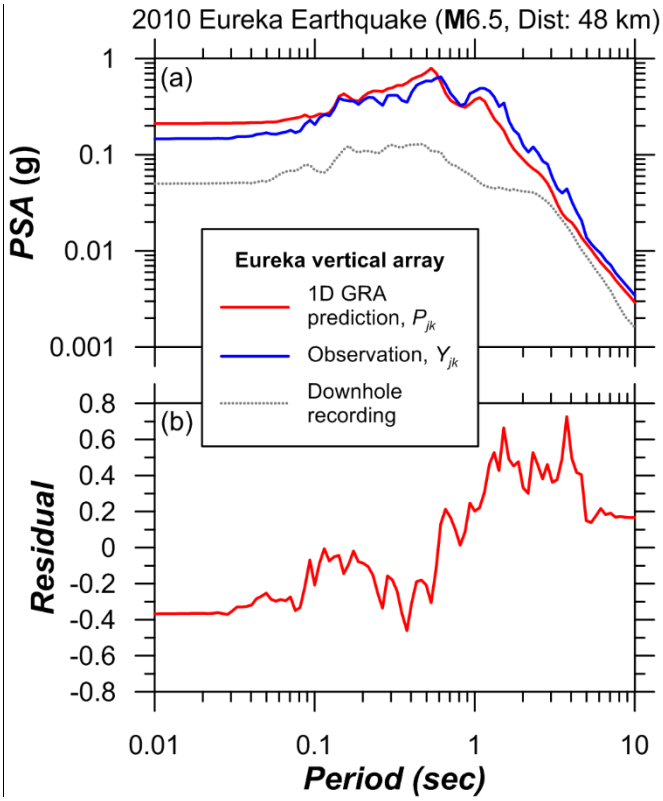

Figure 3. An example of (a) response spectrum plots of the downhole motion, surface recorded motion, and surface predicted motion at Eureka (**M**6.5 epicentral distance: 48 km); (b) The plot of residuals between observed and predicted ground motions.

We perform mixed-effects regression with the LME routine in program R (Pinheiro et al., 2013) to partition the residuals into multiple components:

$$R_{jk} = c_l + \eta_{S,k} + \varepsilon_{jk} \tag{2}$$

where c_l is the overall model bias; $\eta_{S,k}$ is the between-site residual (site term) for site k, which represents the average bias-adjusted deviation of data from the prediction for an individual site; and ε_{jk} is the within-site residual. The residual partitioning does not include an event term, as is typical in most ground motion studies. This is the case because input motions are known from the downhole recording, and those motions would implicitly include the event term.

The overall bias (c_l) is plotted in Figure 4. The relative flat trend and small values of c_l are an indicator that the linear 1D GRA models with damping estimated from Campbell (2009) (Model 1) are providing a relatively unbiased estimate of site response. This is consistent with our previous findings using 10 of the 12 sites from Table 1 (Afshari and Stewart 2015).

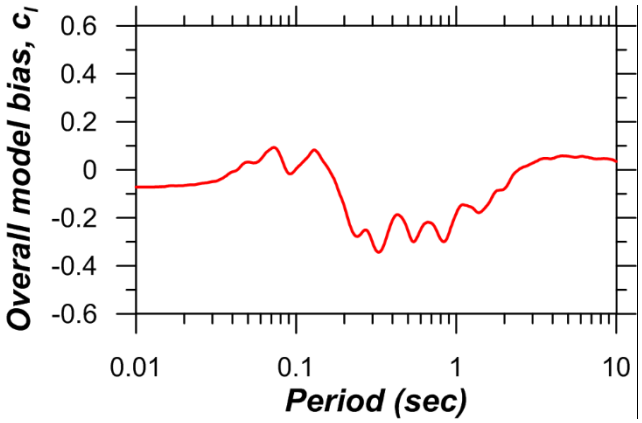

Figure 4. The overall bias (c_l) of GRA model for California vertical array sites in Table 1.

The term $\eta_{S,k}$ indicates misfit of GRA predictions for site k, with large absolute values of η_S indicating poor predictions of site response. Figure 5 shows two examples of η_S-T trends for good- and poor-fit sites (Eureka and San Bernardino, respectively).

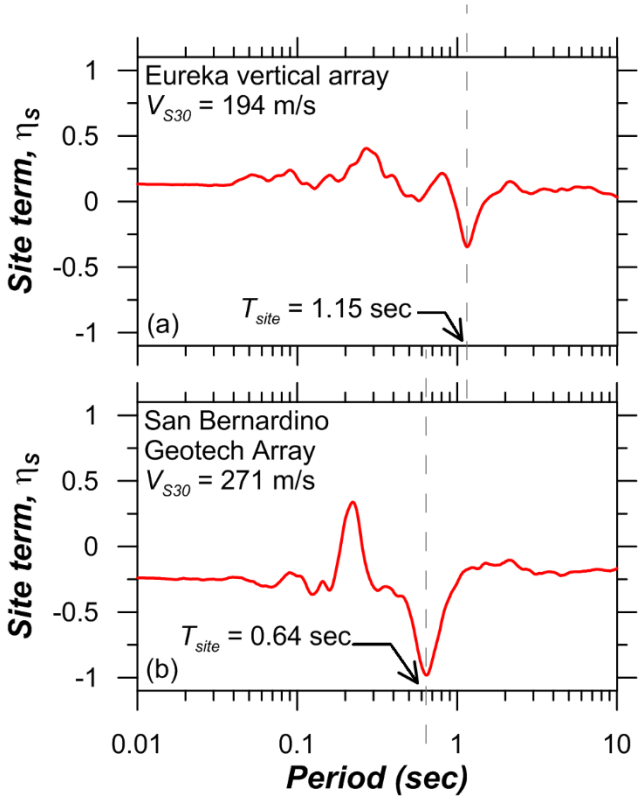

Figure 5. Plots of between-site residuals (η_S) for good-fit and poor-fit sites (Eureka and San Bernardino, respectively). Smaller values of η_S indicate better fit of model to observation.

Standard deviations of the partitioned residuals terms can be combined as follows:

$$\sigma_Y^2 = \tau_S^2 + \phi_{\ln Y}^2 \tag{3}$$

where σ_Y, τ_S, and ϕ_{lnY} are the standard deviations of R_{jk}, $\eta_{S,k}$, and ε_{jk}, respectively. We consider the epistemic uncertainty in GRA predictions to be quantified by τ_S, which represents site-to-site variability. In other words, the epistemic uncertainty regarding how well GRA is able to predict the effects of site response is quantified by τ_S. Term ϕ_{lnY} represents within-site variability in site amplification, which has been shown in prior work to be stable from ground motion array studies from active crustal regions world-wide (Kaklamanos et al. 2013, Rodriguez-Marek et al. 2011, and Lin et al. 2011).

Figure 6 shows our results for τ_S and ϕ_{lnY} along with a prior result based on KiK-net data by Kaklamanos et al. (2013). Also shown in the τ_S plot is the range of site periods among the considered California vertical array sites (0.22-1.41 sec, mean of 0.8 sec). Within the limits of the relatively small data set considered here, we postulate that the values of τ_S for $T < \sim 1.0$ sec comprise a reasonable, first-order estimate of epistemic uncertainty in site response as computed by GRA. Note that these numbers reflect site-response uncertainties only, because they are based on a condition in which input motions are known. Total epistemic uncertainties would be larger,

as a result of uncertainties in input motions. We do not consider the τ_S results for $T > \sim 1.0$ sec to provide a valid representation of epistemic uncertainties, because most of the sites are beyond their site period in this range. At these long periods, the site response is controlled by features beyond the domain of the vertical arrays, which are reflected in both the downhole and surface recordings and accounts for the low values of τ_S in this range. As described by Stewart (2016), site response for these long periods should generally be taken from ergodic models, and the corresponding epistemic uncertainties are discussed elsewhere (e.g., Atkinson et al. 2014).

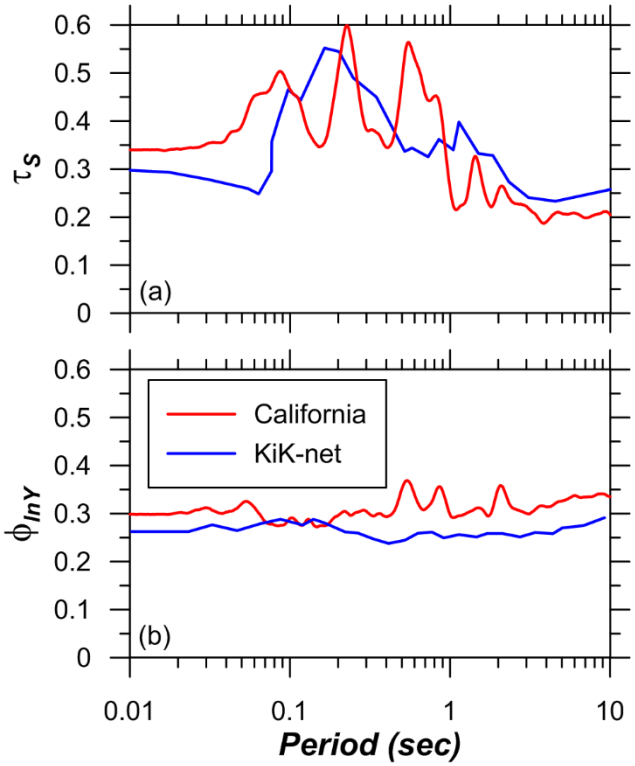

Figure 6. Plots of between-site standard deviation (τ_S) and within-site standard deviation (ϕ_{lnY}) for the sites considered in this study in California and KiK-net sites studied by Kaklamanos et al. (2013).

The results from the present study are similar to the prior results of Kaklamanos et al. (2013) for KiK-net sites. This result is expected for ϕ_{lnY}, but is somewhat surprising for τ_S. We expected larger values of τ_S for KiK-net sites because of the generally lower resolution of shear-wave velocity profiles and other geotechnical data.

Conclusions

California vertical array data indicate a mixed ability for 1D ground response analysis to match observed levels of site amplification. To some extent, this mirrors findings elsewhere from

Japan (Thompson et al, 2012), although the percentage of sites for which site response is reasonably well matched is higher (33% in California, vs. 18% in Japan).

We describe a procedure based on partitioning of prediction residuals to quantify epistemic uncertainties in site response as estimated from 1D GRA. This is an important consideration when PSHA is to be performed using site-specific (non-ergodic) site terms as derived from GRA – for such cases epistemic uncertainties in site response should be considered as part of the logic tree. We find site-to-site variability that ranges from 0.35-0.5 for the period range for which GRA results are valid (up to approximately 1.0 sec for the California sites considered here). At longer period, these uncertainties revert to typical uncertainties for alternate GMMs, which are also appreciable.

Acknowledgments

Funding for this study is provided by California Strong Motion Instrumentation Program, California Geological Survey, Agreement No. 1014-961. This support is gratefully acknowledged. We also thank Tadahiro Kishida for providing access to data processing codes, and Hamid Haddadi for providing geotechnical logs and weak motion records from the Center for Engineering Strong Motion Data FTP folders. We gratefully acknowledge Jamison Steidl of UCSB for facilitating access to the UCSB vertical array site data.

References

Afshari, K. and Stewart, J.P (2015). Effectiveness of 1D ground response analyses at predicting site response at California vertical array sites, *Proc. SMIP2015 Seminar on Utilization of Strong Motion Data*, California Strong Motion Instrumentation Program, Sacramento, CA

Aoi, S. ,Obara, K., Hori, S., Kasahara, K., Okada, Y. (2000). New Japanese uphole–downhole strong-motion observation network: KiK-Net, Seismological Research Letters *Seism. Res. Lett.* 72, 239.

Atkinson GM, Bommer J.J., Abrahamson, N.A. (2014). Alternative approaches to modeling epistemic uncertainty in ground motions in probabilistic seismic- hazard analysis. *Seism. Res. Lett.*, 85, 1141-1144.

Bommer, J.J., Scherbaum, F., Bungum, H., Cotton, F., Sabetta, F., and Abrahamson, N.A. (2005). On the use of logic trees for ground-motion prediction equations in seismic-hazard analysis, *Bull. Seismol. Soc. Am*. 95, 377-389.

Boore, D.M. (2010). Orientation-independent, non geometric-mean measures of seismic intensity from two horizontal components of motion, *Bull. Seism. Soc. Am.* 100, 1830-1835.

Boore, D.M., Thompson, E.M, and Cadet, H. (2011). Regional correlations of V_{S30} and velocities averaged over depths less than and greater than 30 m, *Bull. Seism. Soc. Am*. 101, 3046-3059.

Borja, R.I., Chao, H.-Y., Montans, F.J., and Lin, C.-H. (1999). Nonlinear ground response at Lotung LSST site, *J. Geotech. Geoenviron. Eng.* 125, 187–197.

Campbell, K.W. (2009). Estimates of shear-wave Q and κ_0 for unconsolidated and semiconsolidated sediments in Eastern North America, *Bull. Seismol. Soc. Am*. 99, 2365-2392.

Darendeli, M.B. (2001). Development of a New Family of Normalized modulus reduction and material damping curves, PhD Thesis, Department of Civil Engineering, University of Texas, Austin, TX.

Elgamal, A., Lai, T., Yang, Z., He, L. (2001). Dynamic soil properties, seismic downhole arrays and applications in practice, *Proceedings, 4th International Conference on Recent Advances in Geotechnical Earthquake Engineering and Soil Dynamics*, S. Prakash, ed., San Diego, CA.

Hashash, Y.M.A., Musgrove, M.I., Harmon, J.A., Groholski, D.R., Phillips, C.A., and Park, D. (2016). DEEPSOIL 6.1, User Manual.

Kaklamanos, J., Bradley, B.A., Thompson, E.M., and Baise, L.G. (2013). Critical parameters affecting bias and variability in site-response analyses using KiK-net downhole array data, *Bull. Seismol. Soc. Am*. 103, 1733–1749.

Kaklamanos, J., Baise, L.G., Thompson, E.M., Dorfmann, L. (2015). Comparison of 1D linear, equivalent-linear, and nonlinear site response models at six KiK-net validation sites, *Soil Dyn. Earthq. Eng.* 69, 207-215.

Kim, B., and Hashash, Y.M.A. (2013). Site response analysis using downhole array recordings during the March 2011 Tohoku-Oki Earthquake and the effect of long-duration ground motions." *Earthquake Spectra* 29, S37–S54.

Kim, B., Hashash, Y.M.A., Stewart, J.P., Rathje, E.M., Harmon, J.A., Musgrove, M.I., Campbell, K.W, and Silva, W.J. (2016). Relative differences between nonlinear and equivalent-linear 1D site response analyses, *Earthquake Spectra* 32, 1845–1865.

Lee, C.-P., Tsai, Y.-B., and Wen, K.L. (2006). Analysis of nonlinear site response using the LSST downhole accelerometer array data, *Soil Dyn. Eqk. Eng.* 26, 435–460.

Lin P.-S., Chiou, B. S.-J, Abrahamson, N.A., Walling, M., Lee, C.-T., and Cheng, C.-T. (2011). Repeatable source, site, and path effects on the standard deviation for ground-motion prediction, *Bull. Seismol. Soc. Am*. 101, 2281–2295.

McGuire, R.K., Silva, W.J., and Costantino, C.J. (2001). Technical basis for revision of regulatory guidance on design ground motions: Hazard-and risk-consistent ground motion spectra guidelines. *NUREG/CR-6728*, United States NRC.

Menq, F.Y. (2003). Dynamic Properties of Sandy and Gravelly Soils, PhD Thesis, Department of Civil Engineering, University of Texas, Austin, TX.

Pinheiro, H., Bates, D., DebRoy, S., Sarkar, D., and the R Development Core Team (2013). NLME: Linear and Nonlinear Mixed Effects Models, R package version 3.1-108.

Rodriguez-Marek, A., Montalva, G.A., Cotton, F., and Bonilla, F. (2011). Analysis of single-station standard deviation using the KiK-net data, *Bull. Seismol. Soc. Am.* 101, 1242–1258.

Stewart, J.P., Afshari, K., and Hashash, Y.M.A. (2014). Guidelines for performing hazard-consistent one-dimensional ground response analysis for ground motion prediction, *PEER Report No. 2014/16*, Pacific Earthquake Engineering Research Center, UC Berkeley, CA.

Stewart, J.P. (2016). Joyner Lecture: Site response uncertainty and its implications for seismic risk characterization, EERI 2016 Annual Meeting, San Francisco, CA; SSA 2016 Annual Meeting, Reno, NV, *Seismological Research Letters*, 87:2B, pp 516 (abstract).

Thompson, E.M., Baise, L.G., Tanaka, Y., and Kayen, R.E. (2012). A taxonomy of site response complexity, *Soil Dyn. Earthq. Eng.*, 41, 32–43.

Tsai, C.C. and Hashash, Y.M.A. (2009). Learning of dynamic soil behavior from downhole arrays, *J. Geotech. Geoenv. Eng.*, 135, 745–757.

Van Houtte, C., Drouet, S., Cotton, F. (2011). Analysis of the origins of κ (kappa) to compute hard rock to rock adjustment factors for GMPEs, *Bull. Seismol. Soc. Am.* 101, 2926-2941.

Yee, E., Stewart, J.P., and Tokimatsu, K. (2013). Elastic and large-strain nonlinear seismic site response from analysis of vertical array recordings, *J. Geotech. Geoenv. Eng.* 139, 1789–1801.

Zalachoris, G., and Rathje E.M. (2015). Evaluation of one-dimensional site response techniques using borehole arrays, *J. Geotech. Geoenviron. Eng.*, 10.1061/(ASCE)GT.1943-5606.0001366, 04015053.

IDENTIFICATION OF SPATIAL VARIABILITY IN BRIDGE FOUNDATION INPUT MOTIONS: THEORETICAL BASIS

E. Taciroglu and S.F. Ghahari

Department of Civil & Environmental Engineering
University of California, Los Angeles

Abstract

This paper presents progress made towards the identification of spatial variability in bridge Foundation Input Motions (FIMs) in a project funded by the California Geological Survey. The term spatial variability denotes here the differences in amplitude and phase of seismic motions recorded over extended areas, and it is well accepted that lifeline structures, such as long bridges, are prone to its effects, because they extend over relatively long distances. The specific objective of the project is to identify FIMs from response signals recorded by instrumented bridges during the South Napa 2014 earthquake, decompose them to bedrock motions and site effects, and finally quantify the spatial variability for each bridge structure. In this progress paper, we present initial observations, data selection, and the theoretical basis of the methodology that will be employed to process the recorded data. The overall methodology comprises two novel approaches (*i*) for output-only identification of bridges under multiple support excitations, and (*ii*) for blind identification of bedrock motions and site effects from two (or more) ground-surface motions (FIMs). The said two methods are briefly described and numerically verified in the present paper. The first method will be employed to extract FIMs from spatially sparse measurements of bridge responses, while the second one will be used to further identify the site effects and bedrock motions from the recovered FIMs.

Introduction

Today, highly detailed and accurate Finite Element (FE) models of bridges are created routinely, using broadly available commercial software. However, accurate seismic response predictions for bridges are still constrained by our ability to apply physically accurate/consistent input motions. Long-span bridges are known to be prone to the so-called "*spatially variability*" effects, which is a term used for collectively denoting the differences in amplitude and phase of seismic motions recorded over extended areas (Zerva & Zervas, 2002), due to their longitudinal extents (Zerva, et al., 1988; Hao, et al., 1989; Nazmy & Abdel-Ghaffar, 1992; Lupoi, et al., 2005; Burdette, et al., 2008).

In current practice, California Department of Transportation (Caltrans), for example, takes spatial variability into account by synthetically producing ground motions at each pier of the bridge using one-dimensional site-response analyses. That is, the seismic motion estimated on the bedrock—which is typically a "de-convoluted" version of the Free-Field Motion (FFM)—is transferred to the surface at each pier using specific soil properties at each pier's site. In the presence of kinematic soil-structure interaction effects[1], these Free-Field Motions (FFMs) must

[1] Kinematic interaction is caused by the stiffness contrast of the foundation system from its surrounding soil media.

also be converted to the so-called Foundation Input Motions (FIMs) (see **Figure 1**). Therefore, while ground motions at the bedrock of the bridge site may be uniform, a long bridge may still experience differing excitations at different piers. While, several other factors—such as local soil nonlinearity and path effects—may be involved in spatial variability, the approach currently used by Caltrans only attempts to take the *site effects* into account. Even in this particular issue, the procedure employed has numerous shortcomings. To wit, the procedure assumes vertically propagating horizontally polarized waves, which is not necessarily true. Also, the deconvolution procedure may introduce numerical errors (including unrealistically large motions at the bedrock). Furthermore, conversion of FFMs into FIMs may introduce significant errors—especially when local nonlinearities and other spatial variability effects are present—, and at the present time, there is no validated procedure to carry out this task.

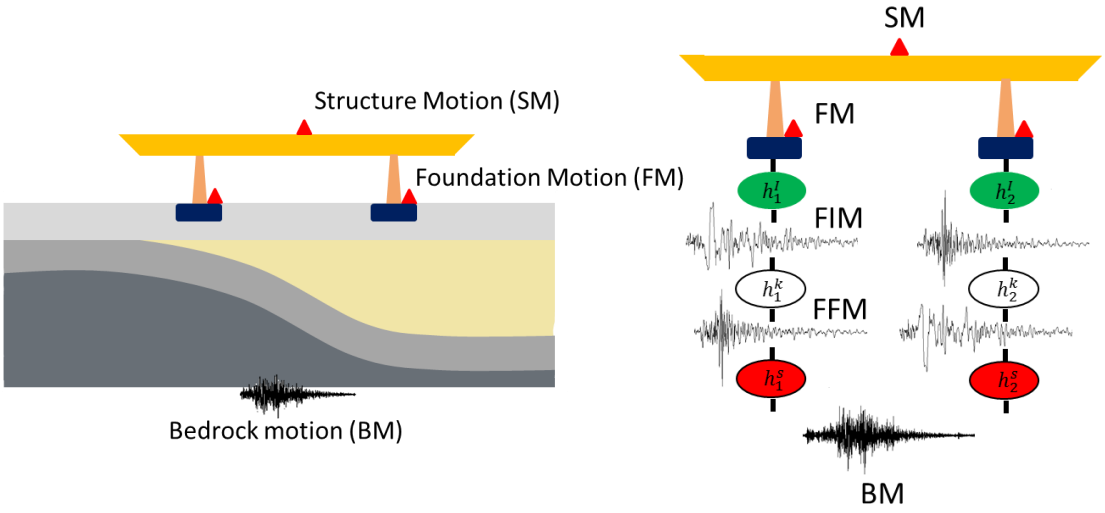

Figure 1. Current approach to bridge analysis under multiple support excitations.

Given these difficulties, the back-calculation of FIMs from real-life data is a key capability to study spatial variability effects and to validate (or to refute) new or existing procedures that predict the foundation input motions. Under the general umbrella of seismic monitoring, a specific motivation for instrumenting long-span bridges in California was indeed to provide a quantitative basis for evaluating how these structures respond to spatially varying ground motions (Kurata, et al., 2012). Simple comparisons of pier to pier motions recorded at the foundation level will not illuminate the subject matter, as these records are polluted by kinematic and inertial interaction effects, and therefore, will only provide a limited understanding/quantification of spatial variability of seismic input motions for bridges. In the current project—the first-half progress of which is presented in this paper—a novel approach is devised to:

(1) back-calculate FIMs from sparsely measured acceleration signals recorded during the 2014 South Napa earthquake at several CSMIP-instrumented bridges;

(2) back-calculate bedrock motions and site effects at each pier (under specific conditions).

To carry out the first step, we adopt a time-domain output-only identification method originally developed by Huang et al. (Huang, et al., 2010) for our problem. To achieve the

second goal, we devise a novel blind identification method (Ghahari, et al., 2016) through which the bedrock motions and site effects can be back-calculated using FIMs identified in the first step.

In what follows, we first present a review of available bridge data from the South Napa event, identify those recorded motions that exhibit evidence of the presence of spatial variability, and select the data sets suitable for the current study. We then provide the details of both of the identification methods mentioned above, as well as their verification through synthetic data sets.

Available Data

As mentioned above, this project will use data recorded during the 2014 South Napa earthquake. This M_w-6.0 earthquake occurred on August 24, 2014 near the well-known West Napa Fault. The epicenter was at 38.216N and 122.312W—i.e., approximately 9 km SSW of Napa, California and 82 km WSW of Sacramento, California. It was the most significant event in Northern California since the M6.9 Loma Prieta earthquake of 1989 (Shakal, et al., 2014).

17 of the 80+ instrumented bridges recorded the South Napa earthquake, which are listed in **Table 1**. The locations of these bridges and the earthquake's epicenter are displayed on **Figure 2**. The table also provides the approximate lengths of the 17 bridges, 11 of which are at least 1km-long. This means that they are ideal candidates for studying and quantifying the effects of spatially variability. Incidentally, the Peak Structural Accelerations (PSAs) recorded on most of these bridges during the 2014 South Napa earthquake are significant, which provides an opportunity to work with favorable Signal-To-Noise (SNR) ratios. Moreover, more than half of the 17 bridges have a nearby ground motion station that recorded Free-Field Motions (FFMs). Data from these stations will enable the calculation of Transfer Functions between the FFMs and FIMs.

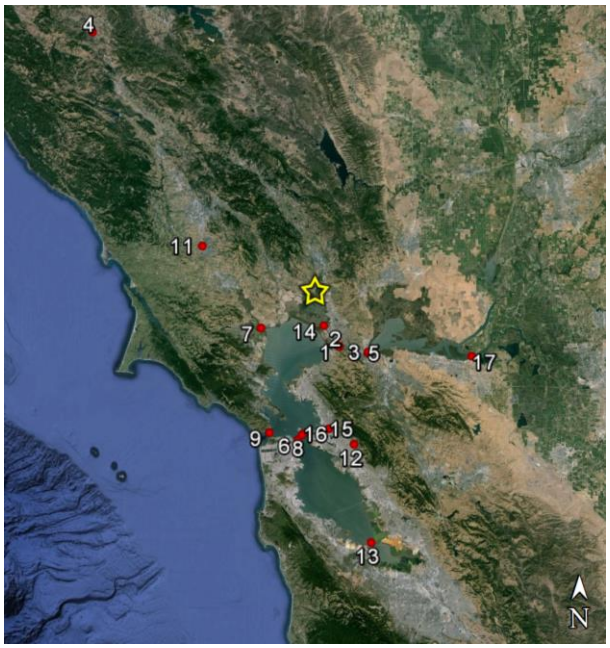

Figure 2. Geographic distribution of the 17 instrumented bridges around the epicenter of the 2014 South Napa Earthquake.

Table 1. List of all bridges that recorded the 2014 South Napa Earthquake.

No.	Name	Station No.	Length (m)	Epic. Dist. (km)	Fault Dist. (km)	PGA (*g*)	PSA (*g*)
1	Vallejo - Carquinez/I80 East Bridge	68184	1021	18.9	19.4	0.149	1.085
2	Vallejo - Carquinez/I80 West Bridge	68185	1056	18.9	19.3	0.085	0.790
3	Benicia - Martinez/I680 East Bridge	68322	2265	25.5	25.7	0.063	0.122
4	Hopland - Hwy 101/Railroad Bridge	69760	94.5	107.0	98.2	0.062	0.017
5	Benicia - Martinez/I680 West Bridge	68682	1894	25.7	25.9	0.031	0.343
6	San Francisco - Bay Bridge/West	58632	3137	46.6	47.2	0.031	0.146
7	Novato -Hwy37 /Petaluma River Bridge	68778	665	19.7	20.6	0.024	0.062
8	Oakland - SF Bay Bridge/East: YBITS	58602	NA	44.8	45.5	0.024	0.047
9	San Francisco - Golden Gate Bridge	58700	2789	46.1	46.8	0.012	0.181
10	Oakland - SF Bay Bridge/East: Skyway	58601	2085	43.9	44.5	0.002	0.054
11	Rohnert Park - Hwy 101 Bridge	68717	86	37.6	33.6	NA	0.119
12	Oakland - Hwy 580/13 Interchange Bridge	58656	86	49.4	49.9	NA	0.027
13	San Francisco Bay - Dumbarton Bridge	58596	2620	80.7	81.2	NA	0.055
14	Vallejo - Hwy 37/Napa River Bridge	68065	1000	11.1	11.6	NA	0.657
15	Oakland - Hwy 580/24 Interchange Bridge	58657	1000	43.1	43.7	NA	0.092
16	Oakland - SF Bay Bridge/East: SAS	58600	NA	44.5	45.2	NA	0.162
17	Antioch - San Joaquin River Bridge	67771	2874	53.9	--	NA	0.092

Initial Observation

Since the FIMs are not directly available due to reasons mentioned earlier, and need to be back-calculated, we study here the spatial variability of input motions by using only the recorded signals on foundations and on the ground surface as a preliminary investigation. To this end, we calculate the cross-covariance among different locations for each bridge. We use the cross-correlation technique in the time-domain to quantify the similarity between two delayed accelerograms (Bendat & Piersol, 1980). This common signal processing technique is frequently used in a variety of engineering applications. The cross-covariance function is the correlation between series (acceleration records) shifted against one another as a function of delay or lag. The function exhibits distinct peaks at the lag value that corresponds to the precise time-delay between two otherwise similar accelerograms. The expression for the cross-covariance function for two discrete-time $s_i[n]$ and $s_j[n]$ accelerograms at lag k is calculated as

$$c_{ij}[k] = \frac{1}{N}\sum_{n=0}^{N-k}(s_i[n] - \bar{s}_i)\ (s_j[n+k] - \bar{s}_j) \qquad 1)$$

where $k = 0, 1, \cdots, N-1$, and N is number of time samples. Here, $\bar{s}_i$ and $\bar{s}_j$ indicate the mean values of the two signals. It is also possible to calculate $c_{ij}[k]$ for negative lags, which are easily obtained by changing the i and j sub-indices at the summation above. $c_{ij}[k]$ are usually normalized with the square-root of $c_{ii}[0]$ and $c_{jj}[0]$ to keep the value of covariance between −1 and +1. This normalized value is termed the *cross-correlation*. A cross-correlation equal to −1 or +1 denotes two signals that are identical except with a time lag, whereas a cross-correlation close to zero means that that they are not similar.

As an example, we present results of correlation analysis for one of the bridges listed in **Table 1** (similar results were observed for other bridges and are omitted here for the sake of brevity). **Figure 3** displays the instrumentation layout for CSMIP station No. 68184. The sensors that are marked with circles on this figure indicate those for which we calculated the cross-correlation values. Maximum values of cross-correlations are also shown in **Figure 3** for both longitudinal and transverse directions. As seen, except for those sensors that are very close to each other, the cross-correlation values are very small. This is more significant for the transverse direction. In the longitudinal direction—for example channels 5 and 47—, the higher values of cross-correlation are actually related to the system's response, but not the ground motions.

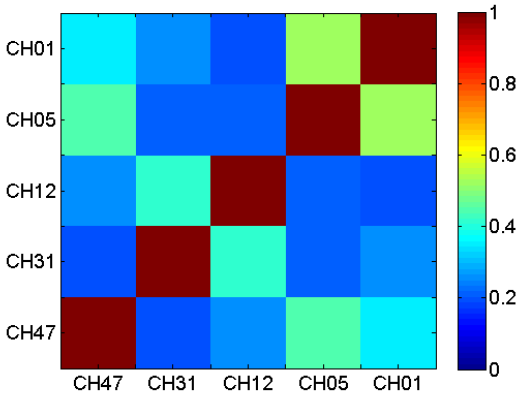

(a) Longitudinal direction

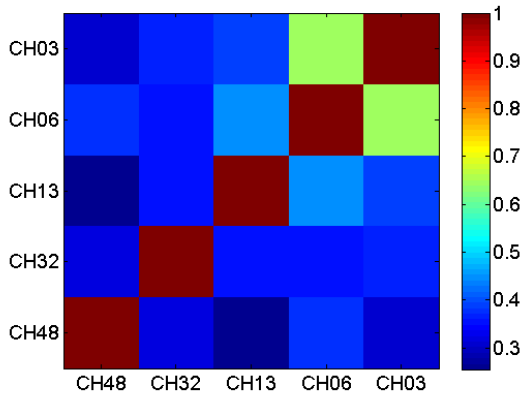

(b) Transverse direction

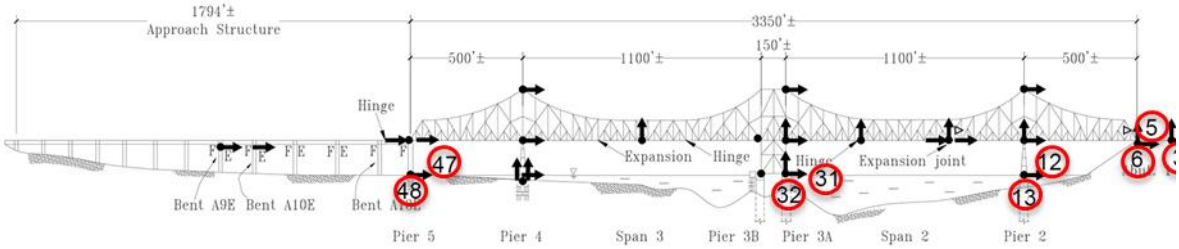

(c) Instrumentation layout

Figure 3. Spatial variability observed in CSMIP68184.

Data Selection

Not all of the 17 bridges introduced earlier are suitable for our study. No data are available for bridge No. 4 (CSMIP69760) in CESMD[2]. Two other bridges (CSMIP68717 and 58656) are very short, so they are not useful for studying spatial variability. Since having instruments on the foundation level is a crucial factor in the present study, bridge No. 7 (CSMIP68778) is also excluded as it does not have any sensor on its foundation level. The same limitation exits for bridges No. 14 and No. 15 (CSMIP68065 and 58657, respectively), and thus, they are also excluded. The level of vibration recorded on bridge No. 13 (CSMIP58596) is too small; the PSA is ~0.05g and is measured on channels 37 and 38 (i.e., two vertical channels at the edge of the main span). This indicates that the recorded motions are mostly free vibration, and thus, this bridge cannot be processed through the proposed identification method. As such, it is excluded as well. The level of vibration on two other bridges CSMIP58601 and 58602 is also very small. However, these two bridges—along with a third one (CSMIP58600)—create a system of connected bridges as shown in **Figure 4**. According to CESMD, a maximum structural acceleration of 0.162g is recorded on CSMIP58600, which makes the analysis of this bridge system a worthy attempt. However, no data appears available for the important channels (see **Figure 5** for instrumentation layout)[3]. As such, this bridge is also excluded.

Having excluded bridges mentioned above, there are then **7 bridges** left, whose data recorded during the 2014 South Napa earthquake can be analyzed to investigate spatial variability of FIMs. These 7 bridges are: CSMIP 68184, 68185, 68322, 68682, 58632, 58700, and 67771.

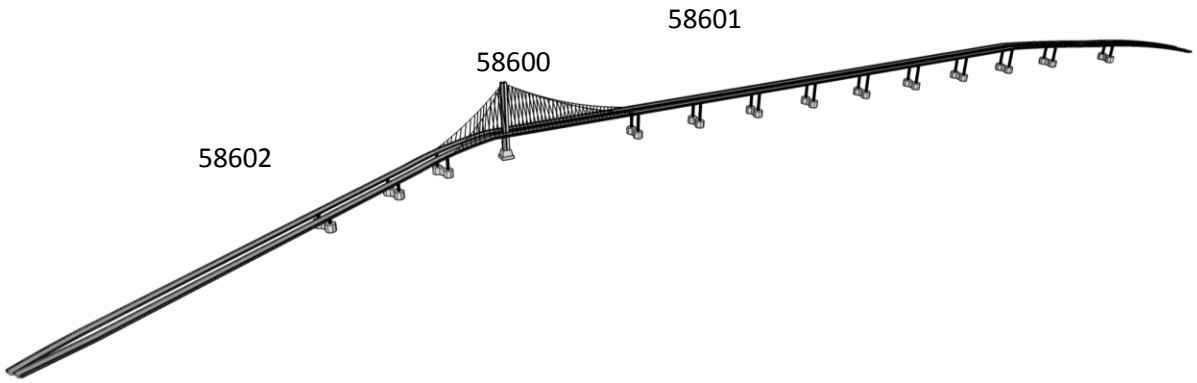

Figure 4. Eastern Oakland – San Francisco Bay Bridge.

[2] www.strong motioncenter.org

[3] For example, there is no data for channels 1 to 6 (foundation level of Pier W2), channels 25 to 30 (foundation level of Pier W2), and channels 68 to 73 (foundation level of Pier W2). Moreover, some channels on the deck—namely, channels 7 to 11, 12 to 15, 31 to 34 or 64 to 67—are missing data (last update 09/24/2016).

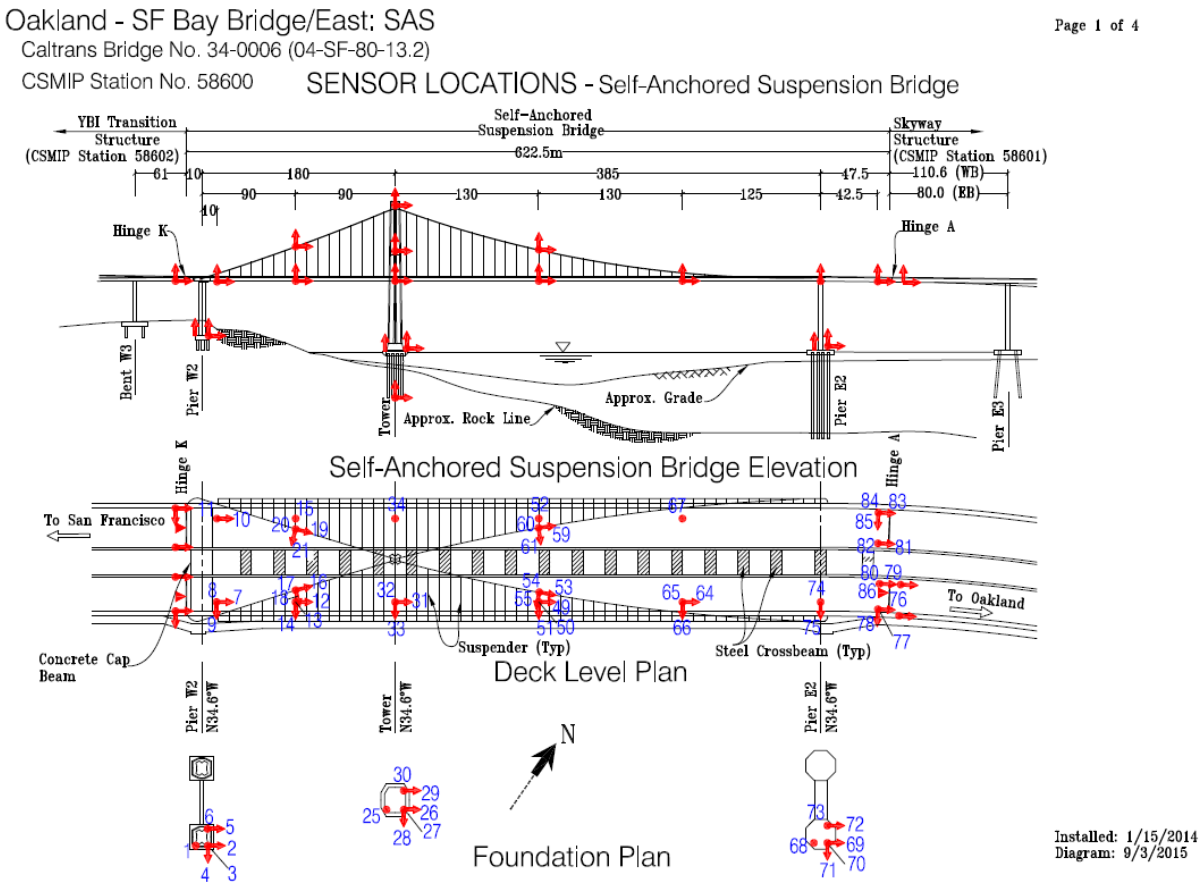

Figure 5. Instrumentation layout of CSMIP Station 58600.

Identification Methods

Part I: FIMs Estimation through Quadratic Sum-Squares Error

Dynamic Equation of Motion of Soil-Foundation-Structure System under Several FIMs

A schematic representation of the problem under study is shown in **Figure 6**. As seen, the bridge structure is subjected to several and different unknown Free-Field Motions (FFMs) at its piers. These FFMs are first converted to FIMs through unknown Kinematic Interaction (KI) filters and excited the bridge supported on flexible soil-foundation Impedance Functions (IFs). Herein, we assume that an initial (*uncertain*) Finite Element (FE) model of the bridge supported on *uncertain* IFs is available. Also, responses of the system at several locations on the bridge and foundation are measured as absolute accelerations through sensors. In what follows, a method is described, with which unknown FIMs, IFs, and unknown parameters of the *superstructure* are all identified simultaneously along with their uncertainties.

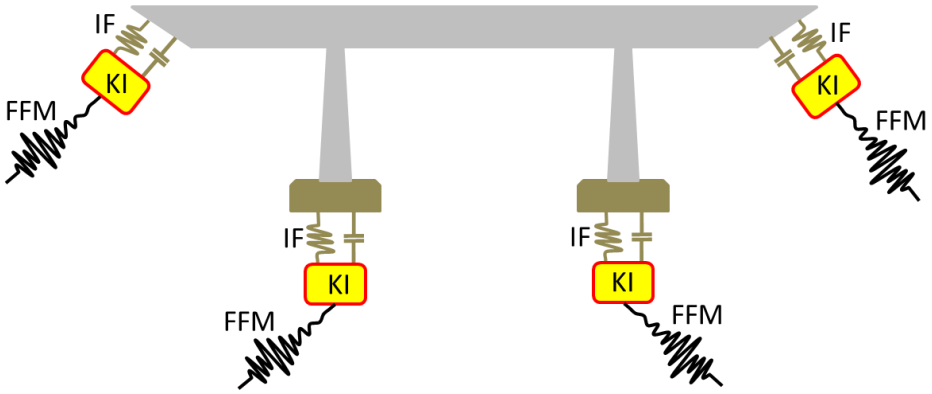

Figure 6. Lumped model of a multi-span bridge.

The equation of dynamic equilibrium for all the Degrees-Of-Freedom (DOFs) (n structure-foundation and n_g foundation-soil DOFs) is written in partitioned form as (Chopra, 2001)

$$\begin{bmatrix} \mathbf{M} & \mathbf{M}_g \\ \mathbf{M}_g{}^T & \mathbf{M}_{gg} \end{bmatrix} \begin{Bmatrix} \ddot{\boldsymbol{x}}(t) \\ \ddot{\boldsymbol{x}}_{\boldsymbol{g}}(t) \end{Bmatrix} + \begin{bmatrix} \mathbf{D} & \mathbf{D}_g \\ \mathbf{D}_g{}^T & \mathbf{D}_{gg} \end{bmatrix} \begin{Bmatrix} \dot{\boldsymbol{x}}(t) \\ \dot{\boldsymbol{x}}_{\boldsymbol{g}}(t) \end{Bmatrix} + \begin{bmatrix} \mathbf{K} & \mathbf{K}_g \\ \mathbf{K}_g{}^T & \mathbf{K}_{gg} \end{bmatrix} \begin{Bmatrix} \boldsymbol{x}(t) \\ \boldsymbol{x}_{\boldsymbol{g}}(t) \end{Bmatrix} = \begin{Bmatrix} \mathbf{0} \\ \boldsymbol{P}_g(t) \end{Bmatrix} \quad 2)$$

where **M**, **D**, and **K** are $n \times n$ mass, damping and stiffness matrices of the foundation-structure, respectively. Matrices $\mathbf{M}_g$, $\mathbf{D}_g$, and $\mathbf{K}_g$ are $n \times n_g$ mass, damping, and stiffness matrices of the foundation-soil interface, while $\mathbf{M}_{gg}$, $\mathbf{D}_{gg}$, and $\mathbf{K}_{gg}$ matrices are related to soil's DOFs. In Eq. (2), $\boldsymbol{x}(t)$ is a vector that contains the absolute displacement response of all n structure-foundation DOFs, while $\dot{\boldsymbol{x}}(t)$, and $\ddot{\boldsymbol{x}}(t)$ are their corresponding velocity and acceleration vectors. $\boldsymbol{x}_g(t) = [x_{g,1}(t) \quad \cdots \quad x_{g,n_g}(t)]^T$ and whose time derivatives $\dot{\boldsymbol{x}}_g(t)$ and $\ddot{\boldsymbol{x}}_g(t)$ are vectors containing prescribed the Foundation Input Motions (FIMs) as displacement, velocity, and acceleration at all n_g foundation-soil interface DOFs. As there is no external force on the structure-foundation DOFs, the only forces needed for applying FIMs is $\boldsymbol{P}_g(t)$, as shown in Eq. (2).

The absolute displacement of the bridge (structure-foundation) can be written as the superposition of displacement produced by the static application of the prescribed FIMs at each time instant $\boldsymbol{u}^s(t)$ and dynamic response with respect to the statically deformed position $\boldsymbol{u}(t)$ as

$$\begin{Bmatrix} \boldsymbol{x}(t) \\ \boldsymbol{x}_g(t) \end{Bmatrix} = \begin{Bmatrix} \boldsymbol{u}^s(t) \\ \boldsymbol{x}_g(t) \end{Bmatrix} + \begin{Bmatrix} \boldsymbol{u}(t) \\ \mathbf{0} \end{Bmatrix} \quad 3)$$

As $\boldsymbol{u}^s(t)$ is produced by static deformation of the bridge under static application of $\boldsymbol{x}_g(t)$, their relationships are governed by static equilibrium as follows

$$\begin{bmatrix} \mathbf{K} & \mathbf{K}_g \\ \mathbf{K}_g{}^T & \mathbf{K}_{gg} \end{bmatrix} \begin{Bmatrix} \boldsymbol{u}^s(t) \\ \boldsymbol{x}_g(t) \end{Bmatrix} = \begin{Bmatrix} \mathbf{0} \\ \boldsymbol{P}_g^s(t) \end{Bmatrix} \quad 4)$$

where $\boldsymbol{P}_g^s(t)$ is needed force at each time to impose $\boldsymbol{x}_g(t)$. It is trivial that $\boldsymbol{P}_g^s(t)$ would be zero if the system is statically determinate or all foundation-soil interface nodes move in compatible manner (e.g., identical horizontal FIMs).

The first partition of the Eq. (2) can be rewritten using mentioned above static and dynamic parts as

$$\mathbf{M}\,\ddot{\boldsymbol{u}}(t) + \mathbf{D}\,\dot{\boldsymbol{u}}(t) + \mathbf{K}\,\boldsymbol{u}(t) = -\left[\mathbf{M}\,\ddot{\boldsymbol{u}}^{s}(t) + \mathbf{M}_g\ddot{\boldsymbol{x}}_g(t)\right] - \left[\mathbf{D}\,\dot{\boldsymbol{u}}^{s}(t) + \mathbf{D}_g\dot{\boldsymbol{x}}_g(t)\right] \quad 5)$$

The term $\left[\mathbf{K}\,\boldsymbol{u}^{s}(t) + \mathbf{K}_g\boldsymbol{x}_g(t)\right]$ has been removed from right-hand-side of the equation above, because it is zero, based on the first partition of Eq. (4). In Eq. (5), it is more favorable to replace the quasi-static velocity and acceleration using their FIMs' counterparts, because $\mathbf{K}\,\boldsymbol{u}^{s}(t) + \mathbf{K}_g\boldsymbol{x}_g(t) = \mathbf{0}$. So, Eq. (5) can be rewritten as

$$\mathbf{M}\,\ddot{\boldsymbol{u}}(t) + \mathbf{D}\,\dot{\boldsymbol{u}}(t) + \mathbf{K}\,\boldsymbol{u}(t) = -\left[\mathbf{M}\,\mathbf{L} + \mathbf{M}_g\right]\ddot{\boldsymbol{x}}_g(t) - \left[\mathbf{D}\,\mathbf{L} + \mathbf{D}_g\right]\dot{\boldsymbol{x}}_g(t) \quad 6)$$

where $\mathbf{L} = -\mathbf{K}^{-1}\mathbf{K}_g$ is $n \times n_g$ influence matrix. Each column of the matrix $\mathbf{L}$, say $\boldsymbol{l}_l$, is a vector that assigns the influence of each input acceleration, $x_{g,l}(t)$, on the system's response; and is a function of internal and boundary stiffnesses. Damping term in Eq. (6) is usually small relative to the inertia term, and may be dropped (it is exactly zero when damping matrices are stiffness proportional). Moreover, for lumped mass systems, the mass matrix is diagonal and off the diagonal matrix $\mathbf{M}_g$ will be zero. So, Eq. (6) can be written in its final form as

$$\mathbf{M}\,\ddot{\boldsymbol{u}}(t) + \mathbf{D}\,\dot{\boldsymbol{u}}(t) + \mathbf{K}\,\boldsymbol{u}(t) = -\mathbf{M}\,\mathbf{L}\ddot{\boldsymbol{x}}_g(t) \quad 7)$$

Finally by replacing $\boldsymbol{u}(t)$ by $\boldsymbol{x}(t) - \boldsymbol{u}^{s}(t)$ in Eq. (7), equation of motion can be expressed in absolute framework as

$$\mathbf{M}\,\ddot{\boldsymbol{x}}(t) + \mathbf{D}\,\dot{\boldsymbol{x}}(t) + \mathbf{K}\,\boldsymbol{x}(t) = \mathbf{D}\,\mathbf{L}\,\dot{\boldsymbol{x}}_g(t) + \mathbf{K}\,\mathbf{L}\,\boldsymbol{x}_g(t) \quad 8)$$

The Identification Method

Eq. (8) can be written in the state-space as

$$\dot{\boldsymbol{z}}(t) = \mathbf{A}_c\,\boldsymbol{z}(t) + \mathbf{B}_c\,\boldsymbol{f}(t) + \boldsymbol{w}(t) \quad 9)$$

where $\boldsymbol{z}(t) = [\boldsymbol{x}(t)^T \quad \dot{\boldsymbol{x}}(t)^T]^T$ is $2n \times 1$ state vector, $\boldsymbol{f}(t) = \left[\boldsymbol{x}_g(t)^T \quad \dot{\boldsymbol{x}}_g(t)^T\right]^T$ is $2n_g \times 1$ excitation vector and continuous-time transition and input matrices $\mathbf{A}_c$ and $\mathbf{B}_c$ are defined as

$$\mathbf{A}_c = \begin{bmatrix} \mathbf{0} & \mathbf{I} \\ -\mathbf{M}^{-1}\mathbf{K} & -\mathbf{M}^{-1}\mathbf{D} \end{bmatrix} \quad 10)$$

$$\mathbf{B}_c = \begin{bmatrix} \mathbf{0} \\ [\mathbf{M}^{-1}\mathbf{K}\,\mathbf{L}, \mathbf{M}^{-1}\mathbf{D}\,\mathbf{L}] \end{bmatrix} \quad 11)$$

$\boldsymbol{w}(t)$ is a model noise (uncertainty) vector with zero mean and covariance matrix $\mathbf{Q}$. Absolute acceleration at any discrete-time instant i can be related to the state and FIMs as

$$\boldsymbol{y}[i] = \mathbf{E}\,\boldsymbol{z}[i] + \mathbf{F}\,\boldsymbol{f}[i] + \boldsymbol{v}[i] \quad 12)$$

where

$$\mathbf{E} = \mathbf{V}\,[-\mathbf{M}^{-1}\mathbf{K} \quad -\mathbf{M}^{-1}\mathbf{D}] \tag{13}$$

$$\mathbf{F} = \mathbf{V}\,[\mathbf{M}^{-1}\mathbf{K}\,\mathbf{L} \quad \mathbf{M}^{-1}\mathbf{D}\,\mathbf{L}] \tag{14}$$

in which $\mathbf{V}$ is an $l \times n$ matrix containing 1s and 0s to show which DOFs are measured. $\boldsymbol{v}[i]$ is a measurement noise vector assumed to be Gaussian zero-mean white with covariance matrix $\mathbf{R}$. $\boldsymbol{v}[i]$ represents difference between exact prediction, $\boldsymbol{h}[i] = \mathbf{E}\,\boldsymbol{z}[i] + \mathbf{F}\,\boldsymbol{f}[i]$ and real-life measurement $\boldsymbol{y}[i]$, i.e., $\boldsymbol{v}[i] = \boldsymbol{y}[i] - \boldsymbol{h}[i]$. According to the assumptions considered for this measurement noise, its Probability Distribution Function (PDF) can be expressed as

$$P(v) = \frac{1}{(2\pi)^{l/2}|\mathbf{R}|^{0.5}}\, e^{-\frac{1}{2}\boldsymbol{v}^T\mathbf{R}^{-1}\boldsymbol{v}} \tag{15}$$

where $|.|$ denotes determinant. Let's put all of the system's uncertain parameters (superstructure and IF parameters) into a vector $\boldsymbol{\theta} = [\theta_1 \quad \cdots \quad \theta_{n_\theta}]^T$. The unknown FIMs ($\boldsymbol{f}$) and system's parameters ($\boldsymbol{\theta}$) can be identified by maximization of joint PDF of $\boldsymbol{f}$ and $\boldsymbol{\theta}$ given measured responses. According to the Bayes' rule (Bayes, 1763), this a posteriori PDF can be expressed as

$$P(\boldsymbol{\theta}, \boldsymbol{f}|\boldsymbol{y}) = c\, P(\boldsymbol{y}|\boldsymbol{\theta}, \boldsymbol{f})\, P(\boldsymbol{\theta}, \boldsymbol{f}) \tag{16}$$

where $P(\boldsymbol{y}|\boldsymbol{\theta}, \boldsymbol{f})$ is the likelihood function, $P(\boldsymbol{\theta}, \boldsymbol{f})$ is the joint a priori PDF, and c is a constant. Assuming independences between $\boldsymbol{\theta}$ and $\boldsymbol{f}$ along with uniform PDFs for them (no initial information), maximization of $P(\boldsymbol{\theta}, \boldsymbol{f}|\boldsymbol{y})$ reduces to the maximization of likelihood function $P(\boldsymbol{y}|\boldsymbol{\theta}, \boldsymbol{f})$ (Ebrahimian, et al., 2015). This PDF at time instant $k+1$ can be calculated as

$$P(\boldsymbol{y}[1\!:\!k+1]|\boldsymbol{\theta}[k+1], \boldsymbol{f}[1\!:\!k+1]) = \prod_{i=1}^{k+1} P(\boldsymbol{v}[i]) \tag{17}$$

which can be rewritten as

$$P(\boldsymbol{y}[1\!:\!k+1]|\boldsymbol{\theta}[k+1], \boldsymbol{f}[1\!:\!k+1]) = \prod_{i=1}^{k+1} \frac{1}{(2\pi)^{l/2}|\boldsymbol{R}|^{0.5}}\, e^{-\frac{1}{2}\boldsymbol{v}[i]^T\boldsymbol{R}^{-1}\boldsymbol{v}[i]} \tag{18}$$

To maximize equation above, it is more convenient to minimize its negative natural logarithm—i.e., the following objective function:

$$J[k+1] = 1.83\,\frac{l(k+1)}{2} + \frac{1}{2}\sum_{i=1}^{k+1}|\mathbf{R}| + \frac{1}{2}\sum_{i=1}^{k+1}\boldsymbol{v}[i]^T\mathbf{R}^{-1}\boldsymbol{v}[i] \tag{19}$$

Two first terms on the right-hand side do not play a role in the objective function, because they are not updated. Thus, the objective function can be simplified as

$$J[k+1] = \sum_{i=1}^{k+1}\boldsymbol{v}[i]^T\mathbf{R}^{-1}\boldsymbol{v}[i] \tag{20}$$

As $\boldsymbol{h}[i]$ is a nonlinear function of $\boldsymbol{\theta}$, it should be linearized through Taylor's expansion so that the objective function becomes a quadratic function of $\boldsymbol{\theta}$ and $\boldsymbol{f}$. To do so, we can approximate $\boldsymbol{h}[i]$ as

$$\boldsymbol{h}[i] \approx \widehat{\boldsymbol{h}}[i] + \mathbf{H}_{\boldsymbol{\theta}}[i]\big(\boldsymbol{\theta}[i] - \widehat{\boldsymbol{\theta}}[i-1]\big) + \mathbf{H}_{\boldsymbol{f}}[i]\big(\boldsymbol{f}[i] - \widehat{\boldsymbol{f}}[i-1]\big) \tag{21}$$

where

$$\widehat{\boldsymbol{h}}[i] = \boldsymbol{h}\left[\hat{\boldsymbol{z}}[i|i-1], \widehat{\boldsymbol{\theta}}[i-1], \hat{\boldsymbol{f}}[i-1]\right] \tag{22}$$

$$\mathbf{H}_{\boldsymbol{f}}[i] = \left.\frac{\partial \boldsymbol{h}[i]}{\partial \boldsymbol{f}[i]}\right|_{\boldsymbol{z}[i]=\hat{\boldsymbol{z}}[i|i-1], \boldsymbol{\theta}[i]=\widehat{\boldsymbol{\theta}}[i-1], \boldsymbol{f}[i]=\hat{\boldsymbol{f}}[i-1]} \tag{23}$$

and $\mathbf{H}_{\boldsymbol{\theta}}[i] = \bar{\mathbf{H}}_{\boldsymbol{\theta}}[i] + \mathbf{H}_{\boldsymbol{z}}[i]\mathbf{Z}_{\boldsymbol{\theta}}[i]$ in which

$$\bar{\mathbf{H}}_{\boldsymbol{\theta}}[\boldsymbol{i}] = \left.\frac{\boldsymbol{\partial h}[\boldsymbol{i}]}{\boldsymbol{\partial \theta}[\boldsymbol{i}]}\right|_{\boldsymbol{z}[\boldsymbol{i}]=\hat{\boldsymbol{z}}[\boldsymbol{i}|\boldsymbol{i-1}], \boldsymbol{\theta}[\boldsymbol{i}]=\widehat{\boldsymbol{\theta}}[\boldsymbol{i-1}], \boldsymbol{f}[\boldsymbol{i}]=\hat{\boldsymbol{f}}[\boldsymbol{i-1}]} \tag{24}$$

$$\mathbf{H}_{\boldsymbol{z}}[i] = \left.\frac{\boldsymbol{\partial h}[i]}{\boldsymbol{\partial z}[i]}\right|_{\boldsymbol{z}[i]=\hat{\boldsymbol{z}}[i|i-1], \boldsymbol{\theta}[i]=\widehat{\boldsymbol{\theta}}[i-1], \boldsymbol{f}[i]=\hat{\boldsymbol{f}}[i-1]} \tag{25}$$

$$\mathbf{Z}_{\boldsymbol{\theta}}[i] = \left.\frac{\boldsymbol{\partial z}[i]}{\boldsymbol{\partial \theta}[i]}\right|_{\boldsymbol{\theta}[i]=\widehat{\boldsymbol{\theta}}[i-1]} \tag{26}$$

In the equations above, $\widehat{\boldsymbol{\theta}}[i-1]$ and $\hat{\boldsymbol{f}}[i-1]$ are, respectively, the estimation of $\boldsymbol{\theta}[i]$ and $\boldsymbol{f}[i]$ at the previous step, and $\hat{\boldsymbol{z}}[i|i-1]$ is an *a priori* estimation of state, which can be obtained by using these estimates through the state equation. That is

$$\hat{\boldsymbol{z}}[i|i-1] = \hat{\boldsymbol{z}}[i-1] + \mathbf{A}_c \Delta t\, \hat{\boldsymbol{z}}[i-1] + \mathbf{B}_c \Delta t\, \hat{\boldsymbol{f}}[i-1] \tag{27}$$

where Δt is the sampling time. $\mathbf{Z}_{\boldsymbol{\theta}}[i]$ is the sensitivity matrix of the state vector with respect to the system's parameters, and can be obtained by differentiating both sides of Eq. (27) with respect to $\boldsymbol{\theta}$ as

$$\mathbf{Z}_{\boldsymbol{\theta}}[i] = \mathbf{Z}_{\boldsymbol{\theta}}[i-1] + \Delta t\left\{\frac{\partial \mathbf{A}_c}{\partial \boldsymbol{\theta}[i]}\hat{\boldsymbol{z}}[i-1] + \mathbf{A}_c\, \mathbf{Z}_{\boldsymbol{\theta}}[i-1] + \frac{\mathbf{B}_c}{\partial \boldsymbol{\theta}[i]}\, \hat{\boldsymbol{f}}[i-1]\right\} \tag{28}$$

By substituting the approximation of $\boldsymbol{h}[i]$ into the objective function, we have

$$J[k+1] = \sum_{i=1}^{k+1}\big(\bar{\boldsymbol{y}}[i] - \mathbf{H}_{\boldsymbol{\theta}}[i]\boldsymbol{\theta}[i] - \mathbf{H}_{\boldsymbol{f}}[i]\boldsymbol{f}[i]\big)^T \boldsymbol{R}^{-1}\big(\bar{\boldsymbol{y}}[i] - \mathbf{H}_{\boldsymbol{\theta}}[i]\boldsymbol{\theta}[i] - \mathbf{H}_{\boldsymbol{f}}[i]\boldsymbol{f}[i]\big) \tag{29}$$

where

$$\bar{\boldsymbol{y}}[i] = \boldsymbol{y}[i] - \widehat{\boldsymbol{h}}[i] + \mathbf{H}_{\boldsymbol{\theta}}[i]\widehat{\boldsymbol{\theta}}[i-1] + \mathbf{H}_{\boldsymbol{f}}[i]\hat{\boldsymbol{f}}[i-1] \tag{30}$$

Huang et al. (2010) showed that the objective function of Eq. (29) can be minimized through following recursive solution

$$\hat{\boldsymbol{f}}[k+1] = \mathbf{S}[k+1]\mathbf{H}_{\boldsymbol{f}}[k+1]^T\mathbf{R}^{-1}(\boldsymbol{I} - \mathbf{H}_{\boldsymbol{\theta}}[k+1]\mathbf{G}_{\boldsymbol{\theta}}[k+1])(\boldsymbol{y}[k+1] - \hat{\boldsymbol{h}}[k+1] + \mathbf{H}_{\boldsymbol{f}}[k+1]\boldsymbol{f}[k]) \quad 31)$$

$$\hat{\boldsymbol{\theta}}[k+1] = \hat{\boldsymbol{\theta}}[k] + \mathbf{G}_{\boldsymbol{\theta}}[k+1]\{\boldsymbol{y}[k+1] - \mathbf{H}_{\boldsymbol{f}}[k+1](\hat{\boldsymbol{f}}[k+1] - \boldsymbol{f}[k])\} \quad 32)$$

where $\mathbf{G}_{\boldsymbol{\theta}}[k+1]$ is the Kalman Gain Matrix (Kalman, 1960) and is calculated as

$$\mathbf{G}_{\boldsymbol{\theta}}[k+1] = \mathbf{P}_{\boldsymbol{\theta}}[k]\mathbf{H}_{\boldsymbol{\theta}}[k+1]^T(\mathbf{R} + \mathbf{H}_{\boldsymbol{\theta}}[k+1]\mathbf{P}_{\boldsymbol{\theta}}[k]\mathbf{H}_{\boldsymbol{\theta}}[k+1]^T)^{-1} \quad 33)$$

in which $\mathbf{P}_{\boldsymbol{\theta}}[k]$ is the covariance matrix of the estimation error of $\boldsymbol{\theta}$, and is calculated as

$$\mathbf{P}_{\boldsymbol{\theta}}[k] = (\mathbf{I} + \mathbf{G}_{\boldsymbol{\theta}}[k]\mathbf{H}_{\boldsymbol{f}}[k]\mathbf{S}[k]\mathbf{H}_{\boldsymbol{f}}[k]^{\boldsymbol{T}}\mathbf{R}^{-1}\mathbf{H}_{\boldsymbol{\theta}}[k])(\mathbf{I} - \mathbf{G}_{\boldsymbol{\theta}}[k]\mathbf{H}_{\boldsymbol{\theta}}[k])\mathbf{P}_{\boldsymbol{\theta}}[k-1] \quad 34)$$

In the equations above, $\mathbf{S}[k+1]$ is also the covariance matrix of the estimation error of $\boldsymbol{f}$ and is obtained as

$$\mathbf{S}[k+1] = \{\mathbf{H}_{\boldsymbol{f}}[k+1]^T\mathbf{R}^{-1}(\mathbf{I} - \mathbf{H}_{\boldsymbol{\theta}}[k+1]\mathbf{G}_{\boldsymbol{\theta}}[k+1])\mathbf{H}_{\boldsymbol{f}}[k+1]^T\}^{-1}. \quad 35)$$

Once the system's parameters and the FIMs are updated at each iteration, the state of the system can be updated similarly. That is,

$$\hat{\boldsymbol{z}}[k+1|k+1] = \hat{\boldsymbol{z}}[k+1|k] + \mathbf{G}_{\boldsymbol{z}}[k+1]\{\boldsymbol{y}[k+1] - \hat{\boldsymbol{h}}[k+1]\} \quad 36)$$

with the Kalman Gain matrix being

$$\mathbf{G}_{\boldsymbol{z}}[k+1] = \mathbf{P}_{\boldsymbol{z}}[k+1|k]\mathbf{H}_{\boldsymbol{z}}[k+1]^{\boldsymbol{T}}(\mathbf{R} + \mathbf{H}_{\boldsymbol{z}}[k+1]\,\mathbf{P}_{\boldsymbol{z}}[k+1|k]\,\mathbf{H}_{\boldsymbol{z}}[k+1]^T)^{-1} \quad 37)$$

where $\mathbf{P}_{\boldsymbol{z}}[k+1|k]$ is an estimation of state error covariance matrix, obtained from the state equation as

$$\mathbf{P}_{\boldsymbol{z}}[k+1|k] = (\mathbf{I} + \mathbf{A}_c\Delta t\,)\mathbf{P}_{\boldsymbol{z}}[k](\mathbf{I} + \mathbf{A}_c\Delta t\,)^T + \mathbf{Q} \quad 38)$$

in which $\mathbf{P}_{\boldsymbol{z}}[k]$ is the last step's error covariance matrix calculated through

$$\mathbf{P}_{\boldsymbol{z}}[k] = (\mathbf{I} - \mathbf{G}_{\boldsymbol{z}}[k]\,\mathbf{H}_{\boldsymbol{z}}[k+1]\,)\mathbf{P}_{\boldsymbol{z}}[k|k-1]. \quad 39)$$

Remark 1: The size of the state vector will be very large, if it is directly applied on most of bridges under study in this project. However, as the method works under unknown excitation, it can be used through a sub-structuring approach. As an illustration, **Figure 7** displays the Antioch - San Joaquin River Bridge, which can be divided into four segments. The cut edges of each substructure are Neumann boundaries with unknown (to be estimated) excitations.

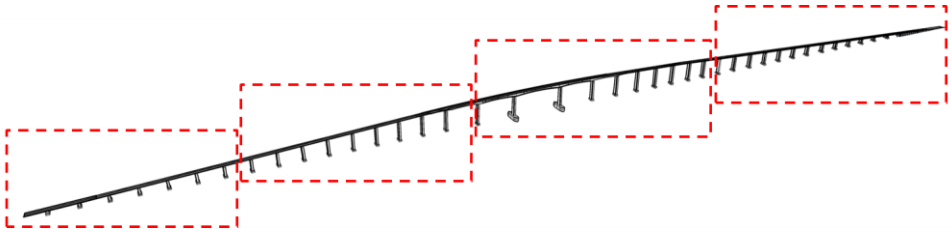

Figure 7. An example of proposed sub-structuring in CSMIP67771.

Remark 2: The proposed method works when the number of measurements is greater than the number of unknown FIMs. While this is almost always satisfied for the bridges under study, we rewrite $\hat{\boldsymbol{f}}[k+1]$ in state and observation equations—as well as other related equations versus acceleration—at the current time instant, and the displacement, velocity, and acceleration at the previous time step using Newmark's β-method (Chopra, 2001), as in

$$\hat{\boldsymbol{f}}[k+1] = \begin{bmatrix} \boldsymbol{x}_g[k+1]^T & \dot{\boldsymbol{x}}_g[k+1]^T \end{bmatrix}^T = \begin{bmatrix} \mathbf{T}_1 \hat{\bar{\boldsymbol{f}}}[k] + \\ \mathbf{T}_2 \hat{\bar{\boldsymbol{f}}}[k] + \end{bmatrix} + \begin{bmatrix} \beta \Delta t^2 \mathbf{I} \\ \gamma \Delta t \mathbf{I} \end{bmatrix} \ddot{\boldsymbol{x}}_g[k+1] \tag{40}$$

where $\hat{\bar{\boldsymbol{f}}}[k] = \left[x_{g_1}[k], \dot{x}_{g_1}[k], \ddot{x}_{g_1}[k], \cdots, x_{g_{n_g}}[k], \dot{x}_{g_{n_g}}[k], \ddot{x}_{g_{n_g}}[k] \right]$ and

$$\mathbf{T}_1 = \begin{bmatrix} \boldsymbol{\varphi}_1{}^T & & \\ & \ddots & \\ & & \boldsymbol{\varphi}_1{}^T \end{bmatrix}_{n_g \times 3n_g} \tag{41}$$

$$\mathbf{T}_2 = \begin{bmatrix} \boldsymbol{\varphi}_2{}^T & & \\ & \ddots & \\ & & \boldsymbol{\varphi}_2{}^T \end{bmatrix}_{n_g \times 3n_g} \tag{42}$$

in which $\boldsymbol{\varphi}_1 = [1 \quad \Delta t \quad (0.5-\beta)\Delta t^2]^T$ and $\boldsymbol{\varphi}_2 = [0 \quad 1 \quad (1-\gamma)\Delta t]^T$. Thus, at the $(k+1)^{\text{th}}$ iteration, $\hat{\bar{\boldsymbol{f}}}[k]$ is a known excitation and the unknown FIMs are collected in $\ddot{\boldsymbol{x}}_g[k+1]$. This, then, reduces the number of unknown excitations by a factor of two.

Remark 3: The proposed identification method is not limited to linear systems. As long as the soil, foundation, and structural nonlinearities can be incorporated into the system equations through parametric models, the proposed method can be used to identify those parameters that the said nonlinearities.

Remark 4: Having a reliable FE model of the bridge is an essential ingredient of the proposed identification method. For the present study, the geometry of these models for the studied bridges are based on SketchUp® models that are available through Google Earth®, which we then manually modify to obtain initial FE models. While the initial FE models are generally very accurate in geometry, they need to be improved by adding further details like constraints, connections, section properties, etc. The said details can be obtained through structural drawings. These modified FE are then employed along with the proposed identification method and data available in CESMD to identify the system parameters and FIMs. This process is schematically shown in **Figure 8**.

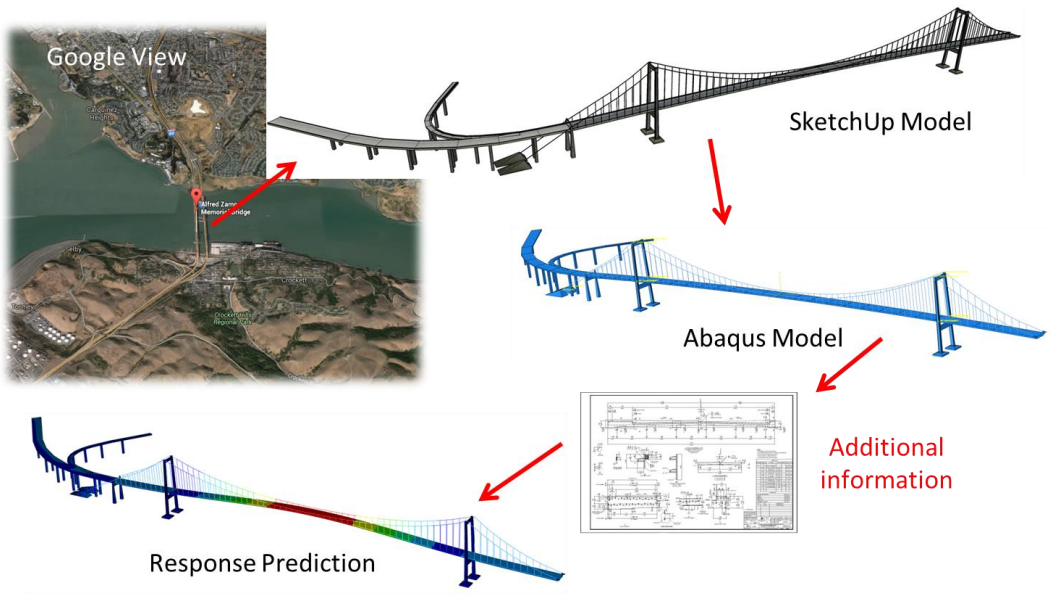

Figure 8. Initial FE modeling process.

Numerical Verification

To verify the proposed output-only identification method, we simulate the responses of a two-span bridge with continuous deck (**Figure 9**). It is assumed that mass of the foundation-bridge system is concentrated at 13 points, and there is no rotational mass moment of inertia. As such, stiffness and damping matrices can be statically condensed. Two horizontal ground motions recorded at the "Alhambra-1st & Woodward Station (CSMIP24030)" during 2001 West Hollywood earthquake are applied the remote ends of the soil-foundation springs at the two abutments (left- and right-ends) of the bridge as shown in **Figure 9**. Also, the abutment motion is multiplied by –1 and applied at the middle pier. These ground motions thus produce a combination of both independent and delayed input motions. Modulus of elasticity and moment of inertia of the deck beam are set at 1×10^9 and 0.05, respectively. Lumped masses, each with a value of 500, are placed at every 10 units of length. The stiffness of three springs are 12000, 12000, and 16000, respectively from left to right (all units are consistent). A Rayleigh damping with mass and stiffness factors of 0.2 and 0.002, respectively, is considered to create a classical damping matrix. Natural frequencies and modal damping ratios of this soil-foundation-bridge structure are listed in **Table 2**. As seen, the system is designed such that it is a fair representation of very long and flexible bridges that will be eventually studied in the present project.

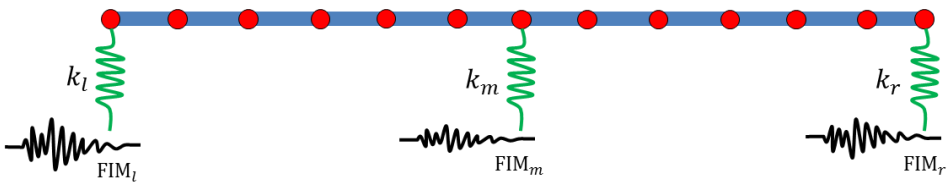

Figure 9. Synthetic bridge model with multiple support excitation.

Out of the 13 DOFs, only 5 channels (three foundations, left mid-span, and right mid-span) are used for identification. Stiffnesses of all tree springs, modulus of elasticity of the bridge, and the two damping coefficients are assumed as the system's unknown parameters (a total of 6 parameters) along with three FIM acceleration signals. **Figure 10** shows the convergence rate of estimation error for all of 6 parameters (as well as ±1 standard deviation). As seen, all errors converge to the zero. Standard deviation around the identified values quantifies how reliable these estimations are. For example, this figure indicates that while the identified damping parameters are very close to their exact values, the uncertainty in these identified values are relatively high compared to the identified spring stiffnesses and the elastic modulus.

The most important results of the identification process are the recovered FIMs. These signals are plotted together with their exact counterparts in **Figure 11**. As seen, the identified FIMs are very accurate. The standard deviation curves are not shown here, because they were very close to the identified signals. These results indicate that the proposed method will be a viable ingredient for the present project, and will produce accurate estimates of FIMs.

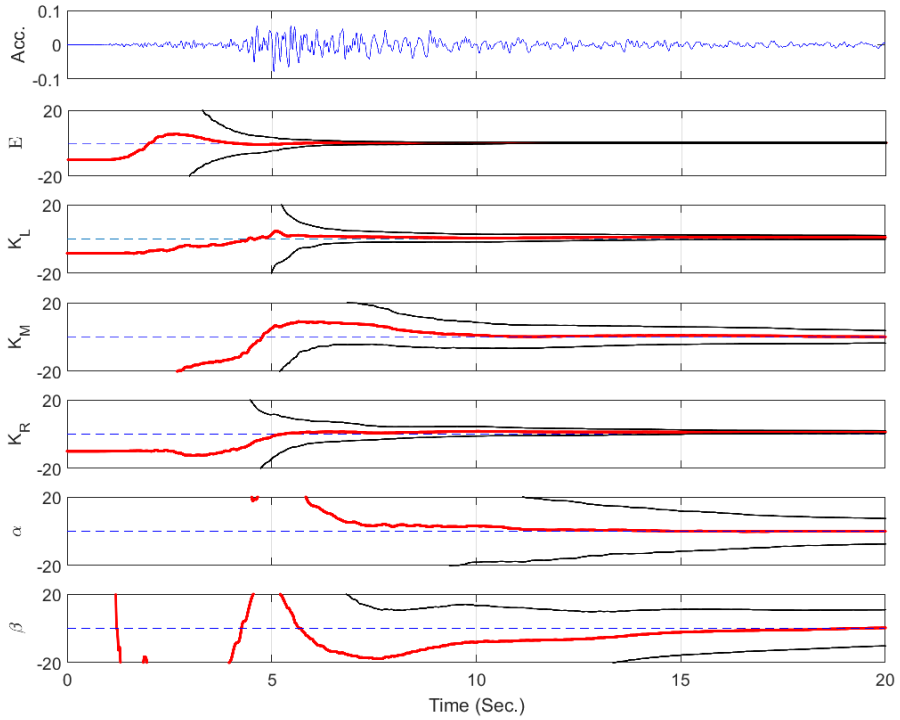

Figure 10. Error convergence rate.

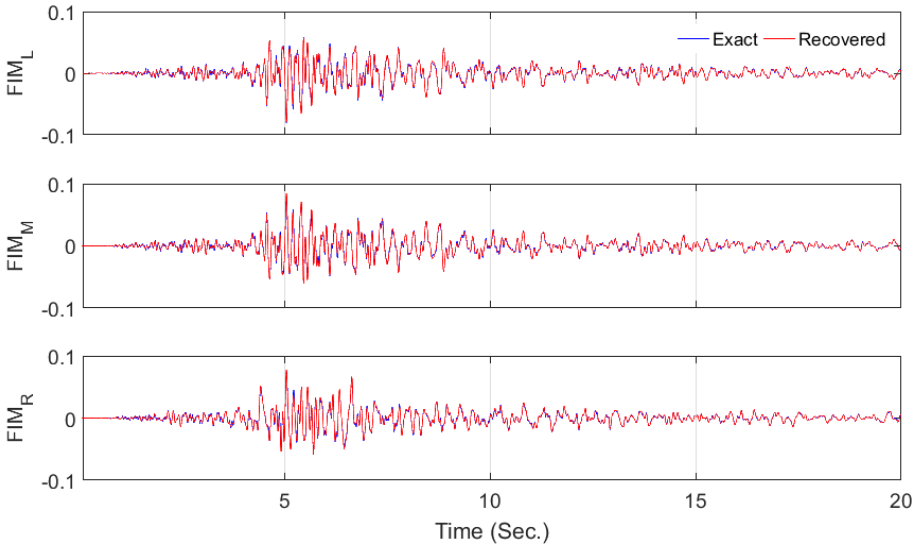

Figure 11. Comparison between exact and identified FIMs.

Table 2. Modal characteristics of the bridge model.

Mode No.	1	2	3	4	5	6	7	8	9	10	11	12	13
$f_n(Hz)$	0.30	0.36	0.65	0.84	1.29	1.97	2.93	4.07	5.40	6.85	8.35	9.69	10.67
$\xi_n(\%)$	5.43	4.59	2.87	2.42	2.04	2.05	2.39	2.95	3.69	4.54	5.43	6.25	6.85

Part II: Decomposition of FIMs to Site Response and Bedrock Motion

The identification of FIMs (e.g., through method described and verified in Part I above) enables a quantitative investigation of spatial variability in real-life ground motions. As already shown in **Figure 1**(right), these FIMs are filtered versions of a common bedrock motion[4] that pass through site response and kinematic interaction filters. Assuming that the kinematic interaction is the same for all piers, which is an acceptable assumption, we can extract the site-response Transfer Function at each pier through a blind channel identification method that will be described below. This new method is based on the assumption that a *common* bedrock motion passes through *different* sites. This means that the recovered bedrock motion is possibly altered by a kinematic interaction filter. While we shall only present a formulation for two sites (piers), the method can be easily extended to any number of sites (piers). In what follows, the ground surface motions represent those FIMs identified in Part I.

A soil deposit, e.g., **Figure 1**(left), can be assumed to be a Multi-Degree-Of-Freedom (MDOF) system with an infinite number of DOFs. Therefore, its dynamic response under rigid bedrock acceleration $\ddot{x}_b(t)$ can be expressed using modal superposition as (Glaser, 1996)

[4] Here, bedrock motion means motion at a location above which the response would be different at different locations. So, it may not be a physical bedrock, but rather a reference depth where the response is identical at different locations.

$$\ddot{x}_s(t) = \sum_{m=1}^{\infty} h_m(t) * \beta_m \ddot{x}_b(t) \tag{43}$$

where $*$ denotes a linear convolution; $\ddot{x}_s(t)$ is the absolute acceleration recorded on the ground surface; β_m is the modal contribution factor; and $h_m(t)$ is the IRF, which is given as (Ghahari, et al., 2013)

$$h_m(t) = \frac{1}{\omega_{d_m}} e^{-\xi_m \omega_{n_m} t}\left[\left(\omega_{d_m}^2 - \xi_m^2 \omega_{n_m}^2\right) sin\left(\omega_{d_m} t\right) + 2\xi_m \omega_{n_m} \omega_{d_m} cos(\omega_{d_m} t)\right] \tag{44}$$

Here ξ_m, ω_{n_m}, and $\omega_{d_m} = \omega_{n_m}\sqrt{1-\xi_m^2}$ denote the damping ratio, and the undamped and damped natural frequencies of the m-th mode, respectively. $h_m(t)$ is an Infinite Impulse Response (IIR) filter. The *Z*-Transform (Oppenheim, et al., 1989) of its discrete-time representation is

$$h_m(z) = \left[\frac{C_m + D_m z^{-1}}{1 - A_m z^{-1} - B_m z^{-2}}\right] \tag{45}$$

where

$$A_m = 2e^{-\xi_m \omega_{n_m} \Delta t}\, cos\left(\omega_{d_m} \Delta t\right), B_m = -e^{-2\xi_m \omega_{n_m} \Delta t},\ C_m = 2\xi_m \omega_{n_m} \Delta t,$$

$$D_m = \omega_{n_m}\, \Delta t\, e^{-\xi_m \omega_{n_m} \Delta t}\left[\frac{\omega_{n_m}}{\omega_{d_m}}\left(1 - 2\xi_m{}^2\right) sin\left(\omega_{d_m} \Delta t\right) - 2\xi_m cos(\omega_{d_m} \Delta t)\right]. \tag{46}$$

The Z-Transform helps to express the IRF in terms of the so-called poles (p_m and p_m^*), and zeros (z_m) as in

$$h_m(z) = C_m\,(z - z_m)/[(z - p_m)(z - p_m^*)] \tag{47}$$

where the superscript $*$ denotes a complex conjugate, and

$$z_m = -D_m/C_m, \qquad p_m, p_m^* = \frac{A_m \pm \sqrt{A_m{}^2 + 4B_m}}{2} \tag{48}$$

Indeed, the poles reflect the internal couplings within the system, while the zeros reflect the way the internal variables are coupled to the input and output signals (Åström, et al., 1984). Due to the frequency band of the bedrock motion, modal summation introduced in Eq. (43) is always finite; and the ground surface response signal can be well approximated by using a few fundamental modes, say n_m. So, Eq. (43) can be rewritten as

$$\ddot{x}_s(t) \cong \tilde{h}(t) * \ddot{x}_b(t) \tag{49}$$

where $\tilde{h}(t) = \sum_{m=1}^{n_m} \beta_m h_m(t)$. Based on the pole-zero representation mentioned above, we have

$$\tilde{h}(z) = \frac{\sum_{m=1}^{n_m}\left[\beta_m C_m (z - z_m)\prod_{l=1,l\neq m}^{n_m}(z-p_l)(z-p_l^*)\right]}{\prod_{m=1}^{n_m}(z-p_m)(z-p_m^*)} \quad 50)$$

The Proposed Algorithm

a. Decomposition

As shown in **Figure 1**(right), both sites (piers) are subject to an identical bedrock motion. So Eq. (49) can be written in discrete-time for both sites as

$$\ddot{x}_{s_1}[n] \cong \tilde{h}_1[n] * \ddot{x}_b[n] \quad 51)$$

$$\ddot{x}_{s_2}[n] \cong \tilde{h}_2[n] * \ddot{x}_b[n] \quad 52)$$

Thus, it is straightforward to show that the following cross-relation holds:

$$\ddot{x}_{s_1}[n] * \tilde{h}_2[n] = \ddot{x}_{s_2}[n] * \tilde{h}_1[n] \quad 53)$$

By applying a Z-Transform to both sites of the equation above, we can write

$$\ddot{x}_{s_1}[n]\,\tilde{h}_2(z) = \ddot{x}_{s_2}[n]\,\tilde{h}_1(z) \quad 54)$$

Based on Eq. (50), each $\tilde{h}_p(z)$ $(p = 1, 2)$ can be expressed as $N_p(z)/D_p(z)$ where $N_p(z)$ and $D_p(z)$ are polynomial functions of z. So, Eq. (54) can be restated as

$$\ddot{x}_{s_1}[n]\,N_2(z)D_1(z) = \ddot{x}_{s_2}[n]\,N_1(z)D_2(z), \quad 55)$$

which can be further restated in a simplified form as

$$\ddot{x}_{s_1}[n]\,g_1(z) = \ddot{x}_{s_2}[n]\,g_2(z) \quad 56)$$

where $g_1(z) = N_2(z)D_1(z)$ and $g_2(z) = N_1(z)D_2(z)$ are two Finite Impulse Response (FIR) filters. The order of polynomial g_1 (g_2) is equal to the sum of the orders of N_2 (or N_1) and D_1 (D_2), which is nominally $2n_{m,1} + 2n_{m,2} - 1$.

From the definition of the Z-Transform, Eq. (56) can be written by the discrete-time samples of $\ddot{x}_s[n]$ and the coefficients of polynomials $g(z)$—i.e., $g_p(z) = g_p[0] + g_p[1]z^{-1} + \cdots + g_p[1]z^{-(L-1)}$ —as follows

$$[\mathbf{X}_1 \quad -\mathbf{X}_2]\begin{bmatrix}\underline{\boldsymbol{g}}_1\\ \underline{\boldsymbol{g}}_2\end{bmatrix} = \mathbf{0} \quad 57)$$

where $\underline{\boldsymbol{g}}_p = [g_p[0] \quad g_p[1] \quad \cdots \quad g_p[L-1]]^T$ (for $p = 1,$ and 2) and

$$\mathbf{X}_p = \begin{bmatrix} \ddot{x}_{s_p}[L-1] & \ddot{x}_{s_p}[L-2] & \cdots & \ddot{x}_{s_p}[0] \\ \ddot{x}_{s_p}[L] & \ddot{x}_{s_p}[L-1] & \cdots & \ddot{x}_{s_p}[1] \\ \vdots & \vdots & \ddots & \vdots \\ \ddot{x}_{s_p}[N] & \ddot{x}_{s_p}[N-1] & \cdots & \ddot{x}_{s_p}[N-L+1] \end{bmatrix}_{(N-L+1)\times L} \quad \text{for} \quad p = 1, 2 \qquad 58)$$

where $L = 2n_{m,1} + 2n_{m,2}$, and N denotes the number of recorded samples. Eq. (57) is a classical equation in the field of Single-Input-Multiple-Output (SIMO) blind channel identification (Xu, et al., 1995; Moulines, et al., 1995; Gürelli & Nikias, 1995). It is a system of $(N - L + 1)$ linear homogenous equations with $2L$ unknowns, which can have a unique solution (up to an arbitrary scaling factor), provided that the number of sample points are adequate $N \geq 3L - 1$ (which is always satisfied in our cases). Indeed, the matrix $[\mathbf{X}_1 \quad -\mathbf{X}_2]$ is rank deficient by 1, and the solution, $[\underline{\boldsymbol{g}}_1 \quad \underline{\boldsymbol{g}}_2]^T$, would be the one-dimensional null space of the matrix, which can be identified as its *right singular vector* corresponding to the zero singular value.

In real-life, due to the presence of noise and modeling errors, Eq. (57) is only approximately valid. In other words, the matrix $[\mathbf{X}_1 \quad -\mathbf{X}_2]$ is full-rank, because the theoretical zero singular value is lost within the noise-corrupted singular values. So, there is no null subspace in the space created by the columns. Therefore, $[\underline{\boldsymbol{g}}_1 \quad \underline{\boldsymbol{g}}_2]^T$ will be the right singular vector corresponding to the *smallest* singular value.

Once $\underline{\boldsymbol{g}}_1$ and $\underline{\boldsymbol{g}}_2$ are identified, the site's Transfer Functions can be easily reconstructed, provided that we can accurately decompose $\underline{\boldsymbol{g}}_1$ ($\underline{\boldsymbol{g}}_2$) to $N_1(z)$ ($N_2(z)$) and $D_1(z)$ ($D_2(z)$). In the following section, we describe an algorithm for the said decomposition.

b. Zero-Pole Pairing, Order Estimation, and Identification of Modal Contribution Factors

Let's assume that we have overestimated the number of modes at each site as $\tilde{n}_{m,1} = n_{m,1} + \bar{n}_{m,1}$ and $\tilde{n}_{m,2} = n_{m,2} + \bar{n}_{m,2}$. Therefore, L is overestimated as $\tilde{L} = L + \bar{L}$ where $\bar{L} = 2(\bar{n}_{m,1} + \bar{n}_{m,2})$. In other words, polynomials $g_1(z)$ and $g_2(z)$ obtained via Eq. (57) have $\bar{L}$ extraneous zeros. But, to satisfy Eq. (56), these $\bar{L}$ extraneous zeros must appear at the same locations[5] for both $g_1(z)$ and $g_2(z)$. Thus, in the absence of noise, $\bar{L}$ can be identified as the dimension of the null space of $[\mathbf{X}_1 \quad -\mathbf{X}_2]$ minus one.

Measurement noise is inevitable, especially in the FIMs recovered from real-life data. As such, the number of zero singular values of $[\mathbf{X}_1 \quad -\mathbf{X}_2]$ would not be helpful to determine the number of extraneous zeros (i.e., $\bar{L}$) or their locations. Here, we make use of stability diagrams (Bodeux & Golinval, 2001) to circumvent this problem. We solve Eq. (57) for a range of $\tilde{L}$ (in 2 incremental steps) and repeat the following steps for each case:

1. Calculate the natural frequencies and damping ratios via equations below for all recovered roots without regarding to these roots being poles, zeros, or extraneous zeros (this information is yet known).

$$\omega_{n_m} = \left|\frac{ln\, p_m}{\Delta t}\right| \qquad 59)$$

[5] We assume here that the two sites have dissimilar poles and zeros.

$$\xi_m = -Re\left\{\frac{ln\, p_m}{\Delta t}\right\}/\omega_{n_m} \tag{60}$$

2. Exclude those roots that predict unusual damping ratios—i.e., negative or higher than %100.
3. Find the closest natural frequency from the previous step for each natural frequency, and calculate the following frequency and damping ratio errors:

$$E(\omega_m) = \frac{\left|\omega_{m,\tilde{L}_i} - \omega_{m,\tilde{L}_{i-1}}\right|}{\omega_{m,\tilde{L}_{i-1}}}, \qquad E(\xi_m) = \frac{\left|\xi_{m,\tilde{L}_i} - \xi_{m,\tilde{L}_{i-1}}\right|}{\xi_{m,\tilde{L}_{i-1}}} \tag{61}$$

4. Accept those modes having frequency and damping errors that are less than pre-specified thresholds as stable roots of $D_1(z)$ and $D_2(z)$.

By plotting the stable roots versus frequency, the actual modes will be revealed, as they will appear as vertical lines on these (stability) plots. So, not only $n_{m,1}$ and $n_{m,2}$ are identified as being the number of stable vertical lines on stability diagram, but also the poles can be picked. Finally, the modal contribution factors can be estimated through the method described (Ghahari, et al., 2016).

c. Bedrock Motion Estimation

Having fully identified $\tilde{h}(z)$ of both sites, the bedrock acceleration, $\ddot{x}_b[n]$, can now be recovered from any of the recorded ground surface signals by inverting $\tilde{h}(z)$, provided that such inversion produces a stable system. Nevertheless, there is no guarantee that our systems will have zeros inside the unit circle, so we have to design Finite Impulse Response (FIR) de-convolution filters $W_1(z)$ and $W_2(z)$ such that

$$\ddot{x}_b[n] = W_1(z)\, \ddot{x}_{s_1}[n] + W_2(z)\, \ddot{x}_{s_2}[n]. \tag{62}$$

In what follows, the process to calculate these FIR deconvolution filters is described. Assuming that the numerator polynomials $N_1(z)$ and $N_2(z)$ have no common zeros, we can find polynomials $V_1(z)$ and $V_2(z)$ for which the following Diophantine polynomial equation is valid

$$N_1(z)\, V_1(z) + N_2(z)\, V_2(z) = 1. \tag{63}$$

The solution of the Diophantine polynomial equation above—i.e., determination of the coefficients of the polynomials $V_1(z)$ and $V_2(z)$—is achieved through the inversion of the following linear system

$$\begin{bmatrix} \mathbf{M}_1 & \mathbf{M}_2 \\ \mathbf{0}_{2(n_1-n_2)\times n_2} & \end{bmatrix} \begin{bmatrix} \underline{\boldsymbol{V}}_1 \\ \underline{\boldsymbol{V}}_2 \end{bmatrix} = \begin{bmatrix} \mathbf{1} \\ \mathbf{0}_{(n_1+n_2)\times 1} \end{bmatrix} \tag{64}$$

where $\underline{\boldsymbol{V}}_1 = [\, V_1[0] \quad V_1[1] \quad \cdots \quad V_1[n_1-1]]^T$, $\underline{\boldsymbol{V}}_2 = [\, V_2[0] \quad V_2[1] \quad \cdots \quad V_1[n_2-1]]^T$, and $\mathbf{M}_1$ and $\mathbf{M}_2$ are the Sylvester matrices defined as below

$$\mathbf{M}_1 = \begin{bmatrix} N_1[0] & & & 0 \\ \vdots & N_1[0] & & \\ N_1[n_1-1] & \vdots & \ddots & \\ & N_1[n_1-1] & & N_1[0] \\ & & \ddots & \vdots \\ 0 & & & N_1[n_1-1] \end{bmatrix}_{(2n_1-1)\times n_1} \quad (65)$$

$$\mathbf{M}_2 = \begin{bmatrix} N_2[0] & & & 0 \\ \vdots & N_2[0] & & \\ N_2[n_2-1] & \vdots & \ddots & \\ & N_2[n_2-1] & & N_2[0] \\ & & \ddots & \vdots \\ 0 & & & N_2[n_2-1] \end{bmatrix}_{(2n_2-1)\times n_2} \quad (66)$$

In the equations above, $n_1 = 2n_{m,1} + 1$ and $n_2 = 2n_{m,2} + 1$ ($n_1 \geq n_2$) denote the number of coefficients of the polynomial $N_1(z)$ and $N_2(z)$, respectively. Now, by multiplying both sides of Eq. (63) with $\ddot{x}_b[n]$, we get

$$\ddot{x}_b[n]\, N_1(z)\, V_1(z) + \ddot{x}_b[n]\, N_2(z)\, V_2(z) = \ddot{x}_b[n] \quad (67)$$

and by replacing $\ddot{x}_b[n]\, N_1(z)$ and $\ddot{x}_b[n]\, N_2(z)$ by $\ddot{x}_{s_1}[n]\, D_1(z)$ and $\ddot{x}_{s_2}[n]\, D_2(z)$, respectively, we have

$$\ddot{x}_{s_1}[n]\, D_1(z)\, V_1(z) + \ddot{x}_{s_2}[n]\, D_2(z)\, V_2(z) = \ddot{x}_b[n] \quad (68)$$

By comparing Eqs. (62) and (68) it can be concluded that the FIR deconvolution filters $W_1(z)$ and $W_2(z)$ are

$$W_1(z) = D_1(z)\, V_1(z) \quad (69)$$

$$W_2(z) = D_2(z)\, V_2(z) \quad (70)$$

It is expedient to note here that the recovered bedrock motion is identified to within a scaling ambiguity. Due to this scaling ambiguity, it is possible to extract two bedrock motions by either $W_1(z)\, \ddot{x}_{s_1}[n]$ or $W_2(z)\, \ddot{x}_{s_2}[n]$.

Numerical Verification

To verify the proposed method, we modeled two sites with different properties as shown in **Table 3**. We considered a cubic variation of shear wave velocity with respect to depth in one site to keep the simulation as realistic/complex as possible. Natural frequencies and modal contribution factors of modes below 10 Hz are shown in **Table 4**. We limited our simulation below 10 Hz, which is typically the frequency range of interest in earthquake engineering applications. **Figure 12** displays the exact Transfer Functions of two sites within the frequency range of interest, which exhibit four and three modes that are contributing to the responses of Sites 1 and 2, respectively. As seen in this figure, the modes of both sites are very close to each

other. This brings more realism to the simulation, because it is reasonable to observe close modes for two neighboring sites.

Ground surface responses are generated by assuming vertically propagating shear waves from rigid bedrock. To make the problem as realistic as possible, ground accelerations recorded by the Corona I-15/Hwy-91 geotechnical array (CSMIP Station 13186) during the 2008 Chino Hills Earthquake at a depth of 42 meters are used as the bedrock motion. Based on the P-S logging test data available at the Center for Engineering Strong Motion Data (CESMD) database, the recorded signal at this level mimics accurately a rock motion. **Figure 13** displays the acceleration time-history of the selected bedrock excitation. In addition to the noise-free simulated data, we also analyzed a noisy case by adding Gaussian distributed white noise with Root-Mean-Square of ~10% of the generated ground surface signals (equivalent SNR = 20).

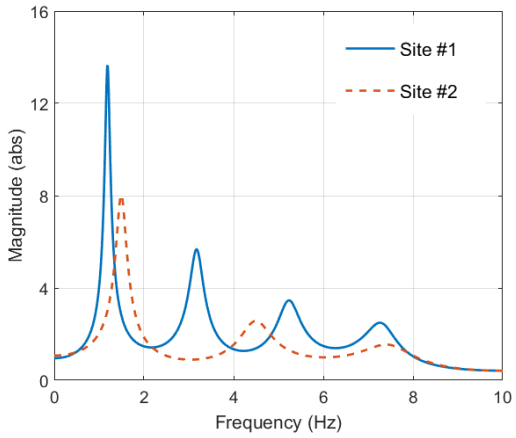

Figure 12. Exact Transfer Functions of two sites under study.

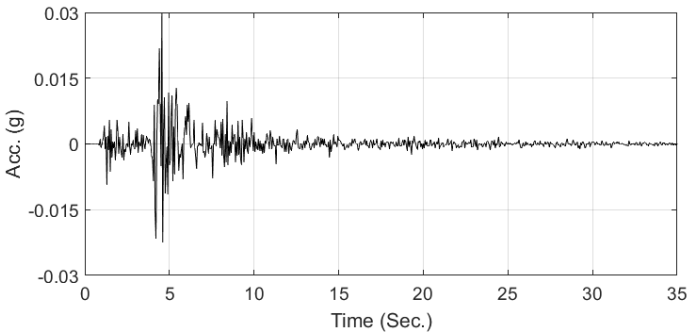

Figure 13. Bedrock acceleration (last accessed on 2/17/2016 at www.strongmotioncenter.org).

Table 3. Soil profiles at two sites.

Site	ρ (kg/m^3)	H (m)	Surface V_s (m/s)	Bottom V_s (m/s)	V_s Variation	ξ (%)*
1	2000	50	150	300	Cubic	5.00
2	2300	50	300	300	Constant	8.00

* The proposed method works for general case of having different modal damping ratios, but it is believed soil's damping is constant for all modes (Park & Hashash, 2004).

Table 4. Natural frequencies (Hz) and modal contribution factors at two sites.

	Site	1	2	3	4
Natural Frequency (Hz)	1	1.19	3.18	5.24	7.30
	2	1.50	4.50	7.50	---
Contribution Factor	1	1.37	−0.57	0.35	−0.26
	2	1.27	−0.42	0.25	---

We first assume that we know the exact number of contributing modes at each site. So, Eq. (57) is solved in one step and the roots of the polynomials $g_1(z)$ and $g_2(z)$ are identified.

Figure 14 shows the comparison between the actual poles and zeros of the two sites and the identified values. As the type of the roots (poles or zero) is not yet known, the identified roots are shown by circles. This figure shows that for the noise-free case, the identified roots match the actual roots perfectly. In the presence of noise, the locations of the poles are still accurate, but the zeros are identified with significant errors. Before employing stability diagram to classify roots as zeros and poles, it is useful to see what we would get if we consider all of the recovered roots as poles; and this comparison should clarify the utility of the algorithm described in §b above.

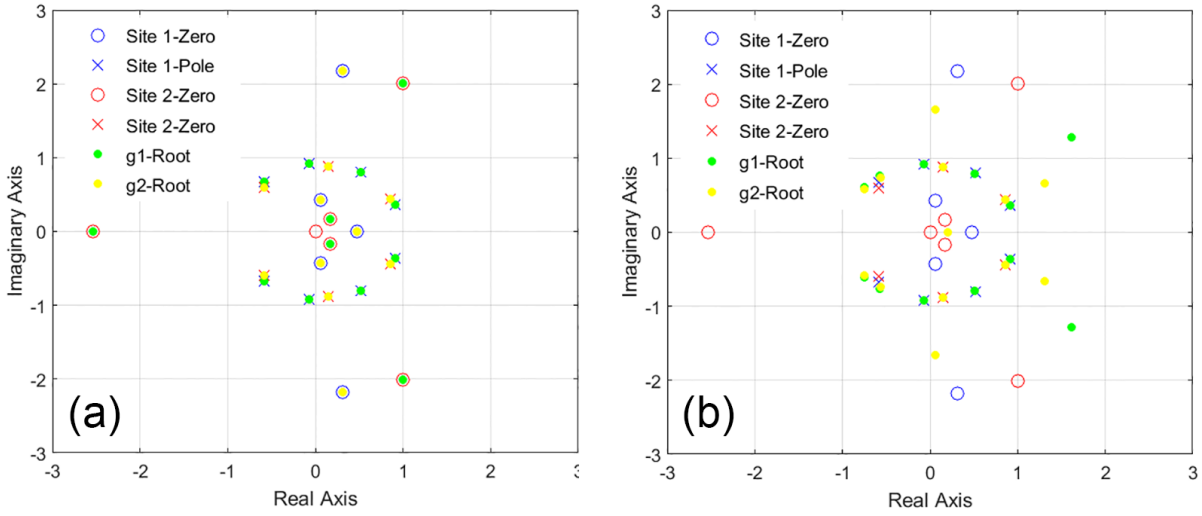

Figure 14. Comparison of the poles and zeros of two systems and roots of $g_1(z)$ and $g_2(z)$ that are recovered through Eq. (57) for (a) noise-free and (b) noisy cases.

Assuming that all of the recovered roots are poles, we can calculate the natural frequencies and damping ratios using Eqs. (59) and (60), respectively. These values are reported in **Table 5** and **Table 6** for the noise-free and the noisy cases, respectively. As seen, the zeros labeled as poles result in unusual damping ratios (see columns 5, 6, 7, 8, and 13 for Site #1 and columns 3, 4, 7, 8 9, 10, and 13 for the Site #2 in **Table 5**). While unusual damping values are observed for most of the spurious poles for the noisy case, there are a few cases that have reasonable damping ratios, which renders the pole picking step inevitable.

Table 5. Candidates of natural frequencies and damping ratios (noise-free case).

	1	2	3	4	5	6	7	8	9	10	11	12	13
Identified Modal Parameters from $g_1(z)$													
$f_n(Hz)$	1.19	1.19	3.18	3.18	4.36	4.36	5.13	5.13	5.24	5.24	7.30	7.30	10.43
$\xi_n(\%)$	5	5	5	5	−58.8	−58.8	87.4	87.4	5	5	5	5	−28.4
Identified Modal Parameters from $g_2(z)$													
$f_n(Hz)$	1.50	1.50	2.35	3.57	4.50	4.50	5.19	5.19	5.28	5.28	7.50	7.50	13.26
$\xi_n(\%)$	8	8	100	−100	8	8	−48.3	−48.3	50.7	50.7	8	8	−65.7

Table 6. Candidates of natural frequencies and damping ratios (noisy case).

	1	2	3	4	5	6	7	8	9	10	11	12	13
	Identified Modal Parameters from $g_1(z)$												
$f_n(Hz)$	1.19	1.19	3.13	3.13	3.18	3.18	5.26	5.26	7.08	7.08	7.81	7.81	7.92
$\xi_n(\%)$	5	5	−73.2	−73.2	5.5	5.5	5.2	5.2	2.0	2.0	1.4	1.4	−100
	Identified Modal Parameters from $g_2(z)$												
$f_n(Hz)$	1.50	1.50	1.91	1.91	4.50	4.50	5.02	5.14	5.14	7.07	7.07	7.90	7.90
$\xi_n(\%)$	8.3	8.3	−63.7	−63.7	7.5	7.5	100	−31.5	−31.5	3.3	3.3	2.1	2.1

In addition to the observations above, we assumed, up to now, that we know the exact number of modes of two sites, which is often not possible in real-life. Also, due to presence of noise, it is necessary to increase the number of roots of $g_1(z)$ and $g_2(z)$ and then to discard the extraneous roots. As such, we carry out the procedure described in §b. We solve Eq. (57) for a range of $\tilde{L}$ from 14 (exact for the noise free) up to 40.

Figure 15 displays all singular values of the matrix $[\mathbf{X}_1 \quad -\mathbf{X}_2]$ corresponding to each order value. Instead of $\tilde{L}$, we use $L^{-}+1$ for the X-axis, because the number of small singular values for each case must be theoretically equal to $L^{-}+1$. As seen from this figure, such relationship is observed for the noise-free case wherein the X-axis denotes the number of small singular values. Yet, a similar observation cannot be made for the noisy case. As such, we cannot determine the exact order of the problem by counting the number of small singular values. Instead, we take advantage of the stability diagram shown in **Figure 16**. In this figure, the roots that have rational/justifiable damping ratios (between zero and %100) are shown by cross marks. As seen, for the theoretical value of L=14, two close frequencies are identified for both sites for the last mode (See **Table 5** and **Table 6**) in the noisy case, and none of them are correct.

By applying the stability criteria $E(\omega_m) \leq \%1$ and $E(\xi_m) \leq \%15$[6], stable modes are detected, which are marked by red circles. As seen, four and three stable vertical lines are clearly detected for Sites #1 and #2, respectively, for both the noise-free and the noisy cases. Also, values of the natural frequencies and damping ratios of these 7 modes are easily obtained from the stable modes at the last $\tilde{L}$ value. These values are reported in **Table 7**. Also, using approach described in (Ghahari, et al., 2016), the modal contribution factors are identified. As seen, the natural frequencies, damping ratios, and modal contribution factors are highly accurate. To visualize the accuracy of the identified results, the exact and reconstructed transfer functions of the noisy case are shown in **Figure 17** (noise-free transfer functions are perfectly matched).

[6] It is well accepted that estimated damping ratios are highly unstable, so we allow much larger variation for damping compared to the natural frequency.

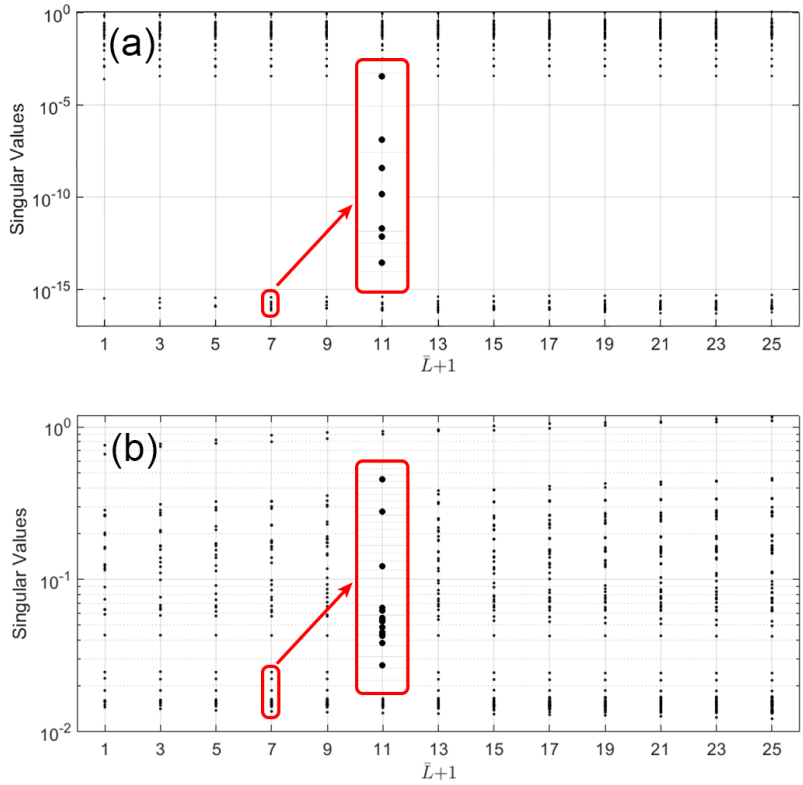

Figure 15. Distribution of singular values versus $\bar{L}+1$ for (a) noise free and (b) noisy cases.

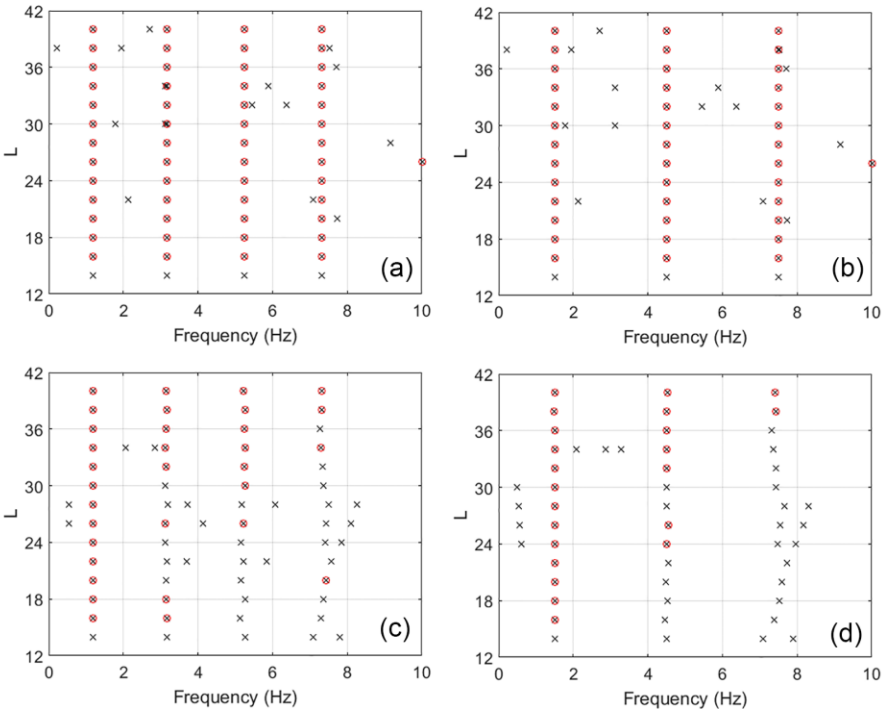

Figure 16. Stability diagrams for (a) Site #1, noise-free, (b) Site #2, noise-free, (c) Site #1, noisy, and (d) Site #2, noisy cases.

Table 7. Comparison between exact and identified modal properties through stability approach.

	Site #1									Site #2								
	$f_n(Hz)$			$\xi_n(\%)$			β_n			$f_n(Hz)$			$\xi_n(\%)$			β_n		
Mode No.	0*	1†	2‡	0	1	2	0	1	2	0	1	2	0	1	2	0	1	2
1	1.19	1.19	1.19	5	5	4.9	1.37	1.37	1.37	1.50	1.50	1.50	8	8	8.3	1.27	1.27	0.97
2	3.18	3.18	3.14	5	5	5.8	−0.57	−0.56	−0.52	4.50	4.50	4.53	8	8	7.4	−0.42	−0.41	−0.51
3	5.24	5.24	5.23	5	5	4.8	0.35	0.34	0.38	7.50	7.50	7.42	8	8	5.2	0.25	0.25	0.18
4	7.30	7.30	7.33	5	5	3.3	−0.26	−0.25	−0.19	---	---	---	---	---	---	---	---	---

* Exact, † Identified from noise-free data, ‡ Identified from noisy data

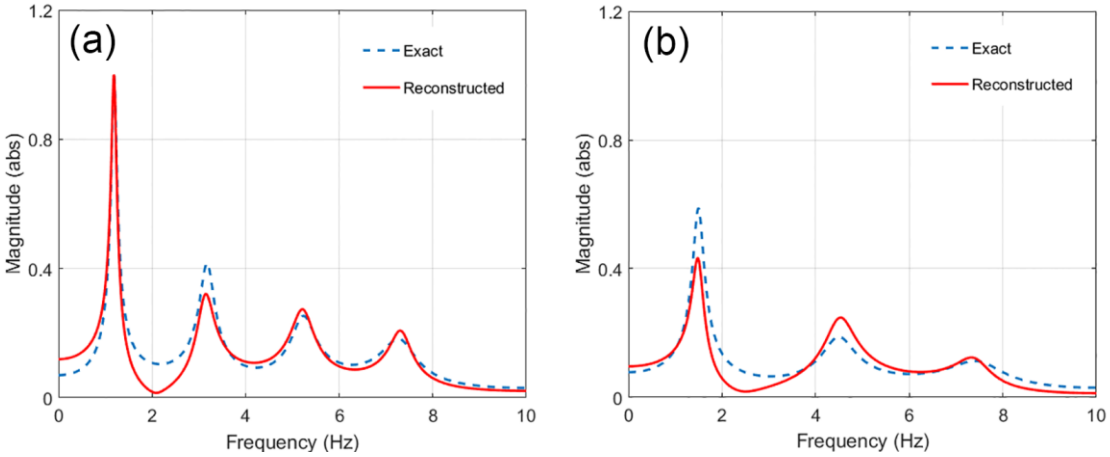

Figure 17. Comparison between the exact and the reconstructed Transfer Functions obtained from noisy data using the stability approach for (a) Site #1 and (b) Site #2.

Now, by having both sites' Transfer Functions identified using the stability diagram approach, we can recover the bedrock motion from recorded ground surface accelerations through approach proposed in §d. The recovered bedrock motion using the said approach is compared with the exact bedrock motion in **Figure 18** in the frequency domain. It is not surprising to see a near-perfect match for the noise-free case, because both the recorded signals and identified systems are exact. For the noisy cases, there are two sources of error observed between the exact and the identified results. First, as it was shown in **Figure 17**, the systems are not identified perfectly and thus we expect to see some errors, especially around 1Hz (see also **Figure 17**b). Second, the recorded signals are highly noisy, so the recovered bedrock motion is a noisy version of the actual bedrock motion. This source of error is mostly observed for high frequencies, where the system's Transfer Function has little amplification.

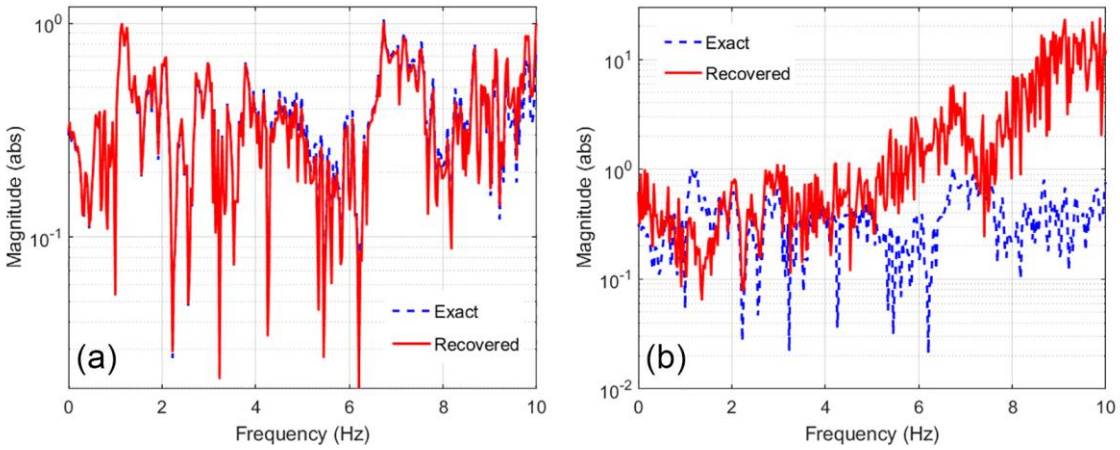

Figure 18. Comparison between Fourier spectrum of exact and recovered bedrock motion for (a) noise free and (b) noisy cases.

Conclusions

This study presented the theoretical basis for an ongoing CGS-funded project whose ultimate objective is to quantify the spatial variability in *bridge* Foundation Input Motions (FIMs) using data recorded during the 2014 South Napa Earthquake. This aspect comprised the development and verification of two distinct (and new) methods. The first of these was an output-only system identification method that yields time-history estimates of FIMs at all bridge piers from accelerations recorded on the bridge. The second was a blind channel identification method that enables the identification of local site effects at each pier provided that all FIMs are caused by a single excitation source and the kinematic interaction is similar at all piers. While these assumptions (especially the latter) can be relaxed, as needed, in future studies, the two methods will combine to produce quantified estimates of spatial variability in real-life ground motions. The accuracy of these two key methods was verified in the present study through synthetic, albeit realistic, datasets.

In addition to developing and verifying the two methods required to achieve the project's objectives, the present study allowed the determination of datasets from the 2014 event that are amenable to detailed analyses (short bridges, and bridges with missing data were excluded). It also provided preliminary evidence—simply by using signals recorded at the foundation levels of instrumented bridges—that there is indeed significant spatial variability in real-life ground motion. The results of the application of the proposed approach to the real-life data recorded during the 2014 event will be presented in SMIP17.

Acknowledgements

The work presented in this manuscript was funded, in part, by the California Geological Survey (Contract No. 1014-963) and by the California Department of Transportation (Grant No. 65A0450). Any opinions, findings, conclusions or recommendations expressed in this material are those of the authors and do not necessarily reflect the views of the sponsoring agencies.

References

Åström, K., Hagander, P. & Sternby, J., 1984. Zeros of sampled systems. *Automatica,* 20(1), 31-38.

Bayes, T., 1763. An essay towards solving a problem in the doctrine of chances. *Philosophical Transactions of the Royal Society of London,* 53(1), 370-418.

Bendat, J. & Piersol, A., 1980. Engineering applications of correlation and spectral analysis. New York: John Wiley.

Bodeux, J. & Golinval, J., 2001. Application of ARMAV models to the identification and damage detection of mechanical and civil engineering structures. *Smart Materials and Structures,* 10, 479-489.

Burdette, N., Elnashai, A., Lupoi, A. & Sextos, A., 2008. Effect of asynchronous earthquake motion on complex bridges. I: methodology and input motion. *J. of Bridge Eng.,* 13(2), 158-165.

Chopra, A., 2001. *Dynamics of Structures.* 2nd ed., Prentice-Hall, Englewood Cliffs, NJ.

Ebrahimian, H., Astroza, R. & Conte, J., 2015. Output-only identification of civil structures using nonlinear finite element model updating. San Diego, SPIE, pp. 1-9.

Ghahari, S., Abazarsa, F., Ghannad, M. & Taciroglu, E., 2013. Response-only modal identification of structures using strong motion data. *Earthquake Engineering and Structural Dynamics,* 42(8),1221-1242.

Ghahari, S. et al., 2016. Blind identification of site effects and bedrock motions from surface response signals. *Soil Dynamics and Earthquake Engineering,* (under review).

Glaser, S., 1996. Insight into liquefaction by system identification. *Geotechnique,* 46(4), 641-655.

Gürelli, M. & Nikias, C., 1995. EVAM: An eigenvector-based algorithm for multichannel blind deconvolution of input colored signals. *IEEE Trans. on Signal Processing,* 43(1), pp. 134-149.

Hao, H., Bolt, B. & Penzien, J., 1989. Effects of spatial variation of ground motions on large multiply-supported structures: Earthquake Engineering Research Center.

Huang, H., Yang, J. & Zhou, L., 2010. Adaptive quadratic sum-squares error with unknown inputs for damage identification of structures. *Struct. Control & Health Mon.,* 17(4), 404-426.

Kalman, R., 1960. A new approach to linear filtering and prediction problems. *Journal of basic Engineering,* 82(1), 35-45.

Kurata, M. et al., 2012. Internet-enabled wireless structural monitoring systems: development and permanent deployment at the new Carquinez suspension bridge. *Journal of Structural Engineering,* 139(10), 1688-1702.

Lupoi, A., Franchin, P., Pinto, P. & Monti, G., 2005. Seismic design of bridges accounting for spatial variability of ground motion. *Earthquake Engineering & Structural Dynamics,* 34(4-5), 327-348.

Moulines, E., Duhamel, P., Cardoso, J. & Mayrargue, S., 1995. Subspace methods for the blind identification of multichannel FIR filters. *IEEE Transactions on Signal Processing,* 43(2), 516-525.

Nazmy, A. & Abdel-Ghaffar, A., 1992. Effects of ground motion spatial variability on the response of cable-stayed bridges. *Earthquake Engineering & Structural Dynamics,* 21, 1-20.

Oppenheim, A., Schafer, R. & Buck, J., 1989. *Discrete-Time Signal Processing* (2nd ed.), Prentice-Hall, Englewood Cliffs, NJ.

Park, D. & Hashash, Y., 2004. Soil damping formulation in nonlinear time domain site response analysis. *Journal of Earthquake Engineering,* 8(02), 249-274.

Shakal, A., Haddadi, H. & Huang, M., 2014. Highlights of strong-motion data from the M6.0 South Napa earthquake of August 24, 2014, Calif. Geological Survey, pp. 111-130.

Xu, G., Liu, H., Tong, L. & Kailath, T., 1995. A least-squares approach to blind channel identification. *IEEE Transactions on Signal Processing,* 43(12), 2982-2993.

Zerva, A., Ang, A. & Wen, Y., 1988. Lifeline response to spatially variable ground motions. *Earthquake Engineering & Structural Dynamics,* 16(3), 361-379.

Zerva, A. & Zervas, V., 2002. Spatial variation of seismic ground motions: An overview. *Applied Mechanics Reviews,* 55(3), 271-297.

INVESTIGATION OF GROUND MOTIONS RECORDED DURING THE 2014 SOUTH NAPA EARTHQUAKE

Tadahiro Kishida[1], Silvia Mazzoni[1], Yousef Bozorgnia[1], Brian Chiou[2], Robert Darragh[3], Hamid R. Haddadi[4], Robert Kayen[5], Christopher Markham[6], Sifat Muin[1], and Walt Silva[3]

[1]Pacific Earthquake Engineering Research Center, University of California, Berkeley
[2]California Department of Transportation. Sacramento
[3]Pacific Engineering and Analysis, El Cerrito
[4]California Geological Survey, Sacramento
[5]US Geological Survey, Menlo Park and University of California, Berkeley
[6]Exponent, Oakland

Abstract

The 2014 South Napa mainshock caused significant damage in the Northern California Bay Area. Time series from a foreshock, mainshock, and three aftershocks were collected from various agencies. These were processed following the Pacific Earthquake Engineering Research Center (PEER) standard data-processing methods, and a ground-motion database was developed. Metadata such as fault style, source-to-site distance, average shear wave velocity in the top 30 m (V_{s30}), and basin depth were collected. Shear wave velocity profiles were also measured by the Spectral Analysis of Surface Wave Dispersion (SASW) technique at selected strong-motion stations. These datasets were combined in the ground motion database and compared to the Ground Motion Models (GMMs) from the NGA-West2 studies to evaluate the regional attenuation of these events. Time series at two geotechnical downhole array sites were also collected from 29 earthquakes to calculate apparent wave velocities from wave travel times and empirical transfer functions to understand wave amplification. Characteristics of pulse-like records from the South Napa and NGA-West2 databases were also analyzed to compare near-fault regions between these databases. The influence of pulse-like records was also investigated using inelastic response spectra to understand the damage potential on structures. These observed ground-motion characteristics are summarized in this study.

Introduction

The M6.0 South Napa earthquake occurred on August 24, 2014. The epicenter was located approximately 9 km south of the city of Napa in northern California. Residential structures and wineries surrounding this area were significantly damaged. After the earthquake, PEER summarized various preliminary observations, in which the following ground motion characteristics were described (Kishida et al. 2014a). In a comparison of the ground motion attenuation from the South Napa earthquake with the median NGA-West2 GMMs (e.g. Campbell and Bozorgnia 2014), the attenuation rate was higher from the South Napa event especially for relatively high-frequency 5%`damped PSA. Baltay and Boatwright (2015) observed similar trends and noted that the northern California Bay Area has stronger attenuation compared to the average value of attenuation in the GMMs. To confirm these observations, the ground motion database was expanded by collecting the time series from one foreshock and three aftershocks of

the South Napa mainshock. The shear wave velocity profiles were also measured by the Spectral Analysis of Surface Wave Dispersion (SASW) technique at selected strong-motion stations. Combining these data, a ground motion database was developed to evaluate the regional attenuation in the northern California Bay Area.

The second characteristic observation was that two geotechnical downhole arrays operated by the California Strong Motion Instrumentation Program (CSMIP) in partnership with California Department of Transportation (Caltrans) (CE68206 and CE68259) located on the south side of the Carquinez Bridge (I-80) recorded PGAs of approximately 1g and 0.42g, respectively, during the 2014 South Napa mainshock. The hypocentral distance was approximately 20 km; hence the observed PGAs were unusually high compared to GMMs. These high PGAs were explained after the earthquake with potential causes such as local site effects, soil–structure interaction effects, or possible basin effects (Kishida et al. 2014a, Çelebi et al. 2015). Çelebi et al. (2015) analyzed the recorded time series and concluded that these large PGAs were caused by local site effects. To further understand wave propagation at the two downhole arrays, time series from 29 previous earthquakes also were collected from the Center for Engineering Strong Motion Data (CESMD 2014). Using this database, apparent wave velocities and empirical transfer functions (ETF) were calculated between sensors at different depths in the downhole arrays from wave travel times and ratios of Fourier amplitude spectrum (FAS), respectively.

The third characteristic was that pulse-like motions were observed in the velocity time series at several stations in near fault region. These large velocity pulses were observed during mainshock especially in the forward directivity direction (Kishida et al. 2014a). These pulses could possibly be related to the extensive damage observed at structures and wineries in the city of Napa. To understand these effects, we evaluated all the time series in the database for pulse characterization and compared these to the NGA-West2 database to define the region with potential damage from pulse-like velocity time histories. We also investigated the inelastic response spectra of the pulse-like waveforms to understand the pattern of observed damage during 2014 South Napa mainshock.

Ground Motion Database

Table 1 is the catalog of processed earthquakes in the South Napa sequence developed in this study. The moment magnitudes (**M**) were obtained from Northern California Earthquake Data Center (NCEDC). Hypocenter locations were similarly obtained from NCEDC using the double-difference method as described in Waldhauser and Ellsworth (2000). Time series were obtained from CESMD, Incorporated Research Institutions for Seismology (IRIS), NCEDC, and the California Department of Water Resource (CDWR). Approximately 1,350 records have been processed and filtered following the standard PEER data processing methods (Chiou et al. 2008, Ancheta et al. 2013) to provide uniformly processed time series, PSA at various dampings and Arias Intensity. Instrument corrections were also applied when the response of sensors was not directly proportional to acceleration. A time window for data processing was selected following the recommendations of previous studies (Goulet et al. 2014, Kishida et al. 2014b). An acausal Butterworth bandpass filter was applied after reviewing the FAS shape and the signal-to-noise ratio between the S-wave and the pre-event noise window (when available) on a component-by-component basis (e.g. Darragh et al. 2004, Chiou et al. 2008, Boore et al. 2012). 5%-damped

PSA were calculated at selected frequencies for all processed time series following Ancheta et al. (2013). The metadata from all the processing steps were also stored in the database such as record start time, location of station, time window locations, and applied high-pass and low-pass filter corner frequency. For approximately 500 stations in the database, estimates of V_{s30} were obtained from SASW performed for this study, the NGA-West2 study (Seyhan et al. 2014), or approaches that followed methodologies in the study by Seyhan et al. (2014) and Wills et al. (2015). The depths to bedrock were obtained from the USGS study (Aaggard et al. 2010). Directivity parameters were also obtained for the mainshock following the approach by Chiou and Youngs (2014) that used the finite fault model of Dreger et al. (2015).

Figures 1(a) – 1(c) show the attenuation of PGA, PSA(1.0s) and PSA(3.0s) with closest distance (R_{rup}) for the South Napa earthquake mainshock. The median of the four GMMs by Abrahamson et al. (2014), Boore et al. (2014), Campbell and Bozorgnia (2014), and Chiou and Young (2014) are also shown. At PGA, the median GMM prediction fits well to the observations at shorter distances (R_{rup} < 20 km), whereas it tends to over-predict as distance increase. At PSA of 1.0 and 3.0 s, the median prediction slightly underestimated the data at shorter distances, but fits better at greater distances. Baltay and Boatwright (2015) observed similar trends and explained that the over-prediction of high frequency at greater distance was due to the stronger regional attenuation in this area of northern California. Figures 1(d)-1(f) shows the residuals plotted on a regional map. Positive residuals become prominent in the region north of the mainshock epicenter as period increases. Figures 1(g)-1(i) show the residuals against delta DPP which was the directivity indicator used by Chiou and Youngs (2014). Clear directivity effects were observed in these figures for PSA(3.0s). These effects become unclear as period decreases. Baltay and Boatwright (2015) similarly observed positive correlations with residuals against DPP. Figures 1(j) – 1(l) show the attenuation of PGA with closest distances (R_{rup}) for the three aftershocks. Stronger attenuation with distance were also observed for all three events compared to the median GMM with R_{rup}.

Table 1. Catalog for the South Napa earthquake sequence in the PEER Database

Earthquake Name	Origin Time (Year-Mo-DyTHr:Mn:Sc)	Latitude (°N)	Longitude (°E)	Depth (km)	**M**
Foreshock	2014-08-05T12:40:01	38.2557	-122.323	8.20	3.03
Mainshock	2014-08-24T10:20:44	38.21517	-122.312	11.12	6.02
Aftershock1	2014-08-24T12:47:12	38.23833	-122.343	8.439	3.60
Aftershock2	2014-08-26T12:33:16	38.1785	-122.301	12.577	3.90
Aftershock3	2014-08-31T08:56:20	38.23583	-122.329	9.55	3.24

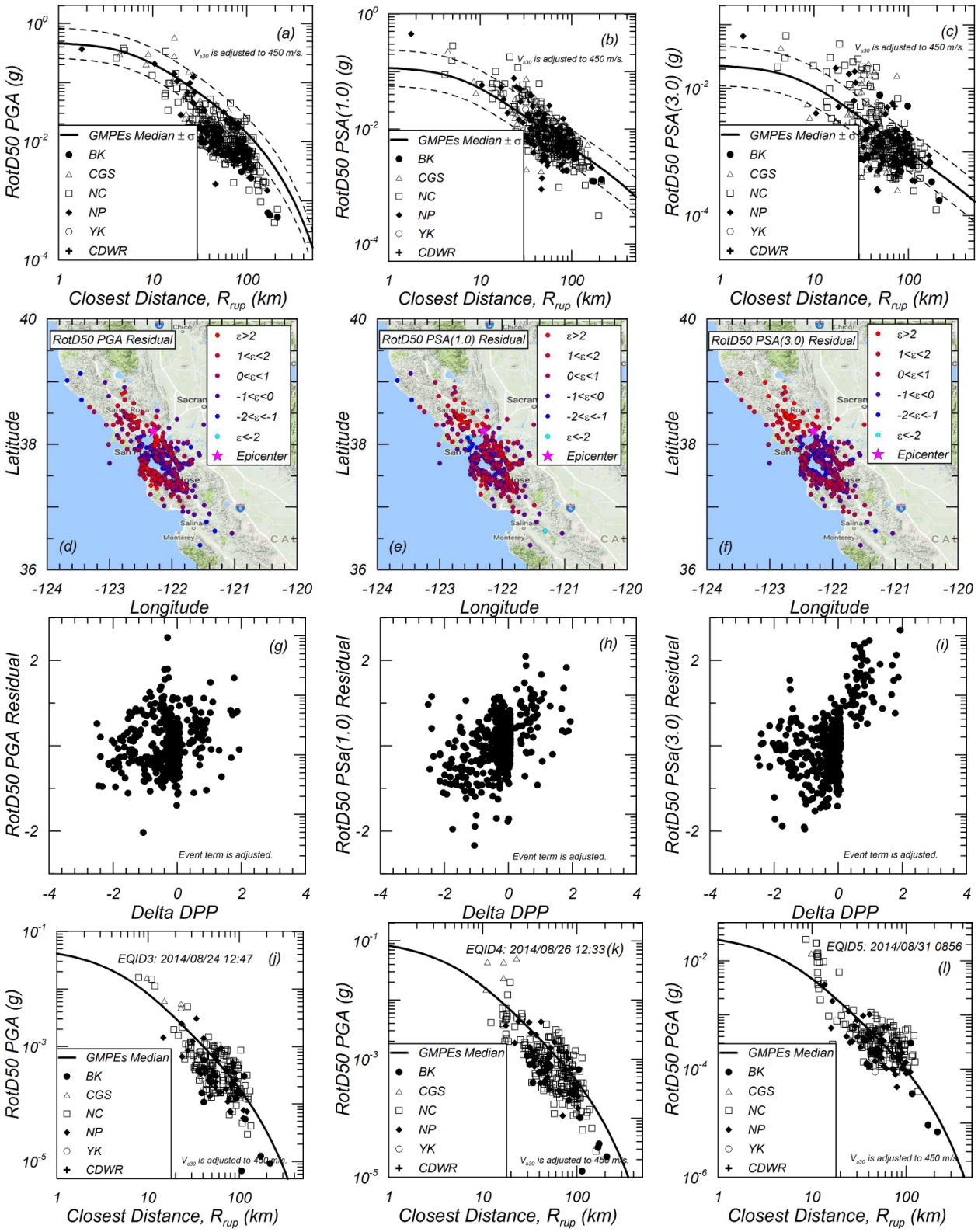

Figure 1. Variations in (a) PGA, (b) PSA(1.0s), (c) PSA(3.0s) against Rrup, variations in residuals of (d)PGA, (e) PSA(1.0s) and (f)PSA(3.0s) on a map, variations in residuals of (g) PGA, (h) PSA(1.0) and (i) PSA(3.0) against Delta DPP for 2014 South Napa mainshock, variations in PGA for three aftershocks (j)EQID3, (k) EQID4, and (l) EQID5 against R_{rup}.

Site Characterization of Strong-Motion Stations by SASW

SASW were performed at 15 strong-motion stations. Table 2 lists these stations, which were selected based on the several factors such as number of recordings in the database, the significance of the strong shaking during the mainshock, and velocity information available in NGA-West2 site database (Seyhan et al. 2013). Figure 2 show pictures of a typical SASW layout. Figure 3 shows an example of the surface wave dispersion curves produced by SASW at the geotechnical downhole array at the south end of the Carquinez Bridge. Surface waves were generated by a truck and recorded by a linear array of seismometers. Figure 4 shows the comparison of the V_s profile from SASW to the suspension logging results from CSMIP (CESMD 2014). These two V_s profiles agree well at depth, while the SASW method provides V_s measurements to the surface.

Table 2. Station list of Vs measurements by SASW

Station Name	Network	Station ID	Latitude (°N)	Longitude (°E)	# of records
Napa - Napa College	CGS	68150	38.270	-122.277	4
Green Valley Road	NC	NGVB	38.280	-122.216	4
Huichica Creek	NC	NHC	38.217	-122.358	5
Lovall Valley Loop Rd	NC	N019B	38.301	-122.402	4
Oakmont	NP	1835	38.442	-122.607	4
Martinez	NP	1847	38.0130	-122.134	4
Glen Ellen	NP	1848	38.367	-122.524	4
McCall Drive, Benicia, CA	NC	C032	38.083	-122.158	5
Main St, Napa, CA	NP	N016	38.299	-122.285	5
Vallejo_FD	NP	1759	38.108	-122.256	2
Napa; Fire Station No. 3	NP	1765	38.330	-122.318	2
NMI	NC	NMI	38.076	-122.259	2
Sonoma	NP	1829	38.290	-122.461	3
Old Carquinez Bridge north free-field	CGS	68184	38.0675	-122.226	1
Carquinez Bridge Geotechnical Array	CGS	68206	38.056	-122.226	3

Figure 2. Example pictures of SASW testing equipment

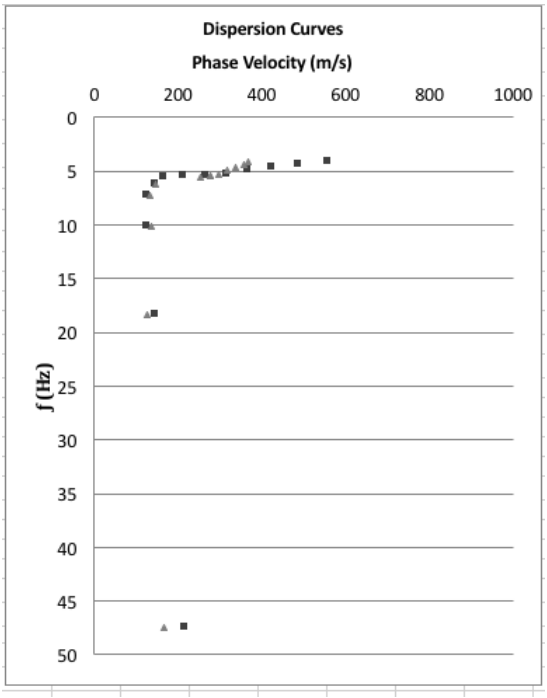

Figure 3. Surface wave dispersion curves at Carquinez Bridge Geotechnical Array (68206)

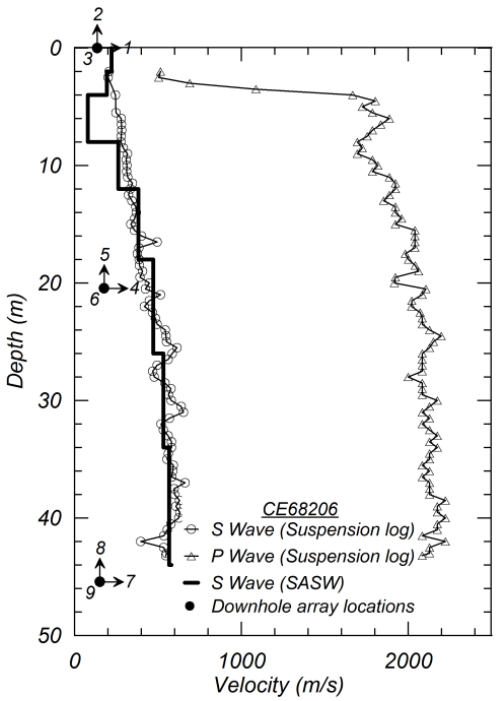

Figure 4. Comparison of the SASW Vs profile with suspension logging results

Carquinez Bridge Geotechnical Array Recordings

The Carquinez Bridge geotechnical array (CE68206) recorded peak ground acceleration of approximately 1.0g at ground surface during 2014 South Napa earthquake. To understand this observation downhole records were collected and processed from 29 previous earthquakes at this array and the nearby CE68259 array. The apparent wave velocities between sensors at depth and empirical wave amplification were estimated. Table 3 lists these earthquakes for which magnitude ranged from 2.2 to 6.0.

Apparent Wave Velocities

Apparent V_s and V_p were calculated between downhole recordings by computing wave travel times. Two analyses were conducted to calculate these velocities. The first was cross-correlation method (CCM) (e.g. Elgamal et al. 1995), and the second was the normalized input-output method (NIOM) (Haddadi and Kawakami, 1998). Incident P- and S-wave-travel times were only considered in the analyses. Figure 5a shows the comparison of apparent wave velocities with field measurements for both of the geotechnical arrays. It shows reasonable agreement between apparent wave velocities and field measurements, where 91% of velocity measurements from CCM and NIOM were within ±30% of the measured velocity. Figure 5b shows the same dataset, however, the x-axis is the difference in apparent velocities between CCM and NIOM methods. The data with large differences between apparent and measured wave velocities also have large differences between the values from CCM and NIOM. Therefore, these data were removed from further analyses when the differences between CCM and NIOM were

greater than 30%. This screening process reduced the percentage of erroneous data (i.e. the difference greater than 30% from the measured velocity) from 9% to 2%.

Table 3. Earthquakes recorded at geotechnical downhole arrays (CE68206 and CE68259)

Earth quake Name	Origin Time (Year-Mo-DyTHr:Mn:Sc)	Earthquake Location	Latitude (°N)	Longitude (°E)	Depth (km)	**M**
1	2006-08-03T03:08:12.86	Glen Ellen	38.3635	-122.589	8.55	4.5
2	2006-12-21T03:12:28.76	Berkeley	37.85717	-122.245	8.643	3.6
3	2007-03-02T04:40:00.75	Lafayette	37.8965	-122.111	15.981	4.23
4	2007-07-20T11:42:22.36	Oakland	37.804	-122.193	5.262	4.2
5	2007-10-31T03:04:54.81	Alum Rock	37.4335	-121.774	9.741	5.45
6	2008-06-04T02:29:04.15	Green Valley	38.24183	-122.184	10.065	3.96
7	2008-09-06T04:00:15.25	Alamo	37.862	-122.008	16.328	4.1
8	2011-01-08T00:10:16.74	Seven Trees	37.28717	-121.658	9.593	4.1
9	2011-08-24T16:57:44.12	San Leandro	37.74517	-122.151	8.632	3.38
10	2011-10-20T21:41:04.26	Berkeley	37.857	-122.253	7.989	3.95
11	2011-10-21T03:16:05.26	Berkeley	37.86083	-122.257	7.939	3.84
12	2011-10-27T12:36:44.46	Berkeley	37.86666	-122.261	7.99	3.62
13	2012-02-16T02:09:14.05	Crockett	38.07667	-122.233	8.827	3.55
14	2012-02-16T17:13:20.58	Crockett	38.07817	-122.234	8.247	3.54
15	2012-03-16T02:56:49.65	Crockett	38.07367	-122.23	7.464	2.48*
16	2014-01-14T04:18:17.60	Vallejo	38.0985	-122.238	8.157	2.76*
17	2014-04-28T21:53:24.41	Vallejo	38.093	-122.253	8.024	2.23*
18	2014-08-24T10:20:44.07	American Canyon	38.21517	-122.312	11.12	6.02
19	2014-08-24T12:47:12.55	Napa	38.23833	-122.343	8.439	3.6
20	2014-08-26T00:02:34.67	Napa	38.24033	-122.341	6.927	2.79*
21	2014-08-26T12:33:16.84	American Canyon	38.1785	-122.301	12.577	3.9
22	2014-08-26T12:35:52.99	American Canyon	38.17567	-122.307	11.473	2.7*
23	2014-08-26T13:12:19.96	American Canyon	38.17933	-122.297	10.006	2.71*
24	2014-08-31T08:56:20.83	Napa	38.23583	-122.329	9.55	3.24
25	2014-09-01T01:41:14.29	American Canyon	38.17717	-122.31	9.141	2.47*
26	2014-09-04T10:56:23.17	American Canyon	38.18033	-122.303	10.937	2.93*
27	2014-09-29T07:17:01.22	American Canyon	38.177	-122.303	11.711	2.5*
28	2015-04-01T14:07:47.16	San Pablo	37.97017	-122.352	4.85	2.67*
29	2015-04-02T07:06:03.87	San Ramon	37.792	-121.987	9.89	3.61

*Magnitude is obtained from Md.

Apparent V_s were calculated by varying the azimuthal angles (rotated by 1°) from the two horizontal time series. Figures 6(a) and (b) show the variation in apparent V_s near the ground

surface with azimuthal angle for CE68206 and CE68259, respectively. The results show the clear negative correlation of apparent velocities with the PGA along the rotated azimuthal angle in the mainshock. Figure 7(a) and (b) show the variation of apparent wave velocity with PGA for the two geotechnical arrays from all the earthquakes. It shows that the wave velocity decreases near the ground surface as PGA increases, which may indicate nonlinear soil behavior due to strong shaking. ETFs are also calculated at CE68206 and CE68259 and compared with the theoretical transfer functions (TTF) in Figure 8(a) and (b), respectively. The figure shows good agreement between these two transfer functions, especially for the resonance modes, although the amplification factors are different between these due to differences in damping. During the South Napa mainshock, there is a clear broadening of resonance periods near 6-10 Hz at CE68206.

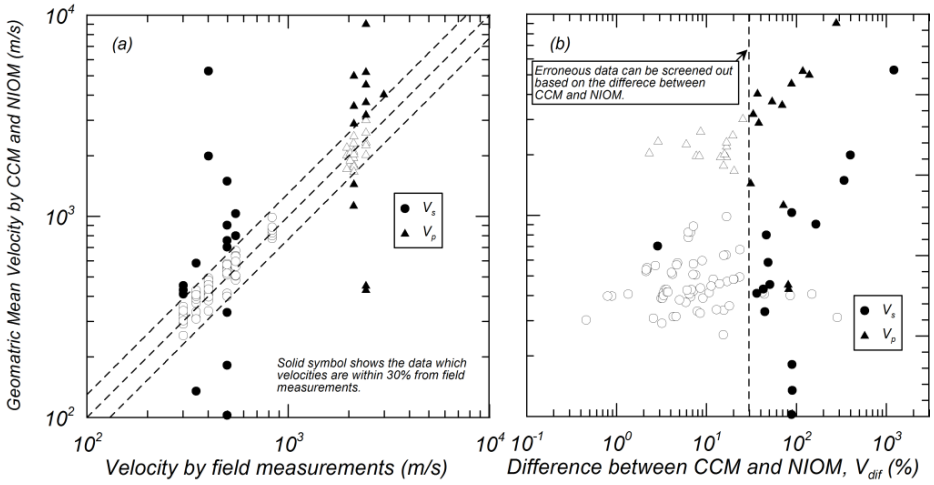

Figure 5. Comparison of apparent wave velocities (a) with field measurements (b) between CCM and NIOM.

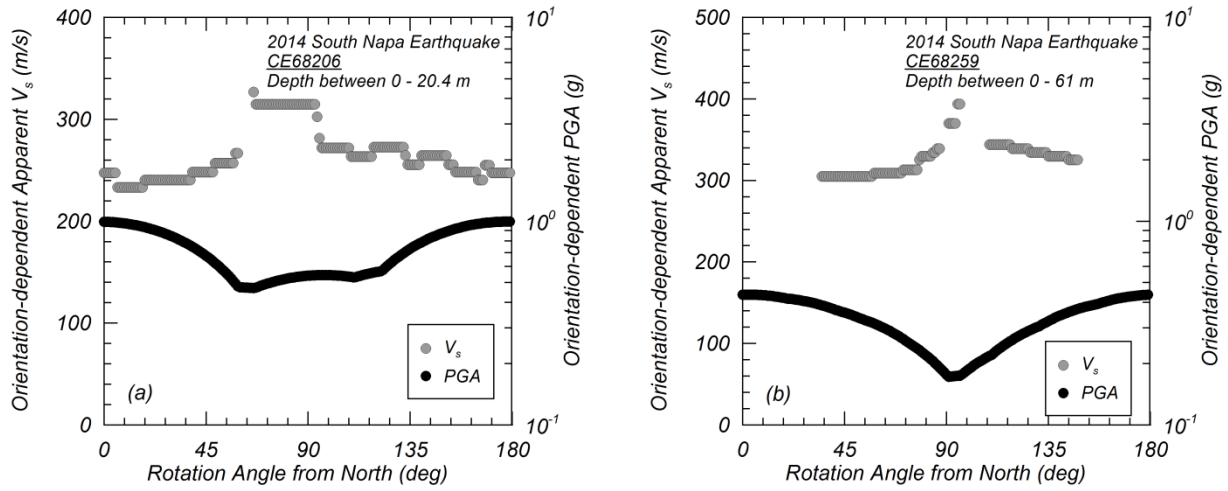

Figure 6. Variation in apparent V_s depending on rotation angle with PGA at (a) CE68206 and (b) CE68259 during the 2014 South Napa earthquake.

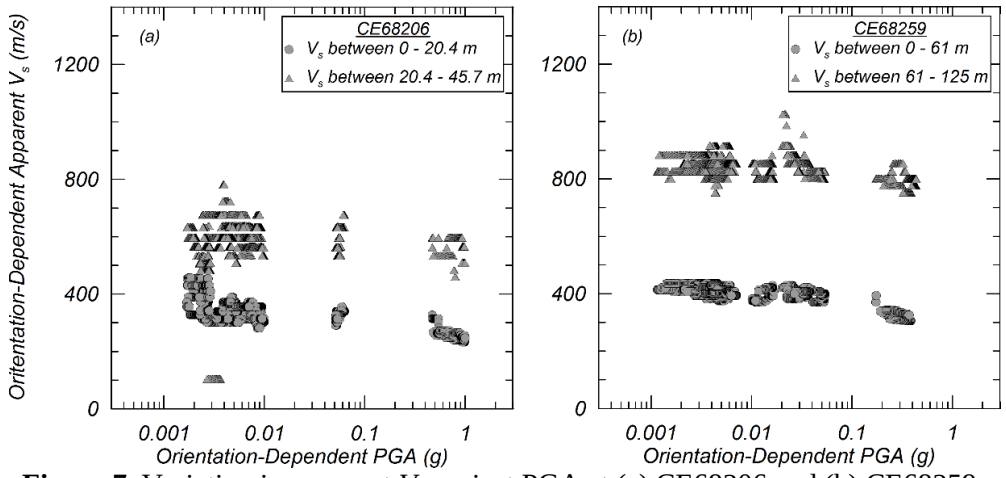

Figure 7. Variation in apparent V_s against PGA at (a) CE68206 and (b) CE68259.

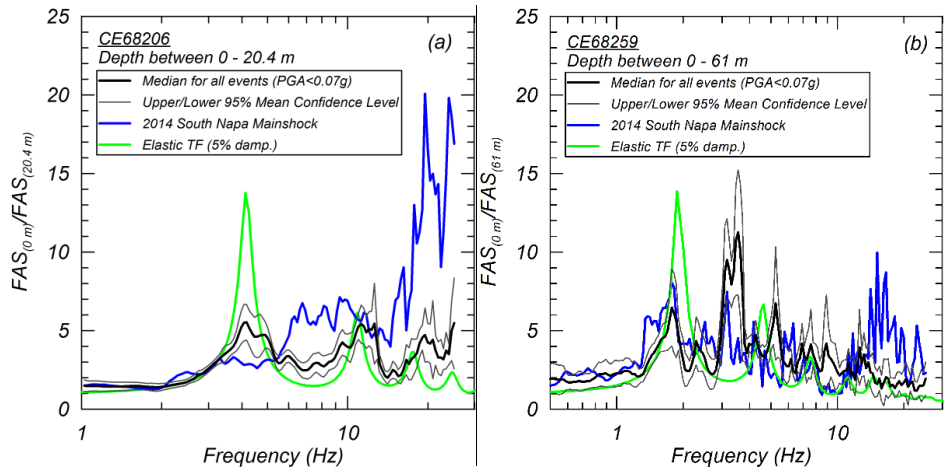

Figure 8. Empirical transfer functions at (a) CE68206 and (b) CE68259.

Identification of Velocity Pulses for Near-Fault Records

Pulses in the velocity time history were observed at near fault stations during the mainshock of the 2014 South Napa earthquake (Kishida et al. 2014a). After the development of the ground motion database, the entire database was analyzed to identify pulse-like records. The methodologies developed by Hayden et al. (2014) and Shahi and Baker (2014) were implemented and compared. Table 4 shows a summary of the recordings identified as pulse-like records in South Napa database; all pulse-like recordings were from the mainshock. A pulse was identified at 7 stations by at least one of the two methods. Differences exist in the calculated pulse period as well as the pulse azimuth (i.e., azimuth of max pulse and azimuth of max peak-to-peak for the Shahi and Baker 2014 and Hayden et al. 2014 methods, respectively) presented in Table 4.

Figure 9 shows example velocity time series, which were identified as pulse-like recordings by both methods. The time series were rotated to the azimuthal angle in which the pulse characteristics were identified. This figure shows maximum velocities of approximately 80 cm/s and clear velocity pulses in both recordings. Figure 10 shows the locations of the stations

where the pulse-like records were identified by either method. Most of the stations were located in the forward directivity region of the fault rupture (e.g. Dreger et al. 2015), whereas the Vallejo – Broadway & Sereno recording site was located in the backward directivity region. The Vallejo – Broadway & Sereno station has a calculated pulse period less than 1.0 s for both methods whereas the other stations in the forward directivity region have pulse periods greater than 1.0 s. The distribution of stations in Figure 10 largely overlaps the station distributions with large positive residuals of PSA (3.0s) in Figure 1(f).

Pulse-like recordings were strongly related to directivity effects in these plots. Similar identifications of pulse-like recordings were performed for the NGA-West2 database (Ancheta et al. 2013). Figure 11 shows scatter plot (R_{rup} versus **M)** of identified pulse-like recordings in the South Napa and NGA-West2 databases. The pulse-like recordings were observed generally within R_{rup} less than 10 km for **M** 5. There was a trend for R_{rup} to increase as **M** increases which could be used to define the near-fault region for design practice.

Table 4. Pulse Identification for recordings from the 2014 South Napa Mainshock

		Hayden et al. (2014)			Shahi and Baker (2014)		
Station Name	RSN	Pulse Identified	Azimuth of Max PPV* (°)	Pulse Period (s)	Pulse Identified	Azimuth of Max Pulse (°)	Pulse Period (s)
Napa College	51	No	160	1.6	Yes	154	2.0
Huichica Creek	89	Yes	171	5.5	Yes	166	2.8
Lovall Valley Loop Rd.	212	Yes	61	3.8	Yes	69	3.6
Fire Station No. 3	217	Yes	62	3.8	Yes	29	4.4
Main St. Napa	219	Yes	56	3.4	No	60	3.9
Atlas Peak	702	Yes	103	2.0	No	177	2.4
Vallejo - Broadway & Sereno	1318	Yes	45	0.6	No	50	0.6

* PPV = Peak-to-Peak Velocity (Hayden et al. 2014)

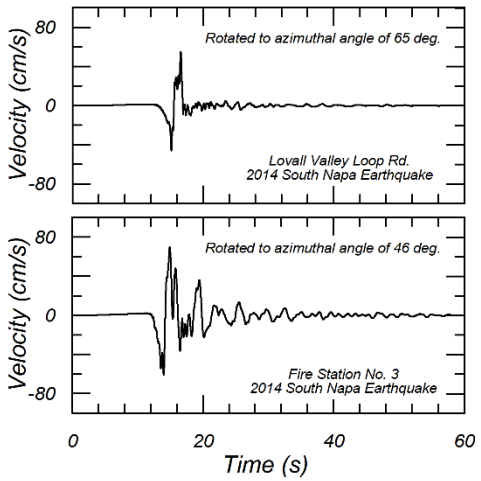

Figure 9. Example of pulse-like time series recorded in the South Napa mainshock.

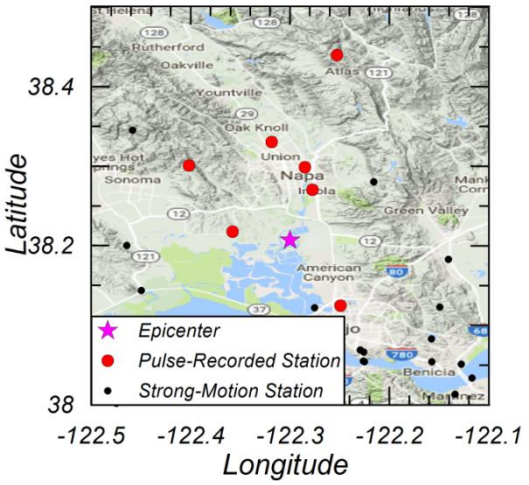

Figure 10. Locations of stations with pulse-like records identified in the 2014 South Napa mainshock.

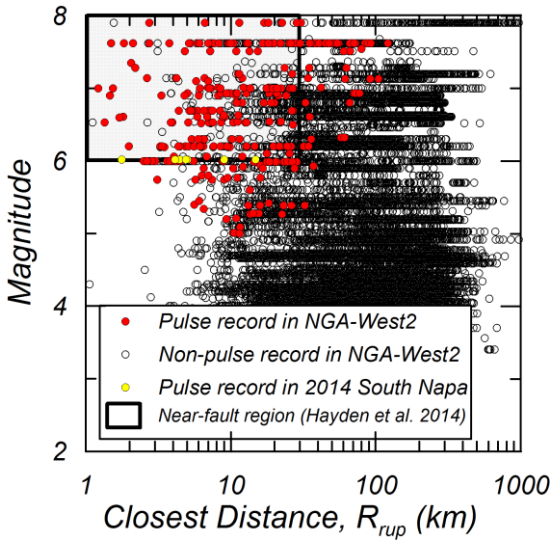

Figure 11. Distribution of pulse-like recordings in the NGA-West2 and South Napa database

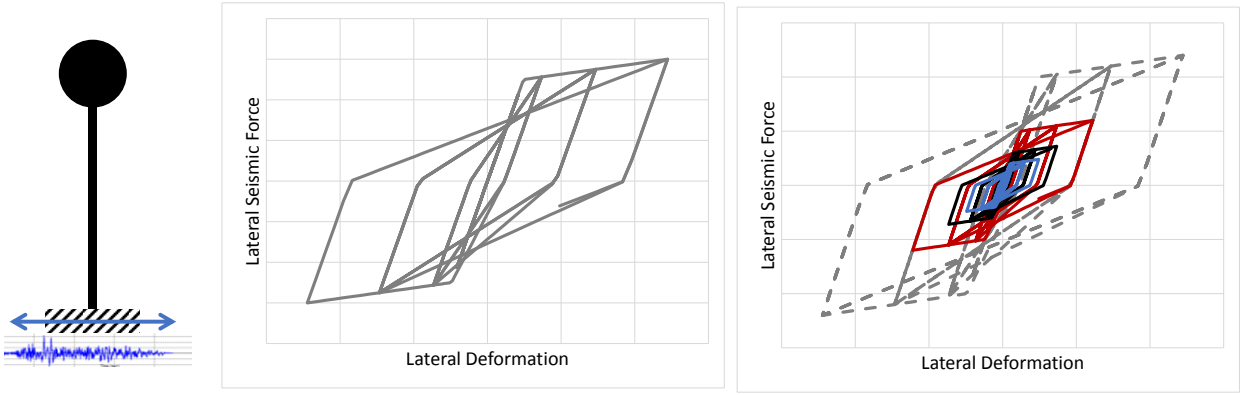

Figure 12. Inelastic-Response Model

Pulse-Motion Characteristics by Inelastic Spectra

Inelastic response spectra were computed for the pulse motions to determine whether the presence of the pulse affected the response of an inelastic system and whether the period shift associated with inelasticity affected the response. The generalized inelastic SDOF model that was used in the analysis is shown in Figure 12, with the analyses performed using OpenSees (McKenna, 1997). This generalized model is consistent with what is assumed in ASCE 7-16. This model was chosen because it represents the critical characteristics of inelastic response – nonlinearity, hysteresis, strength and stiffness degradation due to cycling and ductility. The inelastic spectra were computed for a range of periods and strengths, as shown in Figure 12.

The strength parameter that was used in the analysis is the Estimated-Strength Reduction Factor, Rd, defined as the ratio between the elastic lateral-force demand for design (2/3 MCE_R) and the yield strength of the structure, Vy. This value is equivalent to a combination of the strength-reduction factor R and the strength-amplification factor Ω used in design. (Rd Range:

0.5-10) (Rd >1: structure will yield below 2/3 MCE_R, Rd <1: structure will remain elastic below 2/3 MCE_R). It is important to note that with this definition of Rd, the estimated yield strength of the structure is defined as a function of the site-specific design spectrum. The MCE_R spectrum was computed for each recording station. A graphical representation of the effect of Rd on the design spectra is shown in Figure 13. Because inelastic response of very-stiff structures may yield questionable results, the inelastic spectra were computed for a period range between 0.1 and 10 seconds.

The spectral displacement computed in the inelastic response spectra was normalized to a ductility value to make a graphic comparison over all periods. The inelastic-spectra for two recording stations, "Napa College, RSN 51, JB Dist=3.1 km" and "Lovall Valley Loop Rd, RSN 212, JB Dist=5.0 km", are shown in Figure 14 and 15, respectively, because they display interesting response characteristics. The Napa College record has a pulse at a period between 1 and 2 seconds. This pulse is identified by both identification methods and is evident in the elastic response spectrum, in the Fault-Parallel direction, as shown in Figure 14, top-left figure. The remaining graphs in the figure plot the displacement ductility versus initial elastic period for the Fault-Normal and Fault-Parallel directions, as well as for the azimuth direction for both the Hayden and Shahi pulse characterizations. Each of these inelastic spectra plots the response for different cases of Estimated-Strength Reduction Factor. Figure 14 show that the pulse shape is identified for the cases where the response is near yield (ductility=1, Rd<2). However, for the cases of larger strength reduction, the pulse shape is no longer observed and high ductility demands are evident in all periods below 3 seconds.

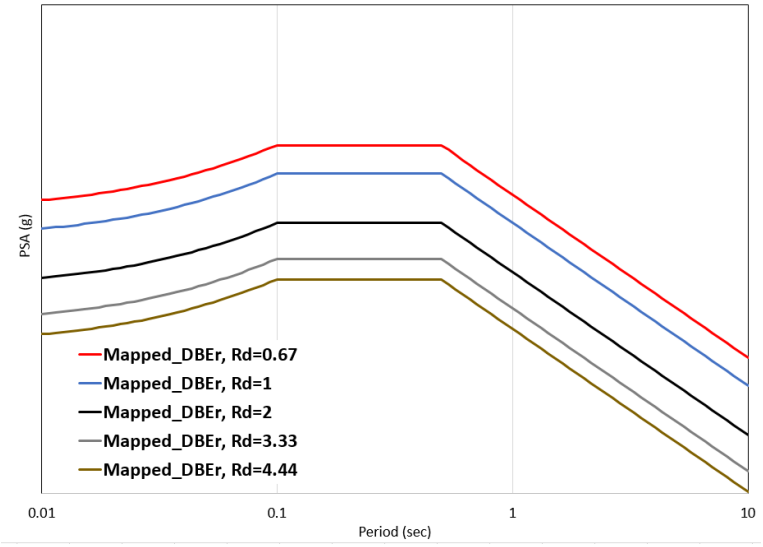

Figure 13. Inelastic Design Spectra

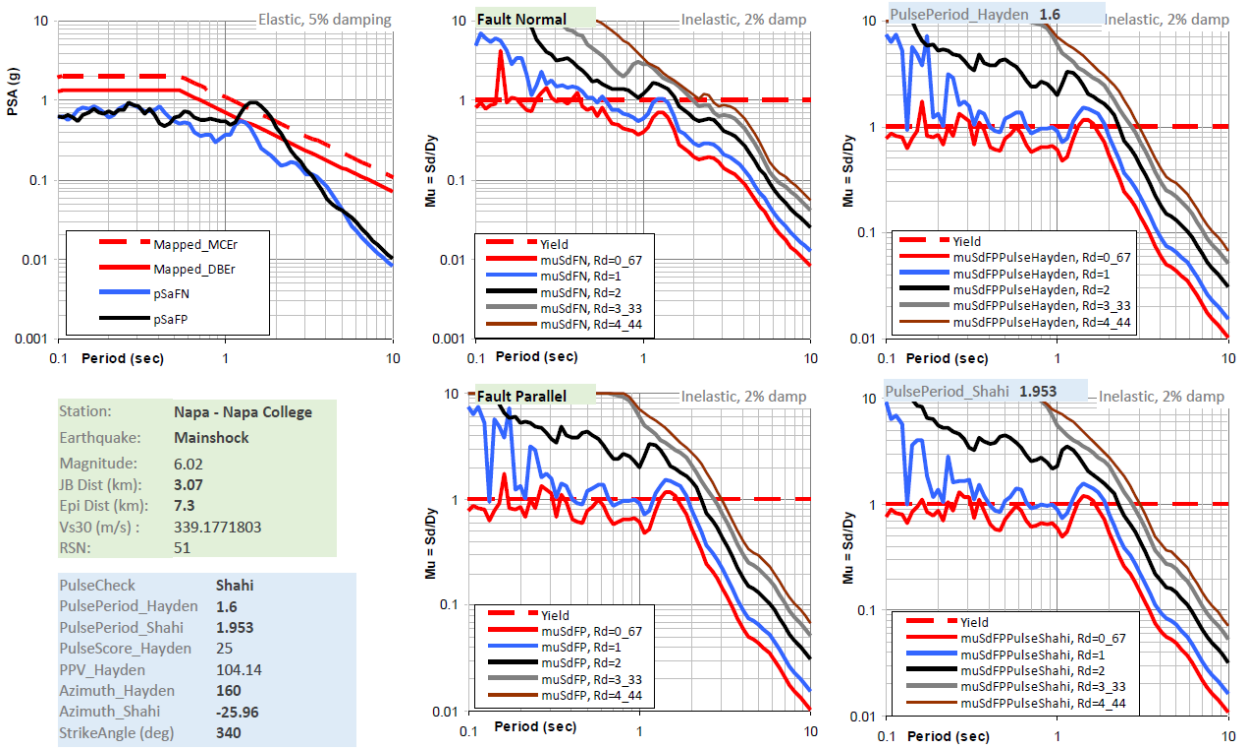

Station:	Napa - Napa College
Earthquake:	Mainshock
Magnitude:	6.02
JB Dist (km):	3.07
Epi Dist (km):	7.3
Vs30 (m/s) :	339.1771803
RSN:	51

PulseCheck	Shahi
PulsePeriod_Hayden	1.6
PulsePeriod_Shahi	1.953
PulseScore_Hayden	25
PPV_Hayden	104.14
Azimuth_Hayden	160
Azimuth_Shahi	-25.96
StrikeAngle (deg)	340

Figure 14. Inelastic Spectra for Napa College, RSN 51, JB Dist=3.1 km

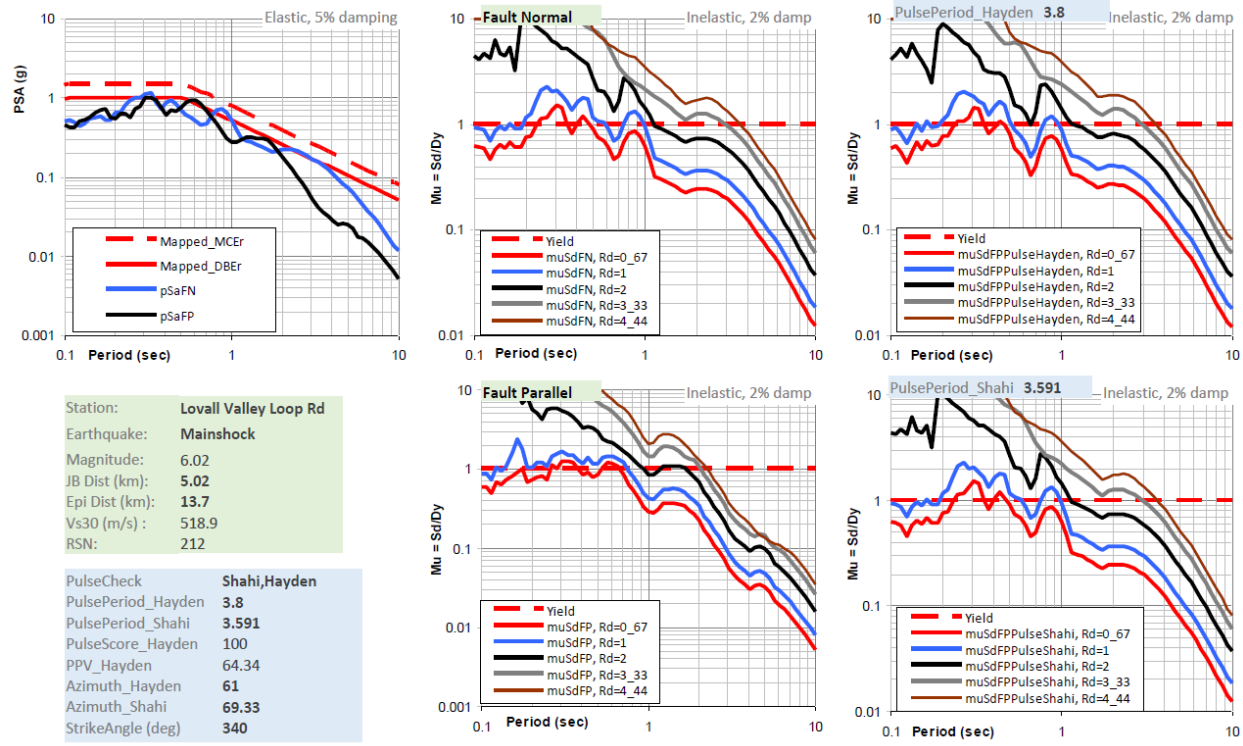

Station:	Lovall Valley Loop Rd
Earthquake:	Mainshock
Magnitude:	6.02
JB Dist (km):	5.02
Epi Dist (km):	13.7
Vs30 (m/s) :	518.9
RSN:	212

PulseCheck	Shahi,Hayden
PulsePeriod_Hayden	3.8
PulsePeriod_Shahi	3.591
PulseScore_Hayden	100
PPV_Hayden	64.34
Azimuth_Hayden	61
Azimuth_Shahi	69.33
StrikeAngle (deg)	340

Figure 15. Inelastic Spectra for Lovall Valley Loop Rd, RSN 212, JB Dist=5.0 km

The inelastic spectra for the Lovall Valley Loop Rd record show that the pulse at between 3 and 4 seconds, identified by both methods and observed in the Fault-Normal response, does affect the inelastic response in that period range. The low levels of ductility demand for the cases of the structures with the lowest strength, however, indicate that the pulse does not cause collapse of the structure, unless its ductility capacity is very low. An evaluation of all inelastic response spectra, however, do indicate that the structures at highest risk at the shorter-period structures. This assessment needs to be verified through a rigorous comparison with the response of records without pulse characteristics.

Conclusions

Ground motion characteristics of the 2014 M6.0 South Napa earthquake have been investigated. The ground motion database was developed by collecting the time series from one foreshock, mainshock and three aftershocks from various agencies. Shear wave velocity profiles were also measured by the Spectral Analysis of Surface Wave Dispersion (SASW) technique at 15 selected strong-motion stations. Combining these data, a ground motion database was developed, and compared to GMMs in NGA-West2 studies. The results show the stronger attenuation of PGA for these events compared to the median of NGA-West2 models, indicating regional attenuation in this region of northern California Bay Area is greater than predicted by the average GMM. This observation was similar to those by Baltay and Boatwright (2015). The study also reviewed time histories from the two geotechnical downhole arrays operated at the south side of the Carquinez Bridge (I-80), which recorded PGAs of approximately 1g and 0.42g, respectively, during the 2014 South Napa mainshock. The apparent wave velocities computed from the downhole arrays show the clear reduction in V_s during mainshock, indicating that reduction of soil stiffness occurred due to strong shaking. The ETFs were also computed from downhole records and compared to the TTF from V_s profiles. The comparison shows good agreement of resonance periods especially at CE68206, where the maximum PGA of 1g was recorded. The ETF also shows the clear broadening of resonance periods at CE68206 during mainshock, which is consistent to the reduction of V_s in apparent wave velocities. Therefore, evaluations based on one-dimensional wave propagation reasonably explain the downhole array observations in mainshock, which is consistent with the results of Çelebi et al. (2015).

The pulse-like velocity time series were investigated by using Hayden et al. (2014) and Shahi and Baker (2014) approaches and utilizing the South Napa and NGA-West2 databases developed in this study. In the South Napa earthquakes, 7 records from mainshock are identified as pulse-like, where most of these stations were located in the forward directivity region. The pulse periods estimated by these two methods were mainly between 2.0 – 4.4 s. The distributions of these stations were consistent with the regions where the positive residuals were observed for PSA(3.0s) compared with GMMs from NGA-West2 studies. The comparison of near-fault regions by pulse-like records between South Napa earthquake and NGA-West2 database also showed that these are reasonably consistent, and increase as magnitude increases. Inelastic response spectra for the recorded ground motions can be used to gain further insight into the expected response of structures with different stiffness (period) and strength characteristics.

Acknowledgements

The project acknowledges Tony Shakal and Moh Huang (CSMIP) for providing the suspension profiles, boring logs and numerous discussions. The assistance by Tom Shantz, Caltrans, who assisted with access at the Carquinez Bridge SASW sites is greatly appreciated. The authors also acknowledge Prof. Stewart and Dr. Gutierrez for providing V_{s30} estimates, and Dr. Aagaard for basin depths at strong-motion stations. The project is funded by CSMIP and the California Department of Transportation and those funds are gratefully acknowledged. The views and conclusions contained in this document are those of the authors and should not be interpreted as necessarily representing the above organizations

Reference

Aagaard B.T., Graves R.W., Rodgers A., Brocher T.M., Simpson R.W., Dreger D., Petersson N.A., Larsen S.C., Ma S., Jachens R.C. (2010). Ground-motion modeling of Hayward fault scenario earthquakes, Part II: Simulation of long-period and broadband ground motions, Bull. Seismol. Soc. Am., 100(6): 2945–2977.

Abrahamson, N. A., Silva, W. J., and Kamai, R., 2014. Summary of the Abrahamson, Silva, and Kamai NGA-West2 ground-motion relations for active crustal regions, Earthquake Spectra 30, 1025–1055.

Ancheta, T. D., Darragh, R. B., Stewart, J. P., Seyhan, E., Silva, W. J., Chiou, B. S.J., Wooddell, K. E., Graves, R. W., Kottke, A. R., Boore, D. M., Kishida, T. Donahue, J. L. (2013), "PEER NGA-West2 Database", Pacific Earthquake Engineering Research Center, PEER Report 2013/03.

Baltay, A. S. and Boatwright, J. (2015). Ground-Motion Observations of the 2014 South Napa Earthquake, Seismological Research Letters Volume 86, Number 2A, doi: 10.1785/0220140232.

Boore, D. M., A. Azari Sisi, and S. Akkar (2012). Using pad-stripped acausally filtered strong-motion data, Bull. Seismol. Soc. Am. 102 751-760.

Boore, D.M., J.P. Stewart, E. Seyhan, and G.M. Atkinson (2014). NGA-West 2 equations for predicting PGA, PGV, and 5%-damped PSA for shallow crustal earthquakes, Earthquake Spectra 30, 1057-1085.

Bozorgnia, Y., Abrahamson, N. A., Atik, L. A.,Ancheta, T. D.,Atkinsone, G. M., Baker, J. W.,Baltay, A., Boore. D. M.,Campbell, K. W., Chiou, B. S.-J.,Darragh, R., Day, D., Donahue, J., Graves. R. W., Gregor, N., Hanks, T., Idriss, I. M., Kamai, R., Kishida, T., Kottke, A., Mahin, S. A., Rezaeian, S., Rowshandel, B., Seyhan, E., Shahi, S., Shantz, T., Silva, W., Spudich, P., Stewart, J. P., Watson-Lamprey, J., Wooddell, K., and Youngs, T. (2014). "NGA-West2 Research Project". Earthquake Spectra, EERI, August 2014, Vol. 30, No. 3, pp. 973-987.

Campbell, K. W., and Bozorgnia, Y., (2014). NGA-West2 ground motion model for the average horizontal components of PGA, PGV, and 5%-damped linear Response Spectra, Earthquake Spectra 30, 1087–1115.

Çelebi, M., Ghahari, S. F. and Taciroglu, E. (2015), Unusual Downhole and Surface Free-Field Records Near the Carquinez Strait Bridges during the 24 August 2014 Mw 6.0 South Napa, California, Earthquake, Seismological Research Letters Volume 86, Number 4. doi: 10.1785/0220150041.

CESMD (Center for Engineering Strong Motion Data) (2014), http://www.strongmotioncenter.org/ (last accessed September 2016).

Chiou, B. S.-J., and Youngs, R. R., (2014). Update of the Chiou and Youngs NGA ground motion model for average horizontal component of peak ground motion and response spectra, Earthquake Spectra 30, 1117–1153.

Chiou, B., Darragh, R., Gregor, N., and Silva, W. (2008), NGA project strong-motion database, Earthquake Spectra, Vol. 24, No. 1, pp. 23–44.

Darragh B, Silva W, Gregor N (2004) Strong motion record processing procedures for the PEER center. In: Proceedings of COSMOS workshop on strong-motion record processing. Richmond, California, pp 1–12.

Dreger, D. S., Huang, M.-H., Rodgers, A., Taira, T. and Wooddell, K. (2015), Kinematic Finite-Source Model for the 24 August 2014 South Napa, California, Earthquake from Joint Inversion of Seismic, GPS, and InSAR Data, Seismological Research Letters Volume 86, Number 2A, pp327-334, doi: 10.1785/0220140244.

Elgamal, A. W., Zeghal, M., Tang, H. T. and Stepp, J. C., "Lotung Downhole Array. I: Evaluation of Site Dynamic Properties", J. Geotech. Engrg., 1995, 121(4): 350-362.

Goulet, C. A., Kishida, T., Cramer, C. H., Darragh, R. B., Silva, W. J., Hashash, Y. M. A., Harmon, J., Stewart, J. P., Wooddell, K. E., Youngs R. R. (2014), "PEER NGA-East Database", Pacific Earthquake Engineering Research Center, PEER Report 2014/09.

Haddadi, H. R. and Kawakami, H. (1998), Modeling Wave Propagation by using Normalized Input-Output Minimization (NIOM) Method for Multiple Linear Systems, Doboku Gakkai Ronbunshu, Vol. 1998 (1998) No. 584 P 29-39

Hayden, C. P., Bray, J. D. and Abrahamson, N. A. (2014), Selection of Near-Fault Pulse Motions, J. Geotech. Geoenviron. Eng., 2014, 140(7): 04014030.

Kishida, T., Kayen, R.E., Ktenidou, O.-J., Silva, W.J., Darragh, R.B. and Watson-Lamprey, J. (2014b), PEER Arizona Strong-Motion Database and GMPEs Evaluation, Pacific Earthquake Engineering Research Center, University of California, Berkeley, CA, PEER Report 2014/09.

Kishida, T., Wang, S., Mazzoni, S., Markham, C., Lu, Y., Bozorgnia, Y., Mahin, S, Bray, J., Panagiotou, M., Stewart, J., Darragh, R., Abrahamson, N., Hollenback, J., Gutierrez, C., Chiou, B., Muin, S., Dreger, D. (2014a), "PEER Preliminary Notes and Observations on the August 24, 2014, South Napa Earthquake, 1. Strong motion records", Pacific Earthquake Engineering Research Center, PEER Report 2014/09.

Seyhan E, Stewart JP, Ancheta TD, Darragh RB, Graves RW (2014): NGA-West2 Site Database. Earthquake Spectra, 31(3), 1007-1024.

Shahi, S. K. and Baker, J. W. (2014), An Efficient Algorithm to Identify Strong-Velocity Pulses in Multicomponent Ground Motions, Bulletin of the Seismological Society of America, Vol. 104, No. 5, pp. 2456–2466.

Waldhauser, F. and Ellsworth, W. L. (2000), A Double-Difference Earthquake Location Algorithm: Method and Application to the Northern Hayward Fault, California, Bulletin of the Seismological Society of America, 90, 6, pp. 1353–1368, December 2000.

Wills, C. J., Gutierrez, C. I., Perez, F. G. and Branum, D. M. (2015), "A Next Generation VS30 Map for California Based on Geology and Topography", Bulletin of the Seismological Society of America, Vol. 105, No. 6, pp. –, December 2015, doi: 10.1785/0120150105.

EVALUATION OF ONE-DIMENSIONAL SITE RESPONSE IN CALIFORNIA DOWNHOLE ARRAYS

Ramin Motamed[1], Gangjin Li[1], and Stephen Dickenson[2]

[1] Department of Civil & Environmental Engineering, University of Nevada Reno, Reno
[2] New Albion Geotechnical, Inc., Reno

Abstract

This paper presents the one-dimensional (1D) site response analysis (SRA) of three geotechnical downhole arrays in California subjected to both strong and weak earthquake shakings. The arrays were initially assessed in terms of effectiveness of 1D SRA using taxonomy exercise. Then SRA were performed utilizing finite element program LS-DYNA to study the site effects of the selected arrays. Lastly, the predictions were compared with the recorded counterparts and the uncertainties of the 1D SRA models were evaluated. Among the analyzed ground motions, we focus on the analysis results of the mainshock and aftershock of 2014 M_w 6.0 South Napa Earthquake.

Introduction

The 2014 M_w 6.0 South Napa Earthquake caused the strongest shaking in much of the Northern San Francisco Bay region since the 1989 M_w 6.9 Loma Prieta earthquake. During this event, 14 geotechnical downhole arrays of California Strong Motion Instrumentaion Program (CSMIP) recorded ground-motion data (Shakal et al., 2014), which are available for download at the Center for Engineering Strong Motion Data (CESMD) website (*http://www.strongmotioncenter.org/*). These recordings have been examined by many researchers to understand the propagation of the seismic waves (Bray et al., 2014, Celebi et al., 2015).

This study investigates the influence of local site effects on the amplification of seismic motions in three CSMIP geotechnical downhole arrays with records of significantly high peak ground accelerations (PGA) during the South Napa Earthquake. Taxonomy evaluation of the arrays was carried out to provide implications for 1D SRA on a priori basis. Furthermore, LS-DYNA, an advanced Finite Element (FE) program, was utilized to develop 1D SRA models for these arrays in order to evaluate the influence of the 1-D approximations on computed site response: (1) all boundaries are horizontal and extend infinitely, and (2) the response is dominated by vertically propagating and horizontally polarized shear (SH) waves. Both strong and weak shaking motions were used to perform SRA for each downhole array. And the analysis results were compared with the observations at every available downhole sensor depth in order to examine the effectiveness of SRA models in capturing soil response. On the basis of the analyses performed to date, the practical limitations of 1D site response analysis for the selected arrays have been identified and discussed in this paper.

Selection of Geotechnical Downhole Arrays

Array Selection Criteria

Considering the fourteen CSMIP geotechnical downhole arrays that recorded motions during the 2014 M_w 6.0 South Napa Earthquake, we carried out a screening procedure to select a few arrays of interest that meet the following criteria:

1. Accelerometers measure bi-directional shaking (i.e. two horizontal components);
2. The array has recorded both small and moderate-to-large amplitude motions (PGA < 0.1 g and PGA > 0.15 g);
3. Recorded ground motions are regarded as free-field motions and are not affected by an adjacent structure;
4. The soil layers are not susceptible to liquefaction and liquefaction has not previously been observed at close proximity to the array;
5. The site geology is relatively simple and a soil column can reasonably represent the subsurface soil behavior (i.e. minor basin or topography effects);
6. Arrays with information on subsurface soil properties such as in-situ test data.

Selected Arrays

Ideally, the candidate arrays meet all the criteria as listed above; however, it is acknowledged that site-specific aspects of the local geology, topography, and level of site characterization will diverge from these criteria to some extent. In most cases, the constraints have to be relaxed for selecting sites. In this study, we eventually identified 3 vertical arrays including (1) Crockett - Carquinez Bridge Geotech Array #1 (CC #1), (2) Crockett – Carquinez Bridge Geotech Array #2 (CC #2), (3) Vallejo - Hwy 37/Napa River E Geo. Array (Vallejo). All these arrays are located to the south of Napa Valley in Northern California. The local geology is complex with the bedrock consisting of interbedded marine claystone, siltstone, and fine-grained sandstone of the Late Cretaceous Panoche Formation. Boreholes were drilled at the selected sites and shear wave velocity (V_s) and compression wave velocity (V_p) were measured using PS suspension logging by California Department of Transportation (Caltrans). The site characteristics of the selected arrays are summarized in Table 1. It is noteworthy that the ground water table (GWT) depth of all three sites are shallow, generally less than 14 ft, but there was no evidence of liquefaction during the South Napa earthquake, and application of liquefaction screening and triggering evaluation procedures indicates that the soils had a very low susceptibility for generation of significant excess pore pressure during the South Napa earthquake. It was determined that all 3 of the selected arrays are located in close proximity to structures (i.e. bridges), therefore the recorded ground motions were examined for evidence of soil-structure interaction.

Crockett - Carquinez Bridge Geotech Arrays #1 & #2

Crockett – Carquinez Bridge Geotech arrays #1 and #2 are located close to the south anchorage structure of the westbound Alfred Zampa suspension bridge and eastbound cantilever truss bridge on Interstate 80 over the Carquinez Strait. At the south end of the suspension bridge,

Table 1. Site characteristics of selected arrays (CESMD, *www.strongmotioncenter.org)*

Station No.	Station Name	Site Geology	Sensor Depths (m)	$V_{s,30}$ (m/sec)	z_{1000} *(m)	Site Class (ASCE 7-10)	GWT Depth ** (m)	Distance to Adjacent Structure (m)
68206	Crockett - Carquinez Br #1	Shallow clay over rock	0, 20.4, 45.7	345	>46	D	4	~10
68259	Crockett - Carquinez Br #2	Shallow clay over soft rock	0, 61, 125	173	>125	D	0.9	0
68310	Vallejo - Hwy 37/Napa River E	Bay mud	0, 17.9, 44.5	509	>35	C	3	~70

Note: (1) Z_{1000}: the depth where V_s reaches 1000m/sec; (2) GWT depth is estimated as the depth where V_p reaches 1500m/sec.

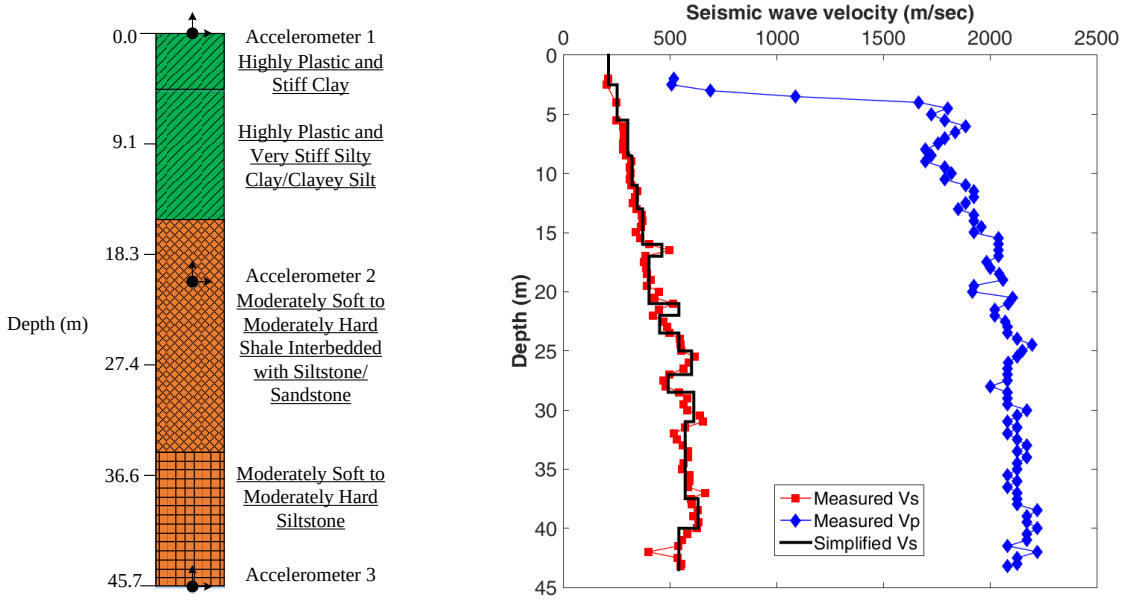

(a) (b)

Figure 1. (a) Geologic section (personal communication with Caltrans) and (b) seismic wave velocity profile of CC #1 (adopted from CESMD, *www.strongmotioncenter.org*)

the site consists primarily of up to 15 feet of fill underlain by soft to stiff clay (about 5-15 feet thick) which is much like young Bay Mud. Below this bay mud is very stiff clay (about 15-30 feet) containing weathered rock fragments. Below the very stiff clay is the bedrock consisting of

interbedded siltstone, claystone and shale with closely spaced factures. Figures 1 and 2 present the soil, V_s and V_p profiles of CC #1 and 2.

Downhole sensors were installed for both CC #1 and CC #2 at three depths (0 m, 20.4 m, 45.7 m for CC #1 and 0 m, 61 m, 125 m for CC #2). In addition, CC #1 is outside the bridge roadways and ramps and is not as close to the bridge ramp as is CC #2. CC #2 is deployed between several bents of the roadway south of the bridge crossing and the Crockett off-ramp. Although they are located nearby each other (roughly 200 m away), the site characteristics of CC #2 are different from CC #1. Compared to CC #1, the site of CC #2 is softer with a deeper bedrock.

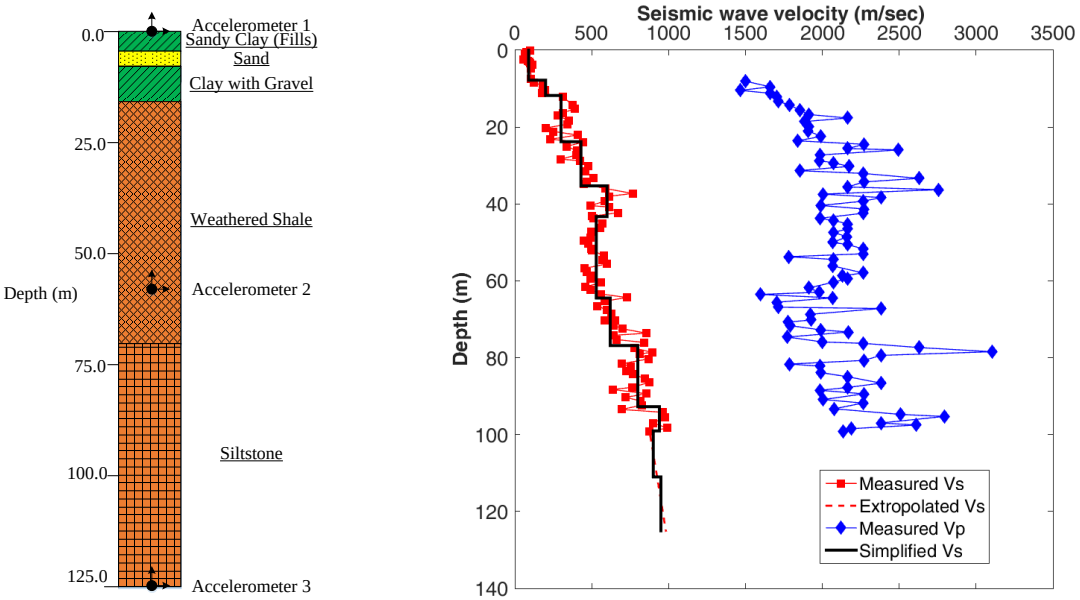

(a) (b)

Figure 2. (a) Geologic section (personal communication with Caltrans) and (b) seismic wave velocity profile of CC #2 (adopted from CESMD, *www.strongmotioncenter.org*)

Vallejo – Hwy 37/Napa River E Geo. Array

Vallejo array is located adjacent to the east abutment of the Hwy37/Napa River Bridge with three downhole accelerometers at depths of 0 m, 17.9 m and 44.5 m. The site is consisted of stiff clay layer underlain by silty clay. Beneath the silty clay is weathered fractured sandstone. The geologic section and seismic wave velocity profile of this array are presented in Figure 3.

Taxonomy Evaluation of Selected Arrays

The site classification scheme (i.e. taxonomy) proposed by Thompson et al. (2012) was employed to quantify site response complexity and assess the validity of the 1D site response assumptions for the selected downhole arrays.

The sites have been separated into four distinct categories, i.e. LG, LP, HP and HG sites, based on the classification scheme of Thompson et al. (2012). The first letter of the taxonomy

notation indicates the inter-event variability (σ) class of empirical transfer functions (ETFs) (H for "high" and L for "low") while the second letter indicates the goodness-of-fit (r) between ETFs and theoretical transfer functions (TTFs) (G for "good" and P for "poor"). The threshold values of σ and r are 0.35 and 0.6, respectively. In order to minimize the potential for nonlinear effects and increase the statistical significance, Thompson et al. (2012) recommended to use at least 10 records with PGA < 0.1g at ground surface for taxonomy evaluation.

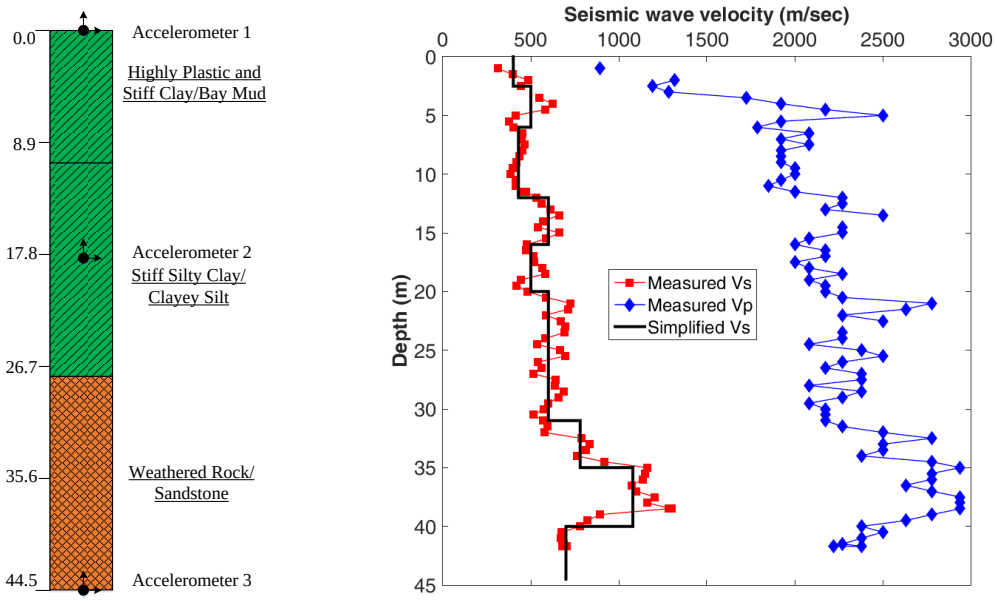

(a) (b)

Figure 3. (a) Geologic section (personal communication with Caltrans) and (b) seismic wave velocity profile of Vallejo (adopted from CESMD, *www.strongmotioncenter.org*)

As illustrated in Figures 4, 5 and 6, we evaluated the taxonomy for each selected downhole array by using the weak ground shaking (PGA at surface instrument < 0.1g) from the CESMD website (*http://www.strongmotioncenter.org/*) and the associated FTP folder containing a database of low-amplitude motions (PGA < 0.5% g) for vertical arrays and surface free-field sites. The number of "linear" motions utilized are 21, 15 and 18 for CC #1, CC #2 and Vallejo, respectively. ETFs were calculated as the ratio of Fourier spectra amplitude between the surficial and deepest accelerometers as given in Eq. (1) (Afshari et al., 2015). The ETF is taken as the geometric-mean of ETFs for the two horizontal components of the recordings (at their as-recorded azimuths) for each site. On the other hand, TTFs were computed according to the viscoelastic theory of Kramer (1996) for multi-layered and damped soil profiles implemented in Matlab (Mathworks, 2015).

$$H(f) = \frac{G(f,x_1)}{G(f,x_2)} \quad (1)$$

where $G(f,x_1)$ and $G(f,x_2)$ are amplitude spectra at surface and the deepest downhole sensor, and $H(f)$ is the ETF.

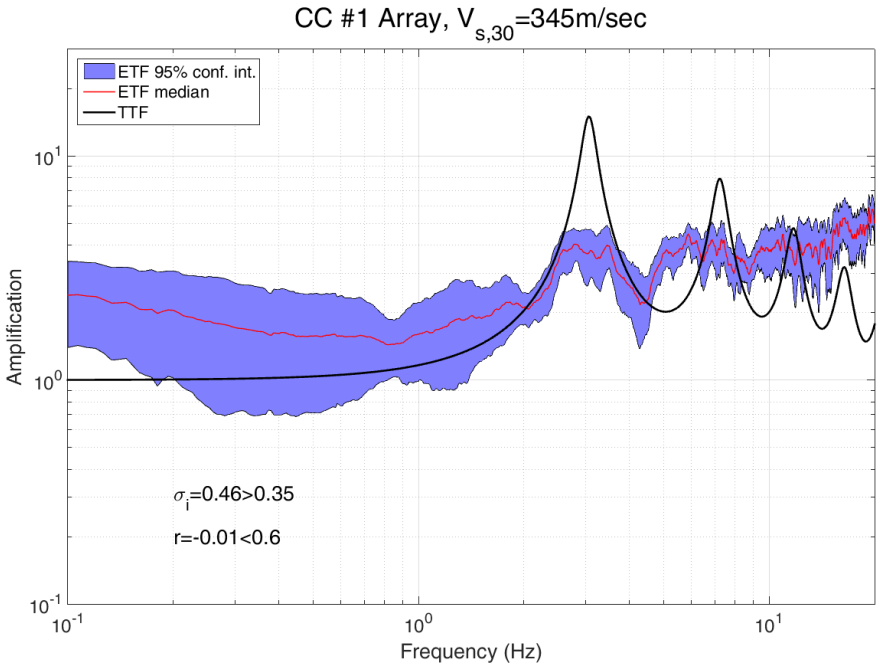

Figure 4. Taxonomy evaluation of CC #1

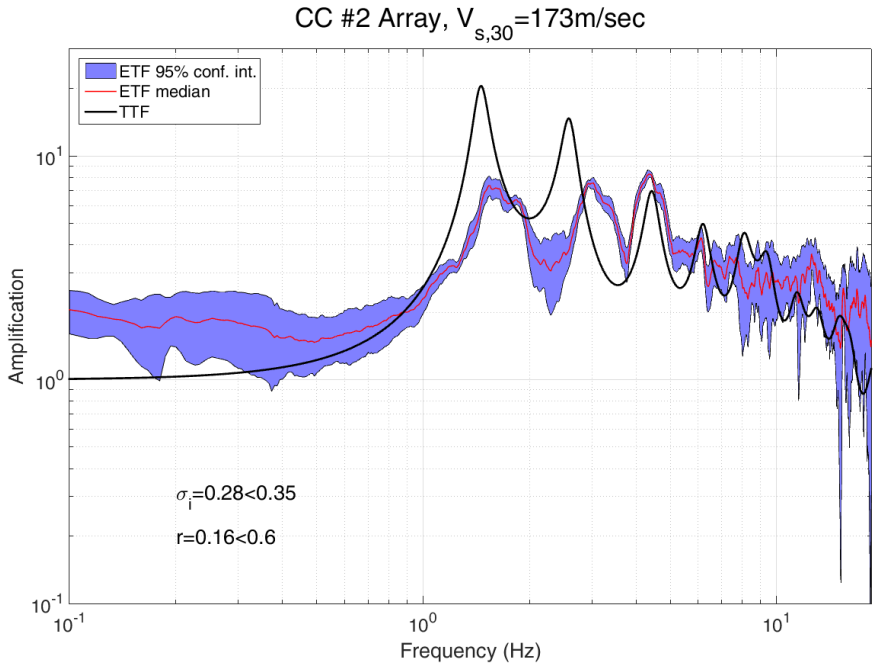

Figure 5. Taxonomy evaluation of CC #2

According to the results presented in Figures 4 to 6, it was found out CC #1 can be classified as a HP site, which means it was not informative for nonlinear constitutive models

unless path and source effects can be accounted for (Thompson et al., 2012). Besides, CC #2 and Vallejo are grouped into LP sites indicating that they are appropriate for nonlinear modeling but care must be taken to identify the source of misfit (Thompson et al., 2012).

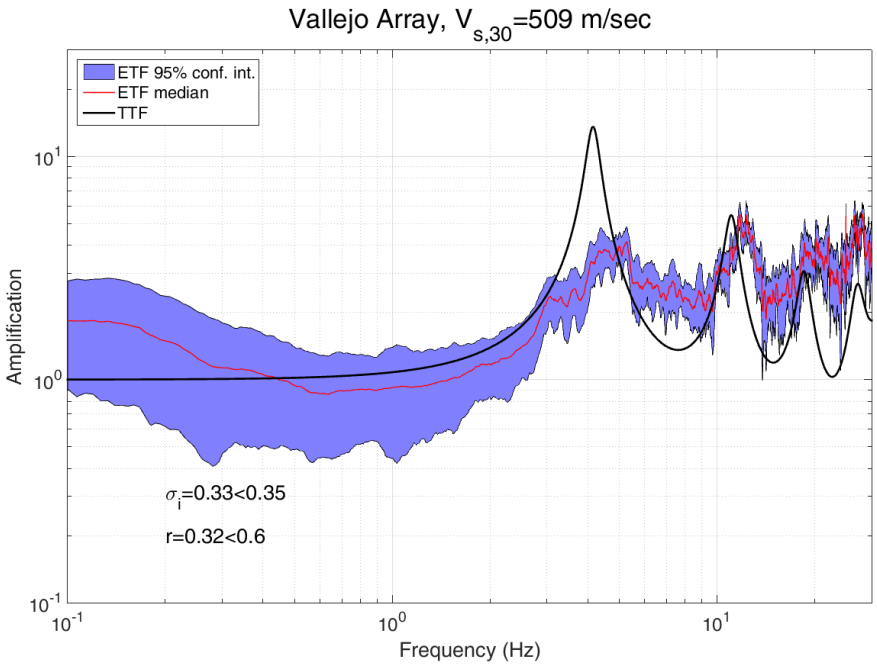

Figure 6. Taxonomy evaluation of Vallejo

1D Site Response Analysis

Methodology

Three bi-directional 1D site response analysis models were developed for CC #1, CC #2 and Vallejo using LS-DYNA (LSTC, 2012). The constraints of 1-D modeling are acknowledged; soil layer boundaries are horizontal and extend infinitely in lateral directions and seismic waves propagate vertically (SH waves). Single soil column models, (Figure 7), were developed for the selected arrays in LS-DYNA using solid elements constrained to move in shear. The soil columns were discretized in such a way that the maximum frequency each layer could propagate was as close to 37.5 Hz as possible. The bases of the soil columns were fixed to represent the "within" profiles (Stewart et al., 2008). In current engineering practice soil deposits are routinely modeled with lumped mass, springs and dampers for 1D SRA (e.g., DeepSoil, Hashash et al., 2016). Alternatively, SRA modeling with advanced FE programs such as LS-DYNA may be advantageous in some situations as they can take the effect of multi-directional shaking into account. In this study, the recorded acceleration data at the deepest downhole sensors of each array were input in both horizontal directions (bi-directional shaking) simultaneously to study the interaction between the horizontal components of the site response.

The influence of dynamic stress-strain behavior on computed site response were investigated using three different soil backbone models, including general quadratic/hyperbolic

backbone curve (Groholski et al., 2016, denoted as GQH hereafter) , modified two-staged hyperbolic backbone curve (Motamed et al., 2016, denoted as MTH hereafter) and linear elastic curve (denoted as L hereafter). For all three models, small strain damping (D_{min}) was applied using the DAMPING_FREQUENCY_RANGE_DEFORM feature in LS-DYNA which provides approximately frequency-independent damping over a range of frequencies to element deformation. D_{min} was set as 2% and 5% for strong and weak shakings in the frequency range of 1~30 Hz, respectively.

Regarding the nonlinear soil models including GQH and MTH, MAT_HYSTERETIC_SOIL model was employed to simulate the dynamic response of the soil deposit, which includes an option to adjust soil stiffness based on the level of strain rate. Dynamic soil behavior was characterized by modified two-stage hyperbolic backbone curve for MTH model and general bivariate quadratic equation for GQH model. These two models were developed to properly account for the maximum shear stress in the constitutive model at large strain. Hysteretic damping of soil materials is governed by the loading-unloading relationship as described by Masing rule (Masing, 1926). Rate-dependent effects of clayey soils were accounted for by applying a 5% increase in stiffness per log cycle of plastic strain rate.

With respect to linear soil model, which assumes the stress-strain response of the soil is viscoelastic and viscous damping ratio is independent of strain and frequency, the linear elastic material was defined by MAT_ELASTIC command. At all strain levels, the viscoelastic formulation uses the small-strain, linear-elastic shear modulus (G_{max}).

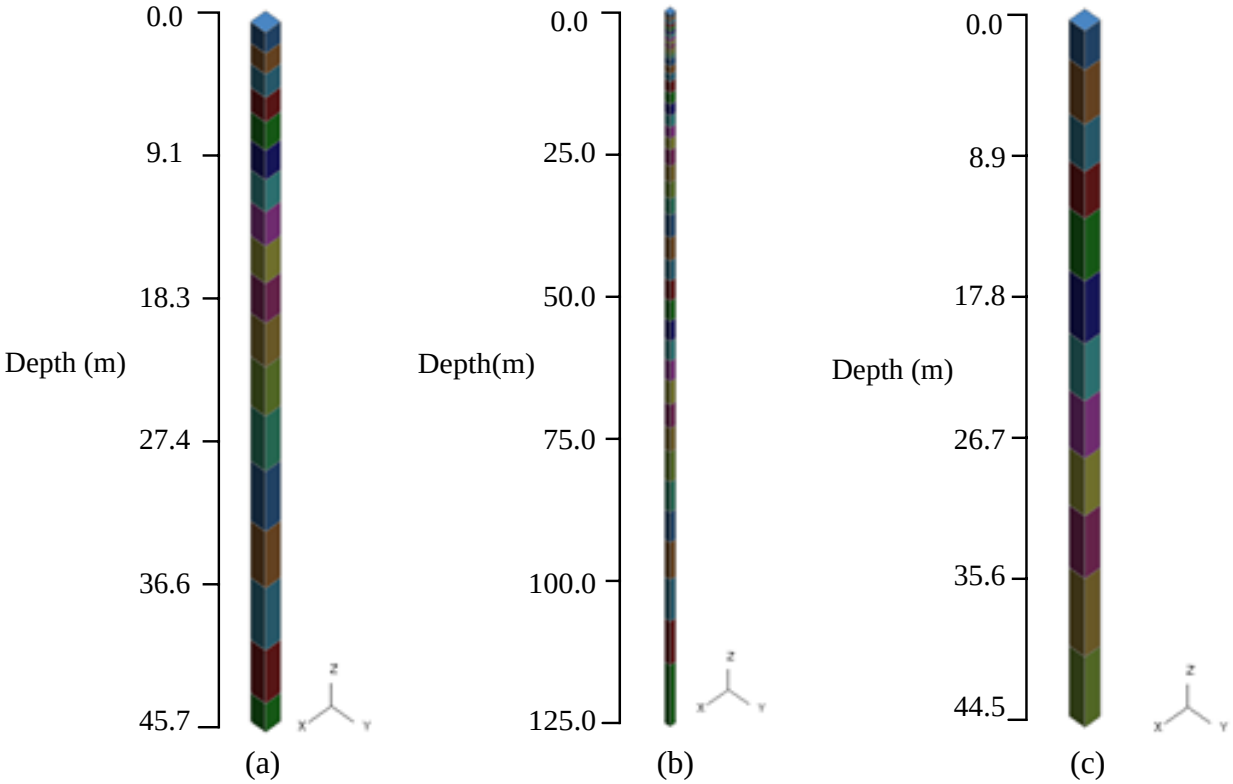

Figure 7. LS-DYNA soil column models for (a) CC #1 (b) CC #2 and (c) Vallejo

Selection of Ground Motions

For each selected downhole array, six individual analyses were performed including one strong shaking case (the mainshock of South Napa Earthquake) and five weak shaking cases (including two aftershocks of South Napa Earthquake, an M_w 3.6 on August 24, 2014 and an M_w 3.9 on August 26, 2014). The processed ground motion time series were downloaded through the CESMD website (*http://www.strongmotioncenter.org/*). The number of records of the three downhole arrays is plotted against PGA level at ground surface ($PGA_{surface}$) in Figure 9. As can be seen from this figure, the majority of the records has relatively small amplitudes (< 0.1 g). Several motions with $PGA_{surface}$ greater than 0.1 g were observed during the South Napa Earthquake mainshock. Specifically, CC #1 with the nearest rupture distance (R_{rup}) of 20.0 km recorded the largest PGA where the north-south (NS) component reached approximately 1.0 g while CC #2 recorded a much smaller PGA of 0.44 g. Also at Vallejo, with R_{rup} of 11.4 km, recorded a PGA of 0.198 g in east-west (EW) direction.

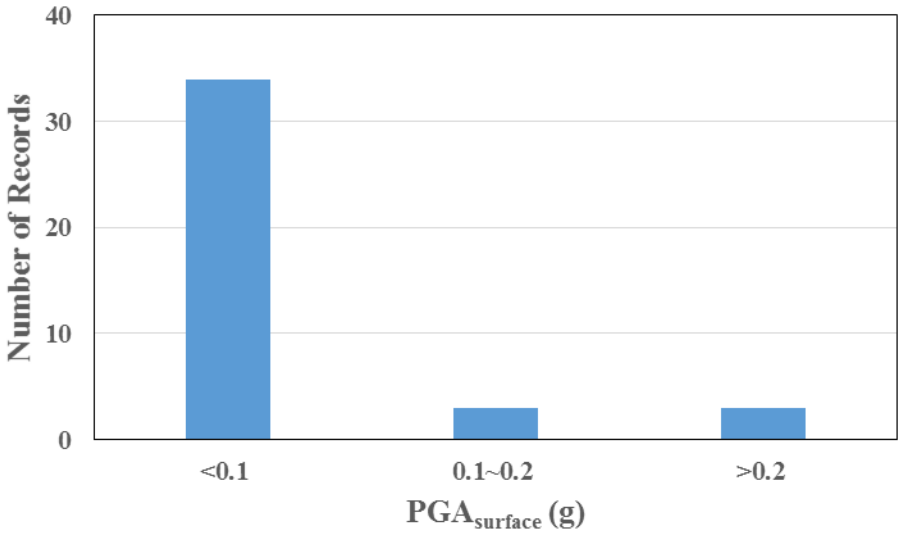

Figure 8. Number of records per PGA level at ground surface in studied arrays

Analysis Results and Discussions

This section discusses the 1D site response analysis results of the selected downhole arrays subjected to the mainshock (M_w 6.0, 2014/08/24) and aftershock (M_w 3.9, 2014/08/26) of South Napa Earthquake.

CC #1, South Napa Earthquake Mainshock

By comparing the recordings of both surficial and downhole sensors in Figure 9, it is observed that the ground motions were similar between depths of 20.4 m to 45.7 m for CC #1. The higher frequency motions were significantly amplified when propagating from the depth of 20.4 m to the surface at CC #1.

It is shown in Figures 9 and 10(a) that the spectral acceleration (Sa) and PGA predictions of GQH and MTH models reach fairly good agreement with the observations at mid-depth of

20.4 m. However, these two backbone models underpredicted spectral acceleration at period less than 0.4 sec and PGA at surface. In contrast, linear elastic model overpredicted the soil response at 20.4 m depth while it surprisingly performed much better in capturing the large amplification at surface, especially in the EW direction. The nonlinear soil behavior was not dominant in the soil profile as shown in Figure 10(b) with peak shear strain smaller than 0.1%.

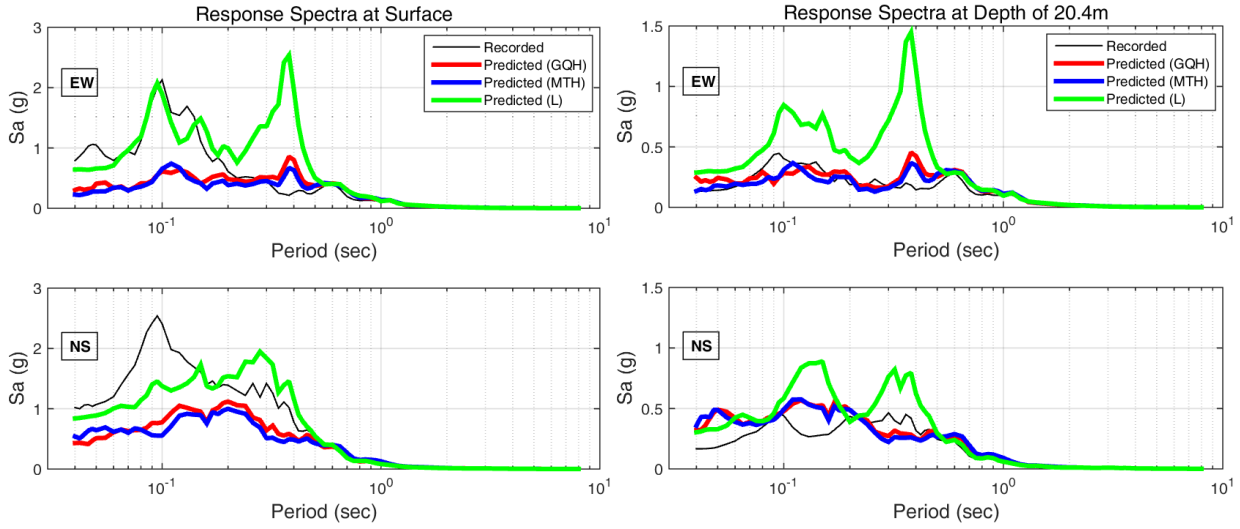

(a) (b)

Figure 9. Comparison of measured and predicted spectral acceleration of CC #1 under the shaking of South Napa Earthquake mainshock at (a) surface and (b) 20.4 m depth

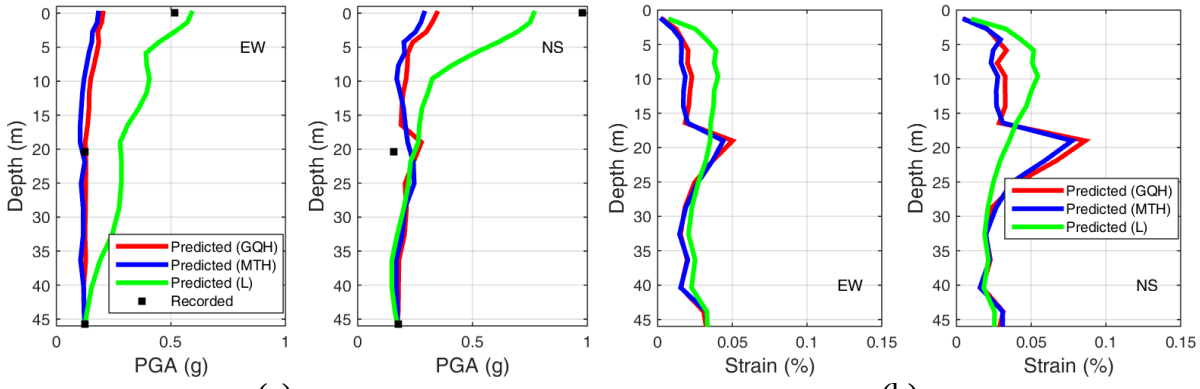

(a) (b)

Figure 10. (a) PGA and (b) max shear strain profiles of CC #1 under the shaking of South Napa Earthquake mainshock

Residuals of acceleration response spectra were computed based on the definition of Stewart et al. (2008) as shown in Eq. 2.

$$R(T) = \ln(S_a(T))_{data} - \ln(S_a(T))_{pre} \quad (2)$$

Where $\ln(S_a(T))_{data}$ is the spectra of recordings and $\ln(S_a(T))_{pre}$ is the spectra of model predictions. The positive residual indicates underprediction while negative residual implies overprediction of the model.

As shown in Figure 11(a), both linear and nonlinear models exhibited quite large residuals at the surface throughout a wide period range. This observation confirmed the taxonomy of CC #1 (HP site) which implied the site tended to yield poor fits for 1D SRA.

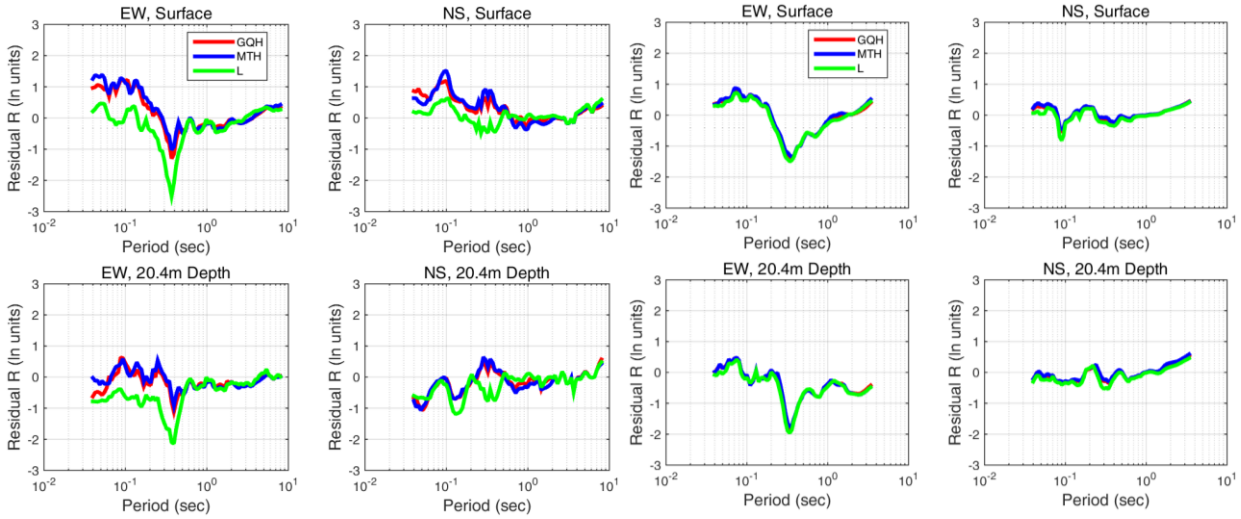

(a) (b)

Figure 11. Spectral acceleration residuals of CC #1 under the shaking of (a) South Napa Earthquake mainshock and (b) South Napa Earthquake aftershock

CC #1, South Napa Earthquake Aftershock (08/26/2016)

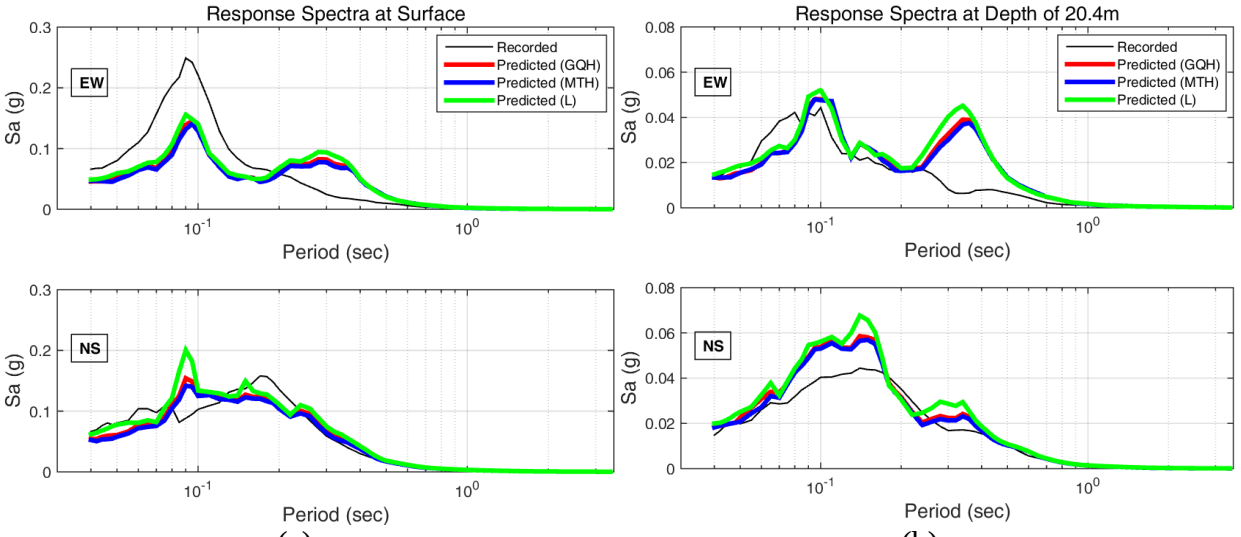

(a) (b)

Figure 12. Comparison of measured and predicted spectral acceleration of CC #1 under the shaking of South Napa Earthquake aftershock at (a) surface and (b) 20.4 m depth

As can be observed in Figures 12 and 13(a), both nonlinear (GQH and MTH) and linear models agreed well with the recorded data at 20.4 m depth (EW and NS components) and surface (only NS component). Nevertheless, all models failed to reproduce the soil response at

surface in the EW direction. Additionally, the soil behaved elastically, which was confirmed by the very similar results produced by both nonlinear and linear models, with peak shear strain smaller than 0.003% as shown in Figure 13(b).

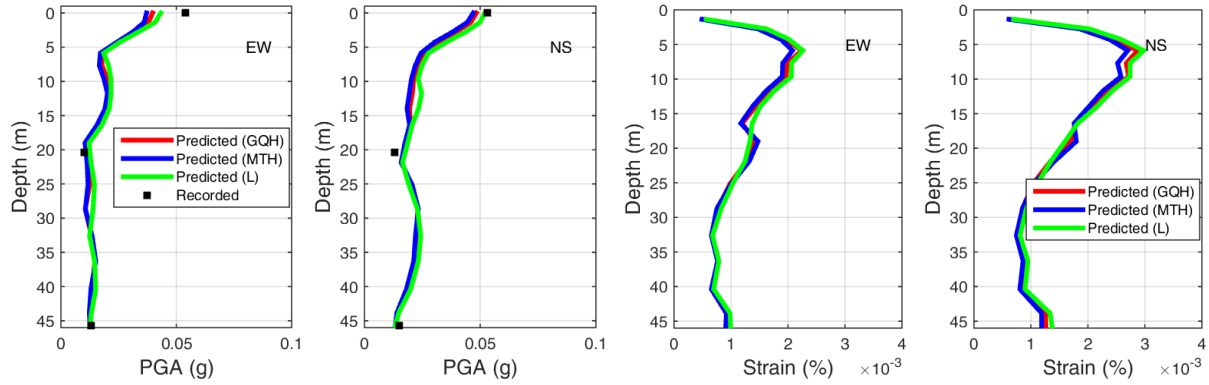

Figure 13. (a) PGA and (b) max shear strain profiles of CC #1 under the shaking of South Napa Earthquake aftershock

Overall, the residuals of the aftershock (weak event) decreased at every depth and both directions in comparison with the counterparts of the mainshock (strong event) as shown in Figure 11(b). The improved performance of nonlinear models at this weak shaking case with very small strain confirmed the taxonomy class of CC #1 (HP) suggesting this site is not suitable for calibrating nonlinear 1D SRA to recorded motions.

CC #2, South Napa Earthquake Mainshock

Similar to CC #1, at CC #2, the ground motions exhibited large amplifications from the mid-depth sensor (61 m) to the surficial sensor as presented in Figure 14. Very minor to negligible amplification was noted at depths between 61 m and 125 m for CC #2.

Figures 14 and 15(a) demonstrates good comparison was achieved for GQH and MTH models with regard to spectral acceleration and PGA in the EW direction at surface and in the NS direction at mid-depth of 61 m. However, they slightly underestimated spectral acceleration and PGA at surface (NS component) and overestimated spectral acceleration and PGA at 61 m depth (EW component). Conversely, general overestimation was noticed at all depths (EW and NS components) for linear elastic model. Figure 15(b) shows the shear strain level in the soil profile reached as high as about 0.4% indicating the soil behavior entered nonlinear stage under this strong shaking.

As illustrated in Figure 16(a), the spectral acceleration residuals of all models approach to 0 at periods longer than about 0.7 sec. The overall performance of nonlinear models with smaller spectral acceleration residuals is significantly better than linear model. These observations reflect that CC #2 is appropriate for calibrating nonlinear SRA as indicated by its taxonomy evaluation (LP site).

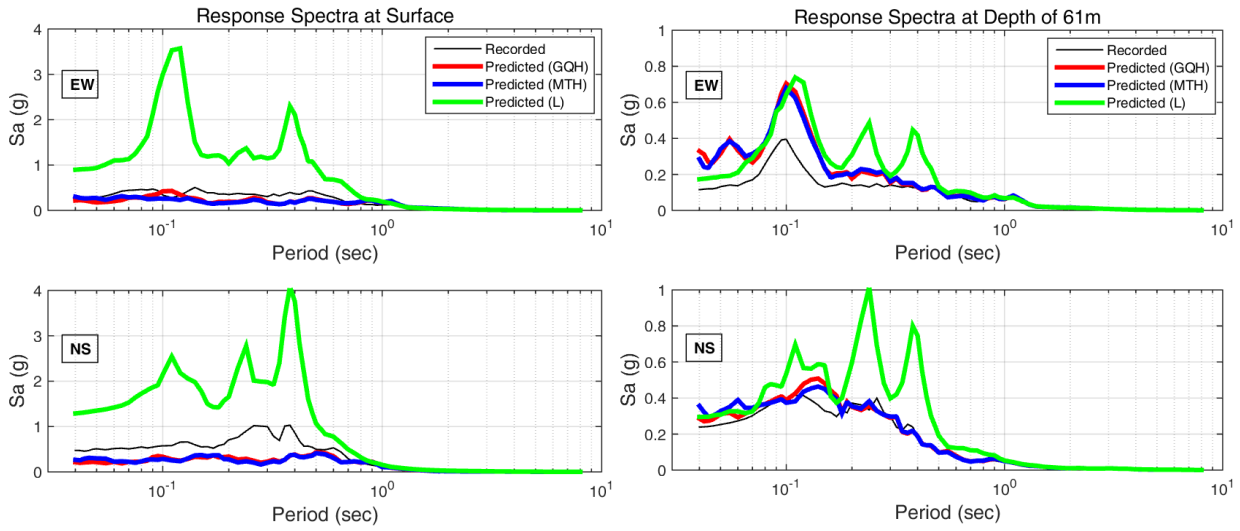

(a) (b)

Figure 14. Comparison of measured and predicted Sa of CC #2 under the shaking of South Napa Earthquake mainshock (a) surface and (b) 61 m depth

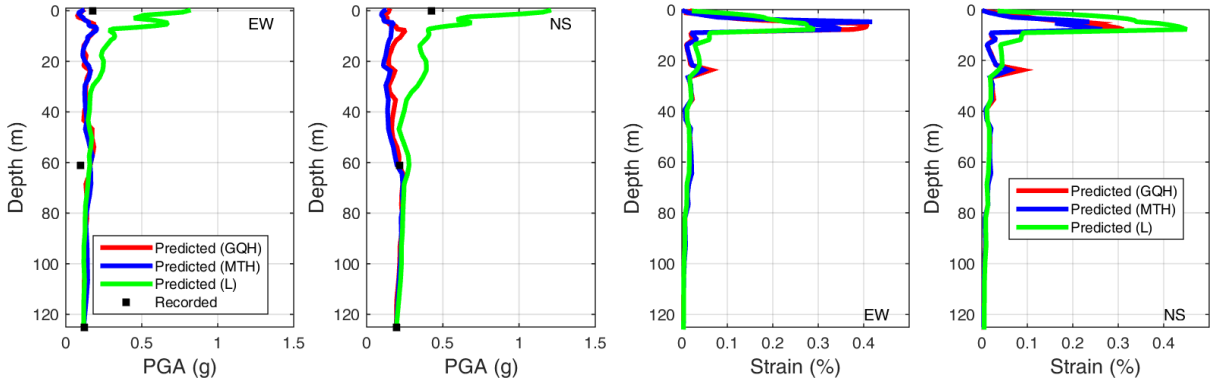

(a) (b)

Figure 15. (a) PGA and (b) max shear strain profiles of CC #2 under the shaking of South Napa Earthquake mainshock

CC #2, South Napa Earthquake Aftershock (08/26/2016)

Figures 17 and 18(a) illustrate the three models (GQH, MTH and L) in general captured the soil response at different depths in both EW and NS directions. The mobilized shear strain level (about 0.01%) as shown in Figure 18(b) is much higher than CC #1 (about 0.003%) although the PGA at CC #1 is larger when subjected to the same event. This is due to the fact that the site of CC #2 is softer than CC #1 as shown in Figures 1 and 2.

As demonstrated in Figure 16(b), all spectral acceleration residuals of linear elastic model are much closer to nonlinear models under the weak shaking compared to the counterparts under the strong shaking. The performance of linear model is improved for this event since the soils behaved essentially linearly and the induced shear strain level was very low.

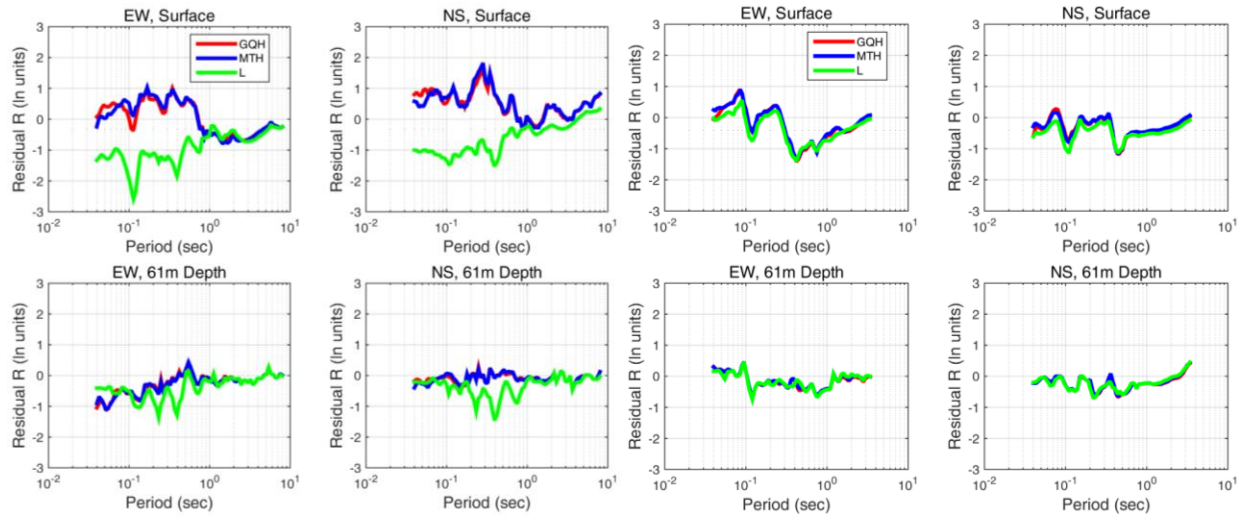

(a) (b)

Figure 16. Spectral acceleration residuals of CC #2 under the shaking of (a) South Napa Earthquake mainshock and (b) South Napa Earthquake aftershock

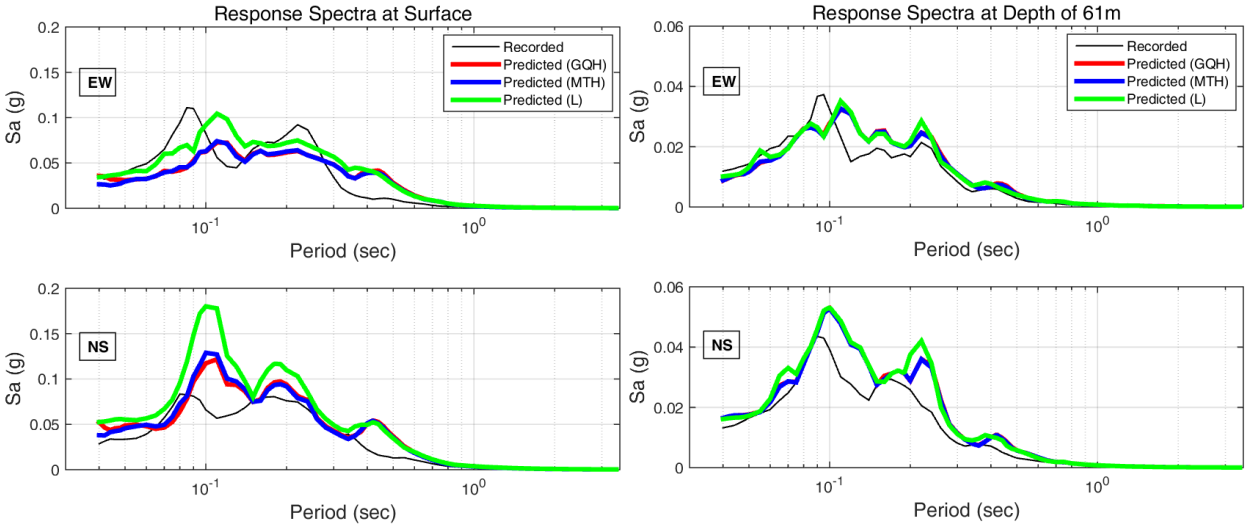

(a) (b)

Figure 17. Comparison of measured and predicted spectral acceleration of CC #2 under the shaking of South Napa Earthquake aftershock (a) surface and (b) 61 m depth

Vallejo, South Napa Earthquake Mainshock

The predictions of GQH and MTH models are in reasonable agreement with the recorded motions in the EW direction at surface and 17.9 m depth in terms of spectral acceleration and PGA as presented in Figures 19 and 20(a). Nevertheless, they in general overestimated the soil response in the NS direction at both depths, especially around 0.3 sec. In addition, the linear elastic model exhibited overestimation in both EW and NS directions at all depths. The maximum shear strain was roughly 0.05% as shown in Figure 20(b), which indicates the nonlinearity is not prevailing in the soil profile.

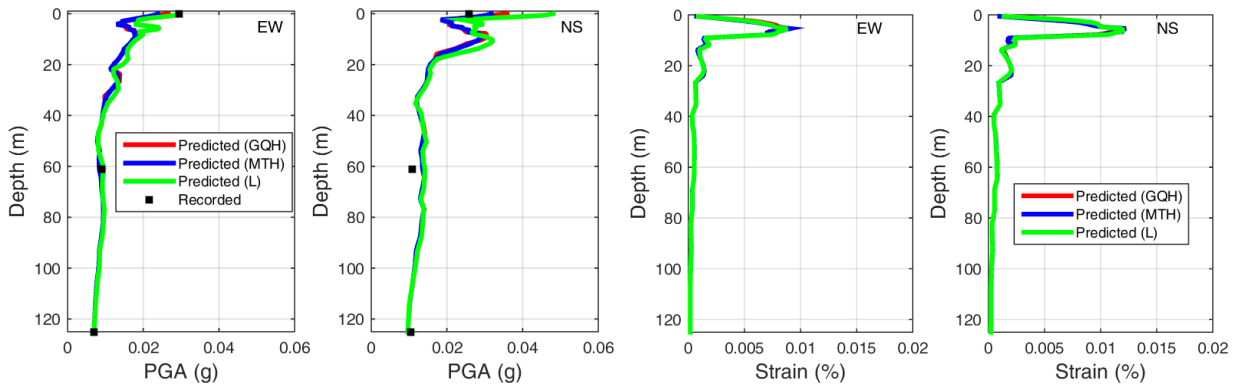

(a) (b)

Figure 18. (a) PGA and (b) max shear strain profiles of CC #2 under the shaking of South Napa Earthquake aftershock

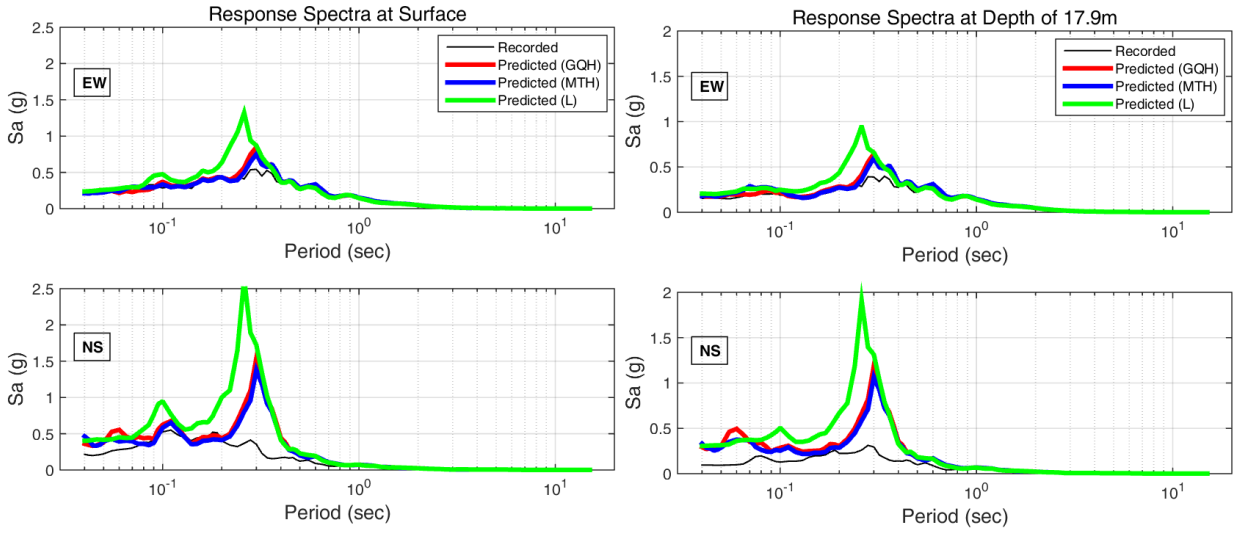

(a) (b)

Figure 19. Comparison of measured and predicted spectral acceleration of Vallejo under the shaking of South Napa Earthquake mainshock (a) surface and (b) 17.9 m depth

As presented in Figure 21, the spectral acceleration residuals are very close to 0 except the NS components at periods smaller than 1.0 sec. This observation is consistent with its taxonomy evaluation (i.e., LP site) demonstrating that Vallejo is ideal for calibration of nonlinear SRA.

Vallejo, South Napa Earthquake Aftershock (08/26/2016)

As can be observed in Figures 22 and 23(a), all three models fairly well reproduced the soil response for all components at various depths. However, remarkable overestimation occurred around 0.25 sec for NS components at surface and 17.9 m depth. The soil behavior remained elastic with peak shear strain approximately 0.001% as shown in Figure 23(b).

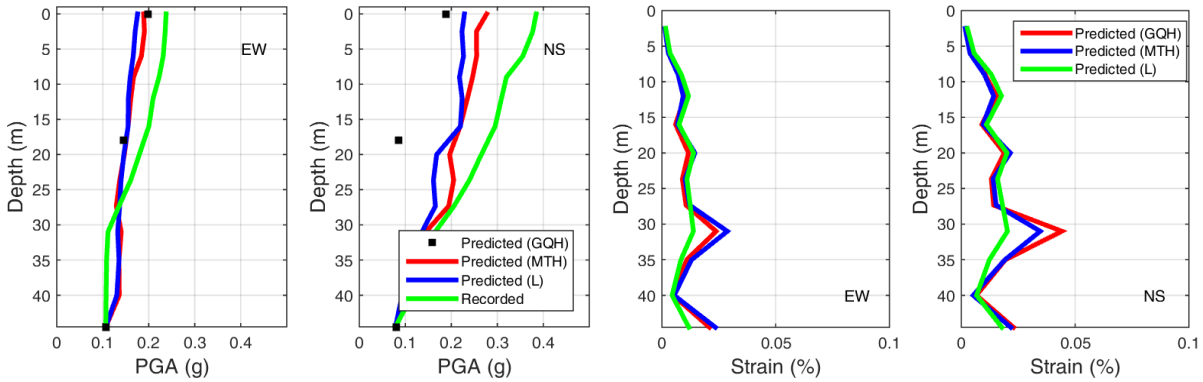

Figure 20. (a) PGA and (b) max shear strain profiles of Vallejo under the shaking of South Napa Earthquake mainshock

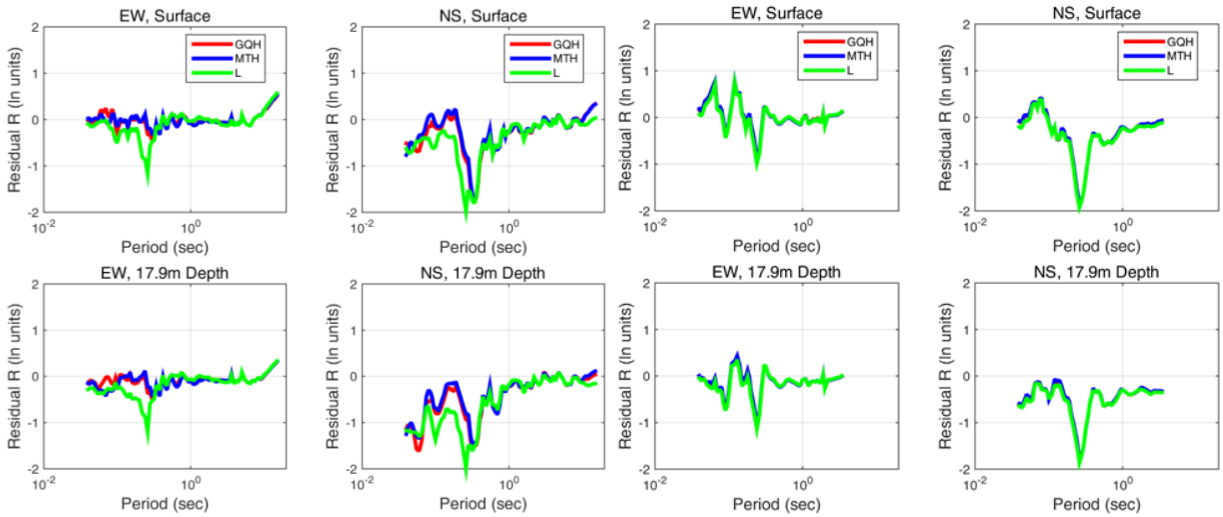

Figure 21. Spectral acceleration residuals of Vallejo under the shaking of (a) South Napa Earthquake mainshock and (b) South Napa Earthquake aftershock

As illustrated in Figure 21(b), the spectral acceleration residuals of all three models are almost identical with each other. In general, the spectral acceleration residuals are negative at surface (NS direction) as well as at 17.9m depth (EW and NS directions). Additionally, spectral acceleration residuals are generally positive at periods smaller than about 0.6 sec and get closer to 0 when periods increase in the EW direction at surface.

Correlation of Taxonomy with Spectral Acceleration Residuals

Figure 24 presents a summary plot to correlate taxonomy designations with surface spectral acceleration residuals of MTH models for CC #1, CC #2 and Vallejo under both strong shaking (the South Napa mainshock) and weak shaking (the South Napa aftershock). Geometric mean was used to combine the two orthogonal horizontal components of ground motion. And the residuals were computed as the average values over short period range (< 0.5 sec) and long

period range (> 0.5 sec). Each subplot is divided by dashed red lines into four panes representing the taxonomy class the sites fall into. Besides, the size of the circles in Figure 24 is linearly proportional to the magnitude of the residuals. The texts adjacent to the circles indicate the actual values of residuals.

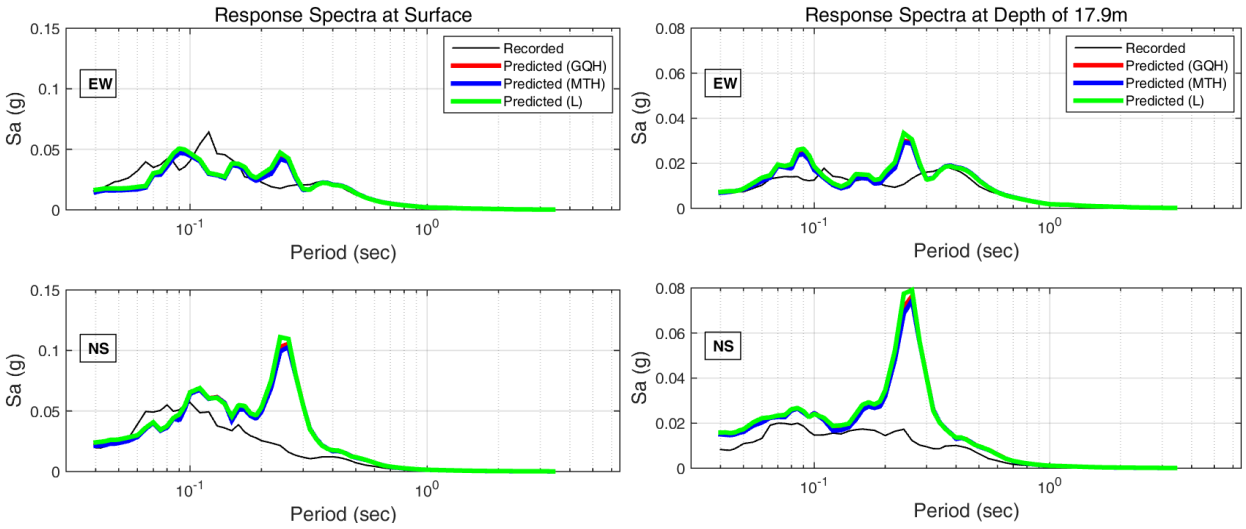

(a) (b)

Figure 22. Comparison of measured and predicted spectral acceleration of Vallejo under the shaking of South Napa Earthquake aftershock (a) surface and (b) 17.9 m depth

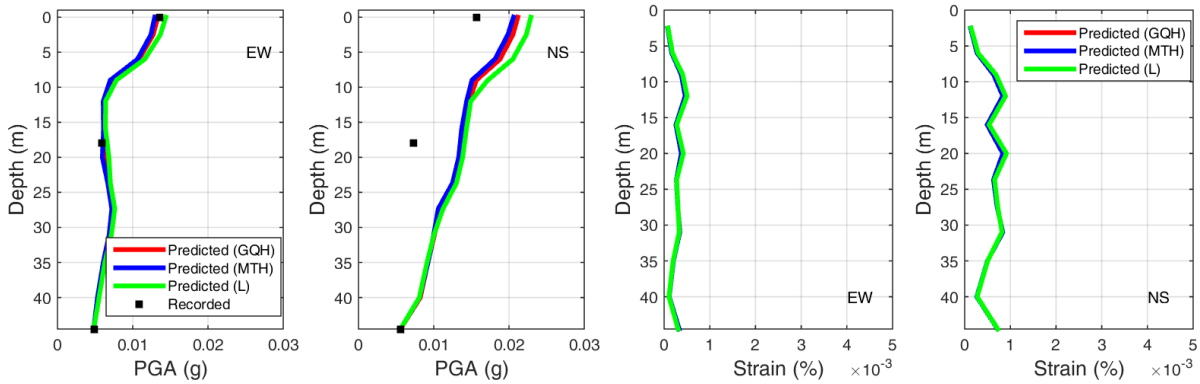

(a) (b)

Figure 23. (a) PGA and (b) max shear strain profiles of Vallejo under the shaking of South Napa Earthquake aftershock

In general, the residuals are larger in magnitude at short period range than at long period range for all arrays and both shaking cases. This means the MTH models were better in reproducing the low frequency contents of the ground motions.

Also, Figure 24 illustrates CC #1 has much larger residuals in magnitude under strong shaking than under weak shaking regardless of period range (0.63 vs. 0.01 throughout short period range and 0.16 vs. 0.01 throughout long period range). This agrees with the indication of taxonomy class of CC #1 as a HP site that it is not a good site for calibrating nonlinear constitutive models.

As implied by taxonomy scheme, Vallejo is a LP site and thus could be well characterized by nonlinear soil models. It is shown in Figure 24 that the residuals of Vallejo are very comparable when subjected to strong and weak shakings at the same period range. This observation is consistent with the implication of taxonomy evaluation.

Similar to Vallejo, the taxonomy class (LP) of CC #2 can be confirmed by the smaller residual of long period range in strong shaking case compared to weak shaking case. However, it is surprising that the residual of short period range is significantly larger in magnitude than the counterpart of long period range. This may be caused by topography effects or soil-structure interaction effects. It is noteworthy that CC #2 has overall higher residuals in magnitude than Vallejo given the same period range and the same shaking case. This can explained by the fact that the goodness-of-fit correlation coefficient of CC #2 is lower than that of Vallejo although these two arrays are both grouped into LP sites.

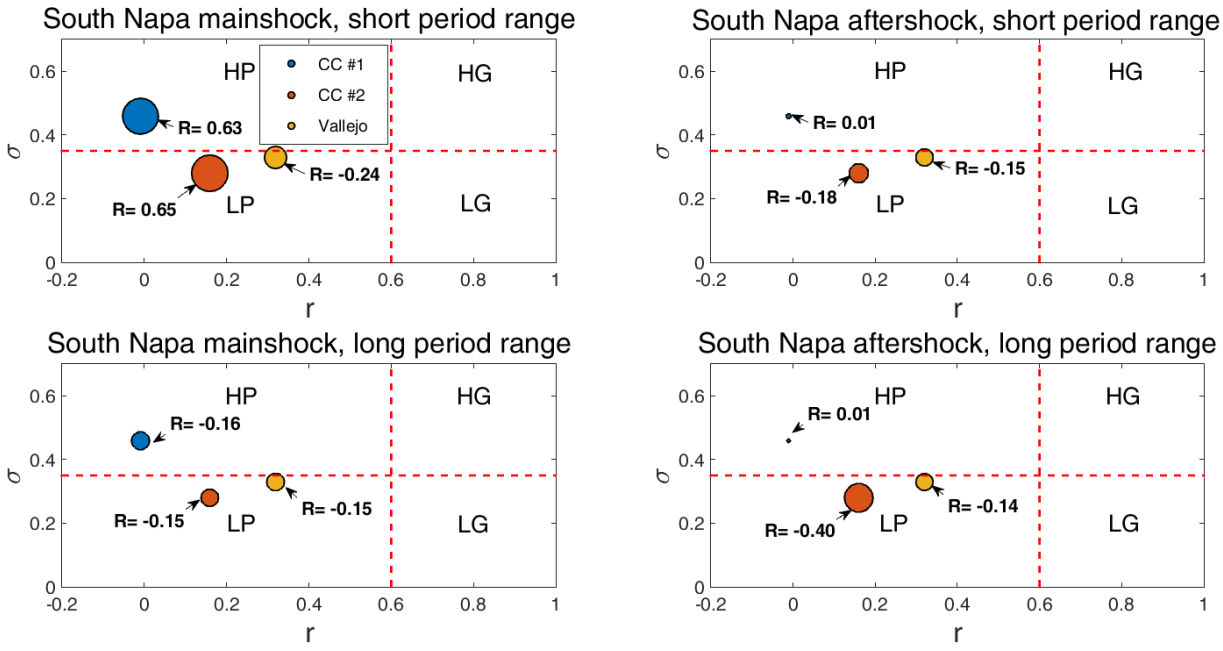

Figure 24. Correlation of taxonomy classes with spectral acceleration residuals at surface of MTH models for all three downhole arrays under the shaking of (a) South Napa Earthquake mainshock and (b) South Napa Earthquake aftershock

Conclusions

This paper evaluated the taxonomy class of three selected CSMIP downhole arrays with the recordings during the 2014 South Napa Earthquake. And the 1D SRA was performed in LS-DYNA for these arrays to study the effect of subsoil conditions on the amplification of ground motions. Both strong and weak shakings were analyzed for each array and the analysis results of the South Napa Earthquake mainshock and aftershock were discussed.

Overall, nonlinear finite element models for all arrays were capable of reproducing the ground motions very well over low frequency range (< 1 Hz) but failed to capture (in most cases

underestimated) the components of the motions intermediate and high frequencies (> 1 Hz). Besides, linear elastic models of arrays in general overestimated the soil response (especially for strong shaking case) and tended to yield intermediate period spectral acceleration peaks caused by resonance of soil profiles.

Regarding CC #1 and #2, GQH and MTH models well captured the soil responses at intermediate depths of soil profiles throughout a wide period range. However, they were unable to reproduce the large amplification of ground motions at surfaces, especially for short period range. These observations suggest that the amplifications of the ground motions at these 2 arrays were significantly influenced by 3D effects (surface waves, basin edge) and possibly structural response with surface waves emanating from the foundations.

As for Vallejo, the predictions of GQH and MTH models agreed fairly well with the observations at both surface and 17.9 m depth. It is noteworthy prominent overprediction was achieved for NS component instead of EW component between 0.2 sec to 0.4 sec for both strong and weak events. This could be attributed to nonhomogenous and anisotropic soil properties (spatial heterogeneity) at the site, which 1D SRA was unable to reproduce.

The strengths and limitations inherent in the practical application of 1D SRA model demonstrates the following: (i) 1D SRA is appropriate for sites with constantly layered stratigraphy in lateral directions, (ii) 1D SRA fails to account for 2D and 3D effects including spatial heterogeneity, nonvertical incidence, basin effects and topographic effects. Considering the presence of complex geologic and topographic conditions, 1D SRA is not quite effective or accurate in estimating site amplification in the selected downhole arrays, especially at shorter periods and large strains, which is consistent with the implications of taxonomy evaluation. As a means to understand the complexity of site response and the validity of 1D SRA assumptions, it is recommended to evaluate taxonomy class of a specific site prior to performing 1D SRA in engineering practice.

Acknowledgements

This project is funded by California Strong Motion Instrumentation Program, California Geological Survey. This support is gratefully acknowledged. We also thank Hamid Haddadi and Moh Huang for providing the needed information to undertake this research. We greatly appreciate Abbas Abghari and Caltrans for providing PS suspension logging data of CC #1 and Vallejo as well as geotechnical reports of all three downhole arrays studied in this paper.

References

Afshari, K., and Stewart, J. P. (2015). Effectiveness of 1D ground response analyses at predicting site response at California vertical array sites. *Proceedings of SMIP 15 Seminar on Utilization of Strong-Motion Data, October 22, 2015, pp. 23 – 40.*

Bray, J., Cohen-Waeber, J., Dawson, T., Kishida, T., and Sitar, N. (2014). Geotechnical engineering reconnaissance of the August 24, 2014 M6 South Napa earthquake. *Geotechnical Extreme Events Reconnaissance (GEER) Association Report Number GEER, 37.*

California Engineering Strong Motion Database (CESMD). *www.strongmotioncenter.org*.

Çelebi, M., Ghahari, S. F., & Taciroglu, E. (2015). Unusual Downhole and Surface Free‐Field Records Near the Carquinez Strait Bridges during the 24 August 2014 Mw 6.0 South Napa, California, Earthquake. *Seismological Research Letters*, 86(4), 1128-1134.

Groholski, D. R., Hashash, Y. M., Kim, B., Musgrove, M., Harmon, J., and Stewart, J. P. (2016). Simplified Model for Small-Strain Nonlinearity and Strength in 1D Seismic Site Response Analysis. *Journal of Geotechnical and Geoenvironmental Engineering, 04016042.*

Hashash, Y.M., Groholski, D.R., Phillips, C.A., Park D., and Musgrove M. *DEEPSOIL 6.1*, User Manual and Tutorial. Univ. of Illinois at Urbana-Champaign: Champaign, Illinois, 2016.

Kramer, S. L. (1996). *Geotechnical Earthquake Engineering*, Prentice Hall, Englewood Cliffs, New Jersey.

LSTC, 2012. LS DYNA Keyword User's Manual Volumes I & II – Release 971 R.6.1.0. Livermore Software Technology Corporation, Livermore, California.

Masing, G. Eigenspannungen und verfestigung beim messing. *In Proceedings of the 2nd international congress of applied mechanics (Vol. 100, pp. 332-5). sn.*

MATLAB, V. (2015). 8.5. 0.197613 (R2015a). The MathWorks Inc., Natick, Massachusetts.

Motamed, R., Stanton, K., Almufti, I., Ellison, K., & Willford, M. (2016). Improved Approach for Modeling Nonlinear Site Response of Highly Strained Soils: Case Study of the Service Hall Array in Japan. *Earthquake Spectra*, 32(2), 1055-1074.

Shakal, A., Haddadi, H., Huang, M., and Stephens, C. (2014). Highlights of Strong−Motion Data from the M6.0 South Napa Earthquake of August 24, 2014. *Proceedings of SMIP 14 Seminar on Utilization of Strong-Motion Data, October 9, 2014, pp. 111– 130.*

Stewart, J. P., Kwok, A. O., Hashash, Y. M. A., Matasovic, N., Pyke, R., Wang, Z., & Yang, Z. (2008). Benchmarking of nonlinear seismic ground response analysis procedures. *Rpt. No. PEER-2008, 4.*

Thompson, E. M., Baise, L. G., Tanaka, Y., & Kayen, R. E. (2012). A taxonomy of site response complexity. *Soil Dynamics and Earthquake Engineering, 41*, 32-43.

TOWARDS IMPROVED GROUND MOTION INTENSITY MEASURES FOR ESTIMATING THE COLLAPSE OF STRUCTURES

Eduardo Miranda and Héctor Dávalos

John A. Blume Earthquake Engineering Center
Dept. of Civil and Environmental Engineering
Stanford University, Stanford

Abstract

Identifying a measure of ground motion intensity that is well correlated with strongly nonlinear response is desirable not only for reducing the required number of response history analyses but also for establishing criteria for selecting ground motion time histories for conducting such analyses. The most commonly used ground motion intensity is the response spectral ordinate of a 5% damped system with a period equal to the fundamental period of the structure being analyzed. In this study we explore and evaluate alternate measure of ground motion intensity with emphasis with those that are well correlated with strongly nonlinear response of multi-degree-of-freedom system and for estimating the probability of collapse of a structure. Preliminary results indicate that using the average of spectral ordinate over a relative wide range of periods including both periods shorter and longer than the fundamental period of vibration leads to significant reductions in the record-to-record variability of ground motion intensities triggering collapse. Other alternatives measure of intensity but based on time domain features of acceleration times histories are also being explored.

Introduction

Currently the large majority of structures located in seismic regions are designed using a linear elastic analysis using either an equivalent static analysis or using a modal response spectrum analysis both of which do not require the use of ground motion acceleration time histories. However, there are several situations where the use of response history analyses becomes necessary or it is mandatory according to current codes. One example is in the calculation of floor response spectrum in which one must compute floor acceleration time histories by conducting response history analyses to then compute response spectra of the computed acceleration response. Floor spectra are then used for the design of secondary systems such as equipment and other nonstructural components attached to structures. In fact, some of the early applications of relatively routinely use of response history analyses was for the design of secondary systems in nuclear power plants in the late 70's and early 80's. Other early use of response history analyses was for the design of seismically isolated structures or for structures incorporating energy dissipation devices for which design procedures for more than 20 years have typically required the use of nonlinear response history analyses. More recently, with the advent of Performance Based Earthquake Engineering, PBEE, nonlinear response history analyses are being used more often (e.g, for the evaluation of existing structures or for the design of tall buildings) and are expected to become even more common in the near future. In particular,

several recent consensus-based documents have highlighted the shortcomings of linear elastic analyses and of nonlinear static analyses and the benefits of using nonlinear response history analyses (FEMA 2005, 2009a, 2009b; NIST 2010). Nonlinear response history analyses are considered the most reliable analytical tool to estimate the seismic performance of a structure.

Unlike equivalent static analyses or modal response spectrum analyses conducting response history analyses requires the selection and scaling of recorded ground motions, the generation of artificial ground motions, or the modification of recorded ground motions to match target spectra. The selection and/or modification of recorded earthquake ground motions as well as the generation of artificial ground motions is closely tied to the parameter or parameters that are used to characterize the level of intensity of a particular ground motion. Moreover, the number of ground motions that are required to conduct the assessment of the seismic performance of a structure is also closely related to the parameter(s) used for characterizing the intensity of a ground motion. In particular, the use of ground motion intensity measures that are well correlated with highly nonlinear response are desirable as a higher correlation leads to a smaller record-to-record variability of the seismic response and therefore to reduced number of ground motions can be used greatly reducing the computational effort involved in the performance assessment.

The main goals of the currently ongoing investigation are: (1) The development of improved intensity measures that are well correlated with strong nonlinear behavior and collapse of structures; (2) Evaluation of improved ground motion intensity measures with emphasis on the level of reduction of record-to-record variability and robustness with respect to intensity measures used today; (3) Development of recommendations for selection and scaling of ground motions based on improved intensity measures.

Shortcomings of Some Ground Motion Intensity Measures

While current code recommend selecting appropriate ground motions from events having magnitudes, fault distance, and source mechanisms that are consistent with those that control the maximum considered earthquake, research by Prof. Cornell and his students (Bazzurro et al. 1998; Shome et al., 1998) has pointed out that such approach requires a very large number of ground motions in order to provide adequate results because of the significant record-to-record variability in the structural response when records are selected based on magnitude and distance bins. Since conventional probabilistic seismic hazard analysis makes use of the five percent damped spectral acceleration at the fundamental period of the structure, $Sa(T_1)$ as a measure of ground motion intensity they proposed scaling all ground motions records to the same spectral ordinate and then computing a measure of response (e.g., mean peak interstory drift demand, probability of exceeding a certain interstory drift or probability of collapse) conditioned on a certain level of spectral acceleration. They noted that this method offered a reduction in record-to-record variability and therefore reduced the required number of ground motions to achieve a certain level of error in the estimate of the response. When using three different sets of records Shome and Cornell (1999) noted that scaling records to $Sa(T_1)$ lead to an average reduction of 40% in the dispersion of peak interstory drift ratios of the structures they analyzed.

While $Sa(T_1)$ provides an exact measure of intensity of the peak deformation of an elastic single-degree-of-freedom (SDOF) system, its efficiency to estimate seismic behavior of structures rapidly diminishes with increasing level of nonlinearity and it leads to large record-to-record variability when used to estimate large nonlinear deformations in multi-degree-of-freedom (MDOF) structures. Figure 1 shows the spectral acceleration $Sa(T_1)$ by which 274 earthquake ground motions need to be scaled to in order to produce the collapse of a post-Northridge 4-story steel moment resisting steel building (Eads et al., 2013). The ground motions were recorded in earthquakes with moment magnitudes between 6.9 and 7.6 and Joyner-Boore distance (horizontal distance between the site and the projection of the fault rupture onto the surface) between 0 and 27 km and on sites classified as NEHRP site classes C or D. It can be seen that the ground motions intensities, when characterized by $Sa(T_1)$, exhibit a very large record-to-record variability with some ground motions producing the collapse of the structure when the record is scaled to a spectral ordinate of 0.48g at T_1=1.33s while others need to be scaled to spectral ordinates as large as 3.27g to produce the collapse of the structure. Also shown in the figure is the median collapse intensity which for this structure is 1.03g, the 5 percentile (ground motion intensity at which only 5% of the ground motions produce collapse in the structure) and 95 percentile (ground motion intensity at which 95% of the ground motions produce collapse). In this case the intensity corresponding to the 95 percentile (2.11g) is 3.64 times larger than the intensity corresponding to the 5 percentile (0.58g) indicating a large variability of the ground motion intensity required to produce collapse one can take the ratio of the 95% intensity to the 5% intensity. The corresponding logarithmic standard deviation is 0.39 which is very large.

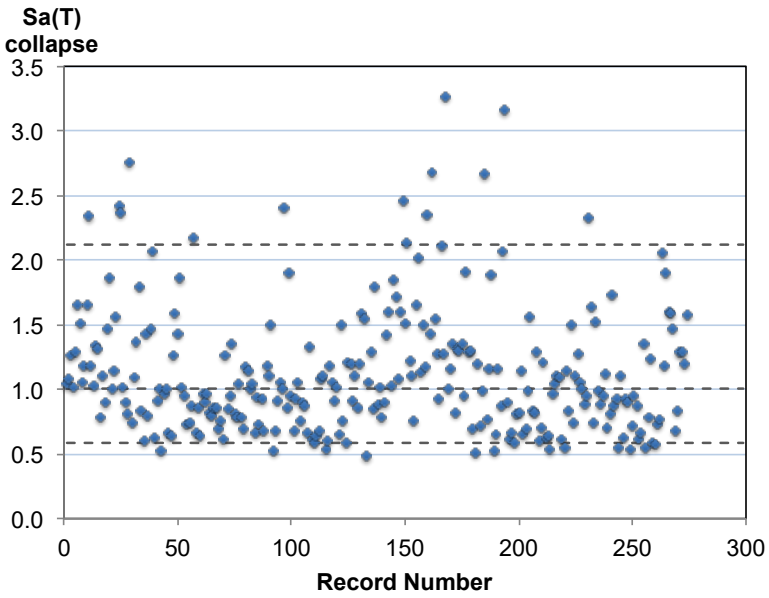

Figure 1. Scaled spectral accelerations at the fundamental period of vibration, $Sa(T_1)$, triggering the collapse of a post-Northridge 4-story steel moment resisting frame building (Eads et al., 2013).

Bazzuro and Cornell (2002) proposed a methodology for evaluating the site-specific seismic hazard of a structure by using a vector of ground motion intensity parameters instead of a

single scalar parameter. Their approach was referred generically as a vector IM. In their simplest case, they proposed a vector comprised of two spectral accelerations, $Sa(f_1)$ and $Sa(f_2)$ at two different oscillator frequencies f_1 and f_2 by using the median spectral ordinate at the two frequencies and correlation between the two spectral ordinates. They noted that this vector *IM* lead to somewhat smaller record-to-record variabilities and therefore better characterization of the seismic demands on the structure than when using $Sa(T_1)$ alone.

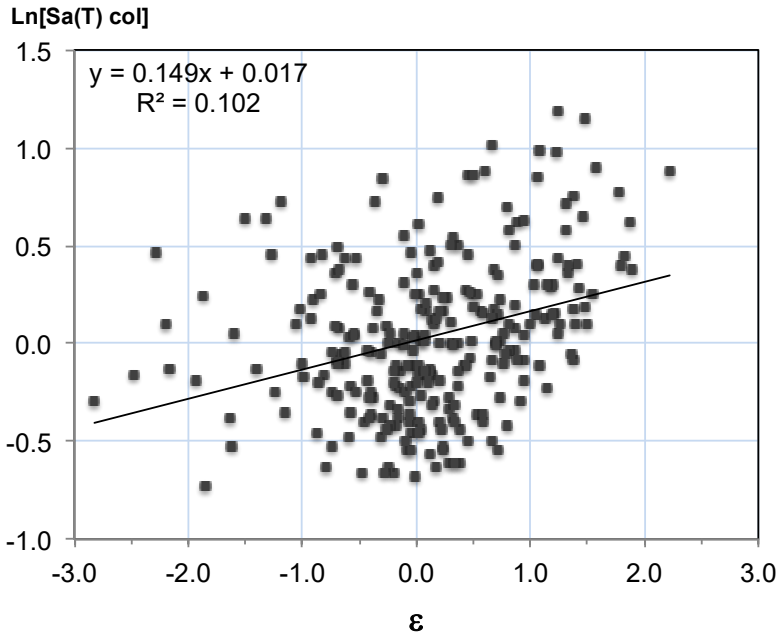

Figure 2. Natural logarithm of $Sa(T_1)$ triggering the collapse of a 4-story SMRF building as a function of the ε of each record (Eads et al., 2013).

More recently, some investigators proposed using another vector *IM* that consists of the five percent damped spectral ordinate at the fundamental period of vibration of the structure $Sa(T_1)$ and the ground motion parameter ε (Baker and Cornell, 2006). The ground motion parameter ε is a measure of the difference between a record's spectral acceleration ordinate at a given period and the median predicted by a ground motion prediction equation (GMPE). They observed that ε could be used as a *proxy* to the spectral shape and when used together with $Sa(T_1)$ it could lead to an improved estimate of the seismic response of a structure. Furthermore, they noted that neglecting the spectral shape could introduce some bias in the results. In particular, they noted that as epsilon increased, that is, as the spectral ordinate at the fundamental period of the structure became larger with respect to the median value estimated by a ground motion attenuation equation the record was more benign, meaning it had to be scaled by a larger factor in order to induce a certain level of response or collapse of a structure. As an example, figure 2 shows a plot of the natural logarithm of the $Sa(T_1)$ by which 274 earthquake ground motions need to be scaled to in order to trigger the collapse of a post-Northridge 4-story steel moment resisting frame building (Eads et al., 2013).

Also shown in figure 2 is a linear fit regressed to the data. As illustrated in the figure, and as previously noted by Baker and Cornell, there is a tendency to increase the collapse intensity as

epsilon increases. They noted that many sites on the west coast of the United States in which design spectral ordinates correspond to values of ε larger than one there would be a tendency to underestimate the median collapse intensity, therefore producing over conservative results if spectral shape was not taken into account when selecting records. In order to avoid conservative results, they proposed a vector *IM* which considers the joint probability distribution of $Sa(T_1)$ and ε. Using this joint probability however, complicates significantly the performance evaluation of structures.

In order to approximately account for the spectral shape when evaluating structures Haselton et al. (2011) proposed a simplified procedure for correcting the collapse capacity of a structure when the spectral shape is not considered in the selection of the records by applying a correction factor whose amplitude is a function of ε. Their method uses a general ground-motion set, selected without regard to ε values, and then corrects the calculated structural response distribution to account for the mean ε expected for the specific site and hazard level. They mention that their method can be applied to all types of structural responses (e.g., interstory drifts and plastic rotations), but their paper focused on the estimation of the collapse capacity of a structure. The correction factor they recommend is based on the linear trend of the spectral shape ε and the natural logarithm of $Sa(T_1)$ from the results of eight reinforced concrete moment resisting frames with heights ranging from 2 to 20 stories. This procedure, which has now also been incorporated into the ATC-63 project and the FEMA P-695 document (FEMA, 2009), avoids having to consider the joint probability distribution of $Sa(T_1)$ and ε. Unfortunately, the procedure focuses on correcting the bias and not on increasing the correlation of the *IM* with collapse and/or in the reduction of the variability/dispersion. As a matter of fact, and contrary to popular belief, considering ε does very little in terms of reducing the record-to-record variability and therefore the vector *IM* consisting on $Sa(T_1)$ and ε remains *a relatively inefficient intensity measure*, meaning it does not leads to a significant reduction in dispersion and hence, although it may correct or partially correct the bias, it still requires a large number of response history analyses in order to estimate the response of the structure with an acceptable level of confidence. Figure 2 also shows the coefficient of determination (R^2) computed from the linear fit on the data which is only 0.1 indicating a relatively poor measure of fit and of correlation of the collapse intensity with ε. This low level of correlations indicates that only about 10% of the large variability in the intensities required to produce collapse is explained by the ε in each record.

To illustrate this important, and often overlooked, aspect of this recently proposed vector *IM*, consider the same four-story steel structure whose results of collapse intensities were previously presented in figures 1 and 2. We now apply a correction of each of the collapse capacities by applying the procedure proposed by Haselton et al. (2011) to account for the effect of ε by decreasing the intensity producing collapse for records with ε's larger than the mean epsilon in the record set and by increasing the intensity producing collapse for records with ε's smaller than the mean epsilon in the record set. Please note that instead of using a generic slope recommended in their paper that is based on their buildings, here we apply the slope that is specific to this structure and this set or records which was previously computed and shown in figure 2 corresponding to the best slope that can be used for this particular structure. The corrected natural logarithms of the collapse intensities as a function of ε are presented in figure 3. As expected, the bias (the slope of the linear trend) has now been fully eliminated, but notice that a large dispersion (variability around the linear fit) remains. To get further understanding on this

important result, the corrected collapse intensities for each record are plotted in figure 4 for each ground motion in the same manner as the uncorrected collapse intensities were plotted in figure 1. Again 5, 50 and 95 percentiles, corresponding to spectral ordinates equal to 0.58, 1.01 and 2.13, respectively, are also plotted in the figure with horizontal dashed lines. By comparing figures 1 and 4 it can be seen that, as previously mentioned, considering ε while it corrects the bias, it does not lead to a significant reduction in dispersion. As a matter of fact, for this structure the ratio of corrected collapse intensities corresponding to 95 percentile to 5 percentile actually has increased to 3.66 which is slightly larger than the ratio of the two percentiles prior to correction for epsilon which was 3.64. The corresponding logarithmic standard deviation does reduce after the correction is applied to consider the effect of ε, but the reduction is minimal, it only reduces from 0.39 to 0.37, which corresponds to only a reduction of approximately 5%.

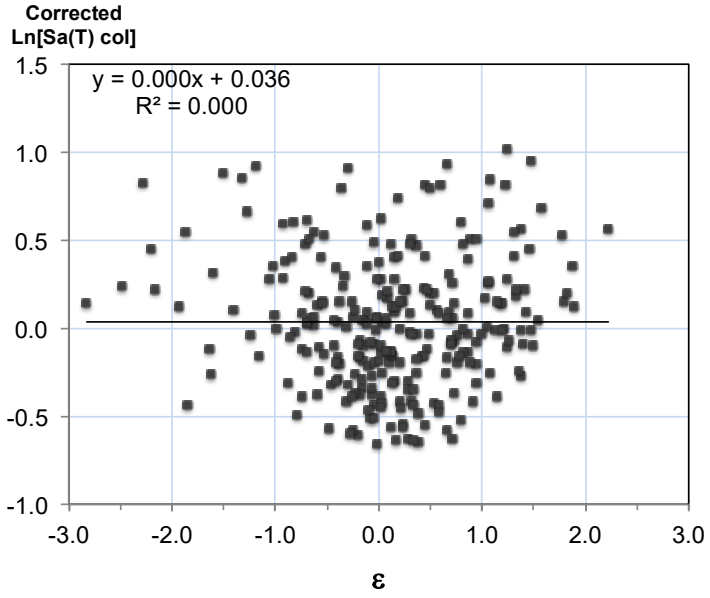

Figure 3. Natural logarithm of spectral accelerations that produce collapse in the four-story steel building after correction to take into account the ε of each record by using the procedure proposed by Haselton et al. (2011).

The reason why consideration of ε does not lead to a significant reduction in dispersion is because ε is not a direct measure of spectral shape but only a proxy to spectral shape as a single spectral ordinate relative to the intensity measured by an attenuation relation by itself cannot provide a measure of spectral shape. With exception of very extreme values, information on ε alone does not provide information on whether the spectral ordinate is in a peak or a valley just like providing the altitude on earth (height relative to sea level) cannot by itself provide an indication whether such point is in a peak or a valley. For example, one could be in a relatively low altitude such as 200 meters above sea level and still be in a peak. One could be in a high elevation such as 2,400 meters above sea level and still be in a valley. Similarly, saying that a spectral ordinate has a negative epsilon, such as -1 does not necessarily imply that such spectral ordinate corresponds to a spectral valley nor a spectral ordinate that has a positive epsilon, such as 1.0 or 1.5 necessarily imply that such spectral ordinate corresponds to a spectral peak.

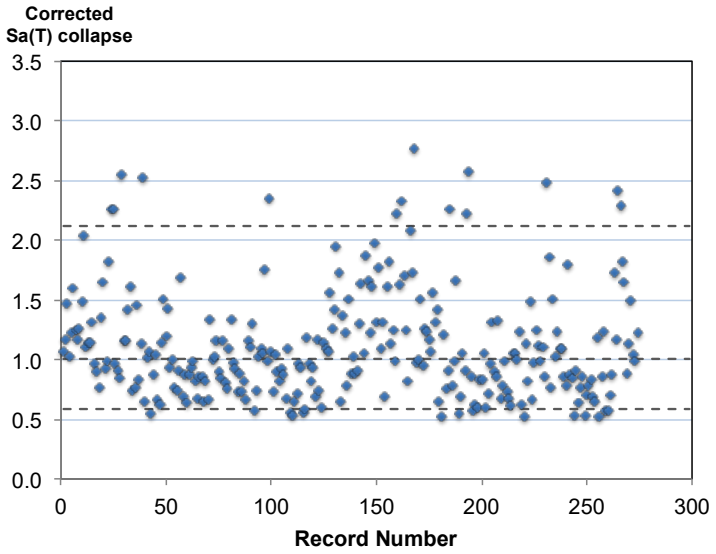

Figure 4. Spectral accelerations that produce collapse the collapse of the four-story steel building after correction by taking into account ε of each record.

As previously illustrated the vector *IM* comprised on $Sa(T_1)$ and ε although it eliminates the bias it does not lead to a significant reduction in record-to-record variability/dispersion hence requiring a relatively large number of ground motions to lead to adequate results. Furthermore, several studies have shown that ε is ineffective in accounting for spectral shape in the case of near-fault pulse-like ground motions (Baker and Cornell, 2006; Bojorquez and Iervolino, 2011). As a matter of fact, Haselton et al. (2011) when proposing their approximate method to consider the effect of ε explicitly wrote in their paper: "*the approach proposed in this paper should not be applied to near-fault motions with large forward-directivity velocity pulses*". This is very important because this type of ground motions is precisely the one that is more likely to produce the collapse of structures. It is then clear that there is a need for improved ground motion intensities.

Towards Improved Ground Motion Intensity Measures

As clearly demonstrated by Shome et al. (1998), having an intensity measure that is strongly correlated with strong nonlinear deformations and collapse of structures has enormous practical consequences for structural engineers. Namely, the level of record-to-record variability achieved in the level of structural response is related to the number of records that the engineer must use for obtaining a reliable estimate of the structural response. In particular, they noted the required number of ground motions required to estimate the structural response within a factor of X (e.g., ± 0.1) with 95% confidence would be given by

$$n = 4\left(\frac{\beta}{X}\right)^2 \tag{1}$$

where β is the level of dispersion in the response when using a certain intensity measure *IM* expressed as the logarithmic standard deviation. From this equation it can be seen that for the same level of desired accuracy the reduction in the necessary ground motions is proportional *to*

the square of the reduction in dispersion. For example, if an improved logarithmic standard deviation is used that leads to a 30% reduction in the level of dispersion, it then allows to obtain an estimate of the response with the same level of accuracy with only half the number of records. This is extremely important because there is a considerable computational effort involved in each nonlinear response history analysis and therefore of the amount of effort involved

Kennedy et al. (1984) noted that the dispersion in the nonlinear response was reduced when each of the ground motion records was scaled with respect to a spectral acceleration found by averaging spectral acceleration over range of periods varying from the fundamental period of the structure T_1 to an elongated equivalent period which depended on the level of nonlinearity in the structure. Shome et al (1998) used this approach with two structures with fundamental periods of vibration of 1.05s and 4.0s and observed reductions of 30% in the dispersion in lateral deformations. The same approach has more recently being used by Bojorquez and Iervolino (2011) who proposed using an improved intensity measure consisting on an average spectral acceleration averaged between the fundamental period of the structure and an elongated period T_N. Bojorquez and Iervolino (2011) proposed using an elongated period $T_N = 2T_1$. They showed that this intensity measure provided a more efficient *IM* than using $Sa(T_1)$ or the vector *IM* comprised on $Sa(T_1)$ and ε.

Here we use a similar, but new and improved intensity measure in which the averaged spectral acceleration takes into account both spectral ordinates that correspond to periods that are smaller than the fundamental period of the structure as well as spectral ordinates corresponding to periods that are longer than the fundamental period of vibration of the structure. Preliminary results suggest that this new improved intensity measure which provides information of the spectral intensity over a much wider range of frequencies leads to smaller dispersions than the one used by Bojorquez and Iervolino. A sample of results are shown in figure 5 which shows average spectral accelerations averaged over a range of period from one fifth of the fundamental period of vibration of the structure (i.e., $0.2T_1$) to three times the fundamental period of vibration of the structure (i.e., $3.0T_1$) that produces collapse of the four-story steel MRF structure previously discussed when subjected to 100 recorded ground motions recorded in earthquakes with moment magnitudes between 6.9 and 7.6 and Joyner-Boore distances (horizontal distance between the site and the projection of the fault rupture onto the surface) between 0 and 27 km and on sites classified as NEHRP site classes C or D. We use information of spectral ordinates of periods much shorter than the fundamental period (up to five times shorter) and spectral ordinates with periods of to three times the fundamental period of vibration, resulting in a period range that is 90% wider (almost twice as wide) than the one previously used by Bojorquez and Iervolino.

Similarly to figures 1 and 4, the 5, 50 and 95 percentiles, which correspond to average spectral ordinates of 0.52, 0.71 and 1.86, respectively, are also plotted in the figure with horizontal dashed lines. By comparing the record-to-record variability in figures 1 and 4 with those in figure 5 it can be readily seen that, a significant reduction in dispersion is produced when using the proposed *IM*. In this case the ratio of the collapse intensities corresponding to 95 percentile to 5 percentile actually is now 1.86 while this ratio was 3.64 for the case in which $Sa(T_1)$ alone was used as an IM or 3.64 when the vector *IM* comprised on $Sa(T_1)$ and ε was used.

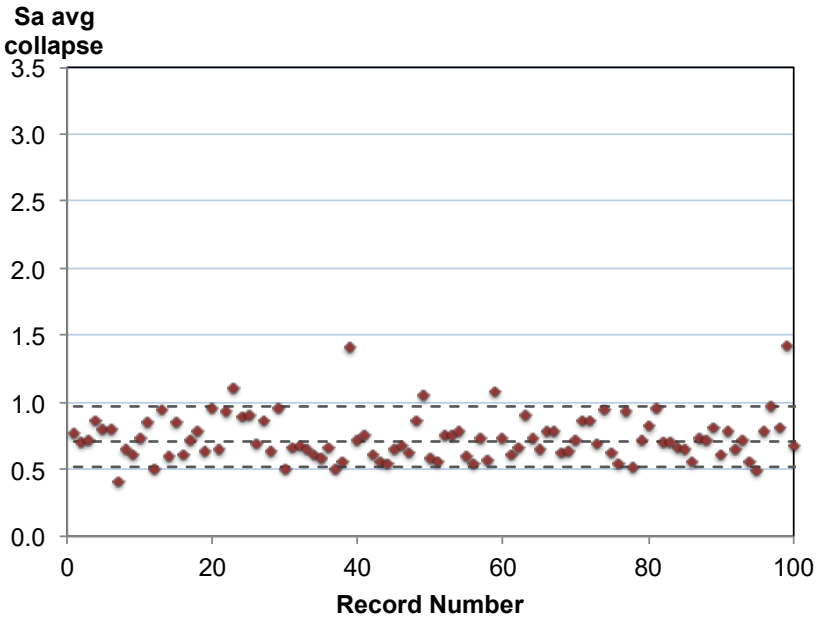

Figure 5. Spectral accelerations averaged over a range of periods from $0.2T_1$ to $3.0T_1$, by which 100 earthquake recorded ground motions need to be scaled to in order to produce the collapse of a post-Northridge 4-story steel moment resisting frame building analyzed by Eads et al. (2013).

The corresponding logarithmic standard deviation for the proposed *IM* is 0.22 which is 44% smaller and 41% smaller the case in which $Sa(T_1)$ alone was used and when the vector *IM* comprised on $Sa(T_1)$ and ε was used, respectively. These reductions in dispersion can translate to being able to use approximately only 31% to 35% of the number of records that would be required when using currently recommended *IM*s, in other words with approximately one third of the computational effort and still be able to achieve a similar level of confidence in the results.

In order to investigate the reason(s) behind the significant reduction in record-to-record variability of ground motion intensities producing the collapse of the structure we plotted the natural logarithm of the spectral intensity triggering the collapse of each record as a function of the ratio of the conventional IM (spectral ordinate at the fundamental period of vibration of the structure) to the average of spectral ordinates of each record averaged over a range of periods from $0.2T_1$ to $3.0T_1$. This ratio is given by

$$SaRatio = \frac{Sa(T_1)}{Sa_{avg}(T_1 \cdot [a, b])} \quad (2)$$

Figure 6 shows the spectral ordinate of 100 ground motions triggering collapse plotted as a function of *SaRatio*, . It can be seen that there is a clear and strong tendency for the collapse-triggering spectral ordinates to increase as *SaRatio* increases, meaning that as Sa(T1) increases relative to the average of spectral ordinates in the range of $0.2T_1$ to $3T_1$) the record becomes more benign and requires a considerably larger intensity to produce collapse in the structure. Also shown in the figure is the equation of the regressed linear trend between *SaRatio* and the natural

logarithm of the spectral ordinate, as well as the coefficient of determination, R^2. Comparing the coefficient of determination previously shown in figure 2 with that shown in figure 6 it can be seen that *SaRatio* provides a coefficient of determination that it is more than six times higher than that of ε. In other words whereas only 10% of the large variability in spectral ordinates of ground motions triggering collapse is due to changes in the ε of each of the records, 62% of the variability is related to changes in *SaRatio*.

Unlike ε which is only a proxy to spectral shape and not a very good one, *SaRatio* is a direct quantitative measure of how much higher or lower is the spectral ordinate at a period equal to the fundamental period of vibration relative to an average spectral ordinates averaged over periods shorter and longer than the fundamental period of vibration. Values higher than one indicate that the spectral ordinate at the fundamental period of vibration of the structure is larger than the average spectral ordinate while values smaller than one indicate that the spectral ordinate at the fundamental period of vibration is lower than the average acceleration. Results shown in figure 6 indicate a records whose spectrum has a peak at the fundamental period of vibration would most likely results in *SaRatio* larger than one and be a more benign record. Similarly, a record with a spectral valley at a period of vibration equal to that of the fundamental period of vibration would tend to have small values of *SaRatio* and be a more damaging record for the structure, meaning it would require to be scaled to a lower level of intensity in order to produce the collapse of a structure. Since *SaRatio* provides, a more direct indication of how high the spectral ordinate is relative to spectral ordinates at periods to the left and to the right of the fundamental period, then it provides a significantly better measure of ground motion intensity.

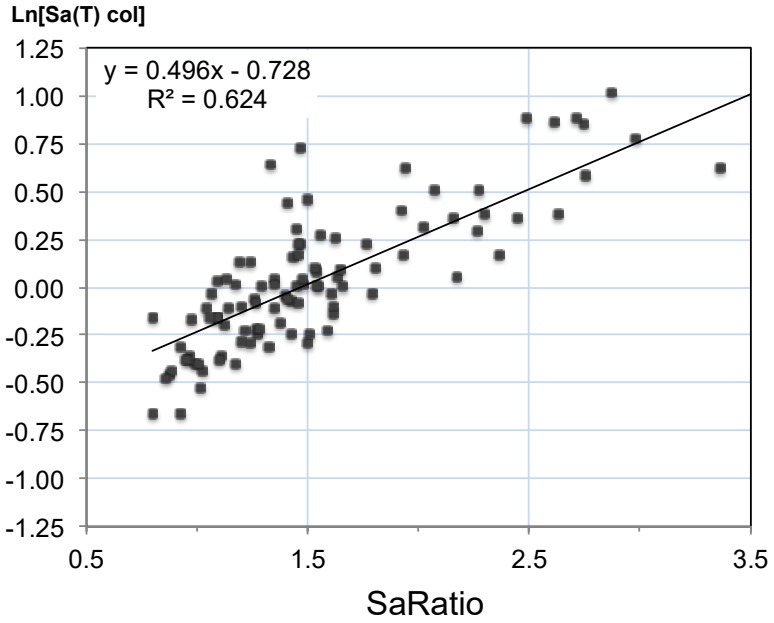

Figure 6. Spectral accelerations of ground motions producing collapse as a function of the *SaRatio* of each record.

But while information of ε is not contained in $Sa(T_1)$ and Baker and Cornell (2006) proposed the use of a vector *IM*, Sa_{avg} is the definition the ratio of $Sa(T_1)$ and *SaRatio* and therefore contain more and better information for describing the intensity of a ground motion. It can be used as a scalar IM just like the conventional Sa(T1). Although results presented in figures 5 and 6 are extremely promising, it is necessary to carefully evaluate the proposed *IM* with: (a) a larger number of ground motions; (b) for different ground motions sets to evaluate if the same *IM* is applicable and equally efficient for other types of ground motions (e.g., near-fault pulse-type ground motions); (c) for different structures with fundamental periods in other spectral regions; (d) explore the optimum period range in which spectral ordinates should be averaged. Furthermore, it is important to also evaluate other alternative improved *IM*s. As part of this ongoing investigation, at present time we are evaluating two alternative *IM*s based in time domain features of acceleration time histories.

Summary and Conclusions

Using the spectral ordinate at the fundamental period of vibration of a structure as a ground motion intensity measure has the advantage that it corresponds to the way in which seismologists and geotechnical engineers have described the intensity of a ground motion and a large and important body of research has been devoted to developing equations to estimate spectral ordinates as a function of the magnitude, distance, focal mechanism and site conditions. However, most structures cannot adequately be modeled as single-degree-of-freedom systems and therefore information or the intensity of the ground motion at other periods/frequencies is neglected. Furthermore, current design provisions allow strong nonlinearities to occur in the structure in the event of strong earthquake ground motions and motions that are well correlated with large responses in linear SDOFs are not necessarily the same as those producing large responses in nonlinear SDOF systems, therefore improved intensity measures are needed to establish the criteria by which ground motions are selected and scaled for conducting nonlinear response history analyses.

The use of a vector *IM* consisting of the spectral ordinate at the fundamental period of vibration and ε was evaluated and was found to provide better results for reducing possible biases in the response, however, the record-to-record variability remains approximately the same as that when using $Sa(T_1)$ alone and therefore the required number of ground motions and the computational effort is not reduced. This is because, with the exceptions of very extreme values, ε does not provide a good measure of spectral shape as it does not contain any information about spectral ordinates at other periods of vibrations.

An improved *IM* consisting of an average spectral ordinates which are averaged between period of $0.2T_1$ and $3T_1$ is being evaluated. This intensity measure is found to have a much stronger correlation with strong nonlinear response and therefore leads to significantly smaller record-to-record variability. The reason why this improved *IM* reduces record-to-record variability is because it contains far more information about the intensity of the ground motion. In particular, it was found the ratio of the spectral ordinate at the fundamental period of vibration of the system to Sa_{avg} is strongly correlated to the spectral ordinate of ground motions triggering the collapse of structures, therefore using Sa_{avg} which corresponds to the ratio of Sa(T1) and

SaRatio provides a better measure of ground motion intensity. The main advantages can be summarized as follows:

1. Has a significantly higher level of correlation with large inelastic deformation and with collapse intensities than currently recommended intensity measures such as $Sa(T_1)$ or the vector *IM* comprised on $Sa(T_1)$ and ε;

2. Requires only about a third of the number of ground motions with respect to current *IM*s to achieve the same level of desired accuracy in the estimated seismic response;

3. Similarly to $Sa(T_1)$ it is a scalar that it is easy to interpret and does not require joint probability distributions between $Sa(T_1)$ and ε or correlations between the spectral ordinates (or ε) at the fundamental period of vibration and those at other periods of vibration;

4. It is somewhat similar to scaling procedures currently used by practicing engineers as specified in chapter 16 of ASCE 7 in which each pair of motions is scaled such that in the period range from $0.2T_1$ to $1.5T_1$, the average of the SRSS spectra from all horizontal component pairs does not fall below the corresponding ordinate of the response spectrum used in the design;

5. It is equally applicable to all types of ground motions, including near fault pulse-like ground motions and therefore does not require the use of different procedures for different types of ground motion.

Acknowledgements

Several aspects of the research being conducted in this study are based on research conducted by Dr. Laura Eads while she was a doctoral student working under the guidance of the first author. Her work provides the basis of some of the spectral-based intensity measures being evaluated in this study and have also provided some guidance for the exploration of new improved intensity measures based on time domain features of the acceleration time histories.

This study is being supported by the California Strong Motion Instrumentation Program of the California Geological Survey. Their financial support is gratefully acknowledged. Special thanks are given to Anthony Shakal, Moh Huang as well as members of the Strong Motion Instrumentation Advisory Committee for their comments and suggestions.

References

American Society of Civil Engineers ASCE (2010), ‘‘Minimum design loads for buildings and other structures.’’ ASCE 7-10, ASCE, Reston, Va.

Baker, J. W., & Cornell, C. A. (2006). *Vector-valued ground motion intensity measures for probabilistic seismic demand analysis*. Pacific Earthquake Engineering Research Center, College of Engineering, University of California, Berkeley.

Bazzurro, P., Cornell, C. A., Shome, N., & Carballo, J. E. (1998). Three proposals for characterizing MDOF nonlinear seismic response. *Journal of Structural Engineering*, *124*(11), 1281-1289.

Bojorquez, E., & Iervolino, I. (2011). Spectral shape proxies and nonlinear structural response. *Soil Dynamics and Earthquake Engineering*, *31*(7), 996-1008.

Eads, L., Miranda, E., Krawinkler, H., & Lignos, D. G. (2012) Deaggregation of Collapse Risk. In *20th Analysis and Computation Specialty Conference* (pp. 521-531). ASCE.

Eads, L., Miranda, E., Krawinkler, H., & Lignos, D. G. (2013). An efficient method for estimating the collapse risk of structures in seismic regions. *Earthquake Engineering & Structural Dynamics*, *42*(1), 25-41.

FEMA 440 (2005), Improvement of nonlinear static seismic analysis procedures. Report FEMA 356, Federal emergency management agency, Washington DC, 2005.

FEMA, P. 440A (2009) Effects of strength and stiffness degradation on seismic response. *Federal Emergency Management Agency, Washington, DC*.

FEMA (2009). Quantification of Building Seismic Performance Factors (FEMA P695 Report), prepared by Applied Technology Council for the Federal Emergency Management Agency. Washington, D.C.: FEMA.

FEMA, P. 58 (2012). *Seismic performance assessment of buildings. Report P-58, Prepared by Applied Technology Council as ATC*, *58*, Federal Emergency Management Agency Washington, D.C.

Haselton, C. B., Baker, J. W., Liel, A. B., & Deierlein, G. G. (2009). Accounting for ground-motion spectral shape characteristics in structural collapse assessment through an adjustment for epsilon. *Journal of Structural Engineering*, *137*(3), 332-344.

Kennedy, R. P., Short, S. A., Merz, K. L., Tokarz, F. J., Idriss, I. M., Power, M. S., & Sadigh, K. (1984). *Engineering characterization of ground motion. Task I. Effects of characteristics of free-field motion on structural response* (No. NUREG/CR-3805). Structural Mechanics Associates, Inc., Newport Beach, CA (USA); Woodward-Clyde Consultants, Walnut Creek, CA (USA).

National Institute of Standards and Technology (NIST) (2010) Applicability of nonlinear multiple-degree-of-freedom modeling for design. Report NIST GCR 10-917-9, prepared by the NEHRP Consultants Joint Venture, Gaithersburg

Shome, N., Cornell, C. A., Bazzurro, P., & Carballo, J. E. (1998). Earthquakes, records, and nonlinear responses. *Earthquake Spectra*, *14*(3), 469-500.